

Investigation of Aerodynamic Braking Devices for Wind Turbine Applications

*D. A. Griffin
R. Lynette & Associates
Seattle, Washington*

NREL technical monitor: Paul Migliore



National Renewable Energy Laboratory
1617 Cole Boulevard
Golden, Colorado 80401-3393
A national laboratory of the U.S. Department of Energy
Managed by Midwest Research Institute
for the U.S. Department of Energy
under contract No. DE-AC36-83CH10093

Work performed under Subcontract No. ZAA-5-12272-05

April 1997

NOTICE

This report was prepared as an account of work sponsored by an agency of the United States government. Neither the United States government nor any agency thereof, nor any of their employees, makes any warranty, express or implied, or assumes any legal liability or responsibility for the accuracy, completeness, or usefulness of any information, apparatus, product, or process disclosed, or represents that its use would not infringe privately owned rights. Reference herein to any specific commercial product, process, or service by trade name, trademark, manufacturer, or otherwise does not necessarily constitute or imply its endorsement, recommendation, or favoring by the United States government or any agency thereof. The views and opinions of authors expressed herein do not necessarily state or reflect those of the United States government or any agency thereof.

Available to DOE and DOE contractors from:
Office of Scientific and Technical Information (OSTI)
P.O. Box 62
Oak Ridge, TN 37831
Prices available by calling (423) 576-8401

Available to the public from:
National Technical Information Service (NTIS)
U.S. Department of Commerce
5285 Port Royal Road
Springfield, VA 22161
(703) 487-4650



FOREWORD

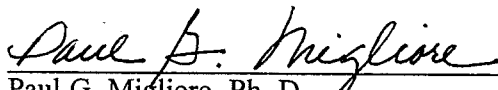
The National Wind Technology Center of the National Renewable Energy Laboratory (NREL) is supporting the efforts of its industry partners to develop advanced, utility-scale wind turbines. Part of the research being conducted focuses on innovative components and subsystems that eventually may be incorporated into these advanced turbines. R. Lynette & Associates chose to investigate, among other technologies, the use of trailing-edge aerodynamic brakes as an alternative to the rotating tips and tip vanes that are typical of stall-controlled wind turbine rotors.

The use of trailing-edge devices for aerodynamic control of wind turbine rotors has attracted renewed interest recently, notably by New World Power Technology Company, Zond Systems, Inc., R. Lynette & Associates and PS Enterprises, Inc.. These companies are seeking improvements in aerodynamic-braking and power-regulation systems with regard to cost, weight (or weight distribution), noise, and reliability. At first, there was considerable speculation regarding the effectiveness of various aerodynamic shapes. Most of this uncertainty has been laid to rest by the comprehensive wind-tunnel tests, and limited atmospheric tests, referenced herein. The next logical questions relate to the cost and weight of realistic implementations of trailing-edge devices. These are the issues that are addressed in this report.

As is the case with all competing technologies, the ultimate success of trailing-edge devices requires them to be embraced by a particular designer and brought to maturity by iterative cycles of design, fabrication, test, and redesign. Only then will the remaining questions of noise, icing, reliability, and maintainability be answered.

The author and his colleagues, Don Roberts, Gene Quandt, Scott Miller and Art Porter, are commended for the formulation and execution of a meticulous engineering process -- literature search, wind-tunnel tests, data analysis and system design -- all executed with precision and scrupulous attention to detail.

NREL and the U. S. Department of Energy are proud to support research activities of the high quality represented by this project and documented in this report.



Paul G. Migliore, Ph. D.
NREL Senior Project Manager

PREFACE

The present work was supported by the National Renewable Energy Laboratory (NREL) under Subcontract #ZAA-5-12272-05, monitored by Paul Migliore. The author would like to thank Paul and others at NREL for their support on this project.

The wide range of flap configurations tested in the wind tunnel, and the quality of the data, formed a solid foundation for the sizing and deployment analyses. Art Porter of the Wichita State University (WSU) machine shop was invaluable in the detailed design and manufacture of the wind tunnel model and instrumentation. The success of the wind tunnel test was due to the outstanding work performed by Bonnie Johnson and the entire crew of the WSU wind tunnel. Scott Miller provided excellent technical support throughout the test.

Much of this project was completed by Richard Beckett, including the origination of the flip-tip concept, preliminary device selection, sizing, loads analysis, and preliminary mechanical designs. Gene Quandt also provided much support through all phases of this work. At Advanced Wind Turbines, Inc., Don Roberts performed the detailed design work, as well as the cost and weight analyses. The author would like to acknowledge and thank Richard, Gene, and Don for their invaluable contributions to this work.

ABSTRACT

This report documents the selection and preliminary design of a new aerodynamic braking system for use on the stall-regulated AWT-26/27 wind turbines. The goal was to identify and design a configuration that offered improvements over the existing tip brake used by Advanced Wind Turbines, Inc. (AWT). Although the design objectives and approach of this report are specific to aerodynamic braking of AWT-26/27 turbines, many of the issues addressed in this work are applicable to a wider class of turbines. The performance trends and design choices presented in this report should be of general use to wind turbine designers who are considering alternative aerodynamic braking methods.

A literature search was combined with preliminary work on device sizing, loads and mechanical design. Candidate configurations were assessed on their potential for benefits in the areas of cost, weight, aerodynamic noise, reliability and performance under icing conditions. As a result, two configurations were identified for further study: the "spoiler-flap" and the "flip-tip." Wind tunnel experiments were conducted at Wichita State University to evaluate the performance of the candidate aerodynamic brakes on an airfoil section representative of the AWT-26/27 blades. The wind tunnel data were used to predict the braking effectiveness and deployment characteristics of the candidate devices for a wide range of design parameters. The evaluation was iterative, with mechanical design and structural analysis being conducted in parallel with the braking performance studies.

A spoiler-flap with active mechanical deployment was selected for detailed design. The system was designed to meet the aerodynamic braking requirements of the AWT-26 turbine. Structural analysis of the design was performed for both the device and the modified turbine blade. Although estimates showed an increased component weight of 4.9 kg (10.8 lb) per blade, this would be partially offset by improvements in weight distribution.

The preliminary estimate of the spoiler-flap system cost was \$150 less than the production AWT-26/27 tip vanes. This represents a reduction of approximately 5% in the cost of the aerodynamic braking system. In view of the preliminary nature of the design, it would be prudent to plan for contingencies in both cost and weight. Nevertheless, the results of this study are encouraging for a first-generation design.

TABLE OF CONTENTS

1. INTRODUCTION.....	1-1
1.1 Background.....	1-1
1.2 Project Schedule.....	1-1
1.3 Purpose.....	1-1
1.4 Objectives	1-2
1.5 Approach	1-2
2. AERODYNAMIC BRAKING DEVICES	2-1
2.1 Overview	2-1
2.2 General Aerodynamic Brake Performance	2-3
3. INITIAL CONFIGURATION DEFINITIONS	3-1
3.1 Baseline Configuration, AWT-26/27 Tip Vane	3-1
3.2 Candidate Configurations.....	3-3
3.2.1 Spoiler-Flap.....	3-3
3.2.2 Flip-Tip.....	3-5
4. WIND TUNNEL EXPERIMENTS	4-1
4.1 Model Design and Instrumentation	4-1
4.2 Test Matrix.....	4-3
4.3 Wind Tunnel Test Results and Discussion	4-4
4.3.1 Baseline S810 Airfoil	4-4
4.3.2 45% Chord Devices.....	4-4
4.3.3 Effect of Device Chord.....	4-12
4.3.4 Reynolds Number Effects.....	4-13
4.3.5 Partial-Span Effects	4-16
5. SIZING AND DEPLOYMENT STUDIES.....	5-1
5.1 AWT-26/27 Braking Requirements.....	5-1
5.2 Sizing of Candidate Devices	5-3
5.3 Aerodynamic Deployment Calculations.....	5-6
5.3.1 Spoiler-Flap.....	5-8
5.3.2 Flip-Tip.....	5-14
5.4 Active Mechanical Deployment	5-14
5.5 Passive Mechanical Deployment	5-18
5.6 Configuration Selection for Detailed Design	5-18
6. DESIGN OF SPOILER-FLAP FOR AWT-26/27 ROTOR	6-1
6.1 Mechanical Design.....	6-1
6.1.1 Overview of Device Construction.....	6-2
6.1.2 Mechanical System Description.....	6-3
6.2 Loads and Structural Analysis.....	6-6
6.2.1 Blade Loads and Structural Analysis	6-6
6.2.2 Device Loads and Structural Analysis.....	6-7
6.3 Cost and Weight Estimates.....	6-8
7. CONCLUSIONS	7-1
8. REFERENCES.....	8-1

LIST OF FIGURES

Figure		Page
2-1	Velocity and Force Diagram at Radial Blade Position	2-3
2-2	Example C_p -TSR Curve for AWT-26 with Deployed Aerodynamic Brake	2-5
3-1	General Configuration of the AWT-26/27 Turbines	3-1
3-2	Major Components of AWT-26/27 Tip Vanes	3-2
3-3	Isometric View of Deployed Spoiler-Flap	3-4
3-4	Isometric View of Deployed Flip-Tip	3-6
4-1	Section View of Wind Tunnel Model	4-1
4-2	End View of Flap Deflection Assembly	4-2
4-3	Effect of Gap Seal on 38% Chord Device	4-5
4-4	Effect of Gap Seal on 45% Chord Device	4-5
4-5	Aerodynamic Coefficients for 45% Chord Plain Flap, Hinge A-1	4-6
4-6	Aerodynamic Coefficients for 45% Chord Spoiler-Flap, Hinge A-3	4-8
4-7	Effect of Hinge Location on Device at $\delta = 75^\circ$	4-10
4-8	Braking Effectiveness per Unit Device Chord	4-12
4-9	Reynolds Number Effect on Spoiler-Flap	4-14
4-10	Sectional View of Model with Partial-Span Plates	4-16
4-11	Effect of Finite Aspect Ratio on Flap Braking Effectiveness	4-17
5-1	AWT-26 Rotor Power at Varying Rotational Speeds	5-1
5-2	Rotor Power Coefficients for AWT-26 at Low TSR	5-2
5-3a	Sizing of Flip-Tip for AWT-26 Aerodynamic Braking	5-5
5-3b	Sizing of Spoiler-Flap for AWT-26 Aerodynamic Braking	5-5
5-4	Estimated Hinge Moment Data for 45% Chord Spoiler-Flap at Hinge Location A-4.5	5-10
5-5	Rotor Power Coefficients for Deployed Spoiler-Flap	5-11
5-6	Improper Spring and Damping Rates for Aerodynamically Deployed Spoiler-Flap	5-13
5-7	Near-Optimal Spring and Damping Rates for Aerodynamic Deployment of Spoiler-Flap	5-13
5-8	Rotor Power Coefficients for Deployed Flip-Tip	5-15
5-9a	Hinge Moment Data for Balanced Spoiler-Flap, Hinge A-3	5-16
5-9b	Hinge Moment Data for Balanced Spoiler-Flap, Hinge A-3.5	5-16
5-10	Rotor Power Coefficients for Deployed Spoiler-Flap	5-17
6-1	AWT-26 Blade Planform with Spoiler-Flap Location Shown	6-2
6-2	Spoiler-Flap Hinge / Thrust Bearing Configuration at Station 464	6-3
6-3	Layout of Mechanical Actuation Driver	6-4
6-4	Sectional Layout of Mechanical Driver	6-5
6-5	Station 374 Blade Section Properties	6-7

LIST OF TABLES

Table		Page
1-1	Major Aerodynamic Brake Development Tasks Completed	1-1
2-1	Characteristics of Current Aerodynamic Brake Designs	2-2
3-1	Cost and Weight for Major Tip-Vane Subsystems	3-2
4-1	Flap Configurations Tested by Standard δ -Sweep	4-3
5-1	Variation of Spoiler-Flap Effectiveness with Spanwise Location.....	5-6
5-2	Blade-Tip Aerodynamics for Normal Operation of AWT-26/27.....	5-10
5-3	Spring and Damping Torque Schedule for Spoiler-Flap Deployment Simulations	5-12
5-4	Actuation Requirements for Active Mechanical Deployment of Spoiler-Flap	5-18
6-1	Actuator Specifications.....	6-5
6-2	Blade Bending Loads at Station 374.....	6-6
6-3	Blade Percentage Stress Increments at Station 374	6-7
6-4	Device Critical Loads	6-8
6-5	Device Critical Stresses.....	6-8
6-6	Cost and Weight Analysis Summary	6-9

ABBREVIATIONS

AWT	Advanced Wind Turbines, Inc.
BEMT	Blade element momentum theory
CER	Combined experiment rotor
cm	Centimeter/centimeters
ft	Feet/foot
FMEA	Failure modes and effects analysis
ID	Inner diameter
in.	Inch/inches
kip	Kilo-pound/pounds force
kg	Kilogram
kPa	Kilopascal
kV	Kilovolt
kW	Kilowatt
LEGR	Leading-edge grit roughness
lbs	Pounds force
m	Meter/meters
mm	Millimeter/millimeters
mph	Miles per hour
N	Newton/Newtons
NGIS	Next-Generation Innovative Subsystems
NREL	National Renewable Energy Laboratory
OD	Outer diameter
OSU	Ohio State University
Pa	Pascal/pascals
psf	pounds per square foot
psi	pounds per square inch
rad	Radian/radians
RLA	R. Lynette & Associates
Re	Reynolds number
rpm	Revolutions per minute
s	Second/seconds
WSU	Wichita State University

LIST OF SYMBOLS

a, a'	Interference factors that account for presence of rotor (defined in Section 2.2)
A_{rotor}	Swept area of rotor
A_{section}	Area of turbine blade section
A_{vane}	Planform area of tip vane
c	Airfoil chord / local blade chord
c_{Device}	Device chord
C_D	Drag coefficient (defined in Section 2.2)
$C_{D\text{max}}$	Maximum value of drag coefficient
C_h	Hinge moment coefficient (defined by Equation 4-1)
C_L	Lift coefficient (defined in Section 2.2)
$C_{L\text{max}}$	Maximum value of lift coefficient
$C_{L\alpha=0}$	Value of lift coefficient at zero angle of attack
$C_{P, \text{rotor}}$	Rotor power coefficient (defined by Equation 2-6)
C_N	Normal force coefficient (defined by Equation 2-2)
C_S	Suction coefficient (defined by Equation 2-1)
$C_{S\text{max}}$	Maximum value of suction coefficient
$C_1, C_2,$	Coefficients to account for drivetrain load/losses (defined in Equation 5-3)
C_3, C_4	Damping and spring coefficients for flap deployment (defined in Equation 5-4)
D	Drag force
I_{Flap}	Rotational moment of inertia of flap about the hinge line (defined in Equation 5-4)
I_{Rotor}	Rotational moment of inertia of the rotor system about the low-speed shaft (defined in Equation 5-3)
L	Lift force
M_{LSS}	Moment or torque about rotor low-speed shaft
P	Power
P_{rotor}	Rotor power
q	Dynamic pressure (defined in Section 2.2)
r	Radial position along turbine blade
R	Total radial dimension of blade
TSR	Tip-speed ratio (defined by Equation 2-7)
$\text{TSR}_{\text{equilibrium}}$	Stable tip-speed ratio under freewheeling rotor conditions (defined by Equation 2-8)
TSR_{max}	Maximum allowable tip-speed ratio
u	axial component of inflow velocity (defined in Section 2.2)
V_o	Free-stream wind speed
W	Resultant velocity vector at wind turbine blade (defined in Section 2.2)
w	"Swirl" velocity (defined in Section 2.2)
y_1, y_2, y_3	State variables for integration of deployment equations (defined by Equations 5-5)
α	Airfoil/ blade angle of attack
δ	Device deflection angle (expressed in radians or degrees as appropriate)
ϕ	Angle of W with respect to the rotor plane of rotation (defined in Section 2.2)
θ	Blade chord angle relative to the rotor plane of rotation (defined in Section 2.2)
ρ	Air density
σ	Material stress
Ω	Rotational rotor speed (expressed in rad/s or rpm as appropriate)
$\Omega_{\text{freewheeling}}$	Rotor speed under freewheeling conditions (defined by Equation 2-8)

1. Introduction

1.1 Background

The R. Lynette & Associates (RLA) Next-Generation Innovative Subsystems (NGIS) Project is designed to develop innovative subsystems which can be used to improve the performance and cost-effectiveness of the AWT-26 wind turbine, and that may be usable on other advanced wind turbine designs. RLA is working cooperatively with the National Renewable Energy Laboratory (NREL) and Advanced Wind Turbines, Incorporated (AWT), on the program. The program includes the development of an improved aerodynamic brake configuration for the AWT-26/27 turbines.

1.2 Project Schedule

Table 1-1 summarizes the major aerodynamic braking tasks of the NGIS Project and compares the original schedule with actual completion dates. The initial tasks were completed on or ahead of schedule. Significant effort went into the selection and design of the wind-tunnel models, and the wind tunnel test was conducted 4 1/2 months later than scheduled. Due to AWT engineering priorities, no significant work was performed on aerodynamic braking between February and July of 1996. As a result, the detailed design was completed approximately 12 months later than scheduled. Prioritization of AWT resources resulted in cancellation of the planned field testing of aerodynamic brakes. This decrease in the scope of the project allowed the Draft Aerodynamic Brake Report to be completed within 6 months of the original schedule.

Table 1-1. Major Aerodynamic Brake Development Tasks Completed

Innovative Subsystems Task	Completion Dates	
	Project Schedule	Actual
3.1.1 Review Current Work	11/01/94	11/30/94
3.1.2 Preliminary Performance and Loads Analysis	02/21/95	01/08/95
3.1.3 Preliminary Designs	02/21/95	02/10/95
3.1.4 Preliminary Specification and Failure Modes and Effects Analysis (FMEA)	02/28/95	01/19/96
3.1.5 Wind Tunnel Tests	07/01/95	11/20/95
3.1.6 Update Cost and Performance	07/14/95	02/08/96
3.1.7 Final Configuration Selection	07/21/95	02/22/96
3.2 Performance, Cost, and Structural Analysis	08/01/95	09/27/96
3.3 Detailed Design	09/14/95	09/27/96
3.4.1 Draft Aerodynamic Brake Report	04/12/96	10/12/96
3.4.2 Final Aerodynamic Brake Report	05/24/96	02/17/96
5.5 Aerodynamic Brake Field Test	04/01/96	Canceled

1.3 Purpose

This report summarizes all significant work performed on the Aerodynamic Brake Development task of the NGIS Project. It documents the initial configuration selection, wind-tunnel testing, detailed analysis of candidate configurations, and the design and analysis of the selected aerodynamic brake configuration.

The scope of this project did not allow for an exhaustive cost/benefit analysis of every possible design option. The design objectives and approach of this work are specific to aerodynamic braking of AWT-26/27 turbines. However, many of the issues addressed in this work may be applicable to aerodynamic braking design for a wider class of wind turbines. The performance trends and design choices presented in this report should be of general use to wind-turbine designers who are considering alternative braking methods.

1.4 Objectives

The objective of this project was to develop an improved aerodynamic brake configuration for use on the AWT-26/27 turbines. Goals for the new configuration included

- Decreased cost (materials and manufacturing)
- Decreased weight or better distribution of weight
- Reduced noise of blade tips and aerodynamic brakes
- More reliable deployment
- More robust (less maintenance)
- Ease of maintenance (accessibility of device and components)
- Device less effected by icing conditions
- Improved device scaling for future turbine modifications (rotor size and tip speed).

1.5 Approach

A literature search was conducted of previously reported work with aerodynamic brakes, with emphasis on applications to wind turbines. Based on initial sizing and loads analysis two candidate configurations were chosen for detailed study: the "spoiler-flap" and the "flip-tip." Two-dimensional wind tunnel tests were conducted to evaluate these devices and to develop the database necessary for performance analysis and design. Wind tunnel data were used to predict the stopping power and deployment characteristics of both the spoiler-flap and flip-tip devices. The spoiler-flap with active mechanical deployment was identified as showing the greatest promise for use on the AWT-26/27 turbines. A preliminary design and structural analysis of the selected configuration was completed. Cost and weight estimates were performed, and compared with cost and weight data for the production AWT-26/27 tip vane.

2. Aerodynamic Braking Devices

2.1 Overview

Many wind turbine designs employ some form of aerodynamic braking to perform one or more of the following:

1. **Overspeed protection** – Restraint of the maximum rotor speed under a freewheeling condition (no mechanical brakes or load).
2. **Power modulation** – Control of power output through adjustments of aerodynamic surfaces which alter lift and drag properties over the modified blade sections.
3. **Assisted mechanical braking** – Aerodynamic brakes are deployed during normal braking sequences, allowing for down-sizing of mechanical brakes and decreased brake wear.

For medium-sized turbines (rated power in the 50-750 kW range), the most common means of overspeed control are either full-span pitch control or pitchable tips [1]. Turbines with full-span pitch control typically use this feature for both power modulation and overspeed protection. Pitchable tips may be used for power modulation, but are more frequently used only for overspeed protection and braking. For stall-regulated turbines, the most common form of overspeed protection is pitchable tips.

Tip vanes, spoiler devices, and ailerons are among the other aerodynamic brakes that have either been used successfully in the past, or are currently being used on production wind turbines. Each of these devices has its own advantages and disadvantages as summarized in Table 2-1. In the present work, alternative designs have been investigated and evaluated for improvements over currently used aerodynamic braking methods.

Table 2-1. Characteristics of Current Aerodynamic Brake Designs

Aerodynamic Brake	Advantages	Disadvantages
Pitchable tips	<p>Combination of reduced lift and increased drag occurs at blade tip, resulting in optimal stopping power.</p> <p>With active control, suitable for power modulation.</p> <p>Simple cut-line, blade/tip interface.</p>	<p>Single tubular spar sees very high loads during braking sequence. Mechanical damping of deployment forces is difficult to achieve.</p> <p>All tip power-production loads are carried through the tip/blade interface.</p> <p>Structural/mechanical requirements lead to high tip weights.</p>
Tip vanes	<p>Flat-plate drag created at maximum radial position leads to high aerodynamic stopping torque.</p> <p>Centripetal/aerodynamic deployment is predictable and robust, naturally has greater tendency to deploy with rotor overspeed.</p> <p>Tip-plate effect gives some reduction of induced drag.</p>	<p>Creates high braking torque, but must overcome all power-production torque of the (unmodified) clean blade.</p> <p>No relief of clean-blade lift results in higher flapwise blade loads.</p> <p>Wetted area of tip vane, along with the corner-flow in the tip/blade junction, can cause increases in both drag and noise during normal turbine operation.</p> <p>Not suitable for power modulation.</p>
Spoilers	<p>Creates effective braking by reducing lift and creating drag over the modified portion of the blade.</p> <p>Active control can be used to restrict peak power, but only by "power shaving."</p> <p>Actuation loads low for power shaving.</p>	<p>Stopping power diminishes in airfoil post-stall as spoiler is engulfed by the wake.</p> <p>Deployment loads high during emergency braking.</p>
Ailerons	<p>With active control, can be used to modify lift and drag of blade section, for either power modulation or for braking.</p> <p>Trailing-edge devices can have small effect on aerodynamic drag when stowed.</p> <p>Potential for active teeter control.</p>	<p>Stopping power diminishes in airfoil post-stall as aileron is engulfed by the wake and overall projected area decreases.</p> <p>Deployment loads high during emergency braking.</p>

2.2 General Aerodynamic Brake Performance

The following aerodynamic analysis uses the blade element momentum theory (BEMT), which relies on the assumption that radial blade sections can be analyzed independently [2]. For blade sections in the vicinity of an aerodynamic braking device, this assumption may be poor. The validity of using BEMT methods to analyze aerodynamic brakes will be addressed further in following sections. Figure 2-1 shows a diagram of a radial blade element, where:

- L \equiv lift force, acting perpendicular to the resultant velocity vector
- D \equiv drag force, acting parallel to the resultant velocity vector
- W \equiv resultant velocity vector at blade section, $(u^2 + (r\Omega + w)^2)^{1/2}$
- V_o \equiv free-stream wind velocity
- u \equiv axial component of inflow velocity
- w \equiv "swirl" velocity
- $r\Omega$ \equiv velocity caused by blade rotation
- α \equiv blade angle of attack relative to the resultant velocity vector, W
- θ \equiv blade chord relative to the rotor plane of rotation
- ϕ \equiv angle of the resultant velocity with respect to the rotor plane of rotation
- a, a' \equiv interference factors which account for presence of rotor.

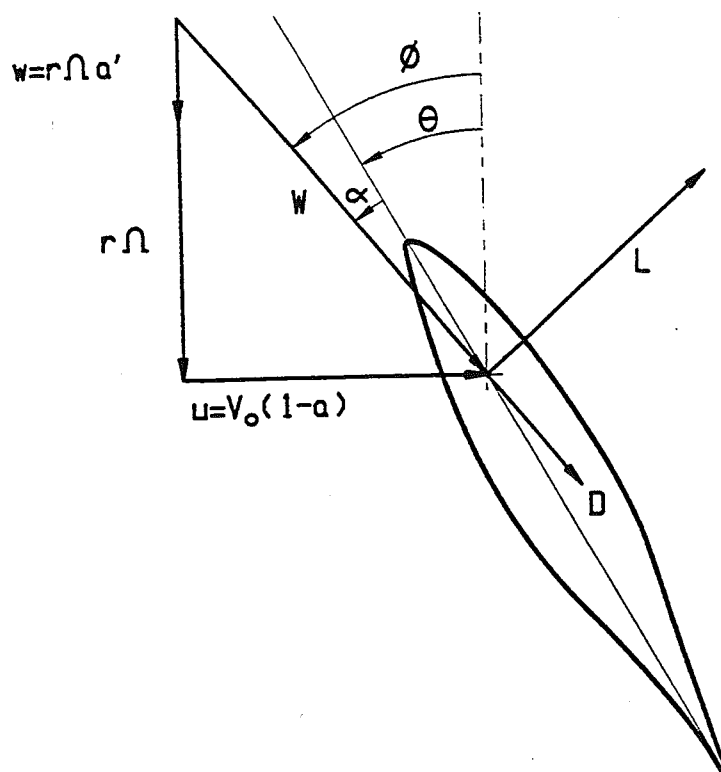


Figure 2-1. Velocity and Force Diagram at Radial Blade Position

The local lift and drag can be expressed in coefficient form as:

$$\begin{aligned} C_L &\equiv L/(q \cdot c \cdot \Delta r) \\ C_D &\equiv D/(q \cdot c \cdot \Delta r) \\ c &\equiv \text{local blade chord} \\ \Delta r &\equiv \text{finite radial dimension of blade section at location, } r \\ q &\equiv \text{dynamic pressure, } (0.5)\rho \cdot W^2 \\ \rho &\equiv \text{mass density of air.} \end{aligned}$$

Resolving force vectors into the rotor plane of rotation, a "suction" coefficient can be defined that is related to the production of useful torque:

$$C_s = C_L \cdot \sin(\phi) - C_D \cdot \cos(\phi). \quad (2-1)$$

Similarly, a "normal force" coefficient can be defined which is related to blade thrust loading:

$$C_N = C_L \cdot \cos(\phi) + C_D \cdot \sin(\phi). \quad (2-2)$$

Based on the above definitions, expressions can be obtained for the incremental torque (Q), thrust (T), and power (P) generated by a single blade section located at radius r:

$$\Delta Q = q \cdot r \cdot C_s \cdot c \cdot \Delta r \quad (2-3)$$

$$\Delta T = q \cdot C_N \cdot c \cdot \Delta r \quad (2-4)$$

$$\Delta P = \Omega \cdot \Delta Q = \Omega [q \cdot r \cdot C_s \cdot c \cdot \Delta r]. \quad (2-5)$$

The above definitions and equations contain the essentials of normal turbine power production, as well as aerodynamic braking. Within the assumptions of BEMT, an iterative solution is available for the interference factors a and a' . For a given wind speed, V_o , the blade angle of attack, α , can be related to ϕ through the rotor geometry, blade pitch setting, and twist.

Assuming that no mechanical torque is applied to the rotor shaft, an equilibrium freewheeling speed is attained when the negative torque produced by the blade sections with deployed aerodynamic brakes is exactly balanced by the positive torque contributions from the remaining blade. Inspection of Equation 2-1 shows that at low blade angles of attack, generating negative values of C_s is achieved more directly by increasing drag than by decreasing lift.

Rotor performance is often expressed in terms of power coefficient (C_p) versus tip-speed ratio (TSR):

$$C_{P, \text{rotor}} \equiv \frac{P_{\text{rotor}}}{0.5 \cdot \rho \cdot V_o^3 \cdot A_{\text{rotor}}} \quad (2-6)$$

$$\text{TSR} \equiv \frac{\text{Rotor Tip Speed}}{\text{Wind Speed}} = \frac{R \cdot \Omega}{V_o} \quad (2-7)$$

where:

A_{rotor} \equiv swept area of rotor ($\pi \cdot R^2$ for a horizontal-axis wind turbine)

R \equiv radius of turbine rotor

Ω \equiv rotational speed of rotor (rad/s).

Note that the rotor power coefficient is normalized with respect to the free-stream wind speed. By contrast, the expressions for torque, thrust, and power are all in terms of the resultant velocity vector which has a large rotational component. TSR is a non-dimensional tip speed, and the geometric angle of attack for each blade section is equal to $\tan^{-1}(V_o / r \cdot \Omega)$.

Figure 2-2 shows C_p -TSR curves for the AWT-26 turbine, including the effect of an aerodynamic brake at several deployment angles. Such a plot can easily be used to determine the equilibrium tip-speed ratio for a turbine in the freewheeling condition. Using Figure 2-2 as an example, the C_p curve for $\delta = 30^\circ$ has its highest zero crossing at a tip-speed ratio of about 7.5. For tip speeds lower than this value, the rotor will create positive mechanical power and accelerate. Conversely, the rotor will decelerate for tip-speed ratios above this zero crossing. For a deployed aerodynamic brake, the equilibrium tip-speed ratio will determine the maximum freewheeling rotor speed as a function of wind speed. Rearranging Equation 2-7, and evaluating for the equilibrium condition, yields:

$$\Omega_{\text{freewheeling}} = \frac{\text{TSR}_{\text{equilibrium}} \cdot V_o}{R} \quad (2-8)$$

This report will make frequent use of C_p -TSR curves for device sizing and for evaluating aerodynamic brake performance, as the curves may be used to represent a wide range of wind conditions and turbine rotational speeds.

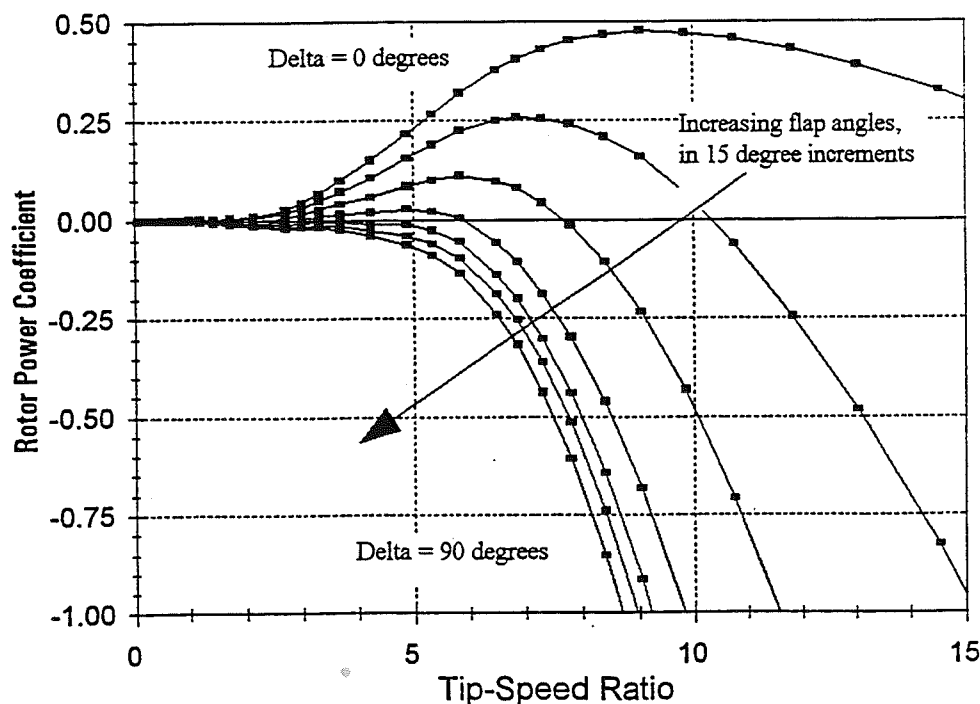


Figure 2-2. Example C_p -TSR Curve for AWT-26 with Deployed Aerodynamic Brake

3. Initial Configuration Definitions

3.1 Baseline Configuration, AWT-26/27 Tip Vane

The baseline configuration for this work is the AWT 26/27 tip vane, which has been used successfully on several AWT-26 prototypes, and on production AWT-27 turbines. Figure 3-1 shows the general configuration of the AWT-26/27, which is a downwind, free-yaw turbine. The rotor is a two-bladed, fixed-pitch, stall-regulated design, which achieves high efficiency through the use of NREL S815/S809/S810 airfoils. The blades are made of wood-epoxy laminates, reinforced with carbon fiber. The AWT-26 has a diameter of 26.2 m (86 ft) and a nominal rotational speed of 57 rpm. The AWT-27 has a 27.4 m (90 ft) diameter with a nominal rotational speed of 53 rpm.

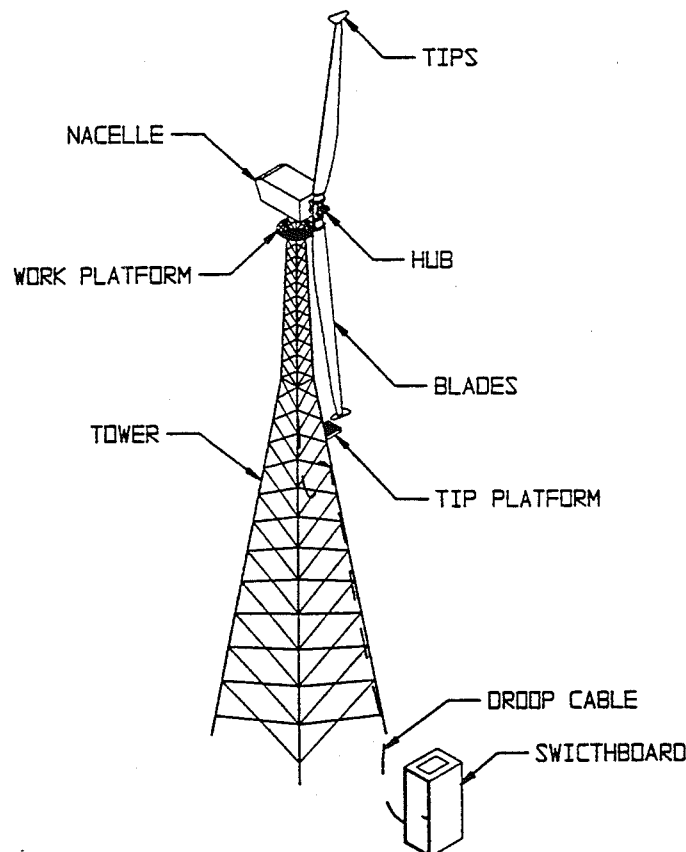


Figure 3-1 General Configuration of AWT-26/27 Turbines

Figure 3-2 identifies the major tip-vane components and illustrates the vane orientation in both stowed and deployed positions. The tip brakes provide assistance to the mechanical brakes during all rotor stopping sequences, as well as being a redundant means of preventing rotor overspeed for all wind speeds. The tip brakes consist of a vane and an aerodynamic fairing that covers the deployment hardware (striker plate, hinge, baseplate, damper, spring, electrical magnet, and tip studs). The vane is a composite construction of structural foam overlaid with carbon fiber fabric, epoxy, and gelcoat. The hinge assembly allows the brake to move from the stowed (turbine operating) to the braking position.

During normal turbine operation, the magnet and springs hold the vane perpendicular to the blade axis so that the vane produces minimal resistance as the rotor turns. A tip brake deploys when electric current is cut off from the electrical magnet while the rotor is turning. Centrifugal forces cause the trailing edge of the vane to move outward, exposing the relatively flat surface of the vane to the incident wind direction. Drag generated by the tip vane opposes the torque applied to the rotor by aerodynamic lift on the blades. As the rotor slows, the vane is returned to its operating position by the balance of centrifugal, aerodynamic, and spring forces. The return motion is moderated by a viscous damper.

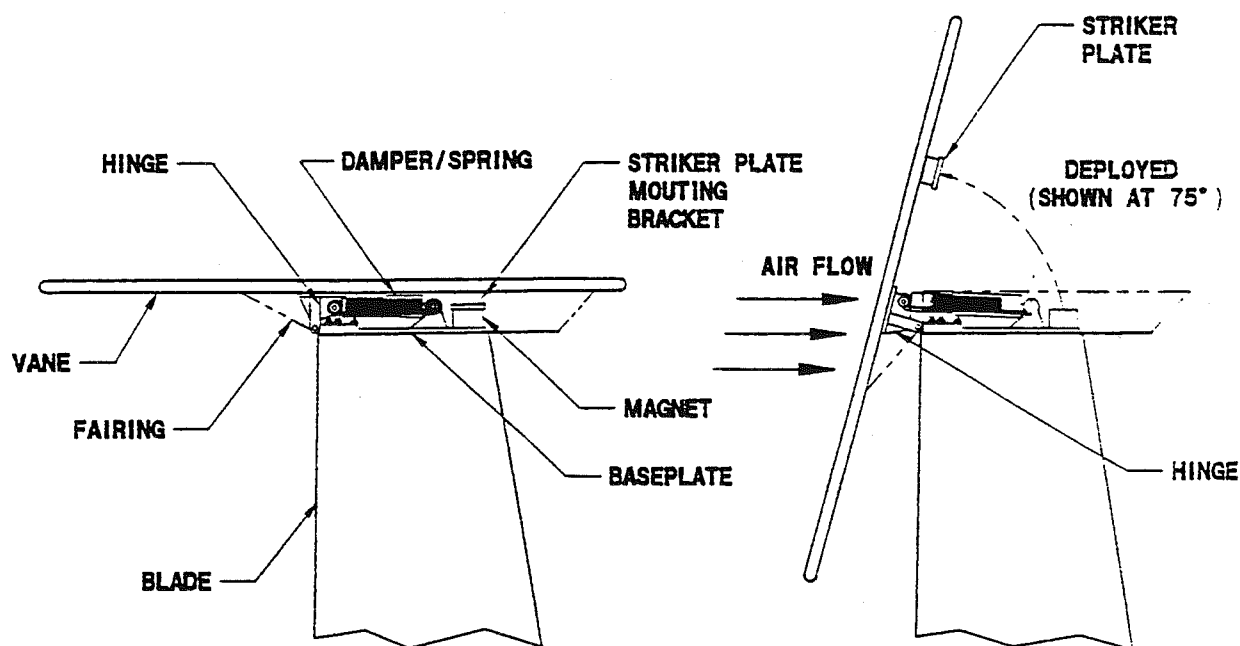


Figure 3-2. Major Components of AWT-26/27 Tip Vanes

A slip-ring assembly is used to carry 120-volt AC power across the rotating interface between the nacelle and the hub. An AC to DC rectifier is located in a small junction box on the hub. The rectifier converts the AC electricity coming from the turbine controller to DC electricity used to energize the electromagnets at the blade tips. The tip vanes are fail safe, and will deploy any time there is a loss of DC power to the electromagnets (loss of grid power, failed connection, etc.).

Table 3-1 shows production costs and weights for the major subsystems of the AWT-26/27 tip vanes. The entry titled "mounting hardware" includes the mounting plate, hinge assembly, spring, damper, electromagnet, and all miscellaneous studs, pins, bushings, and other hardware.

Table 3-1. Cost and Weight for Major Tip-Vane Subsystems

Major Components / Subsystem	# Per Turbine	Cost (\$)	Weight	Cost/Weight
Vane and Fairing	2	833.34	6.3 kg (13.9 lbs)	132 \$/kg (60.0 \$/lb)
Mounting Hardware	2	465.35	6.4 kg (14.0 lbs)	16.5 \$/kg (33.3 \$/lb)
Slip Ring and Rectifier	1	1,712.00	14.4 kg (31.8 lbs)	26.7 \$/kg (53.8 \$/lb)

The aerodynamic performance of the tip vane is relatively simple. Ignoring tip-plate effects, deployment of the tip brakes leaves the turbine rotor aerodynamically unchanged. To a good approximation, the negative (stopping) power provided by the tip vanes can be added linearly to the positive power produced by the turbine blade. The tip vane remains nearly neutral with respect to the free-stream wind vector both while stowed and while deployed. The apparent velocity of the tip brake can then be completely characterized by the rotational velocity of the blade tip, $R \cdot \Omega$, and the stopping power related to the device drag by the following equations (for one vane):

$$D = q \cdot C_D \cdot A_{\text{vane}} = 0.5 \cdot \rho \cdot V^2 \cdot C_D \cdot A_{\text{vane}} \quad (3-1)$$

$$\Delta P = -D \cdot \Omega \cdot R = -0.5 \cdot \rho \cdot C_D \cdot A_{\text{vane}} \cdot (\Omega \cdot R)^3 \quad (3-2)$$

where the substitution of $V^2 = (R \cdot \Omega)^2$ has been used. Multiplying the right-hand side by $(V_o/V_o)^3$ yields (for one vane):

$$\Delta P = -0.5 \cdot \rho \cdot C_D \cdot A_{\text{vane}} \text{TSR}^3 \cdot V_o^3. \quad (3-3)$$

Equations 3-3 and 2-6 can be combined to express aerodynamic braking power in terms of rotor power coefficient (for two tip vanes):

$$\Delta C_{P, \text{rotor}} = -2 \cdot C_D \cdot \text{TSR}^3 \frac{A_{\text{vane}}}{A_{\text{rotor}}} \quad (3-4)$$

Equation 3-4 provides a simple expression for the aerodynamic effectiveness of tip vanes, and clearly illustrates some of the functional dependencies. For a given $\Delta C_{p, \text{required}}$, the vane area must scale linearly with the rotor swept area, and the device effectiveness increases rapidly with tip-speed ratio. In terms of rotor scaling, Equation 3-4 must be interpreted with care. Note that C_p is normalized by rotor area, so at fixed values of rotor power and TSR, the $\Delta C_{p, \text{required}}$ for effective braking would decrease as $1/A_{\text{rotor}}$ for larger rotor diameters.

3.2 Candidate Configurations

To identify promising configurations for aerodynamic braking devices, a review of existing literature was conducted. Data obtained through the literature review, including recent wind tunnel testing of trailing-edge aerodynamic brakes [3 and 4], were used as a basis for a preliminary sizing and loads analysis. Based on the analysis, two candidate configurations were selected for further investigation, the "spoiler-flap" and the "flip-tip." These configurations were identified as showing the greatest promise for incorporating into the AWT-26/27 design, and for meeting the objectives as listed in Section 1.4.

3.2.1 Spoiler-Flap

The spoiler-flap was jointly conceived by Gene Quandt and NREL, and is shown schematically in Figure 3-3. The trailing edge of the spoiler-flap is rotated downward during deployment. The forward portion of the device disrupts the flow on the low-pressure side of the airfoil as it protrudes upward. The effectiveness of the spoiler-flap is based on a moderate amount of drag creation, coupled

with large reductions in torque-producing lift. An important feature is the venting of air flow from the high-pressure to low-pressure side of the airfoil, which tends to prevent the flap from acting as a high-lift device.

The hinge moments of spoiler-flaps can be strongly affected by the relative position of the hinge line. Spoiler-flaps are generally suitable for deployment by either aerodynamic, active mechanical, or passive mechanical methods, any of which may make use of the centripetal accelerations acting on the device or other mechanisms. Deployment methods are addressed in greater detail in Section 5.0.

In addition to the work of References 3 and 4, wind-tunnel tests of spoiler-flaps and ailerons have been conducted by Ohio State University (OSU) [5], and atmospheric testing has been conducted using the NREL Combined Experiment Rotor (CER) [6]. The publication of these recent tests results is pending. Quandt is currently working on the testing of prototype spoiler-flaps [7], and has published the preliminary design of spoiler-flaps for a Micon 65/13 [8].

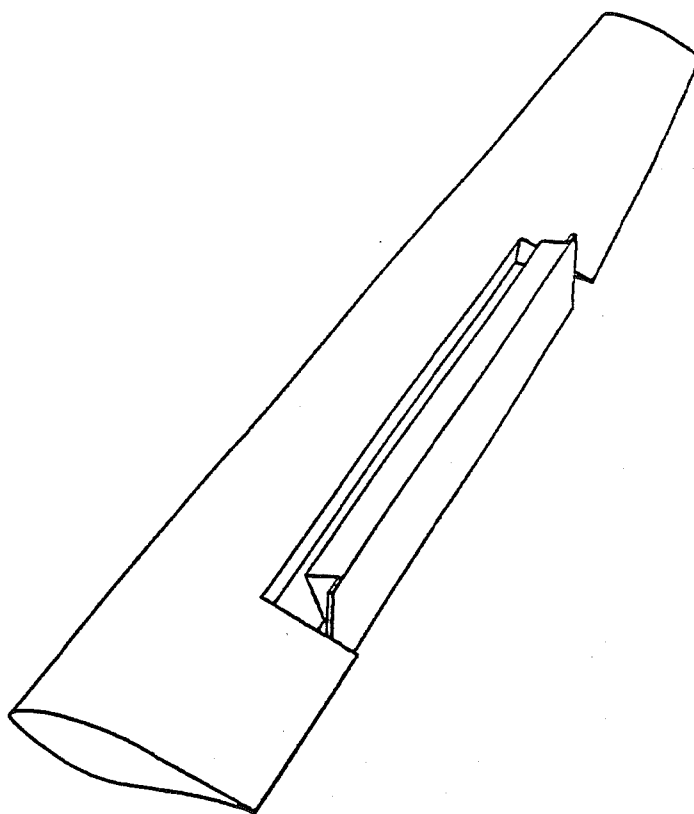


Figure 3-3. Isometric View of Deployed Spoiler-Flap

Beginning with the force and velocity vectors defined in Figure 2-1, and making use of Equations 2-1 through 2-7, expressions can be derived for the effects of a device which modifies the local blade aerodynamic properties (such as a spoiler-flap). From Figure 2-1:

$$W = \frac{r \cdot \Omega (1 + a')}{\cos(\phi)} \quad (3-5)$$

Near the tip regions of a wind turbine blade, the radial interference factor, a' , is generally small. Therefore, a good approximation to the resultant velocity vector, W , is given by:

$$W \approx \frac{r \cdot \Omega}{\cos(\phi)} \quad (3-6)$$

Using Equation 3-6 in a derivation similar to that for the tip vane leads to expressions for the incremental changes in rotor power and rotor power coefficient (for both blades modified):

$$\Delta P = \rho \cdot \frac{\{\Delta C_L \sin(\phi) - \Delta C_D \cos(\phi)\}}{\cos^2(\phi)} \cdot A_{\text{section}} \cdot \left(\frac{r}{R}\right)^3 \cdot \text{TSR}^3 \cdot V_o^3 \quad (3-7)$$

$$\begin{aligned} \Delta C_{P, \text{rotor}} &= 2 \cdot \left(\frac{r}{R}\right)^3 \cdot \text{TSR}^3 \frac{\{\Delta C_L \sin(\phi) - \Delta C_D \cos(\phi)\}}{\cos^2(\phi)} \cdot \frac{A_{\text{section}}}{A_{\text{rotor}}} \\ &= 2 \cdot \left(\frac{r}{R}\right)^3 \cdot \text{TSR}^3 \frac{\Delta C_s}{\cos^2(\phi)} \cdot \frac{A_{\text{section}}}{A_{\text{rotor}}} \end{aligned} \quad (3-8)$$

Where ΔC_L , ΔC_D , and ΔC_s are the incremental changes in lift, drag, and suction coefficients of the local blade sections due to the deflection of the spoiler-flap device, and r is a radial position which characterizes the device. In terms of functional dependencies, Equations 3-8 and 3-4 are very similar. The device effectiveness scales linearly with the area of the modified blade section, and as a cubic of both the tip-speed ratio and the radial position.

The spoiler-flap has several favorable attributes for wind turbine aerodynamic braking. Wind tunnel data show that spoiler-flaps can maintain high negative values of C_s over a wide range of airfoil angles of attack. The device aerodynamic surfaces and supports are aft on the blade, reducing the drag penalty due to the device gap as well as minimizing the loads carried during normal power production. Spoiler-flaps may also be used for power modulation, as they can produce significant negative ΔC_s at low deflection angles.

3.2.2 Flip-Tip

The flip-tip, which was conceived at AWT and is a hybrid of a pitchable tip and a plain flap, is shown in Figure 3-4. The flip-tip was designed to be aerodynamically deployed (trailing-edge down). With proper sizing and hinge location, the tip region provides positive opening moments for all blade angles of attack. The tip region provides maximum braking torque as it is deployed towards stall at higher angles of attack. The flap region is intended to provide aerodynamic damping so that the flip-tip assembly reaches an equilibrium deployment angle prior to experiencing a hard mechanical stop. The aerodynamic stopping loads of the tip are transferred to the main blade structure through the flap and hinges.

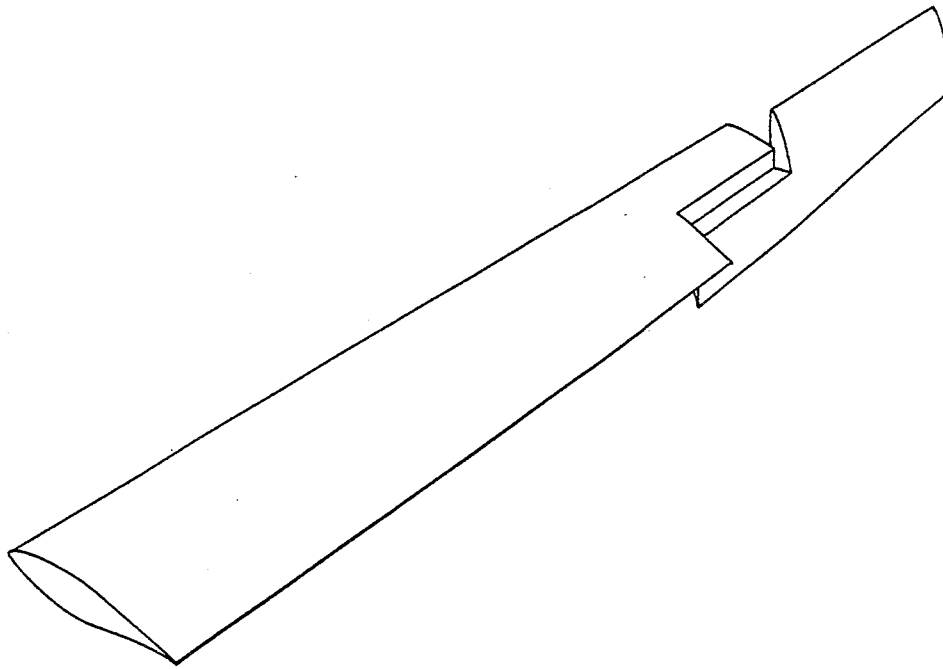


Figure 3-4. Isometric View of Deployed Flip-Tip

The aerodynamic performance of the flip-tip may be approximated by a linear superposition of the tip and flap regions. The resulting expression for the change in rotor power coefficient shows the same functional dependencies as noted for the spoiler-flap:

$$\Delta C_{P, \text{rotor}} = \frac{2 \cdot \text{TSR}^3}{A_{\text{rotor}}} \left[\left\{ \left(\frac{r}{R} \right)^3 \cdot \frac{\Delta C_s}{\cos^2(\phi)} \cdot A_{\text{section}} \right\}_{\text{flap}} + \left\{ \left(\frac{r}{R} \right)^3 \cdot \frac{\Delta C_s}{\cos^2(\phi)} \cdot A_{\text{section}} \right\}_{\text{tip}} \right] \quad (3-9)$$

4. Wind Tunnel Experiments

Wind tunnel experiments were conducted to develop the database necessary for detailed sizing and deployment studies of the candidate configurations. The test was conducted during November of 1995 at the Wichita State University (WSU) Walter H. Beech Memorial 7 x 10 foot low-speed wind tunnel [9]. The tunnel is a closed-return design capable of test section dynamic pressures of up to 2873 Pa (60 psf). Although the experiments were similar to those reported in References 3 and 4, the new tests included several variations and improvements over the previous work, and have substantially contributed to the growing body of data on trailing-edge aerodynamic brakes.

4.1 Model Design and Instrumentation

A two-dimensional model was designed and constructed at WSU. The baseline airfoil shape was scaled directly from the 97.5% radial position of the AWT-26 blade, which is an NREL S810 with a thickened trailing edge. The model had a chord of 45.7 cm (18 in.) and a nominal length of 2.1 m (7 ft), which spanned the test section from floor to ceiling. The mounting arrangement allowed an angle of attack range from -6° to $+90^\circ$.

Figure 4-1 shows a sectional view of the model, with the dashed lines indicating cove inserts that were bolted between the forward and rear model elements. With a cove insert bolted to the forward element, the flap portion of the model was 38% of the airfoil chord. Alternately, a cove insert could be bolted into the rear portion of the model, resulting in a 45% chord flap. Either size flap could then be pivoted around any of the hinge positions designated A-1 through C-5. The modular design allowed 30 different flap configurations, including plain unvented flaps, plain vented flaps, and spoiler-flaps.

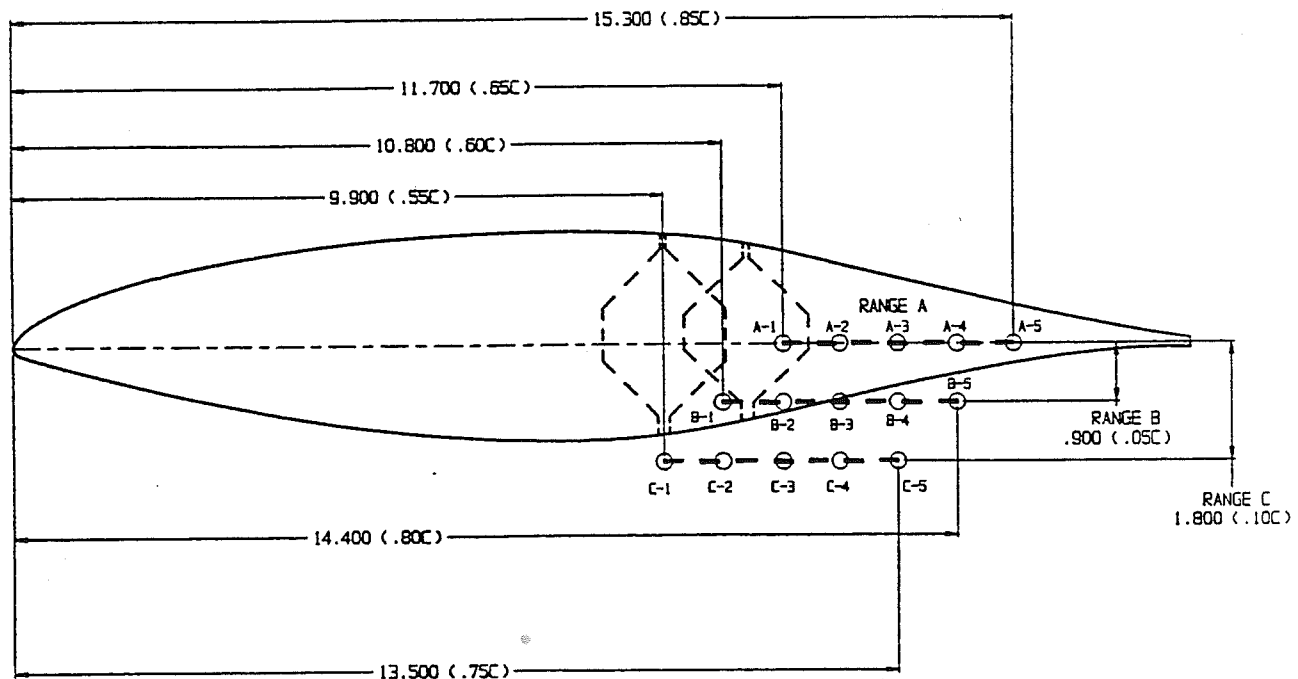


Figure 4-1. Section View of Wind Tunnel Model (primary dimensions in inches)

The model was supported at the floor and ceiling by balances that measured the lift, drag, and quarter-chord pitching moment on the model. The floor balance recorded approximately half of the lift and drag forces, and all of the moment data. The remaining lift and drag forces were resolved by the ceiling balance. Additional documentation on WSU two-dimensional force balances can be found in Reference 9. End plates of 68.6 cm (27 in.) diameter and 6.4 mm (0.25 in.) thickness were mounted on each end of the model, approximately 9.5 mm (0.375 in.) from tunnel walls. The end plates had rounded edges to minimize flow disturbance.

To deflect the flaps, an electronically-controlled actuator assembly was designed and constructed at WSU. As shown in Figure 4-2, the actuator assembly was below the tunnel floor. The device deflections were driven through a flexure (linkage designed to support only axial loads). Hinge moments were measured by the use of strain gages, which were mounted on the flexure and calibrated in-situ during the model installation. The calibration was checked periodically throughout the test by repeat runs of selected configurations. To convert to coefficient form, hinge moment data were normalized with respect to device (flap) chord:

$$C_h = \frac{\text{Device Hinge Moment}}{q \cdot b \cdot c_{\text{Device}}^2}, \quad (4-1)$$

where b is the airfoil span, and opening hinge moments are defined as positive (trailing-edge down).

Standard wind-tunnel corrections were applied during the data reduction [9]. No attempt was made to measure or correct for turntable interference or tare drag. The authors of Reference 3 used wake deficit measurements to evaluate interference and tare drag, and applied a constant value of $\Delta C_D = 0.020$ for turntables of similar dimensions. In the present work it was decided to avoid the expense of conducting wake deficit surveys. The data were intended to be used in an incremental fashion and the tare drag measurements would have been of no practical use.

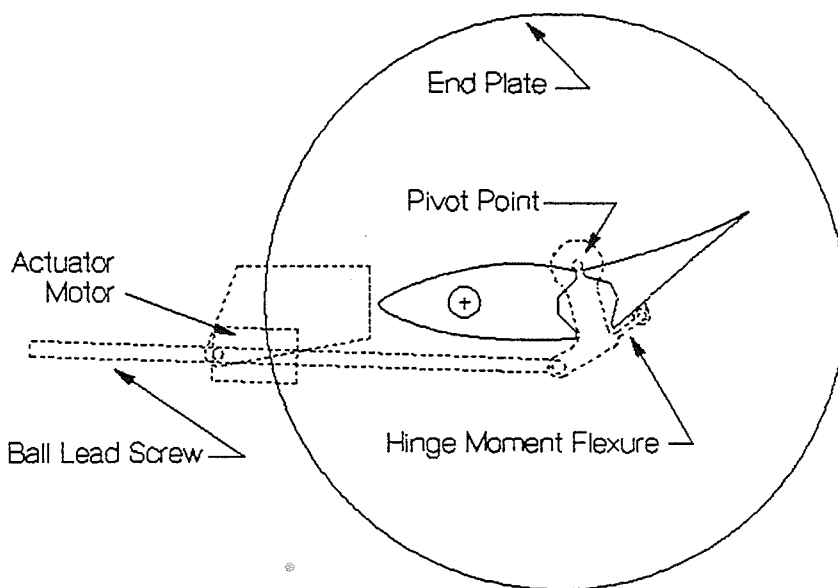


Figure 4-2. End View of Flap Deflection Assembly (dashed lines indicate below floor level)

4.2 Test Matrix

A typical test run was at constant dynamic pressure with a fixed flap-deflection angle and variable angle of attack. For a given flap size and hinge location, a δ -sweep was conducted by test runs performed at a schedule of fixed flap deflections. The resulting data could then be viewed in a matrix form, aerodynamic performance as a function of both α and δ . The majority of runs were conducted at a dynamic pressure of 479 Pa (10 psf), which corresponds to a Reynolds number of approximately 1.0 million based on the model chord (including standard WSU corrections for turbulence effects). The typical angle of attack range was $-6^\circ \leq \alpha \leq 90^\circ$. Table 4-1 summarizes the 15 configurations that were tested in the δ -sweep manner.

Table 4-1. Flap Configurations Tested by Standard δ -Sweep

Flap Chord (% of airfoil)	Hinge Location	Configuration Type	Flap Deflections Tested (degrees)
38	A-2	Plain Flap	0, 15, 30, 45, 60, 90
38	A-3	Spoiler-Flap	0, 5, 10, 30, 60, 90
38	A-4	Spoiler-Flap	0, 5, 10, 20, 30, 40, 60, 75, 90
38	A-5	Spoiler-Flap	0, 5, 10, 20, 30, 40, 60, 75, 90
38	B-1	Plain Flap	0, 15, 30, 45, 60, 75, 90
38	C-2	Vented Flap	0, 15, 30, 45
45	A-1	Plain Flap	0, 15, 30, 45, 60, 75, 90
45	A-2	Spoiler-Flap	0, 15, 30, 45, 60, 75, 90
45	A-3	Spoiler-Flap	0, 15, 30, 45, 60, 75, 90
45	A-4	Spoiler-Flap	0, 5, 10, 15, 30, 45, 60, 75, 90
45	B-3	Spoiler-Flap	0, 15, 30, 45, 60, 75, 90
45	B-5	Spoiler-Flap	0, 15, 30, 45, 60, 75
45	C-1	Vented Flap	0, 15, 30, 45, 60, 75, 90
45	C-3	Spoiler-Flap	0, 15, 30, 45, 60, 85
45	C-5	Spoiler-Flap	0, 15, 30, 45, 60

The determination of device type was in some cases subjective. For instance, the 45% chord device at hinge location A-1 was clearly a plain flap, and at hinge A-3 it was clearly a spoiler-flap, but hinge A-2 was somewhat in between. The device was labeled as a spoiler-flap if a significant portion of the device leading edge protruded above the upper-airfoil (low-pressure) surface as the flap was deployed. Where plain flaps showed significant venting at low deployment angles, they have been labeled as "vented flaps." Inspection of Table 4-1 shows that the δ -sweeps generally emphasized spoiler-flaps, and more tests were conducted for the 45% chord device than for the 38%. The test matrix shown in Table 4-1 bracketed the parameter space of interest, and provided an excellent database from which to predict the aerodynamic performance of both the spoiler-flap and flip-tip.

In addition to the configurations shown in Table 4-1, several special studies were conducted, including tests to determine the effects of Reynolds number, device gap leakage, leading-edge roughness, and device aspect ratio. Throughout the test, selected configurations were repeated to ensure that all instruments were holding their calibrations. These special studies will be discussed in greater detail in the following sections.

A total of 165 runs were completed during the test. A complete run log that documents the test configurations and conditions is provided in Appendix A, along with graphical data for 119 of the test runs. An ASCII text file of the complete data set is available from NREL or WSU by request.

4.3 Wind Tunnel Test Results and Discussion

4.3.1 Baseline S810 Airfoil

As shown in Figure 4-1, the forward and rear elements of the airfoil model were separated by gaps with an open cavity (cove) in between. The gap dimensions were 0.5% chord on the low-pressure side of the airfoil, and 1.0% chord on the high-pressure side. During all standard wind-tunnel runs these gaps were unsealed, resulting in a surface discontinuity and allowing leakage from the high-to low-pressure surfaces.

To assess the impact on airfoil drag, special runs were conducted with the gaps taped. Figures 4-3 and 4-4 show the results of these tests, and indicate a significant drag penalty when the gaps are open, particularly at the pre-stall angles of $6^\circ \leq \alpha \leq 9^\circ$. The effect is most pronounced for the 45% chord device, where the gap occurs at the 55% airfoil chord location. For both devices, drag penalties are in the range of 40 to 100 drag counts over a large portion of the drag bucket, where a drag count is an increment of 0.0001 in drag coefficient. For the S810 airfoil at 1.0 million Reynolds number, an increase of 10 drag counts represents a 14% increase relative to the clean airfoil drag.

Full lift, drag, and suction coefficient curves for the baseline S810 airfoil are shown in Figures 4-5 and 4-6 of the following sections, as they represent the $\delta = 0^\circ$ case for each flap configuration tested. The data show a maximum lift coefficient of $C_{L_{\max}} \approx 1.0$, which occurs at $\alpha = 12^\circ$, and a smooth stall progression to $C_L \approx 0.7$ at $\alpha \approx 25^\circ$. The data show a relatively flat drag bucket between $-6^\circ \leq \alpha \leq 10^\circ$. As the airfoil approaches stall, the drag increases rapidly to a value of $C_{D_{\max}} \approx 1.7$ at $\alpha = 90^\circ$. The positive suction peak of $C_{S_{\max}} \approx 0.15$ coincides with the maximum lift coefficient at $\alpha = 12^\circ$.

4.3.2 45% Chord Devices

Aerodynamic coefficients for the 45% plain flap are shown in Figures 4-5, where the hinge location is A-1. The curves show typical flap behavior, with $C_{L_{\alpha=0}}$ and $C_{L_{\max}}$ both strictly increasing with flap deflections up to $\delta = 75^\circ$. Although the flap acts as a high-lift device, it also produces significant drag, and the suction coefficients remain negative for all flap deflections greater than 15° . Hinge moments, which are strongly negative (closing), increase smoothly with both flap deflection and airfoil angle of attack.

Figures 4-6 show aerodynamic coefficients for a 45% chord spoiler-flap hinged at A-3. At moderate deflection angles the spoiler-flap exhibits some high-lift behavior, particularly at post-stall airfoil angles of attack. However, for the spoiler deployed to 75° or greater, the lift is greatly diminished at all angles of attack. The effect of lift spoiling on suction coefficients is most apparent at angles of attack near the clean-airfoil suction peak ($5^\circ < \alpha < 15^\circ$). A comparison of Figures 4-5c and 4-6c shows that for angles less than $\alpha \approx 20^\circ$, the fully deployed spoiler-flap has suction coefficients which are approximately 20% more negative than those for the plain flap. Above $\alpha \approx 25^\circ$, the plain flap becomes considerably more effective. Hinge location A-3 is very close to neutral in terms of hinge moments. Figure 4-6d shows that hinge moment coefficients are nearly invariant with angle of attack, and remain near zero or slightly negative (closing) over most deflection angles.

Figures 4-7 show the variation of 45% chord devices with hinge location at a fixed deflection angle of $\delta = 75^\circ$. Hinge location A-1 is a plain unvented flap, location C-1 is a plain vented flap, and the remainder of the locations are spoiler-flaps. This is particularly obvious in the lift curves of

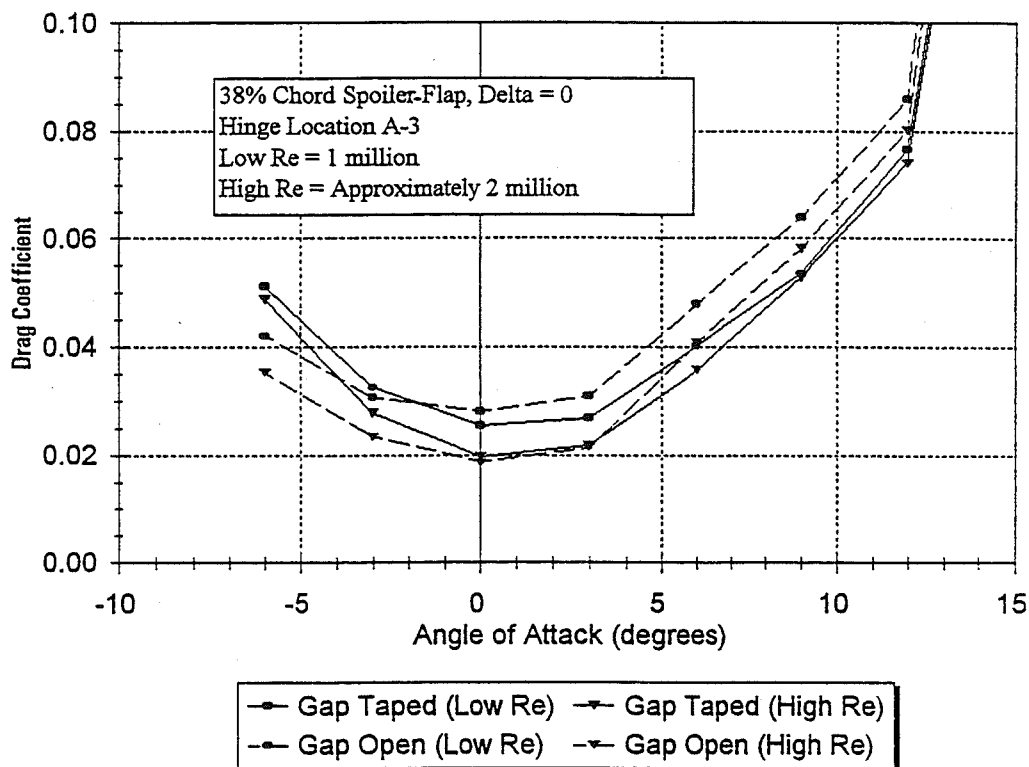


Figure 4-3. Effect of Gap Seal on 38% Chord Device

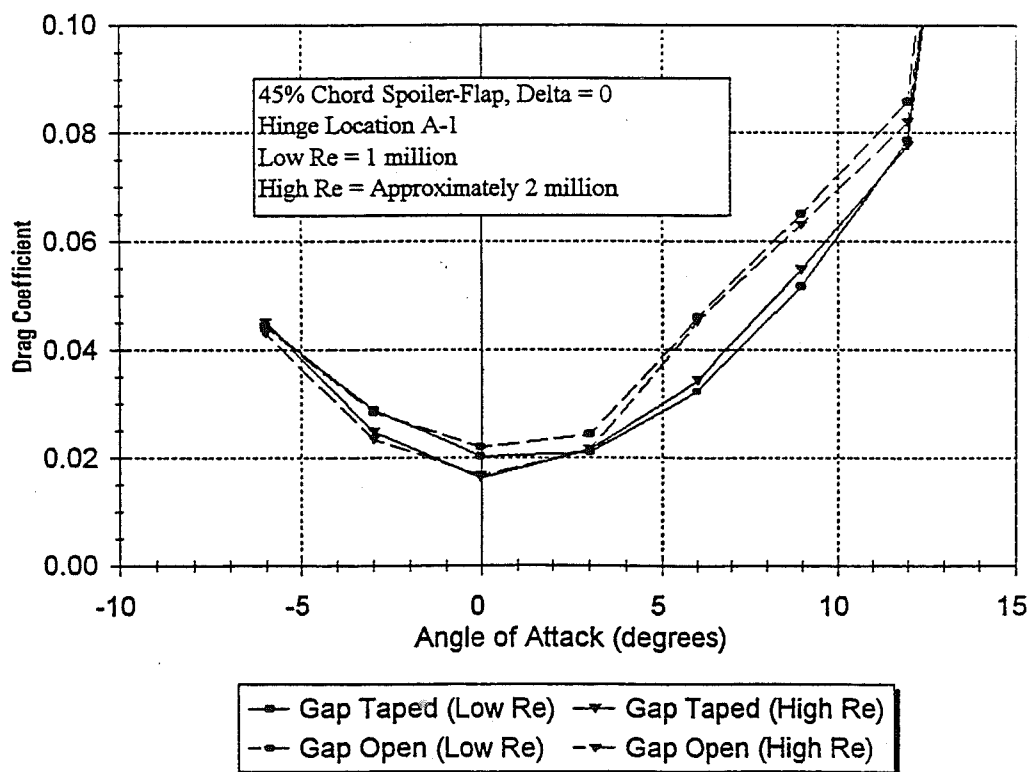


Figure 4-4. Effect of Gap Seal on 45% Chord Device

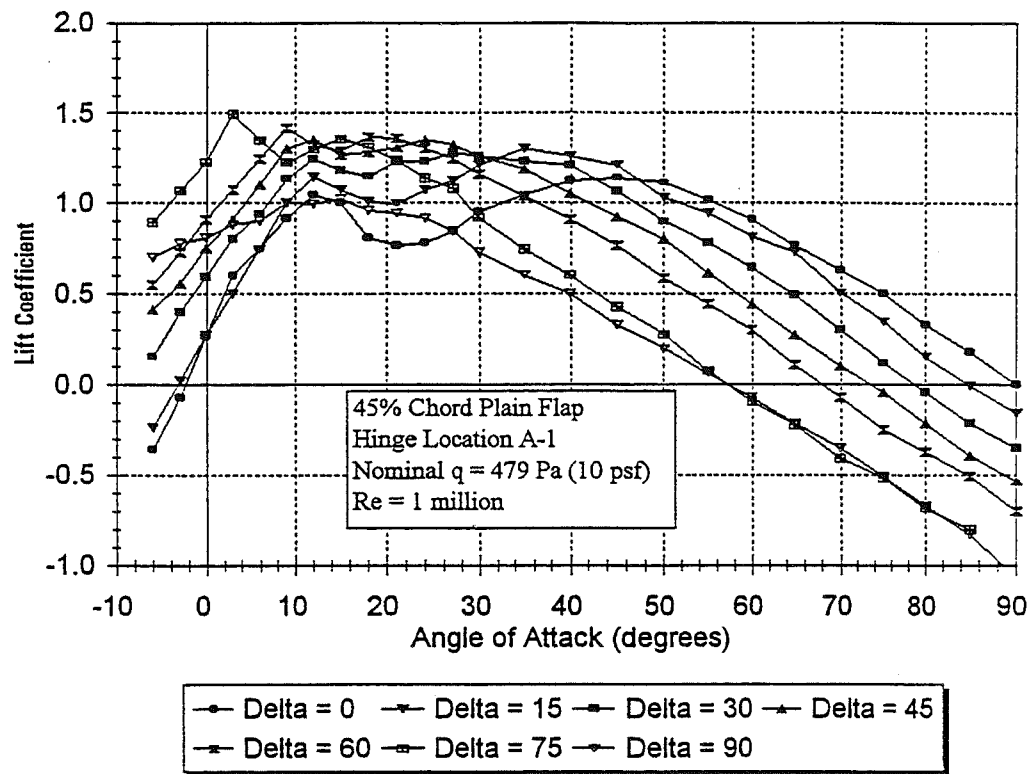


Figure 4-5a. Lift Coefficients for 45% Chord Plain Flap, Hinge A-1

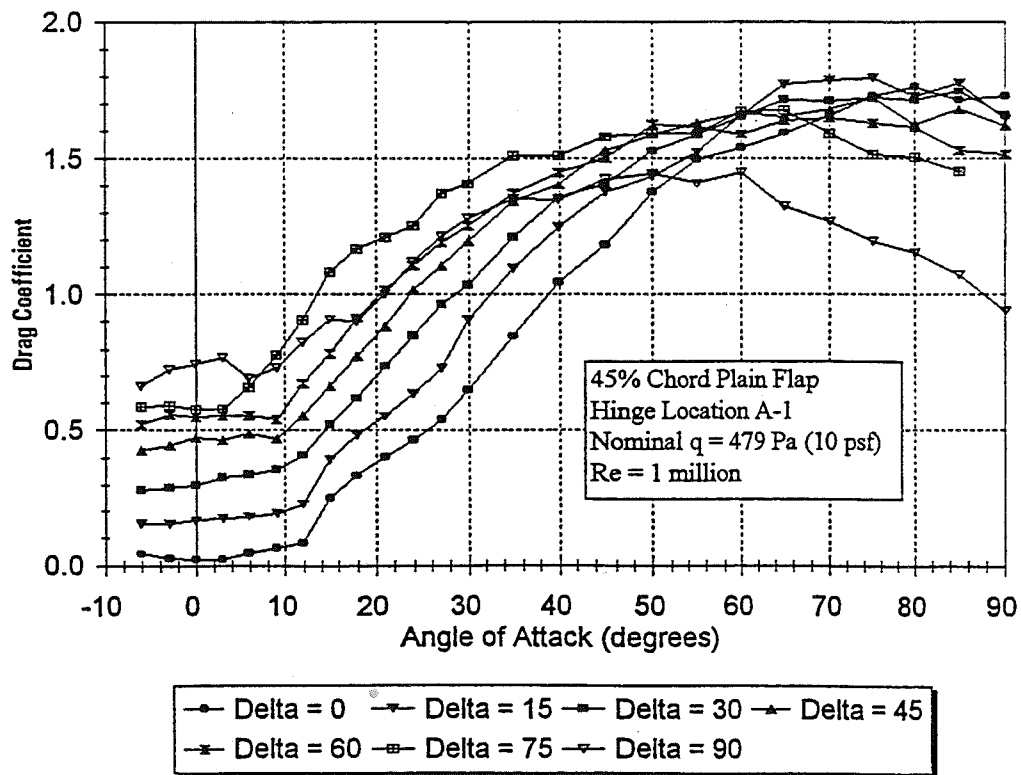


Figure 4-5b. Drag Coefficients for 45% Chord Plain Flap, Hinge A-1

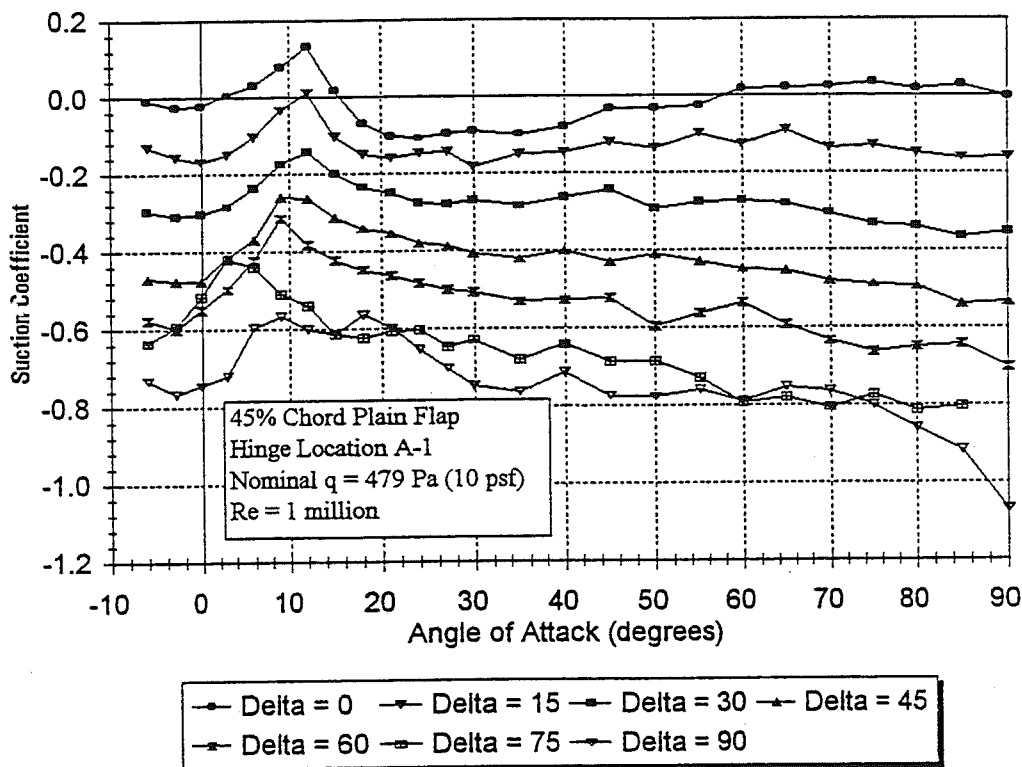


Figure 4-5c. Suction Coefficients for 45% Chord Plain Flap, Hinge A-1

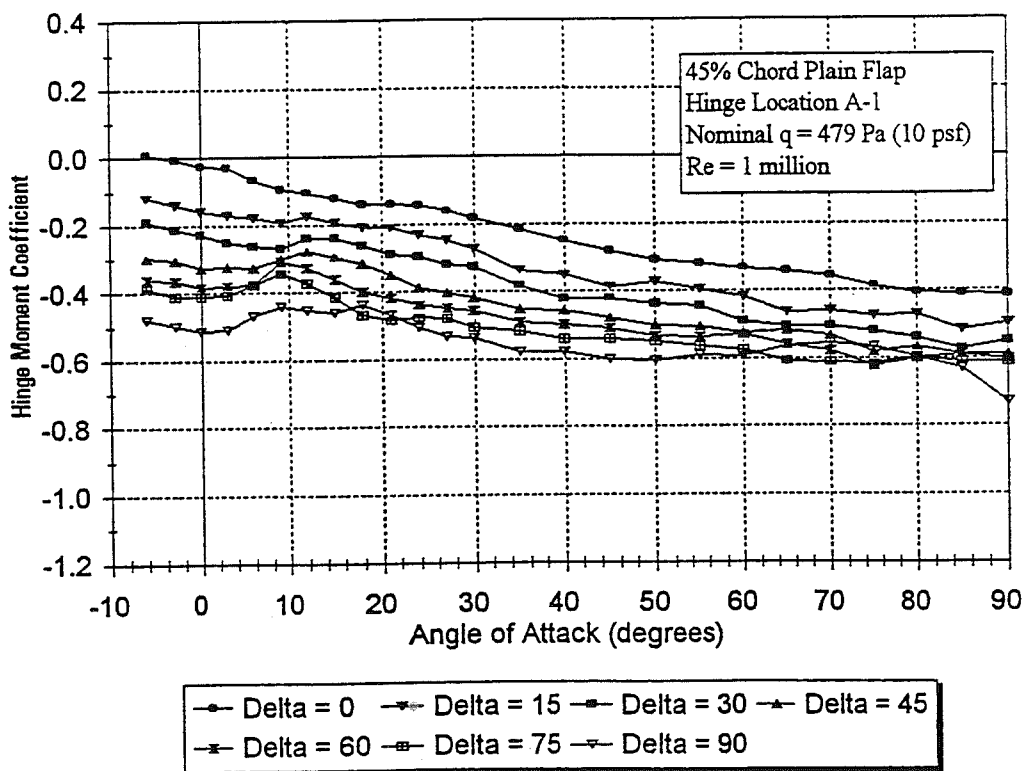


Figure 4-5d. Hinge Moment Coefficients for 45% Chord Plain Flap, Hinge A-1

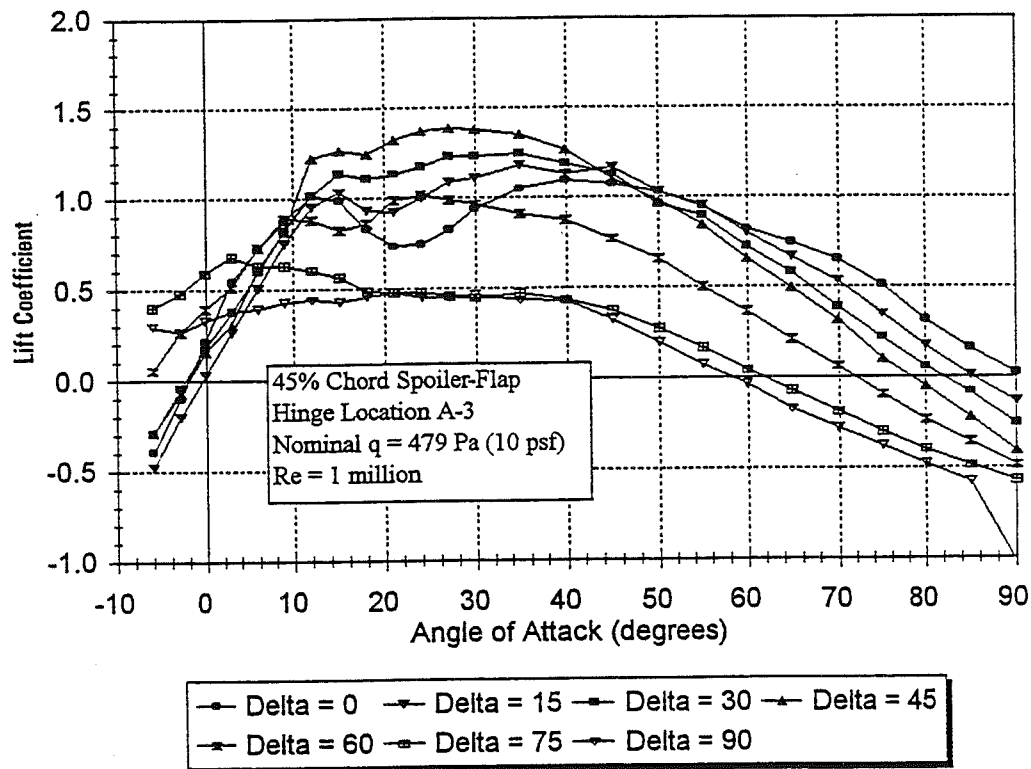


Figure 4-6a. Lift Coefficients for 45% Chord Spoiler-Flap, Hinge A-3

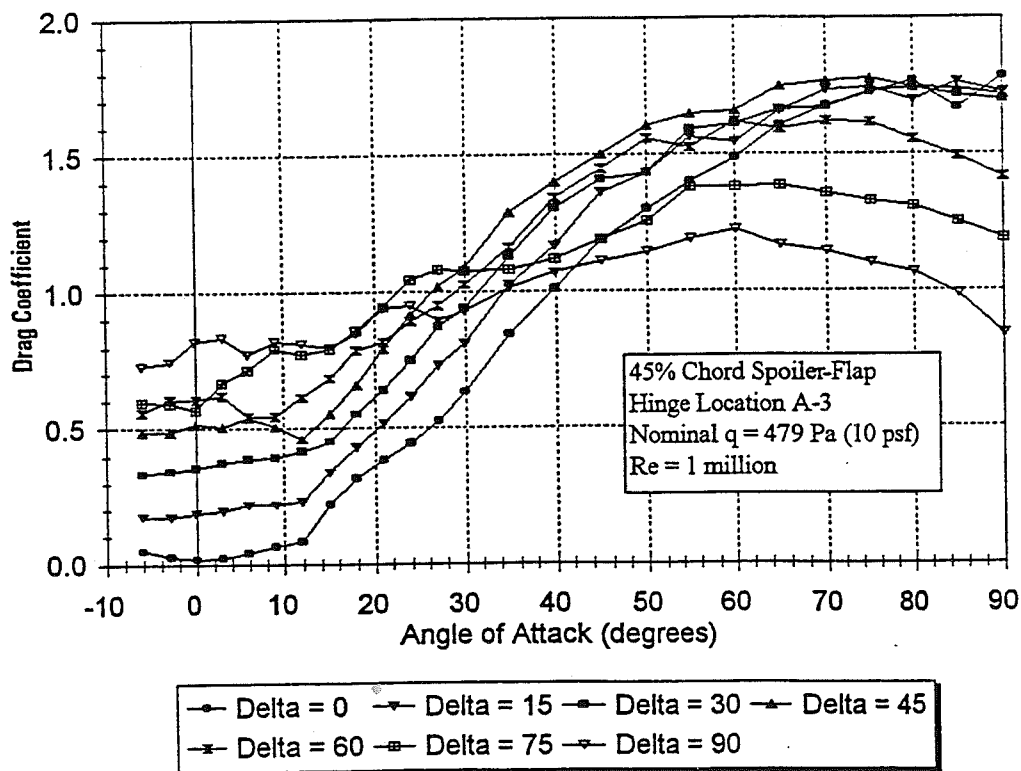


Figure 4-6b. Drag Coefficients for 45% Chord Spoiler-Flap, Hinge A-3

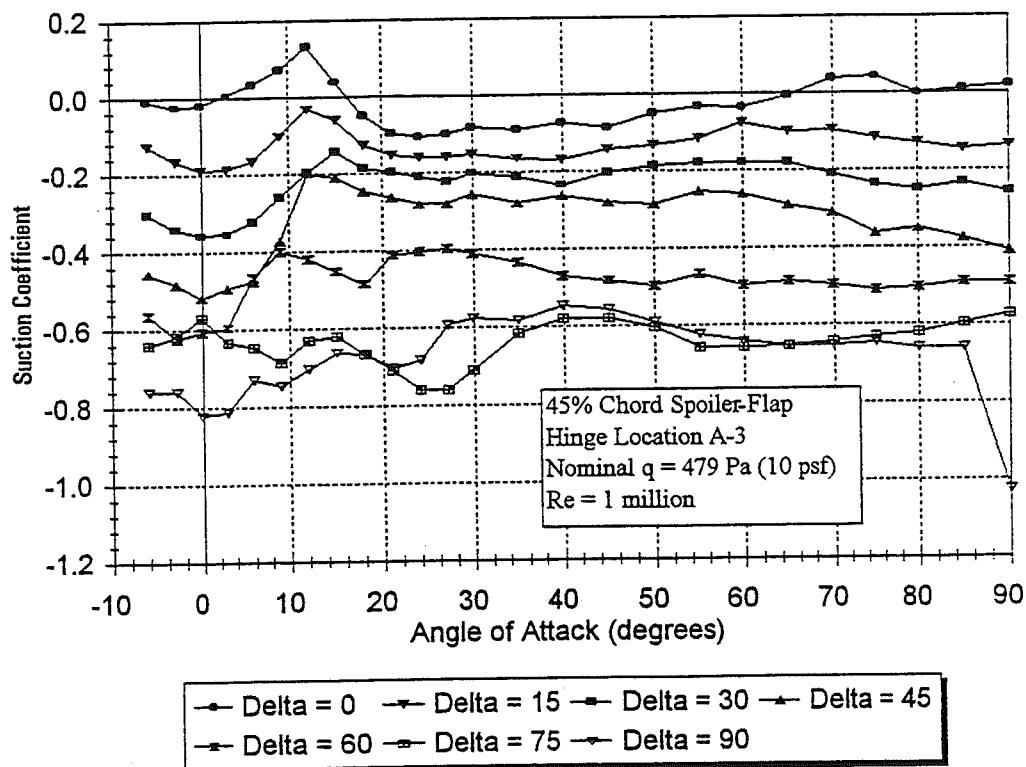


Figure 4-6c. Suction Coefficients for 45% Chord Spoiler-Flap, Hinge A-3

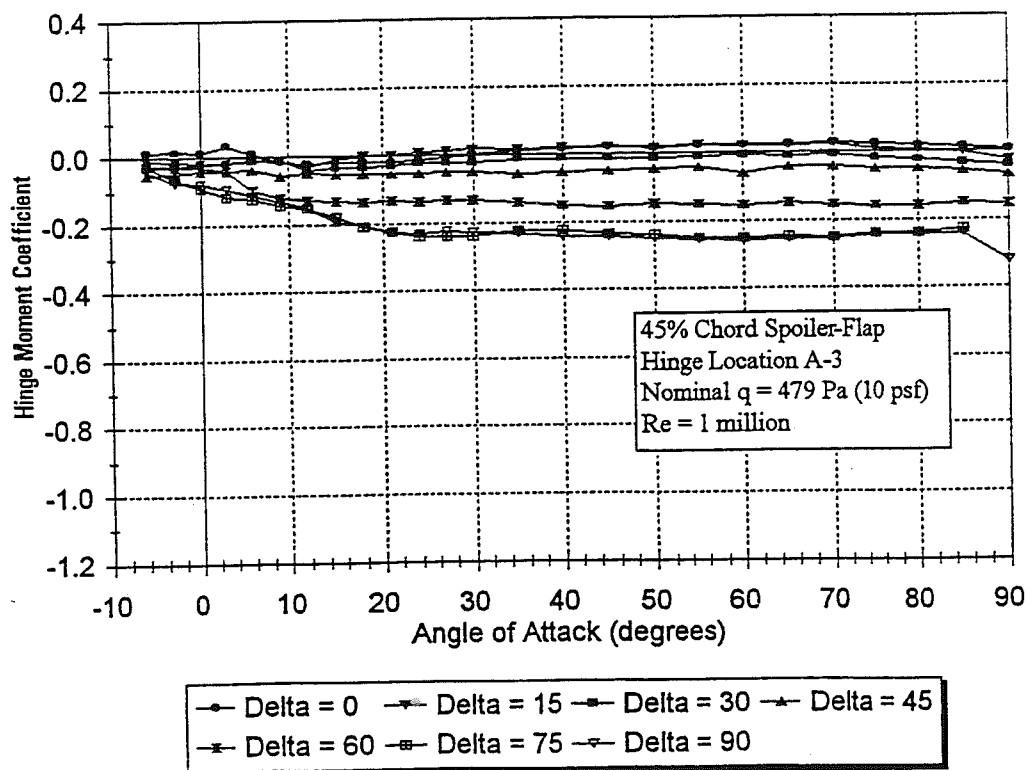


Figure 4-6d. Hinge Moment Coefficients for 45% Chord Spoiler-Flap, Hinge A-3

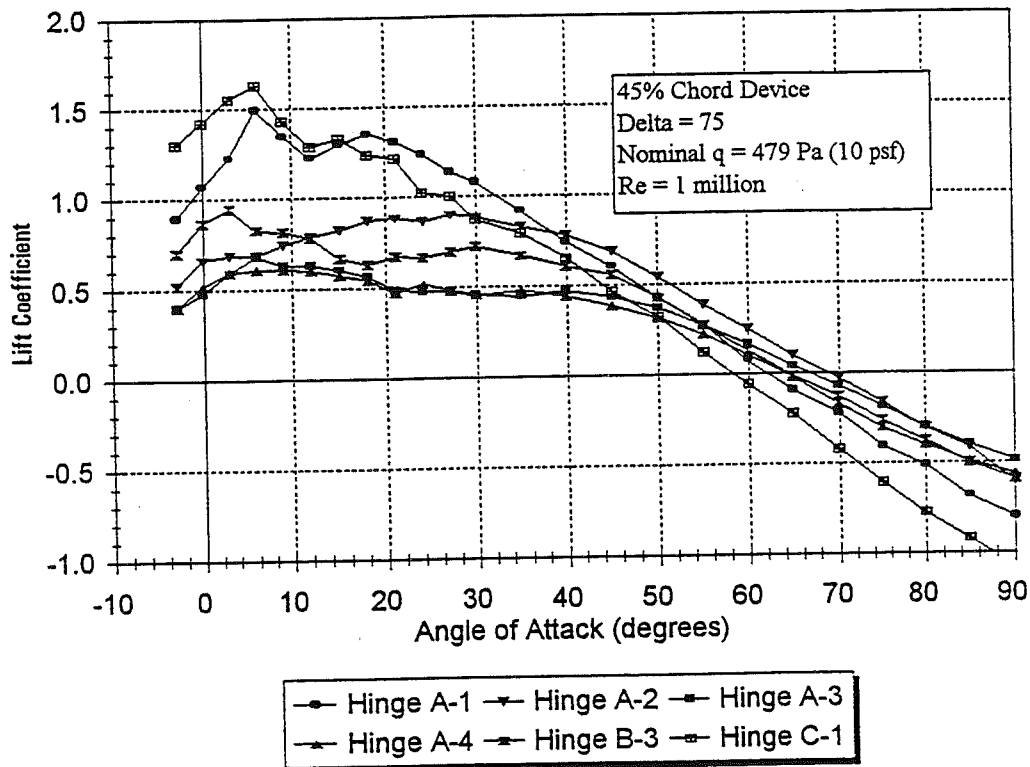


Figure 4-7a. Lift Data, Effect of Hinge Location on Device at $\delta = 75^\circ$

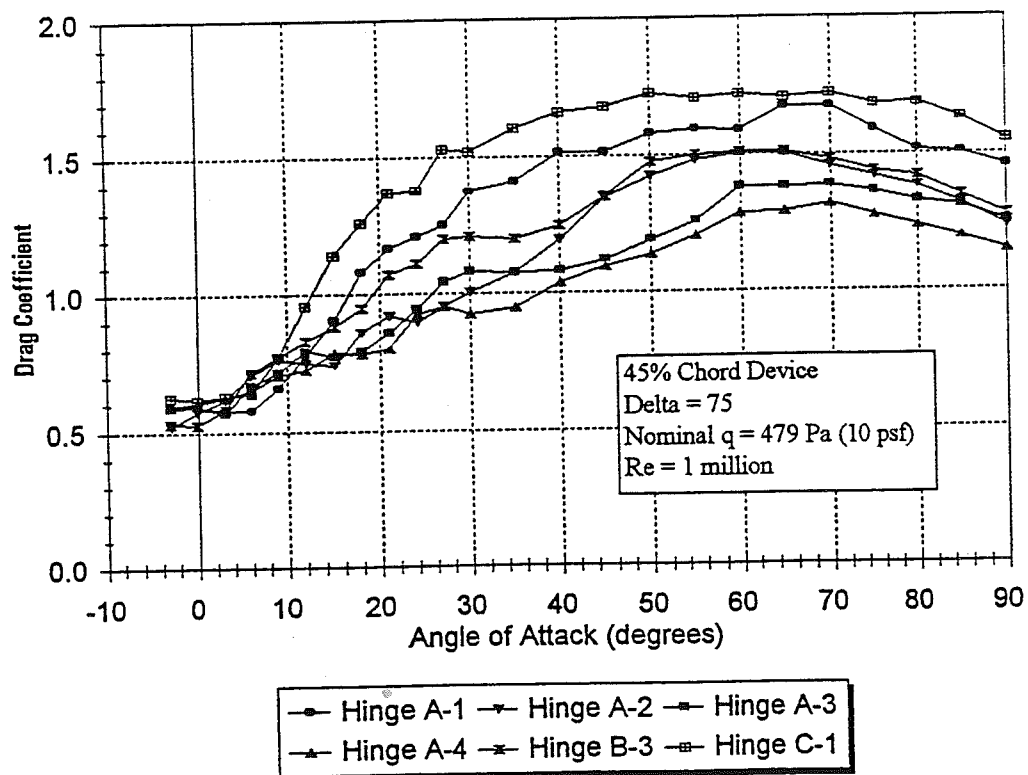


Figure 4-7b. Drag Data, Effect of Hinge Location on Device at $\delta = 75^\circ$

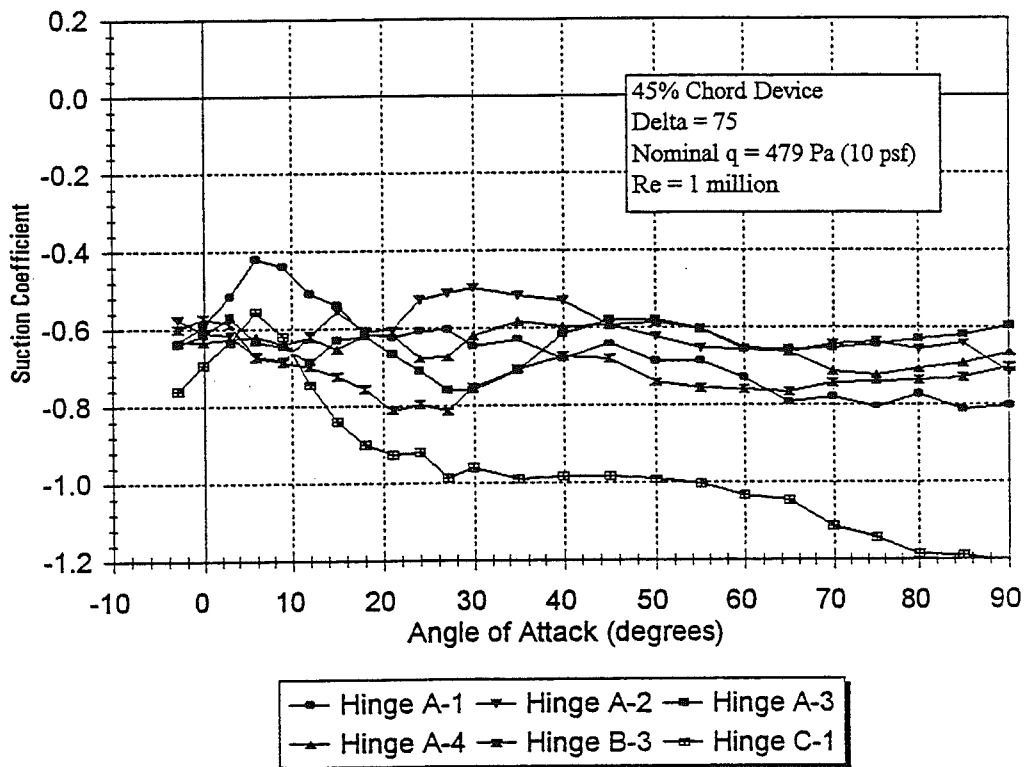


Figure 4-7c. Suction Data, Effect of Hinge Location on Device at $\delta = 75^\circ$

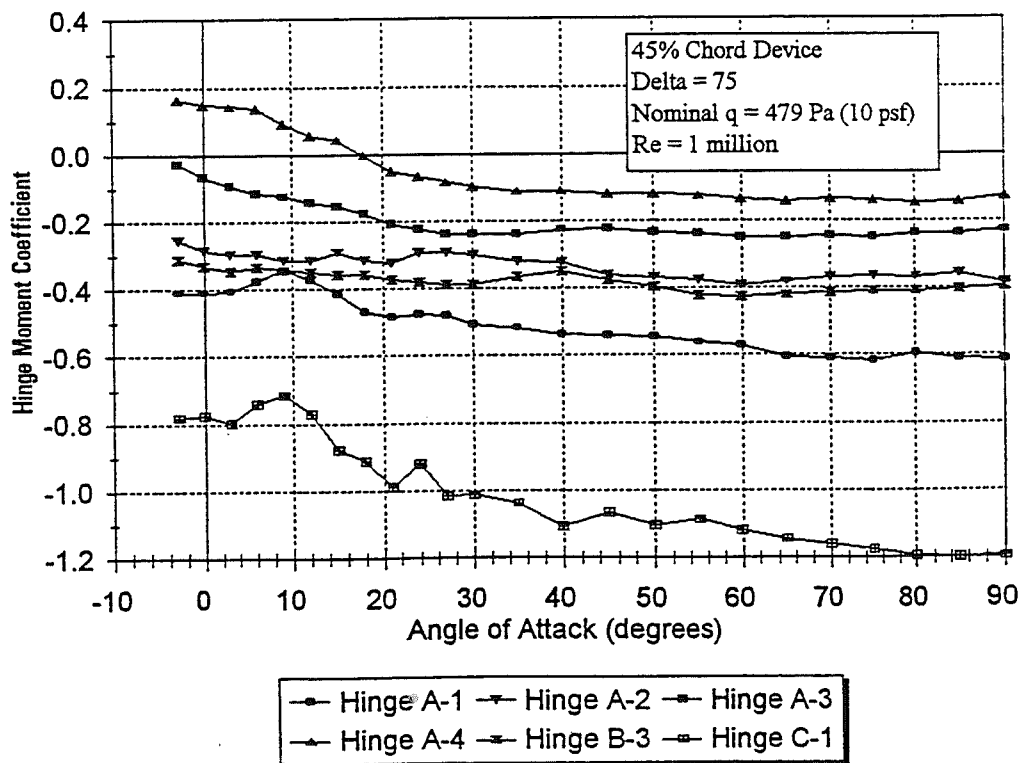


Figure 4-7d. Hinge-Moment Data, Effect of Hinge Location on Device at $\delta = 75^\circ$

Figure 4-7a, where the plain and vented flaps show significant high-lift behavior. In terms of suction coefficient, the vented flap (hinge C-1) exhibits the largest variation with angle of attack, showing a noticeable suction peak at $\alpha = 9^\circ$ and large negative suction coefficients at $\alpha > 20^\circ$. At pre-stall angles of attack, the spoiler-flap configurations show little variation of suction coefficient with hinge location, with values generally ranging between -0.6 and -0.7.

Figure 4-7d shows that the vented flap has very high closing hinge moments. Both the force and hinge-moment data for the vented flap are consistent with the fact that the hinge position allows larger aerodynamic surfaces to be exposed to the free-stream air than for the other hinge points considered. At $\delta = 75^\circ$, the spoiler-flap data show smoothly varying hinge moment trends, with an increasing tendency towards opening as the devices are hinged further aft.

4.3.3 Effect of Device Chord

A limited discussion of the effect of varying device chord is presented here, with the complete set of aerodynamic data for the 38% chord devices available in Appendix A. As might be expected, the 38% chord devices generally resulted in smaller changes to the aerodynamic forces and smaller hinge moments. However, Figure 4-8 shows the effectiveness per unit device chord to be quite similar. The figure shows changes in suction coefficient for both the 38% and 45% chord devices, where the quantity plotted is:

$$\frac{\Delta C_s}{\text{Unit Device Chord}} = \frac{C_{s, \text{device deflected}} - C_{s, \text{clean airfoil}}}{(\text{Device chord} / \text{Airfoil Chord})} \quad (4-2)$$

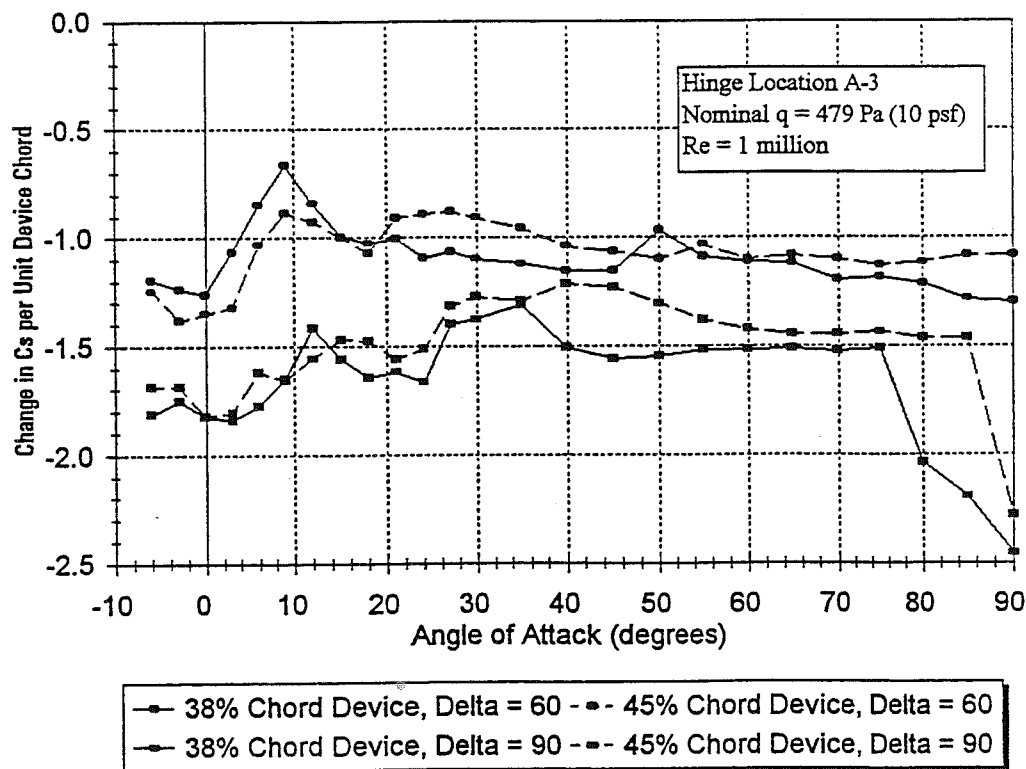


Figure 4-8. Braking Effectiveness per Unit Device Chord

4.3.4 Reynolds Number Effects

As discussed in Section 4.2, the majority of wind-tunnel test runs were conducted at a nominal Reynolds number of 1.0 million. This is significantly lower than the operational Reynolds numbers of the AWT-26/27 turbines, which range between 2.0 and 3.0 million in the blade-tip regions. Selected runs were therefore conducted at high Reynolds number to confirm that the wind tunnel data could be used to predict the full-scale performance of devices.

During the wind tunnel tests, maximum Reynolds numbers were generally constrained by balance limits. With flaps deflected, running at high dynamic pressures resulted in large side loads (in the standard wind tunnel frame of reference). To obtain high Reynolds number data, the tunnel operators would maintain the highest possible dynamic pressure without exceeding any balance limits. This resulted in runs where the Reynolds number varied with angle of attack, and the data from these runs must therefore be interpreted with care.

Although the procedure for obtaining high Reynolds number data was somewhat cumbersome, the objective was satisfied. At pre-stall airfoil angles of attack, and at small device deflection angles, the tunnel operators were able to maintain Reynolds numbers of about 2.0 million. At post-stall airfoil angles and at high device deflections the maximum Reynolds numbers were as low as 1.4 million. Therefore, the highest Reynolds numbers were obtained at the conditions for which the greatest effect was expected.

Figures 4-9 shows that the measured effect of Reynolds number on the spoiler-flap performance was fairly subtle. The insensitivity of aerodynamic performance to Reynolds number was confirmed for several flap configurations throughout the test, with results similar to those shown in Figures 4-9.

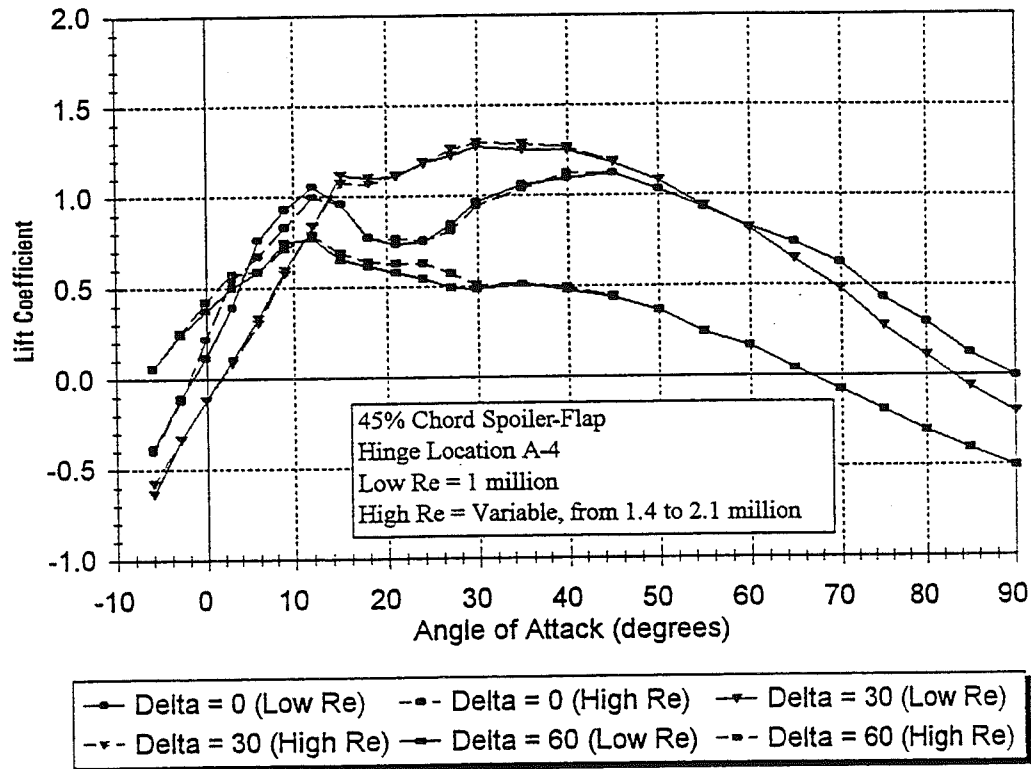


Figure 4-9a. Lift Data, Reynolds Number Effect on Spoiler-Flap

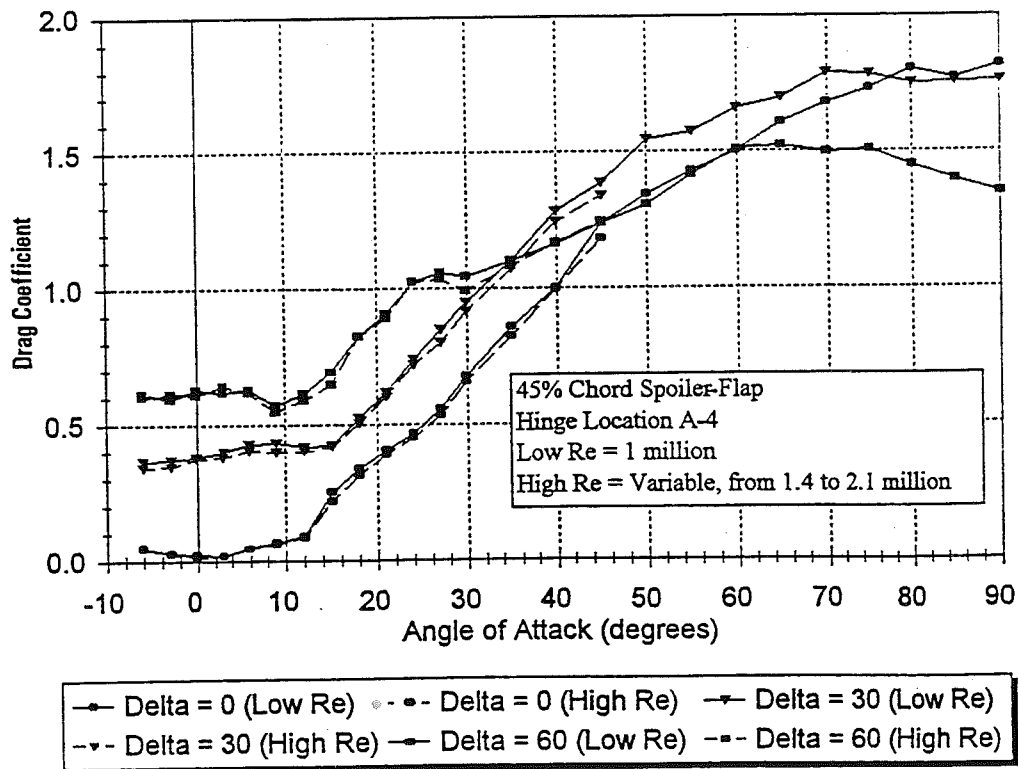


Figure 4-9b. Drag Data, Reynolds Number Effect on Spoiler-Flap

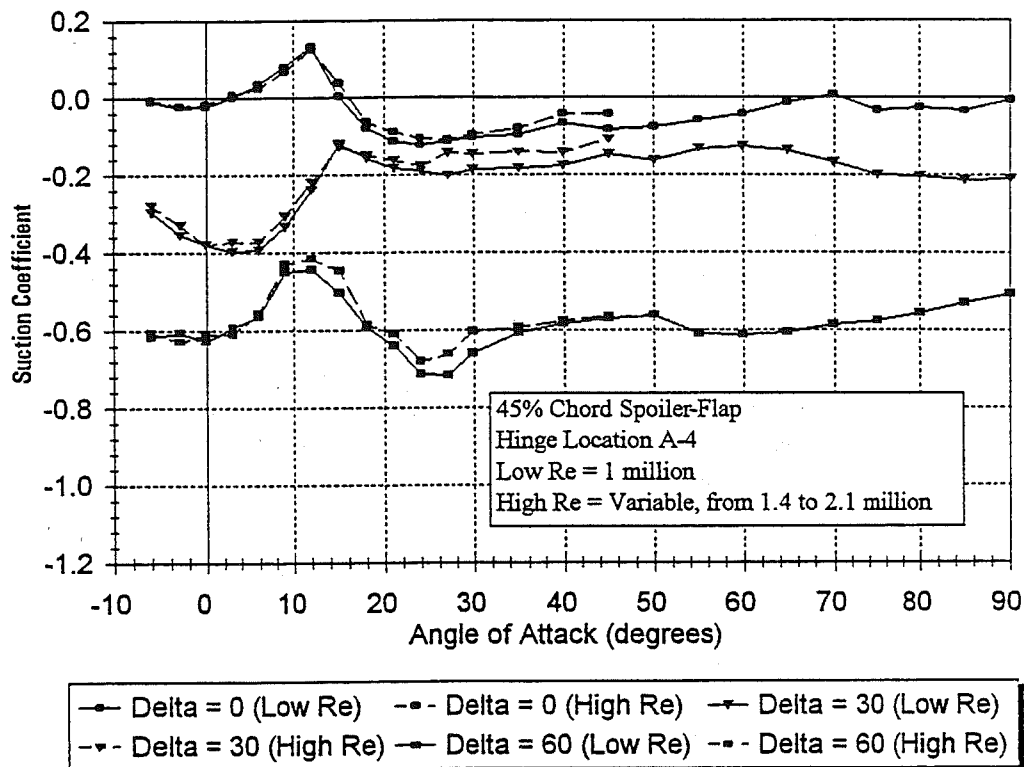


Figure 4-9c. Suction Data, Reynolds Number Effect on Spoiler-Flap

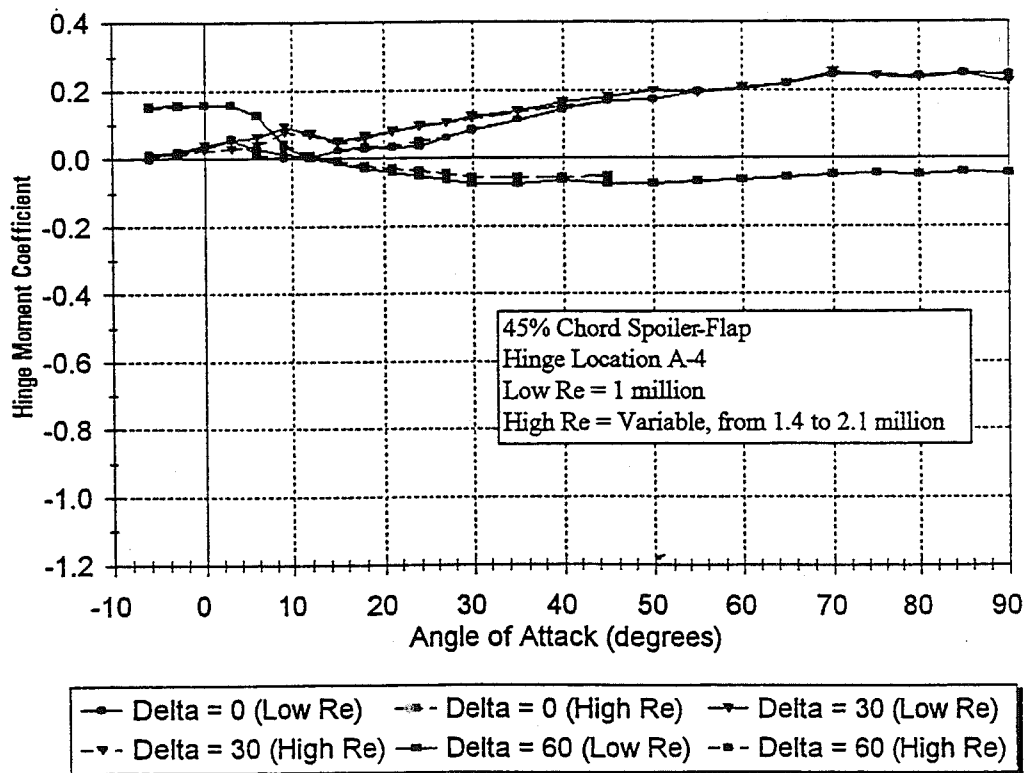


Figure 4-9d. Hinge-Moment Data, Reynolds Number Effect on Spoiler-Flap

4.3.5 Partial-Span Effects

The motivation for considering partial-span effects was to determine whether the two-dimensional flap data could be used directly to predict the stopping power of actual (finite aspect ratio) devices, or whether a three-dimensional "knock-down" should be applied. As an example, the drag coefficient of an infinite flat plate is approximately 2.0, but drops rapidly to a value of 1.2 for plates of finite aspect ratio [10]. For flat-plate drag coefficients, this would suggest a finite aspect ratio knock-down of 40% from the two-dimensional value. Although the flap configurations which were tested are more than simple drag devices, it is still important to consider the impact of aspect ratio on their aerodynamic effectiveness.

The baseline model for the wind tunnel tests had flaps that were of infinite aspect ratio, extending the entire airfoil span from floor to ceiling. Although the importance of aspect ratio effects was recognized, the design and construction of a segmented model (capable of partial-span flap deployment) was beyond the resources of this project.

As a compromise, inexpensive bolt-on plates were designed to approximate the effect of aspect ratio on flap performance. Figure 4-10 shows the dimensions and placement of the plates on the WSU model. The plates were constructed in three lengths: 1/3-span, 1/2-span, and full-span. The partial-span plates were installed such that the center of their span was at or near the center of the airfoil span.

The plates could be bolted on in a modular fashion to model various devices. For example, the installation of plate #2 would model a split-flap deployed to $\delta = 45^\circ$. In terms of projection into the free-stream, installation of both plates #1 and #3 would closely resemble a spoiler-flap deployed to 90° . Unfortunately this arrangement does not allow for the venting of flow that would occur for an actual deployed spoiler-flap, which is considered to be a key feature of the device aerodynamics. In all cases, the partial-span plates were considered to accurately model flaps only at low airfoil angles of attack, prior to significant impingement of the free-stream flow on the trailing edge of the rear model element.

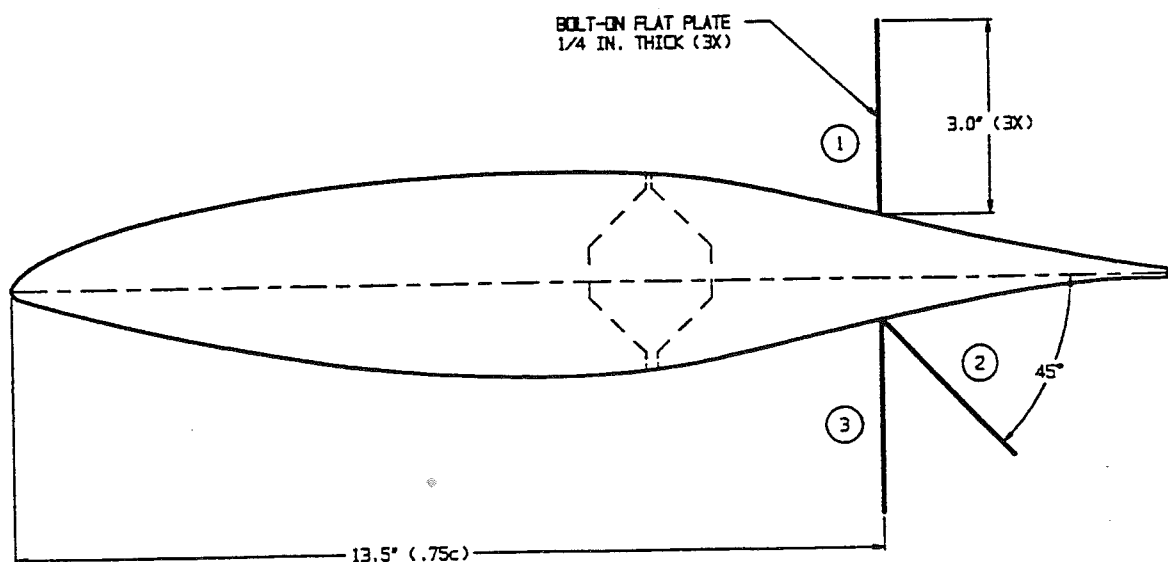


Figure 4-10. Sectional View of Model with Partial-Span Plates

During the wind tunnel test, the total resultant aerodynamic forces on the partial-span models were normalized with respect to the full-model dimensions. Therefore, the coefficients for partial-span configurations require additional analysis to be correctly interpreted. The total force on a model with a partial-span flap could be considered as a superposition of the aerodynamic forces on the modified and unmodified portions of the airfoil. The wind tunnel coefficients shown in this report were re-reduced assuming such a linear superposition of forces, although this is an admitted oversimplification of the flow around the partial-span model.

Figure 4-11 shows an example of suction coefficient behavior from the partial-span tests. The data are given in knock-down form, expressed as a percentage loss of effectiveness due to finite aspect ratio:

$$\Delta C_S \text{ knock-down} = 100 * \frac{\Delta C_{S, \text{full-span flap}} - \Delta C_{S, \text{partial-span flap}}}{\Delta C_{S, \text{full-span flap}}} \quad (4-3)$$

For $\alpha < 12^\circ$, the data show a fairly consistent knock-down of 20% to 30%, which is consistent with flat-plate drag effects. The data become erratic at post-stall angles of attack, which is understandable as the assumptions of linearity become less valid and airflow begins impinging on the trailing-edge of the model. The legend in Figure 4-11 shows the flap configurations tested, with 90/90 indicating 90° plates on both the upper and lower surfaces (Plates #1 and #3 shown in Figure 4-10) and 90/45 indicating a 90° plate on the upper surface and a 45° plate on the lower surface (Plates #1 and #2).

Although a strong dependence on aspect ratio was found, the application of these data to spoiler-flap and flip-tip design is uncertain. The partial-span models did not include flow venting, which is considered to be a key feature of spoiler-flap aerodynamics. The work of References 5 and 6 is intended to assess the full three-dimensional effects on both ailerons and spoiler-flaps, but the results of this work have not yet been published.

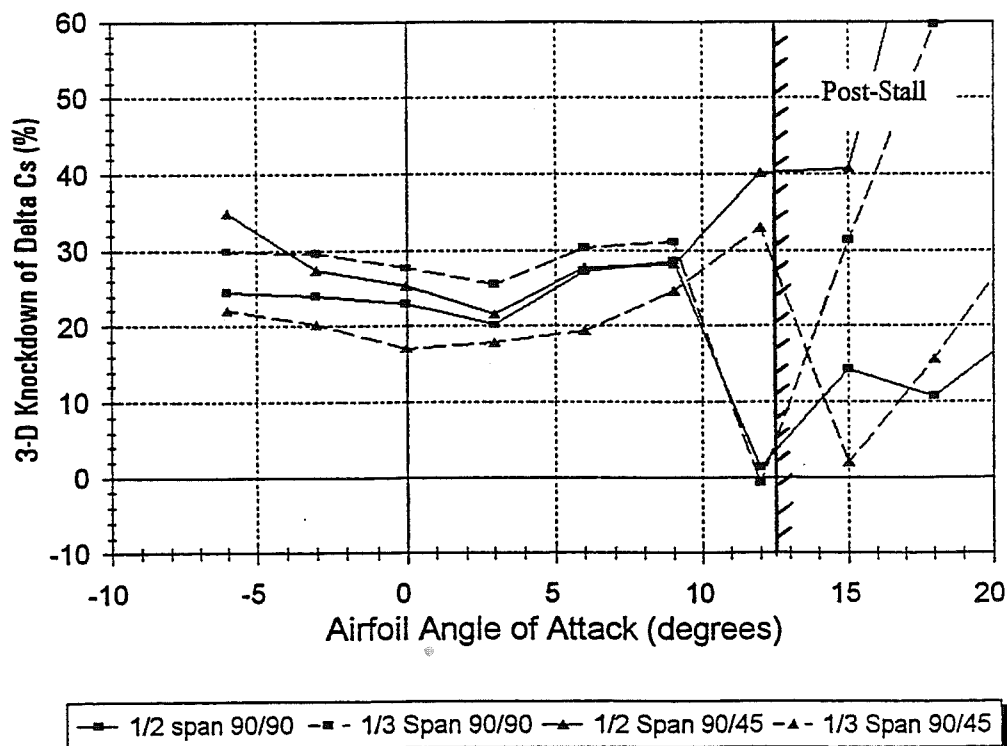


Figure 4-11. Effect of Finite Aspect Ratio on Flap Braking Effectiveness

5. Sizing and Deployment Studies

5.1 AWT-26/27 Braking Requirements

The braking requirements for AWT-26/27 turbines are dependent on the magnitude of the power that is captured by the rotor under various operating conditions. The rotor power can be related to torque at the low-speed shaft by

$$P_{\text{Rotor}} = M_{\text{LSS}} \cdot \Omega, \quad (5-1)$$

where M_{LSS} is the low-speed shaft torque and Ω is the rotor speed expressed in radians per second. Direct measurement of low-speed shaft torque is possible, but can be difficult. An alternative method of determining rotor torque is by measuring electrical power output, then adjusting for drivetrain losses. This second method has been used to generate Figure 5-1. The original data were in the form of a generator power curve measured from the AWT-26 prototype turbine, P1. Drivetrain efficiencies were used along with Equations 2-6 and 2-7 to establish a rotor C_p -TSR curve for the AWT-26 at an operating speed of 57 rpm. With the assumption that the C_p -TSR curve remained unchanged, the rotor power curves of Figure 5-1 were developed for wind speeds up to 30 m/s (67 mph) and rotor speeds between 50 and 75 rpm. Each curve has been labeled with the maximum low-speed shaft torque.

This figure shows the relationship between rotor speed and braking requirements. The AWT-26/27 rotors were designed for normal operating speeds between 50 and 60 rpm. The 75 rpm curve therefore

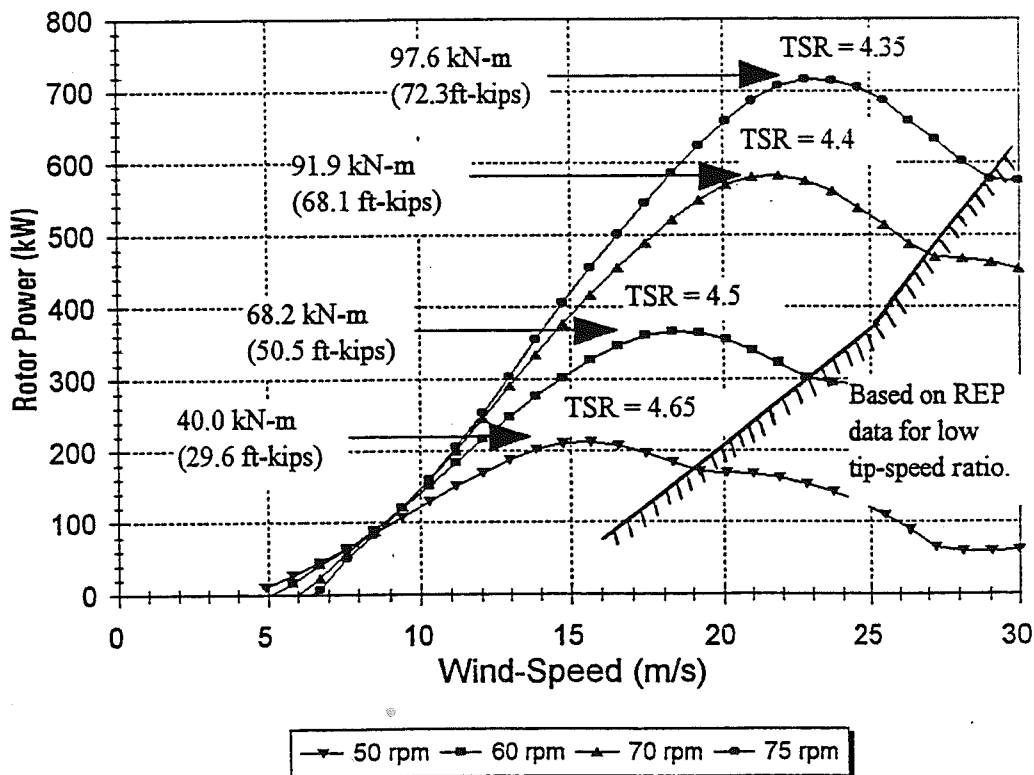


Figure 5-1. AWT-26 Rotor Power at Varying Rotational Speeds

represents a 25% overspeed beyond the maximum normal operation of the AWT-26. The curves show a doubling of maximum rotor power due to this overspeed condition, and a 43% increase in the peak low-speed shaft torque. In the absence of external load (i.e., freewheeling rotor), these values represent the amount of power that must be extracted from the rotor by either mechanical or aerodynamic brakes in order to prevent the rotor from further acceleration.

The tip-speed ratio at maximum rotor power is noted on each of the power curves of Figure 5-1. At wind speeds above peak power (decreasing tip-speed ratios), the power levels are strictly decreasing for all wind speeds shown. It should be noted that the power curve for the P1 prototype included only measured tip speeds of 3.5 and greater, which are shown as data to the left of the hashed lines on Figure 5-1. The data for tip-speed ratios below 3.5 were obtained during the AWT ESI-80 Performance and Reliability Enhancement Program (REP) [11]. The REP data were obtained with AWT-26 blades retrofitted to an ESI-80 turbine, and the rotor pitched to a peak generator power of 35 kW at a rotor speed of 30 rpm. Therefore, the REP configuration was somewhat different than the current AWT-26 design, and the low TSR data presented here are not considered of high enough confidence for aerodynamic brake design.

All specific sizing and performance calculations in the following sections have been made for the AWT-26 turbine. Although Figure 5-1 presents data in terms of rotor power and shaft torque, the majority of the work in this report will be expressed in coefficient form. This is done because C_p -TSR curves are able to represent the wide range of wind and rotor speeds over which the aerodynamic brakes must be effective. It will be shown that the most critical point of operation for aerodynamic brakes occurs at low tip-speed ratios. Due to the need for low TSR data, the baseline AWT-26 C_p -TSR curve has been generated by calculations using the PROP93 analytic code [12]. Figure 5-2

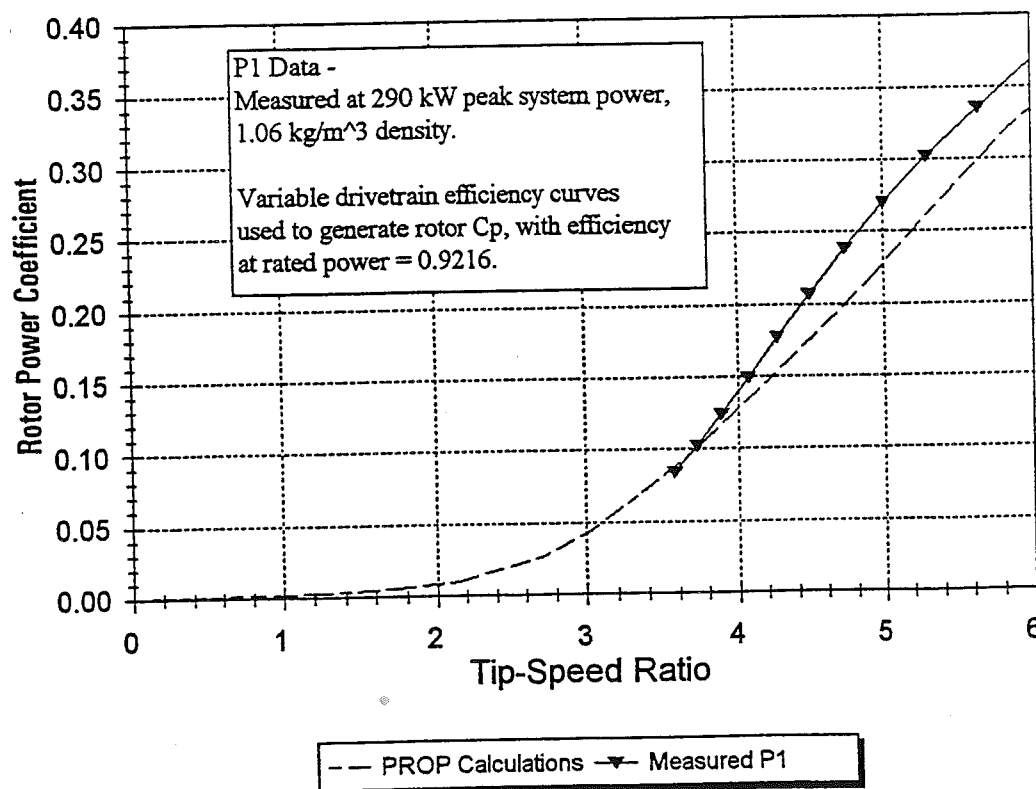


Figure 5-2. Rotor Power Coefficients for AWT-26 at Low TSR

shows a comparison of PROP93 versus measured P1 power coefficients at low tip-speed ratios. The curves show very close agreement for tip-speed ratios between 3.5 and 4.0, which represent the AWT-26 at post-stall wind speeds near 22 m/s (50 mph). Peak power for normal AWT-26 operation occurs at a TSR of about 4.5, where the PROP93 values for C_p are somewhat low. The sizing of aerodynamic brakes for the AWT-26 is strongly dependent on the power coefficients near a tip-speed ratio of 3.0, where the PROP93 calculations show $C_p \approx 0.04$. For this rotor, low tip-speed ratios correspond to high blade angles of attack ($\alpha_{tip} \geq 18^\circ$), and the accuracy of the PROP93 calculations is uncertain. However, in the absence of a better method, the analytic data shown in Figure 5-2 will be used as a baseline for the following aerodynamic braking calculations.

5.2 Sizing of Candidate Devices

AWT engineers have specified design load cases for the aerodynamic braking system [13] that are consistent with international wind turbine design standards [14, 15]. The AWT specifications have been developed for a Class II wind site as defined by Reference 14. This report will only address the load cases that have been found to dominate the sizing and deployment characteristics of the aerodynamic brakes.

The AWT-26/27 turbines are designed for a range of operational speeds from 50 to 60 rpm. Per the requirements of Reference 15, the braking system design will assume that a maximum rotor speed of 25% above synchronous may occur during an overspeed condition. The aerodynamic braking system will therefore be required to prevent rotor speeds in excess of 75 rpm for all design load cases.

Several load cases include turbine faults that may lead to loss of load and mechanical brakes. In these cases the rotor is freewheeling, and the aerodynamic braking system must prevent rotor speeds from exceeding 75 rpm. In accordance with Reference 14, the freewheeling condition was assumed to occur during a 1-year extreme operating gust described by:

$$V = V_{hub} + 0.5 \cdot V_{gust} [1 - \cos(2\pi t / T)], \quad (5-2)$$

where $T = 12$ s. For a Class II wind site, the normal turbulence model of Reference 14 defines the standard deviation of wind speed as $\sigma = 0.153 \cdot V_{hub} + 0.277$ (m/s), and a 1-year gust as $V_{gust,1} = 3.75 \cdot \sigma$. The highest value of $V_{gust,1}$ would be obtained for a turbine operating near cut-out wind speeds, nominally 22.3 m/s (50 mph) for the AWT-26/27 turbines. Thus, for the AWT-26/27 turbines, the 1-year extreme operating gust would result in a maximum wind speed of 36.2 m/s (81.0 mph), with the gust event occurring over a 12-second interval.

It was found that the above case dominated the sizing of candidate aerodynamic brakes. A device sized to restrain freewheeling rotor speeds to $\Omega_{max} \leq 75$ rpm during a 1-year extreme operating gust was generally suitable for all other design cases (assuming adequate deployment). The sizing and deployment studies presented in the following sections are all based on the 1-year extreme operating gust.

Equation 2-8 can be used to determine the maximum freewheeling tip-speed ratio allowed for given rotor and wind-speeds. Substituting values of $\Omega_{max} = 7.85$ rad/s (75 rpm), $V_o = 36.2$ m/s, and $R = 13.1$ m (43 ft) yields a value of $TSR_{max} = 2.8$ for the AWT-26 turbine. Equilibrium tip-speed ratios greater than 2.8 would allow the freewheeling rotor to exceed 75 rpm during a 1-year gust. This illustrates the importance of low tip-speed ratios for aerodynamic braking of the AWT-26/27 turbines.

A review of the wind-tunnel data for spoiler-flap devices shows that the ΔC_s supplied by the devices is dependent on the deployment angle. In particular, there is a significant increase in device effectiveness between the angles of $60^\circ < \delta < 75^\circ$, with a much smaller performance increment for angles greater than 75° . The sizing of aerodynamic brakes is therefore dependent on the specifics of the design, including deployment rates and equilibrium deployment angles. The trade-off between device size and deployment characteristics will be addressed in Section 5.3.1. The present sizing analysis assumes all devices are fully deployed to $\delta = 90^\circ$.

Results from the sizing studies will be presented in coefficient form. Equation 2-1 has been used with the wind-tunnel data to calculate ΔC_s for each device geometry and deployment angle ($\delta = 90^\circ$ for device sizing). As discussed below, an adjustment has been applied to the two-dimensional data to account for loss of effectiveness due to finite aspect ratio. Equations 3-8 and 3-9 have then been used to determine the rotor ΔC_p for each device geometry. This process included PROP93 calculations to account for the effect of rotor interference on turbine-blade angles of attack.

Figures 5-3 show results from this method, where the TSR range has been truncated to emphasize the results at low tip-speed ratios. Finite aspect ratio knock-downs of 20% have been applied to the flap sections (spoiler and plain) and 30% for the tip region of the flip-tip. Note that the 30% knock-down for the tip region was determined as the factor required to adjust the WSU wind-tunnel data to obtain the finite flat-plate result of $C_{Dmax} = 1.2$. As the actual finite aspect ratio adjustments for these devices are unknown, the data on Figures 5-3 should not be considered absolute, but are rather meant to illustrate the sizing trends of the devices. Several different knock-down factors were used in the course of this work. Each analysis shown in this report will be labeled with the knock-down factors that were used in converting the two-dimensional wind tunnel data.

Figure 5-3a shows sizing results for the flip-tip, where adequate braking is obtained for devices with a total span as low as 10%. The figure also demonstrates that the flip-tip remains effective for a variety of tip/flap area ratios. The correct size-weighting of the tip and flap regions will be of greatest importance when determining deployment characteristics.

With a 20% knock-down, Figure 5-3b shows the 15% span spoiler-flap to be undersized, with an equilibrium tip-speed ratio of 3.7. Although the spoiler with 17.5% span maintains negative values of C_p for all TSR > 1.0 , inspection of the curves near TSR = 3.0 shows that this device is marginally sufficient.

Similar sizing studies were performed for the 38% chord spoiler-flap. The general result was not surprising; 38% chord spoiler-flaps require a longer span (by about 5% R) to have stopping power equivalent to the 45% chord device. The 38% flap would remove less chordwise structure from the existing blade, but the cut-line would occur over a larger span. Additionally, hinge design for the 38% chord spoiler would be more challenging, as the maximum device cross section would be smaller. After consideration of the structural and mechanical issues involved in the sizing, AWT engineers concluded that the 45% chord device was preferable for implementation on the AWT-26/27 blades. Further analysis and discussion of spoiler-flaps will, therefore, be restricted to 45% chord devices.

Note that the sizing results shown are for spoiler-flaps that extend to the blade tip, which is the furthest outboard placement possible. Equation 3-8 shows a cubic dependency on radial position of the device that favors outboard placement. This implies a significant penalty for moving the device inboard.

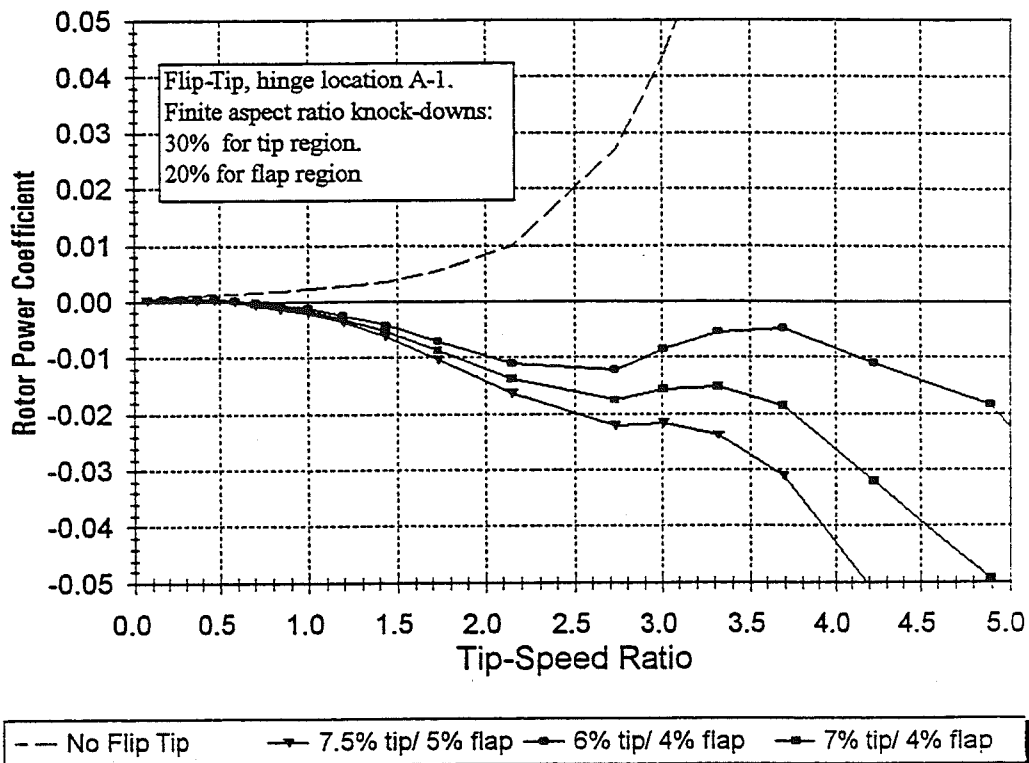


Figure 5-3a. Sizing of Flip-Tip for AWT-26 Aerodynamic Braking

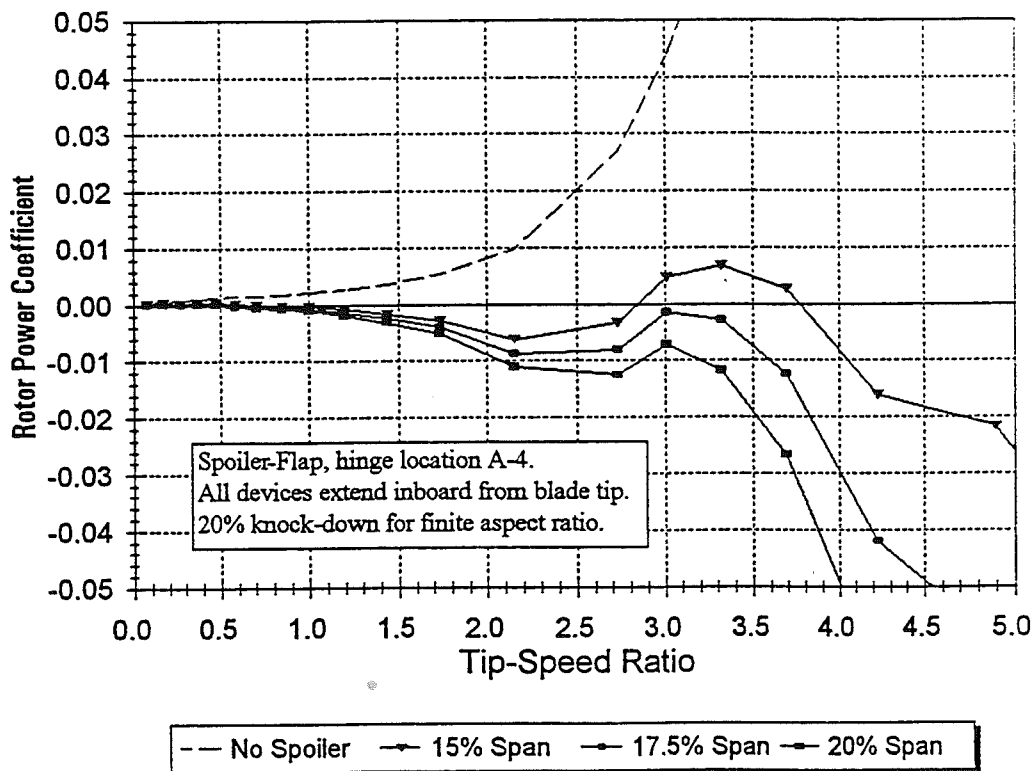


Figure 5-3b. Sizing of Spoiler-Flap for AWT-26 Aerodynamic Braking

However, ΔC_p also varies linearly with the area of the modified blade section, and the overall effectiveness will scale as the product $(r/R)^3 \cdot A_{\text{section}}$. For turbines with significant blade taper at the tip, the increase in modified blade area can outweigh the loss in $(r/R)^3$. This is demonstrated for the AWT-26/27 turbine in Table 5-1, which shows overall effectiveness increasing slightly and then falling off slowly as the device is moved inboard.

Table 5-1. Variation of Spoiler-Flap Effectiveness with Spanwise Location

Device Center (r/R)	Blade Chord at Device Center (cm)	Blade Thickness at Device Center (cm)	Blade Area at Device (m ²)	$(r/R)^3 \cdot A_{\text{section}}$ (m ²)
0.925	52.7	9.22	1.007	0.797
0.900	57.0	9.98	1.096	0.799
0.875	61.3	10.73	1.184	0.793
0.850	65.5	11.46	1.250	0.767
0.825	68.9	12.06	1.333	0.748

Note: Assumes 15% span spoiler-flap on AWT-26 blade.

5.3 Aerodynamic Deployment Calculations

The AWT-26/27 tip-vane deployment is governed by a combination of aerodynamic and centripetal forces, with the centripetal effects dominating the hinge moments at small deployment angles, and aerodynamics dominating at large angles. In principle, either the spoiler-flap or flip-tip configuration could be aerodynamically deployed in a manner very similar to the AWT-26/27 tip vanes. However, the orientation of the spoiler-flap and flip-tip configurations tends to diminish centripetal moments about the device hinge lines. Section 5.3 will focus on deployment by a combination of aerodynamics and passive mechanical forces (springs and dampers), neglecting centripetal effects. Sections 5.4 and 5.5 will include details of how centripetal forces may be used to assist in either active or passive mechanical deployment methods. With proper design, of course, centripetal forces could be used to assist aerodynamically deployed devices.

Analysis of aerodynamic deployment for the spoiler-flap and flip-tip configurations begins with the general equations of motion:

$$\sum M_{\text{Rotor}} = I_{\text{Rotor}} \cdot \ddot{\Omega} + C_1 \cdot \dot{\Omega} + C_2 \quad (5-3)$$

where:

- M_{Rotor} = all moments contributing to rotation about the low-speed shaft
- I_{Rotor} = rotational moment of inertia of the rotor system and drivetrain about the low-speed shaft
- $\ddot{\Omega}$ = rate of change of rotor speed
- $C_1 \cdot \dot{\Omega}$ = accounts for variable-speed component of generator and gearbox load
- C_2 = accounts for constant drivetrain load or losses

and,

$$\sum M_{\text{Hinge-Line}} = I_{\text{Flap}} \cdot \ddot{\delta} + C_3 \cdot \dot{\delta} + C_4 \cdot \delta \quad (5-4)$$

where:

- $M_{\text{Hinge-Line}}$ \equiv all moments that induce flap rotation about the hinge line
- I_{Flap} \equiv rotational moment of inertia of the flap about the hinge line
- δ \equiv flap deployment angle
- $\dot{\delta}$ \equiv flap deployment speed
- $\ddot{\delta}$ \equiv rate of change of flap deployment speed
- C_3 \equiv damping coefficient
- C_4 \equiv spring coefficient.

Equations 5-3 and 5-4 are second-order, nonlinear differential equations that are fully coupled. Any change of wind or rotor speed would change the aerodynamic condition of both the rotor and the flaps. Conversely, a change in flap deployment would change the aerodynamic torque (power) supplied to the rotor. Equation 5-3 is written in a turbine-fixed frame of reference while Equation 5-4 is in a rotating blade-fixed frame. These equations can be solved simultaneously so long as the appropriate auxiliary equations are introduced that relate the two reference frames. The equations can be reduced to a system of first-order differential equations in a form suitable for Runge-Kutta integration by the introduction of state variables.

let:

$$y_1 = \Omega$$

$$y_2 = \delta$$

$$y_3 = \dot{\delta}$$

then:

$$\dot{y}_1 = [I_{\text{Rotor}}]^{-1} \cdot (\sum M_{\text{rotor}} - C_1 \cdot y_1 - C_2) \quad (5-5a)$$

$$\dot{y}_2 = y_3 \quad (5-5b)$$

$$\dot{y}_3 = [I_{\text{Flap}}]^{-1} \cdot (\sum M_{\text{Hinge-line}} - C_3 \cdot y_3 - C_4 \cdot y_2) \quad (5-5c)$$

With initial conditions for Ω , δ , and $\dot{\delta}$, a time history of the aerodynamic brake deployment can be obtained through integration of Equations 5-5. This requires that the right-hand side of these equations be evaluated at each time step. Several of the inputs, such as I_{Rotor} , I_{Flap} , C_1 , C_2 , C_3 , and C_4 , are constant or are available from mechanical considerations. The remaining terms on the right-hand side of Equations 5-5 involve externally applied moments.

The low-speed shaft moments, $\sum M_{\text{Rotor}}$, can be evaluated in terms of C_p versus TSR curves for the rotor with and without deployed aerodynamic brakes (refer to Figure 2-2). For a given flap deflection, the C_p -TSR curves can be used along with wind speed and air density to find the rotor power, which can be used to solve for the rotor's aerodynamic contribution to the low-speed shaft torque. Any mechanical braking can be subtracted directly from the right-hand side of Equation 5-5a.

The $\Sigma M_{\text{Hinge-moment}}$ term is made up of two major contributors: aerodynamic and centripetal. The aerodynamic hinge moments are functions of the type and size of device, hinge location, air density, wind speed, Ω , δ , and α . Centripetal moments are functions of flap mass, location of device center of gravity, hinge-line location and orientation, blade coning angle, δ , and Ω . As discussed above, the present analysis neglects centripetal hinge moments.

A FORTRAN code was written to perform the integration of Equations 5-5. The code allows fast simulations of aerodynamic brake deployments, with user-specified inputs of initial conditions, wind speed, mechanical braking applied, and mechanical characteristics of the devices. Quatro-Pro workbooks were designed to convert wind-tunnel data into families of C_p -TSR and C_h - α curves, which represent the geometry, size, and placement of each candidate device. Graphical examples of these curves will be shown in the following sections. Tabular forms of the curves were read by the deployment code as look-up tables, allowing the calculations to update the aerodynamic performance of both the device and the rotor at each time step.

5.3.1 Spoiler-Flap

During the course of this work several iterations of spoiler-flap sizing, deployment simulation, and preliminary mechanical design were performed. This section discusses some of the general trends and design issues that were identified as a result of these iterations. Some of these results may be specific to the design of spoiler-flaps for use on the AWT-26/27 rotors. Nonetheless, the discussion should be instructive towards the use of spoiler-flaps with other turbine designs.

This work focused on an aerodynamic deployment strategy that was very similar to the current AWT-26/27 tip vane:

1. The aerodynamic brake assists with all normal and emergency stopping sequences, and provides overspeed protection for the case of a freewheeling rotor.
2. The spoiler-flap is hinged far enough aft so that it would have a strong aerodynamic tendency to deploy (positive aerodynamic hinge moments).
3. During normal turbine operation the flap is held closed by a combination of electromagnetic force and spring pre-load.
4. De-energizing the electromagnet allows the device to open aerodynamically, with the deployment rate controlled by a combination of aerodynamic, spring, and damping forces.
5. Equilibrium deployment occurs when the aerodynamic opening moment is balanced by the restraining mechanical forces.
6. With the rotor stopped, the spring pre-load is sufficient to stow the flap.
7. The electromagnet is re-energized as part of a normal starting sequence.

For the 45% chord spoiler-flap, it was determined that hinge location A-4 was not far enough aft to provide sufficient aerodynamic opening moments. As the WSU wind-tunnel test did not include the hinge location A-5 for the 45% spoiler, data from hinge locations A-3 and A-4 were extrapolated to estimate the device characteristics at intermediate positions. The best deployment characteristics were found at a hinge location midway between A-4 and A-5, hereafter referred to as hinge location A-4.5. Figure 5-4 shows the C_h - α curves for a 45% chord spoiler-flap hinged at A-4.5. Figures 5-5 show the C_p -TSR curves for this device with a 17.5% span. As indicated on the figures, these curves assume a 15% knock-down for finite aspect ratio.

Table 5-2 shows some of the normal points of operation for the AWT-26 turbine, and the general aerodynamic condition of the blade-tip sections. Table 5-2 and Figure 5-4 can be used together to develop an envelope of operational requirements for aerodynamic deployment of the spoiler-flap. This process can provide much insight into the design issues involved.

First note that for blade angles near $\alpha = 0^\circ$ the hinge moment coefficients are positive and strictly increasing with device deflection angle. As the spoiler is hinged fairly far aft, this is easily understood as being similar to a car door swinging open in a strong wind. The further the door opens, the larger the opening forces become. The spoiler-flap would see this condition during a normal low-wind stop. For this case the dynamic pressure is high due to the rotor's rotation and the blade angle of attack is small due to the low wind speed. This case established a lower limit for the restraining spring torque and damping rates required to prevent a hard mechanical stop of the device. Alternately, an impact stop of the device may be deemed acceptable if properly cushioned.

Next, observe that the device hinge moment coefficients at small deflection angles are small. For $\delta = 0^\circ$, C_h remains below 0.05 for angles of attack up to 15° . The low values of hinge moment coefficients in this range determines the maximum amount of spring pre-load that will allow the device to begin deployment. This constraint will be shown to conflict with the requirements for normal high-wind restarts (rotor parked and blades at $\alpha \approx 90^\circ$ in high winds). Figure 5-4 shows that the hinge moment coefficients are a maximum at small device deflection angles and $\alpha = 90^\circ$. In this case the device is acting similar to a weather vane, with the aerodynamic forces resisting closing. Although dynamic pressures are greatly reduced due to the lack of rotor rotation, this case establishes the amount of spring pre-load needed to close the device for restart in high winds.

Inspection of Figures 5-5 shows that the 17.5% span spoiler-flap is adequate for overspeed protection only if the flap is deployed to at least 75° (assuming the 15% knock-down applied). This will determine the amount of restoring spring torque that is allowable at moderate-to-large deflection angles. Figure 5-4 shows that for $60^\circ < \delta < 90^\circ$ the hinge moments coefficients change rapidly with α for $5^\circ < \alpha < 30^\circ$. Unfortunately, the freewheeling condition must be assumed to occur over a wide range of wind and rotor speeds, which correspond to a large range of blade angles of attack and associated dynamic pressures. The steep slope of the hinge moment coefficients in this α range adds to the challenge of designing restoring springs and dampers which allow adequate device deployment for all design cases. The above discussion illustrates many of the issues and constraints in the design of aerodynamically deployed spoiler- flaps, and demonstrates the need for a code capable of rapid deployment simulations.

Table 5-2. Blade-Tip Aerodynamics for Normal Operation of AWT-26/27

Normal Mode of Operation	Aerodynamic Conditions of Blade-Tip Sections
High-wind stop	Maximum operating dynamic pressure, the resultant of V_o and $R \cdot \Omega$. High blade angle of attack, 15° to 20° .
Low-wind stop	Dynamic pressure still high, with large $R \cdot \Omega$ component but small contribution from V_o . Low blade angle of attack, 0° to 3° .
Stopped in high winds	Dynamic pressure entirely due to V_o , which may significantly exceed the turbine cut-out wind speed. Blade angle of attack $\approx 90^\circ$.
Restart in high winds	Dynamic pressure entirely due to V_o , which is likely in the range from 17.9 to 20.1 m/s (40 to 45 mph). Blade angle of attack $\approx 90^\circ$.

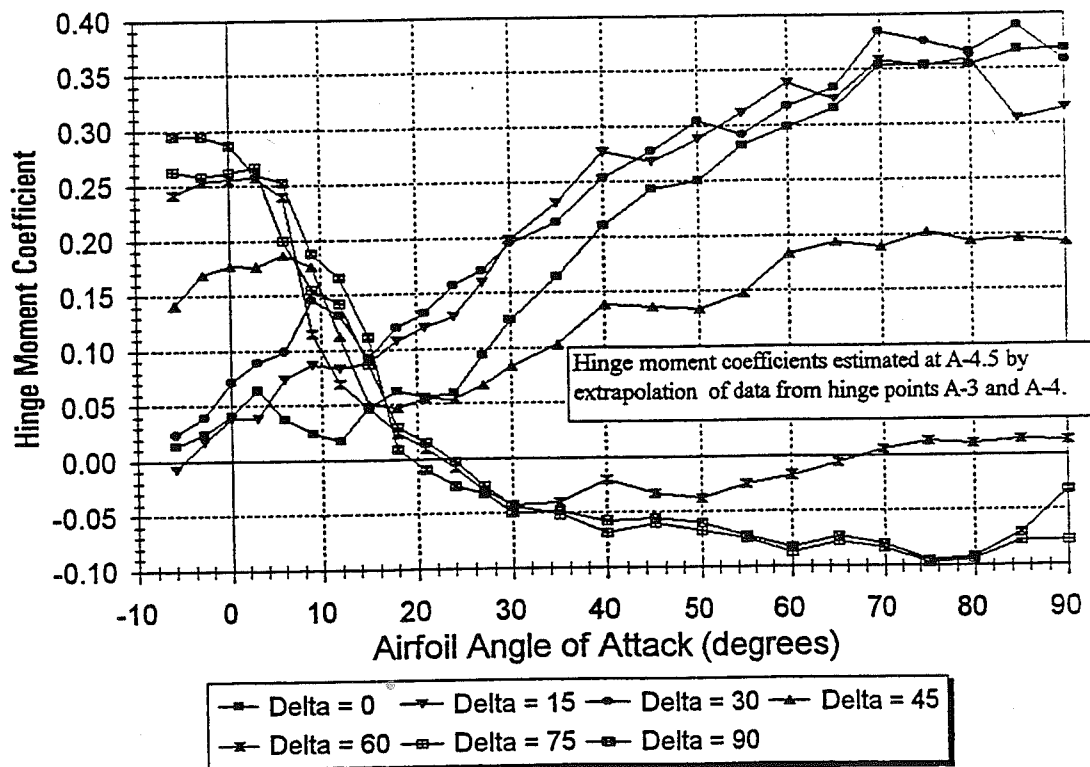


Figure 5-4. Estimated Hinge Moment Data for 45% Chord Spoiler-Flap at Hinge Location A-4.5

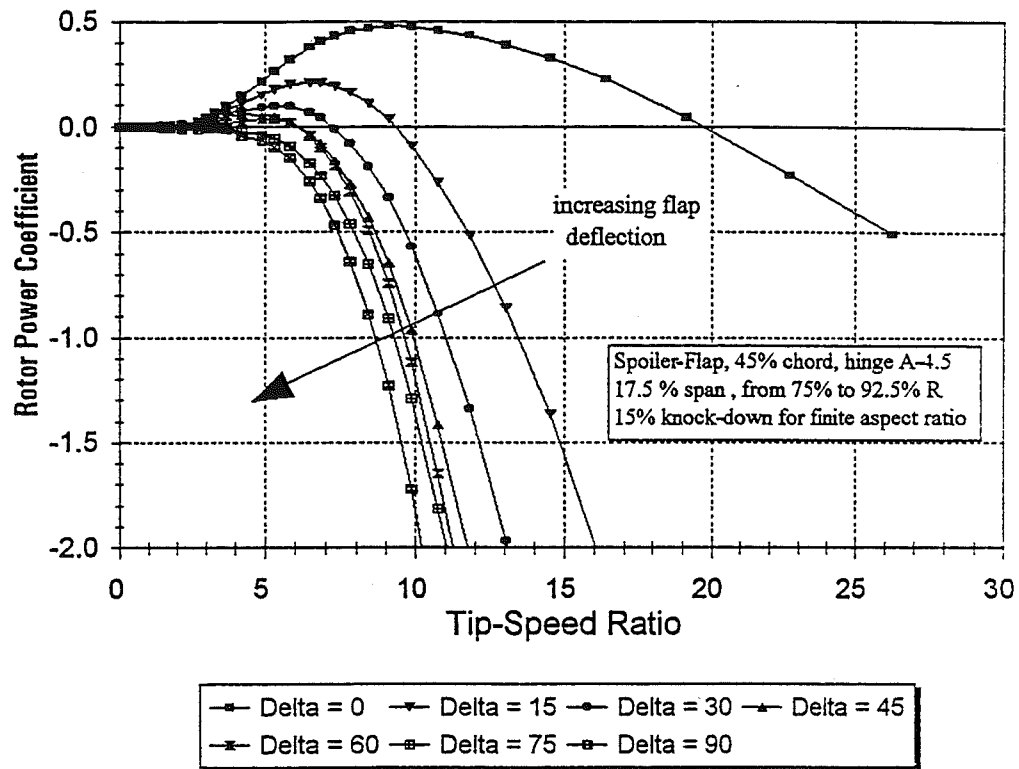


Figure 5-5a. Rotor Power Coefficients for Deployed Spoiler-Flap (full TSR range)

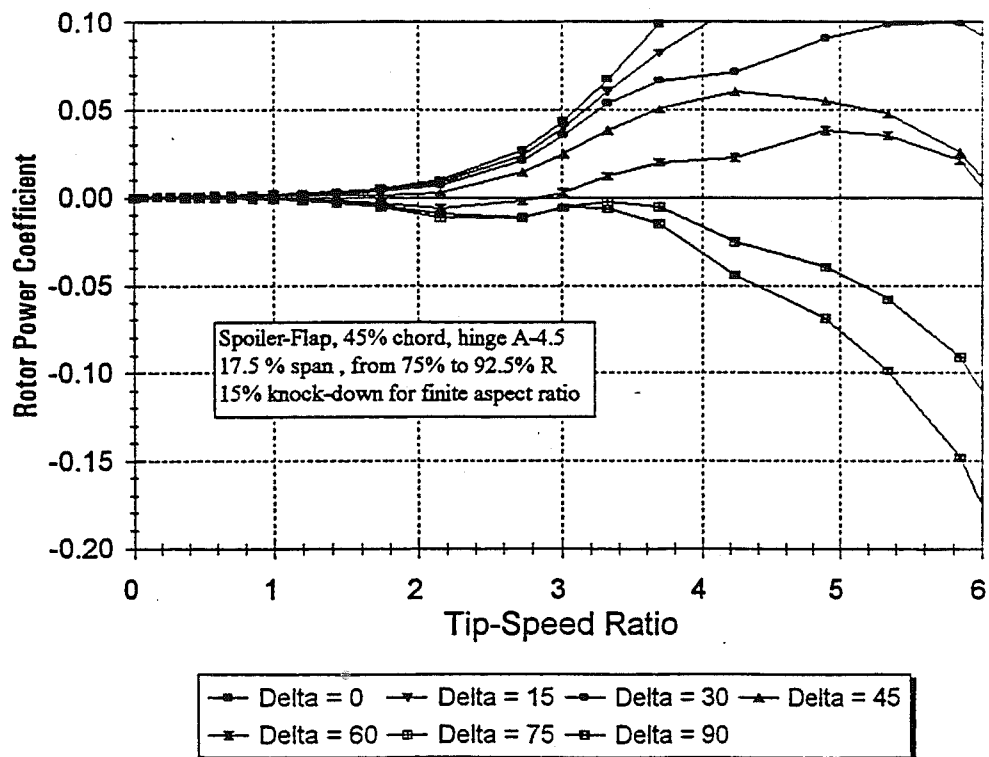


Figure 5-5b. Rotor Power Coefficients for Deployed Spoiler-Flap (truncated TSR range)

Figures 5-6 and 5-7 show two examples of data from deployment time-history simulations. In each case the spoiler-flap is a 45% chord, 17.5% span device hinged at location A-4.5. The initial conditions were representative of an AWT-26 turbine that begins freewheeling in wind speeds near cut-out, and subsequently experiences a 1-year extreme operating gust. Table 5-3 shows the spring pre-load, spring-force, and damping schedules used for each simulation. Note that the spring and damping schedules are given in torsional units applied at the hinge. In practice, the restraining and damping torque could either be supplied by torsional devices or by linear devices acting with lever-arms about the hinge line.

Figure 5-6 demonstrates the result of excessive spring rate and inadequate damping. During the first 30 seconds of the simulation the wind condition is held constant. However, the device does not reach a stable equilibrium. This cyclic behavior illustrates the coupling between the rotor speed and the aerodynamically deployed spoiler. As the rotor decelerates, the blade angle of attack increases by several degrees and the dynamic pressure drops. Due to the steep slope of the C_h - α curves, the change in α leads to a significant drop in the hinge moment coefficient. The combination of lower hinge moment coefficients and dynamic pressure causes the aerodynamic hinge moments to decrease, and the spring-force begins to close the device. As the device closes, its stopping power is diminished to the point where the rotor begins to accelerate. The accelerating rotor causes decreasing angles of attack and increasing dynamic pressure, and the cyclic behavior continues.

An extreme cycle is initiated by the 12-second cosine gust, which begins 30 seconds into the simulation. During the gust, the rotor accelerates to 96 rpm which greatly exceeds the maximum allowable rotor speed of 75 rpm. The simulation shows an emergency application of the mechanical brakes at 45 seconds which stops the rotor completely. As the rotor is stopped, the flap angle approaches 10° asymptotically, indicating that the spring pre-load is not quite sufficient to stow the device at a wind speed of 22.3 m/s.

Figure 5-7 shows a near-optimal simulation of freewheeling rotor control by aerodynamically deployed spoiler-flaps. After an initial overspeed to near 75 rpm, the flaps deploy sufficiently to slow the rotor. The rotor and flap quickly reach an equilibrium condition, with the rotor speed stable at 61 rpm and the flap deployed to $\delta = 70^\circ$. During the cosine gust, the rotor accelerates but still remains below 75 rpm. Inspection of Table 5-3 shows that the spoiler of Figure 5-7 had a slightly lower spring rate and significantly more damping. This configuration was run with a wide variety of initial conditions, and in each case the maximum rotor speed remained below 75 rpm.

Table 5-3. Spring and Damping Torque Schedule for Spoiler-Flap Deployment Simulations

Spoiler-Flap Deflection (degrees)	Figure 5-6		Figure 5-7	
	Spring Torque (N·m)	Damper Torque (N·m·s/degree)	Spring Torque (N·m)	Damper Torque (N·m·s/degree)
0	13.5	0.34	13.5	1.24
10	18.0	0.34	14.9	1.24
20	22.6	0.34	16.4	1.24
30	27.0	0.34	17.8	1.24
40	31.6	0.34	19.2	1.24
50	36.1	0.34	20.6	1.24
60	40.6	0.34	22.0	1.24
70	45.1	0.34	23.4	1.58
80	84.6	0.34	68.5	1.58
90	124.1	0.34	113.9	1.58

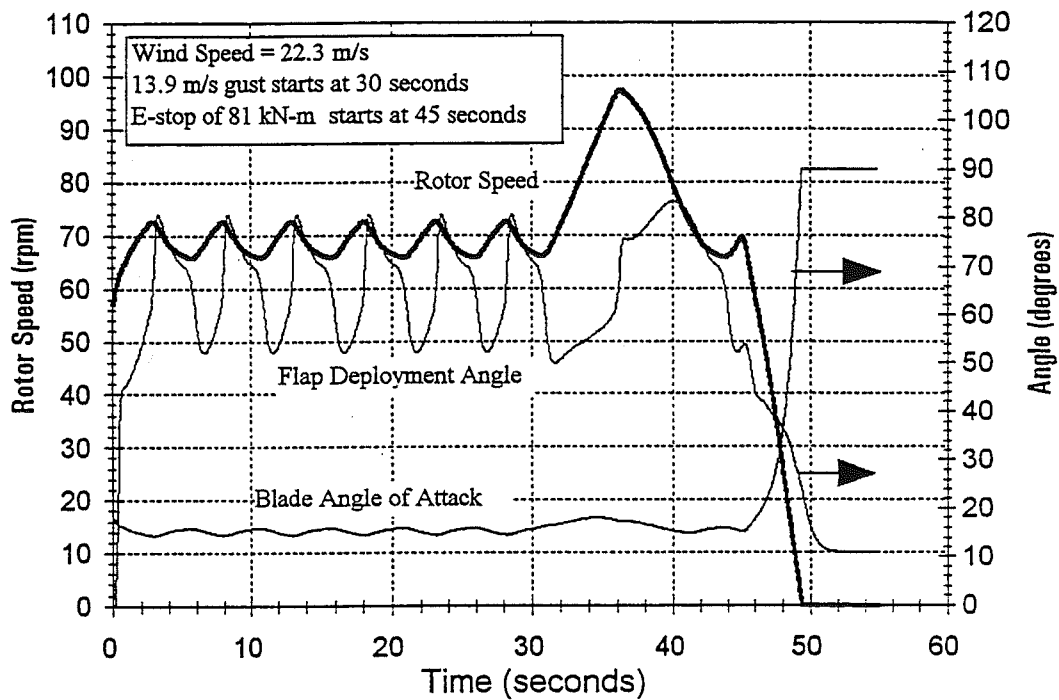


Figure 5-6. Improper Spring and Damping Rates for Aerodynamically Deployed Spoiler-Flap

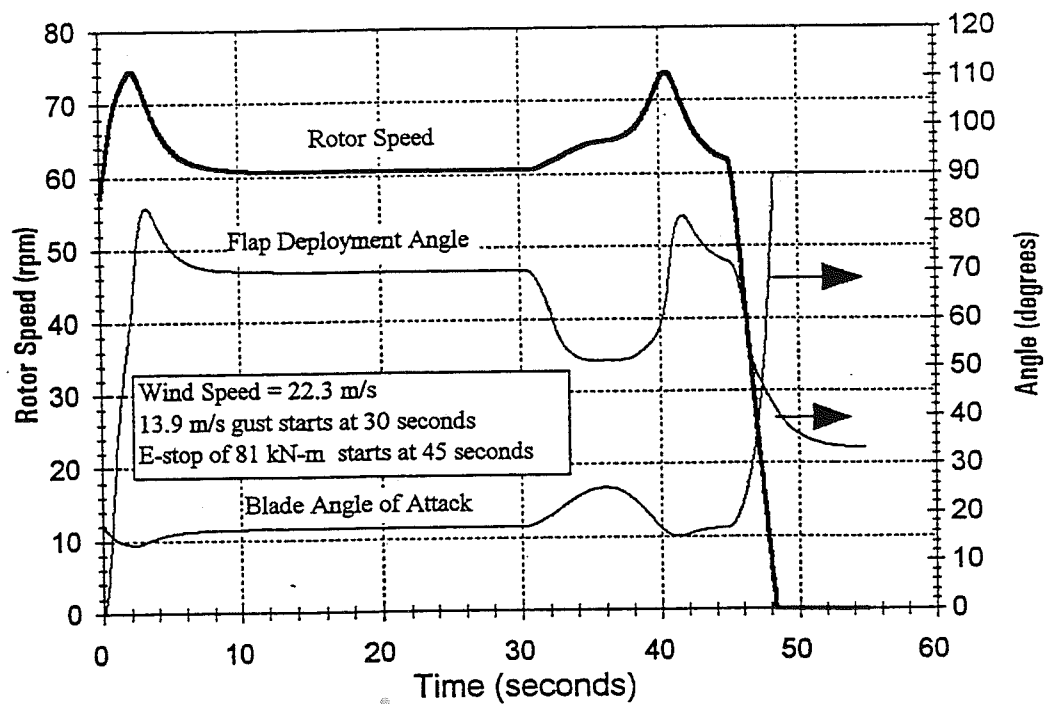


Figure 5-7. Near-Optimal Spring and Damping Rates for Aerodynamic Deployment of Spoiler-Flap

Inspection of the above figures shows that the deployment behavior could be improved by the use of dual-rate dampers that provide more resistance to closing than to opening. This would be particularly beneficial in reducing the oscillations seen in Figure 5-6. Note that the spring torque schedules for both Figures 5-6 and 5-7 show a significant change in rate at $\delta = 70^\circ$. Below 70° , the low spring torque allows the device to achieve the large deployment angles required for effective braking. Above 70° , the rate was increased to prevent a hard stop of the device at $\delta = 90^\circ$.

5.3.2 Flip-Tip

Figures 5-8 show C_p -TSR curves for a deployed flip-tip with 12% total device span. As was shown in Section 5.2, the flip-tip shows excellent stopping power. This is not surprising since the device is essentially an aerodynamically balanced pitchable tip. For the configuration of Figure 5-8, the tips need only deploy to $\delta = 60^\circ$ to provide adequate overspeed protection.

The flip-tip was conceived as a device with favorable aerodynamic deployment characteristics. However, accurate prediction of the flip-tip's deployment may prove to be difficult. For tip and flap sections of low aspect ratio, the mutual aerodynamic influence of these regions may be large. Methods that rely on linear superposition of hinge moments from the tip and flap regions may therefore be erroneous. The correct aerodynamic balance between tip and flap regions would most easily be obtained through field testing, with bolt-on tip sections available in a range of sizes and/or geometries.

Several simulations were run for flip-tip deployments. A general result of the flip-tip simulations was that the device could only be partially aerodynamically balanced, due to the large range of α and δ through which the device must operate. As a result, the flip-tip was determined to have aerodynamic deployment characteristics that are less favorable than expected, with mechanical damping requirements similar to the spoiler-flap.

5.4 Active Mechanical Deployment

In this discussion a deployment system is considered to be active mechanical if the primary source of opening and closing moments is positively controlled. Active mechanical devices may be driven by hydraulics, pneumatics, or linear or rotary actuators. Conversely, a passive mechanical system would lack an actively controlled source of torque. The passive system would primarily use aerodynamic forces, centripetal accelerations, springs, and dampers.

In principle, the flip-tip could be deployed by either active or passive mechanical methods. However, a major attribute of the device is its potential for favorable aerodynamic deployment. The following sections, therefore, will focus on mechanical deployment of the spoiler-flap device. Although these deployment methods have been treated in separate sections, it is understood that a continuum of design features is possible. For example, an active mechanical system can be designed to take advantage of available aerodynamic forces, and would likely contain one or more passive elements.

For braking and overspeed protection, the most natural way to use active mechanical deployment is to drive the device to a deployment angle at which the full aerodynamic brake effectiveness is realized. To minimize the required actuation forces, a neutral hinge location is desired for active deployment. Hinge moment data are shown in Figures 5-9 for two possible locations. The data show coefficients for both hinge points A-3 and a point halfway between A-3 and A-4, hereafter referred to as hinge point A-3.5. Figure 5-9a shows that hinge location A-3 is very well balanced at deflection angles up to 45° ,

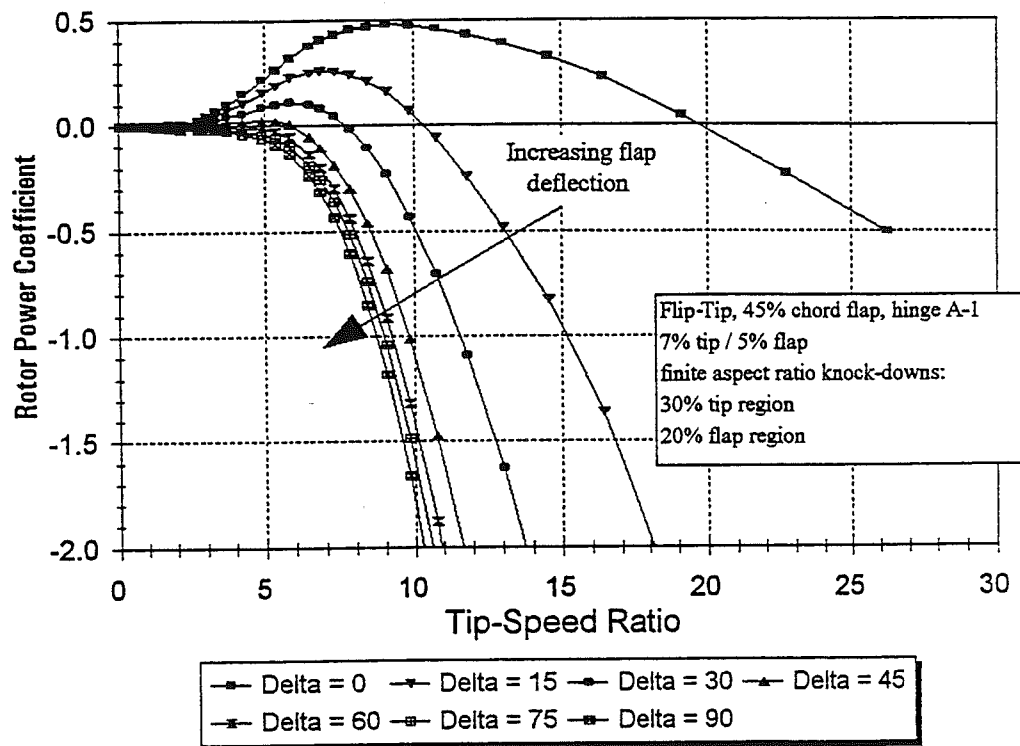


Figure 5-8a. Rotor Power Coefficients for Deployed Flip-Tip (full TSR range)

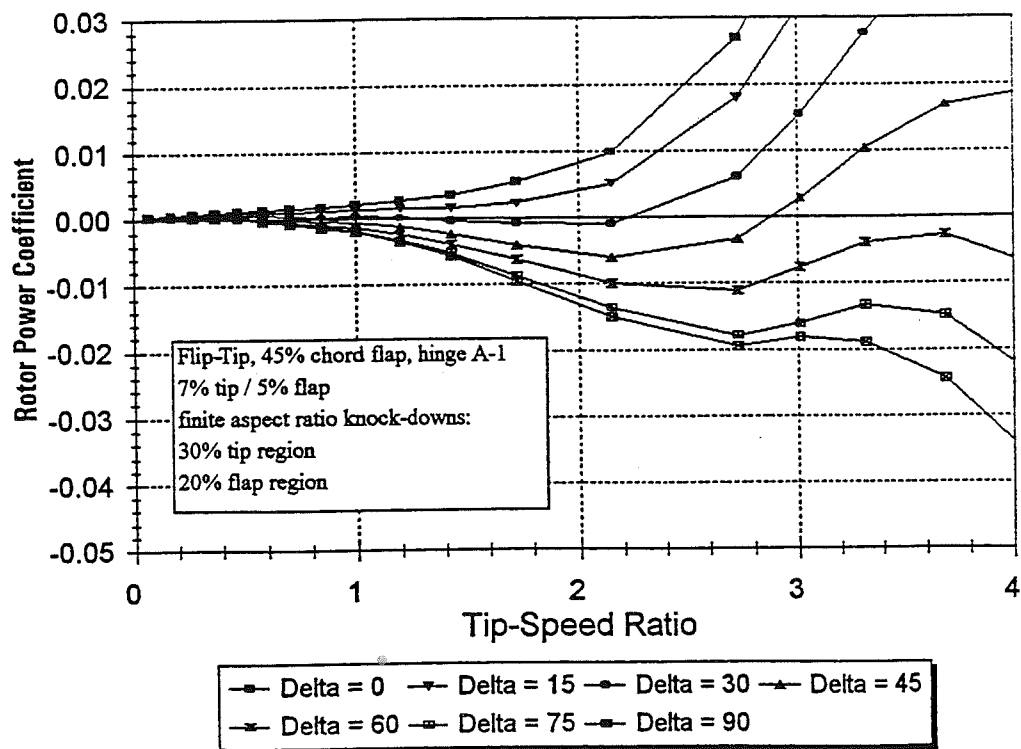


Figure 5-8b. Rotor Power Coefficients for Deployed Flip-Tip (truncated TSR range)

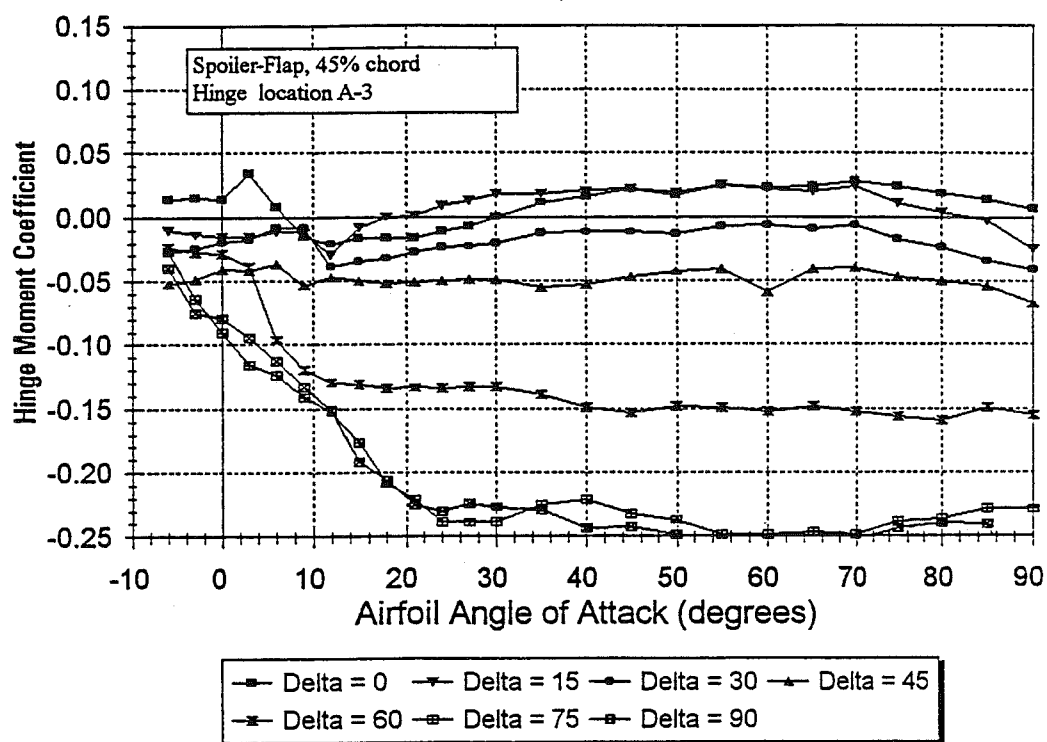


Figure 5-9a. Hinge Moment Data for Balanced Spoiler-Flap, Hinge A-3

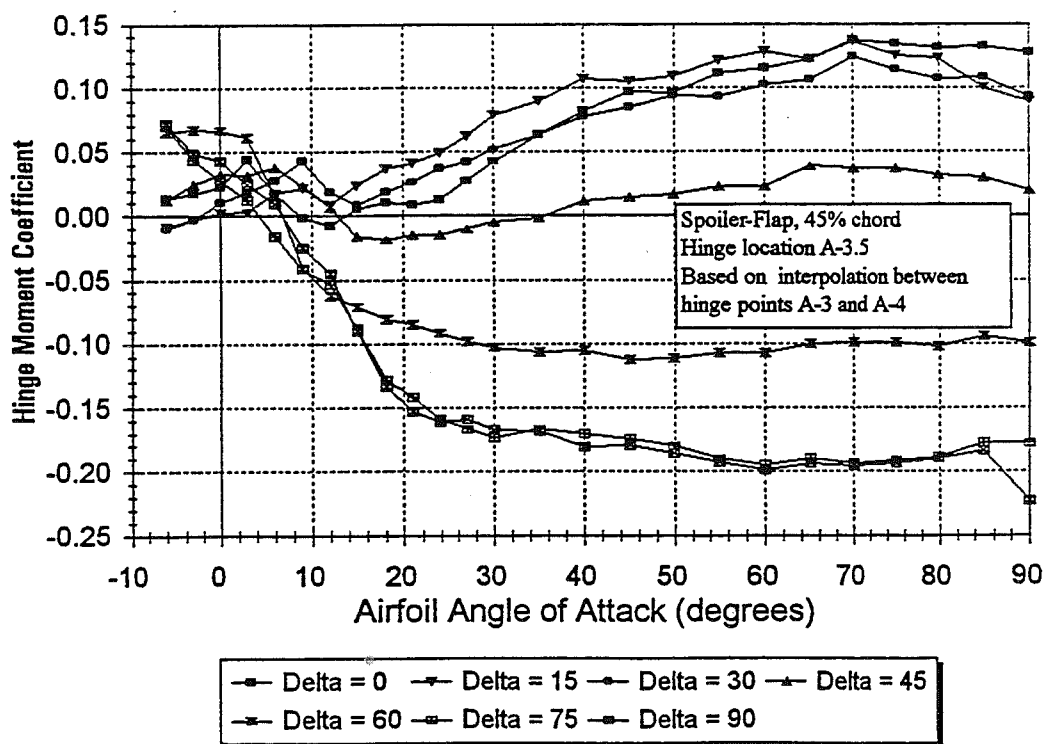


Figure 5-9b. Hinge Moment Data for Balanced Spoiler-Flap, Hinge A-3.5

then tends towards closing hinge moments at higher deflection angles. Hinge location A-3.5 shows a higher tendency towards opening moments, particularly at small deflection angles.

Figure 5-10 shows C_P -TSR data for a 45% chord spoiler-flap with 17.5% span, hinged at location A-3. Note that these curves assume a 10% knock-down of the two-dimensional data for finite aspect ratio. The C_P curves for the device at location A-3.5 are very similar to Figure 5-10. Inspection of the C_P -TSR curves show that adequate braking and overspeed protection will be achieved when the device is deployed to $\delta \geq 75^\circ$.

Data from Figures 5-9 and 5-10 can be used to develop an envelope of actuation torque required for active mechanical deployment. This is shown in Table 5-4 for a spoiler-flap of 17.5% span which extends from 72.5% to 90% R. The table shows that the actuator must supply 333.3 N-m of opening torque to sufficiently deploy the spoiler hinged at location A-3. Moving the hinge line aft to location A-3.5 would decrease the actuator torque requirement to 242.2 N-m. In both cases, the torque required to keep the device closed during normal turbine operation is relatively small.

An additional feature of active mechanical deployment is that it is compatible with the modulation of turbine power. Even at small deployment angles the spoiler-flap efficiently reduces lift and creates drag. This would allow for the use of spoiler-flaps to regulate peak turbine power. Noise impact and behavior under icing conditions are likely to be two primary issues in the design of spoiler-flaps for active power control.

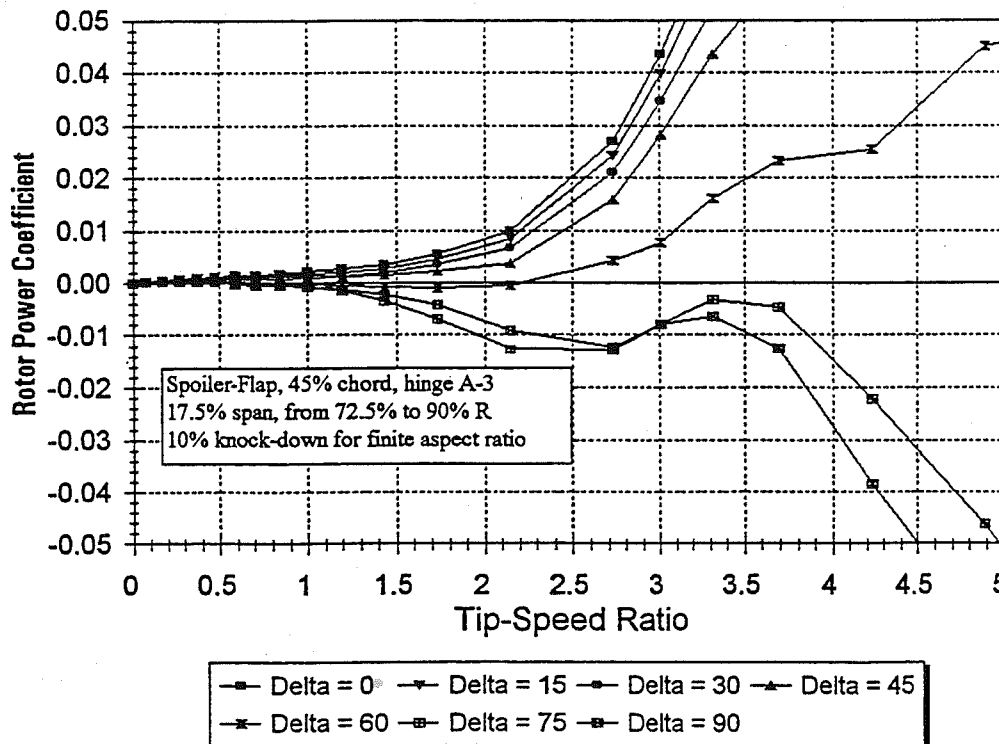


Figure 5-10. Rotor Power Coefficients for Deployed Spoiler-Flap (truncated TSR range)

Table 5-4. Actuation Requirements for Active Mechanical Deployment of Spoiler-Flap

Operational Mode, System Requirements, and Defining Parameters	Hinge A-3		Hinge A-3.5	
	C_h	M_h (N-m)	C_h	M_h (N-m)
Normal power production, device must stay closed over all operating wind speeds. Maximum operating dynamic pressure, maximum positive C_h for $\delta = 0^\circ$, $-6^\circ < \alpha < 20^\circ$.	0.034	25.4	0.044	32.9
Braking / overspeed protection, device must stay open to $\delta \approx 75^\circ$ for all wind speeds up to 36.2 m/s. Maximum overspeed dynamic pressure, maximum negative C_h for $\delta = 75^\circ$, $-0^\circ < \alpha < 30^\circ$.	-0.238	-333.2	-0.173	-242.2
Device stowing, actuator must close the device for high wind restart, wind speeds up to 20.1 m/s. Dynamic pressure due to V_o , maximum positive C_h for all δ , $\alpha = 90^\circ$.	0.007	0.6	0.128	12.6

5.5 Passive Mechanical Deployment

This section will outline some of the design issues and possible benefits of passive mechanical deployment, but will not treat the subject in depth. Passive deployment would be similar to the design for active mechanical deployment in that it would likely favor neutral hinge locations with small actuation-moment requirements. Of course, a passive mechanical system may be designed to make judicious use of aerodynamic forces at some points of operation.

The greatest advantage for passive deployment methods on the AWT-26/27 turbines would be realized by eliminating the electrical slip-ring and rectifier, which send power to the electromagnets of the existing tip brakes. As shown in Table 3-1, this system totals \$1,700 in cost. However, the loss of an electrical circuit across the hub-nacelle interface would require a fundamental change in the braking strategy of the AWT-26/27 turbines. One possibility is to eliminate the use of aerodynamic brakes during normal stopping sequences, using the spoilers only as overspeed protection. This option would increase the turbine's mechanical braking requirements, but could potentially be offset by the savings in eliminating the slip-ring.

5.6 Configuration Selection for Detailed Design

The configuration selection process was iterative, with sizing and deployment studies being conducted in parallel with preliminary structural and mechanical design. Although this process was not exhaustive, a large number of device geometries and deployment methods were considered throughout this work. In each case, candidate designs were assessed by their potential for meeting the objectives of Section 1.4, with benefits in the areas of cost, weight, and reliability considered of greatest importance. The following paragraphs summarize some of the general conclusions reached during this process, and describe the configuration selected for detailed design.

Flip-Tip – The flip-tip showed excellent stopping power which was primarily due to the effectiveness of the tip region. Deployment calculations showed that the aerodynamic damping provided by the flap was favorable, but did not eliminate the need for significant mechanical damping. The correct area-weighting of the tip and flap regions would likely be difficult to predict, but could easily be resolved during a field test program. The major difficulties with the flip-tip device were in the structural design. Significant reinforcement would be required through the flap region and at the tip/flap transition. Structural considerations also favored an external hinge which would potentially be a source of noise and drag. When all advantages and difficulties were considered, it was deemed unlikely that the present flip-tip concept would prove superior to a pure pitchable tip.

Spoiler-Flaps (aerodynamic deployment) – Deployment simulations determined that the spoiler-flap could be designed to deploy aerodynamically, but would require mechanisms to provide specific torsional restraint and damping. Quandt has designed several such spring-damper mechanisms, and is currently testing a prototype aerodynamically deployed spoiler-flap of his own design [7]. However, there are several features of the AWT-26/27 rotor that present difficulties for aerodynamic deployment of spoiler-flaps. First-generation design efforts by both Quandt and AWT engineers showed that the aerodynamically deployed device could be made to work, but may offer little promise in terms of cost and weight benefits.

Spoiler-Flaps (active mechanical deployment) – Considerable structural and mechanical simplicity may be achieved by moving the hinge location forward for active mechanical deployment. Reliability would also be gained by the use of fail-safe mechanisms to drive the spoiler-flap to effective deployment angles ($\delta \geq 75^\circ$). Initial design work and cost estimates showed that the advantages gained from active deployment may offset some of the additional cost and weight of the actuation system.

Spoiler-Flaps (passive deployment) – Passive deployment on the AWT-26/27 turbines could result in substantial cost savings by eliminating the electrical slip-ring and rectifier. However, the loss of an electrical circuit across the hub-nacelle interface would require a fundamental change in the AWT braking strategy. It is possible that an increase in the turbine's mechanical braking requirements could be offset by the savings in eliminating the slip-ring, although detailed cost trades were not performed during the course of this work.

When all of the above issues had been considered, the spoiler-flap with active mechanical deployment was identified as showing the greatest promise for implementation on the AWT-26/27 turbines. This configuration was thus selected for a detailed design effort, which is presented in the following section. The selected configuration is a 45% chord spoiler-flap, with 17.5% total span, located between 72.5% and 90% R, and hinged at location A-3. The assumed C_h - α and C_p -TSR characteristics of the device are shown in Figures 5-9a and 5-10.

6. Design of Spoiler-Flap for AWT-26/27 Rotor

This section documents the design and analysis of an aerodynamic braking system for the AWT-26/27 rotors. The design process includes the following steps:

- Device sizing
- Loads development
- Trade studies
- Detailed design of selected approach.

As noted in the previous section, the configuration selected for detailed design is a 45% chord spoiler-flap, with 17.5% total span, located between 72.5% and 90% R, and hinged at location A-3. The dimensions and blade station numbers presented in this section are all specific to the AWT-26 rotor blade. A design with the same physical dimensions could be implemented on the AWT-27, but quantities expressed in percent rotor radius would be slightly different.

The actuation system has been designed to ensure device deployment to $\delta = 75^\circ$. Figure 5-10 shows that this deployment angle will provide sufficient aerodynamic braking for all design cases, and that deployment angles beyond 75° show a minimal increase in braking effectiveness. Additionally, 75° represents the upper limit for mechanical system bellcrank-to-pushrod clearances for the selected approach (Figure 6-3). The maximum opening and closing requirements (specified as torque required at the hinge line) for this configuration are given in Table 5-4.

Once the hinge moment requirements for the actuation system have been specified, many different approaches may be pursued. Driving devices may be hydraulic, pneumatic, or electromechanical. Devices can provide torque directly, or a linear driver may be arranged to act with a lever-arm about the pivot point. For a linear driver, mechanical advantage may be gained through the use of levers, linkages, cams, and cranks. Linear drivers typically scale with their force capacity. A large driver can be located at the hub and simultaneously actuate both aerodynamic brakes through the use of tie-rods or cables. This arrangement ensures that the devices will deploy together, may decrease the outboard weight on the blade, and may have the benefit of one large driver being less expensive than two (or more) smaller drivers. If linear drivers are located at the flap, a chordwise orientation can be used, but may cause problems in terms of fitting the actuator into the available blade structure. Considerable freedom may be gained by orienting a linear driver in the spanwise direction and using a bellcrank to turn the linear action into the chordwise direction.

Many of the above options were considered during the course of this work, with initial assessment of cost, weight, structural issues, and reliability. The scope of this project did not allow a rigorous cost-benefit analysis of the potential actuation methods. The design presented in this section represents one of many ways in which spoiler-flaps may be implemented on the AWT-26/27 turbines.

6.1 Mechanical Design

This section presents the design of a pneumatically closed, centripetally opened spoiler-flap. The pneumatic system was chosen versus a hydraulic system due to the low force requirements of the actuator. Initial comparisons of pneumatic and hydraulic system components show that the pneumatic system would be lower cost but higher weight than the equivalent hydraulics.

Typical operating pressure for the pneumatic system is 150 psi versus 1200 psi for a hydraulic system. To supply a given force, the pneumatic system would therefore require a larger actuator cylinder. In addition, pneumatic pumps and air reservoirs are generally bulkier than their hydraulic counterparts. In terms of fitting the actuation system components into the available blade structure, the pneumatic system therefore is the more demanding case. If the pneumatics can be sized to fit in the blade structure, then certainly the hydraulics will fit.

An electromechanical actuator could also replace the pneumatic actuator, but this option was not rigorously pursued. One benefit of both the hydraulics and pneumatics is that the design for fail-safe operation is straightforward, with system pressure required to keep the device stowed, and any loss of pressure resulting in device deployment. Electromechanical actuators may prove to be a cost-effective alternative to the pneumatic/hydraulic systems, but the design would need to include appropriate fail-safe features.

6.1.1 Overview of Device Construction

Figure 6-1 shows the AWT-26 blade planform, including the proposed aerodynamic brake. The figure shows station numbers for the blade root and tip, and for the inboard, outboard, and middle positions of the spoiler-flap. The station numbers shown in Figure 6-1 have been taken from AWT-26 blade drawings, and will be referred to in the sections which follow.

The least-cost manufacturing option for the spoiler-flap would allow the device to be cut away from the blade structure during production, then appropriately retrofitted and reinstalled on the blade. The cutting operation would utilize a template to guide a saw or router. Radiused and/or tapered corners are envisioned (but not shown) to reduce stress concentrations from loads transitioning into the uncut blade shell.

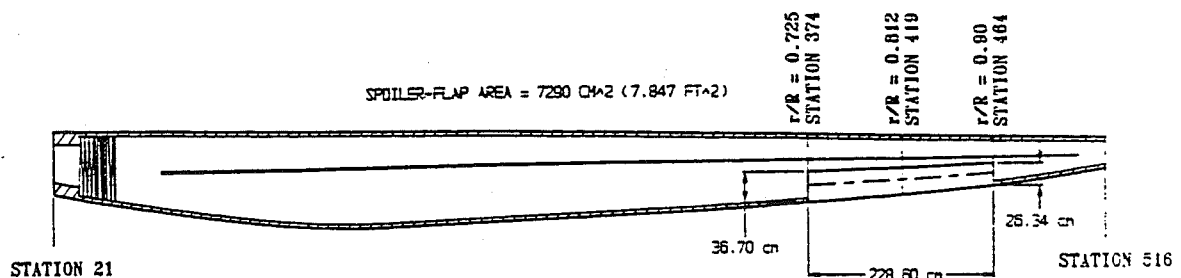


Figure 6-1. AWT-26 Blade Planform with Spoiler-Flap Location Shown

In order to provide structural reinforcement and sealing of exposed internal surfaces and hardware, the blade and device openings are closed out with spanwise webs and chordwise ribs. Webs have been initially sized using 6.35 mm (0.25 in.) birch plywood, and ribs are initially sized as 12.7 mm (0.5 in.) thick wood/epoxy laminate. Webs can be cut from plywood sheet stock. Ribs can readily be cut from a parent billet composed of five Douglas Fir veneers 2.54 mm (0.1 in.) thick, laminated with epoxy at room temperature under pressure.

For access to system hardware, panels need to be installed in the blade and device webs. In addition, slotted openings in the webs must be cut for the device control linkages. Many of the openings may be cut during initial trimming from the plywood sheet. To reduce leakage from the low-pressure to the high-pressure surface of the blade, the spanwise gaps should be sealed with an appropriate rubber seal. Chordwise gaps are more difficult to seal due to the requirements for device freedom of motion under high loads. The aerodynamic impact (both noise and performance) of through-flow at the device ends would need to be assessed to determine whether a design remedy is warranted.

The device is mounted to the blade using hinge pins at the inboard and outboard edges of the device. Centripetal forces from the device are transferred to the blade structure through a large-area thrust bearing located at the hinge, as shown in Figure 6-2. Bearing loads are shared by the outboard blade rib and the blade laminate, thus reducing concentration of loads into the blade rib and subsequent high shear stresses in the bond-line.

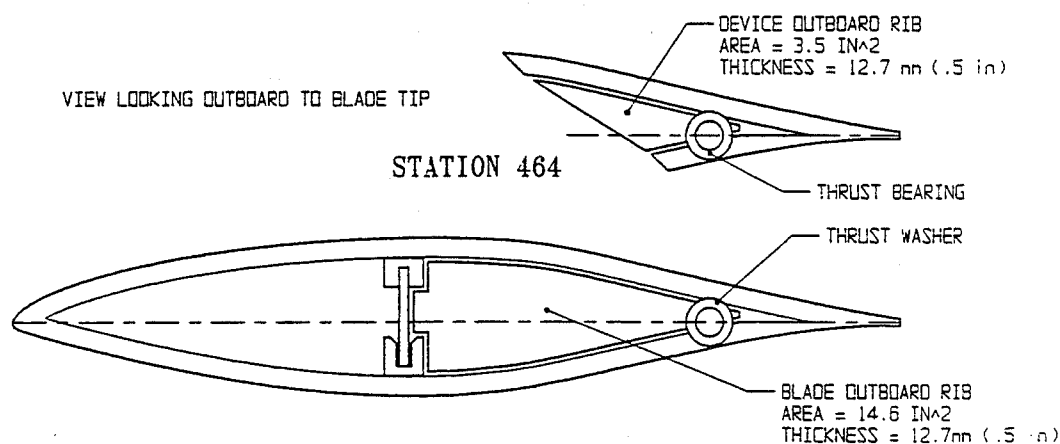


Figure 6-2. Spoiler-Flap Hinge / Thrust Bearing Configuration at Station 464

6.1.2 Mechanical System Description

Figures 6-3 and 6-4 provide layout sketches of the mechanical system used to open and close the device. The primary driver consists of an actuator, a bellcrank, and a pushrod that open and close the device at mid-span. Secondary (passive) drivers are gas springs located at either end of the device. The gas springs help hold the ends open during braking and hold the corners closed during normal turbine operation.

Pneumatic pressure provided by a hub-mounted pump is used to retract the cylinder in each blade, thus closing the device. To reduce cycling of the pump, a hub-mounted air reservoir would be added to the system. To open the device, a pneumatic valve would dump line pressure, allowing the cylinder to extend as a result of the actuator mass subjected to centripetal loading. Due to the high centripetal loads at the 10-meter span location of the actuator during normal and overspeed operating conditions, a 5.5 kg cylinder mass is capable of driving the device open. For this reason, the actuator pushrod is fixed to the shear web, while the heavier cylinder body is allowed to exert its mass radially outboard during deployment. If the installation is reversed, or if the cylinder body does not have sufficient mass to provide the centripetal force required, additional weight would have to be added to the actuator.

Both aerodynamic hinge moment and centripetal force change proportionally with the square of rotor rotational speed, so opening force will be maintained throughout the braking envelope. In designs with large overspeed margins, it may be possible to set system pressure such that a large overspeed will overcome the actuator closing force, thus forcing the device open without relying solely upon disconnection of electrical current to the normally-open pneumatic valve.

Two additional design features assist the centripetal operation: the low hinge moment due to the neutral hinge location, and a 2:1 bellcrank ratio that doubles the effect of the actuator centripetal force. Pressure dumping is achieved by using a normally-open pneumatic solenoid valve located in the hub. The valve is electrically closed by the nacelle controller (via the slip-ring) to stow the spoiler for normal turbine operation.

A normal or emergency braking condition would result in disconnection of the pneumatic valve electrical circuit and subsequent centripetal opening of the device as pressure bleeds off. Pressure dump rates can be adjusted to reduce opening shock by using a metered orifice. The system is designed to be fail-safe, as any loss of power would also result in device deployment. Table 6-1 summarizes the actuator specifications required to drive the present spoiler-flap design. A variety of standard clevis ends and mounting brackets are available to facilitate the installation of the actuator.

An additional consideration in the design of the pneumatic system is the prevention of moisture and particulate accumulation during compressor operation. If the pump does not include moisture and particle filters, they will have to be designed into the system. A practical choice might be the miniature "piggyback" filter/regulator, which is available commercially.

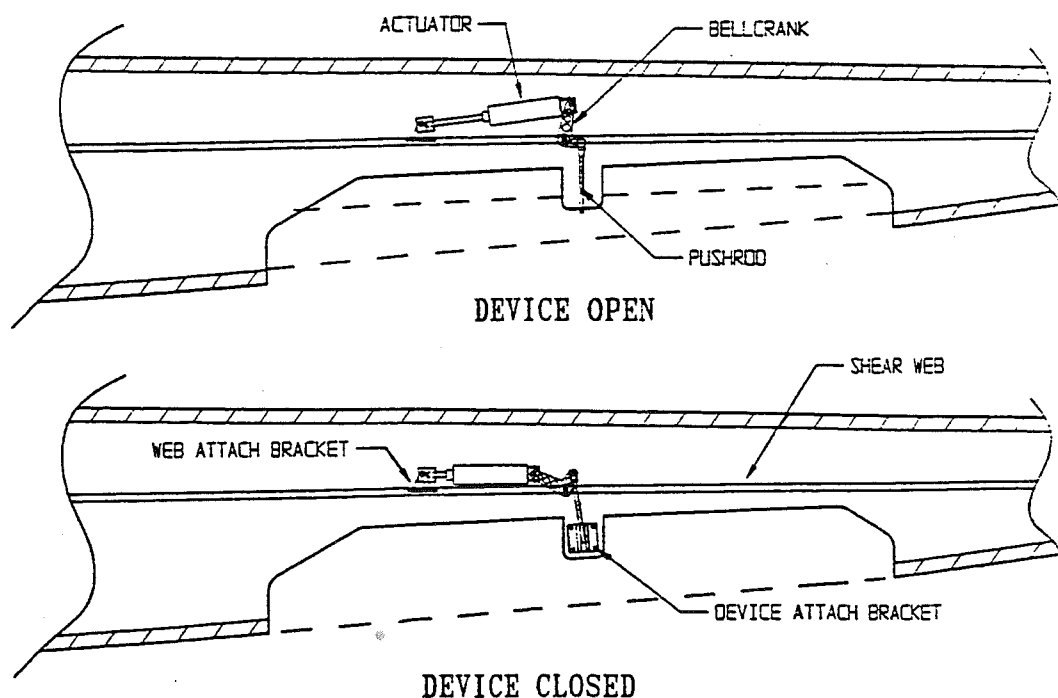


Figure 6-3. Layout of Mechanical Actuation Driver

Table 6-1. Actuator Specifications

Stroke	16.8 cm (6.6 in.)
Bore	6.35 cm (2.5 in.)
Operating pressure	1035 kPa (150 psi)
Closing force at 60 rpm rotor speed (normal turbine operation)	2277 N (512 lb)
Body mass required to drive device open at 75 rpm (overspeed)	5.5 kg (11.1 lb)

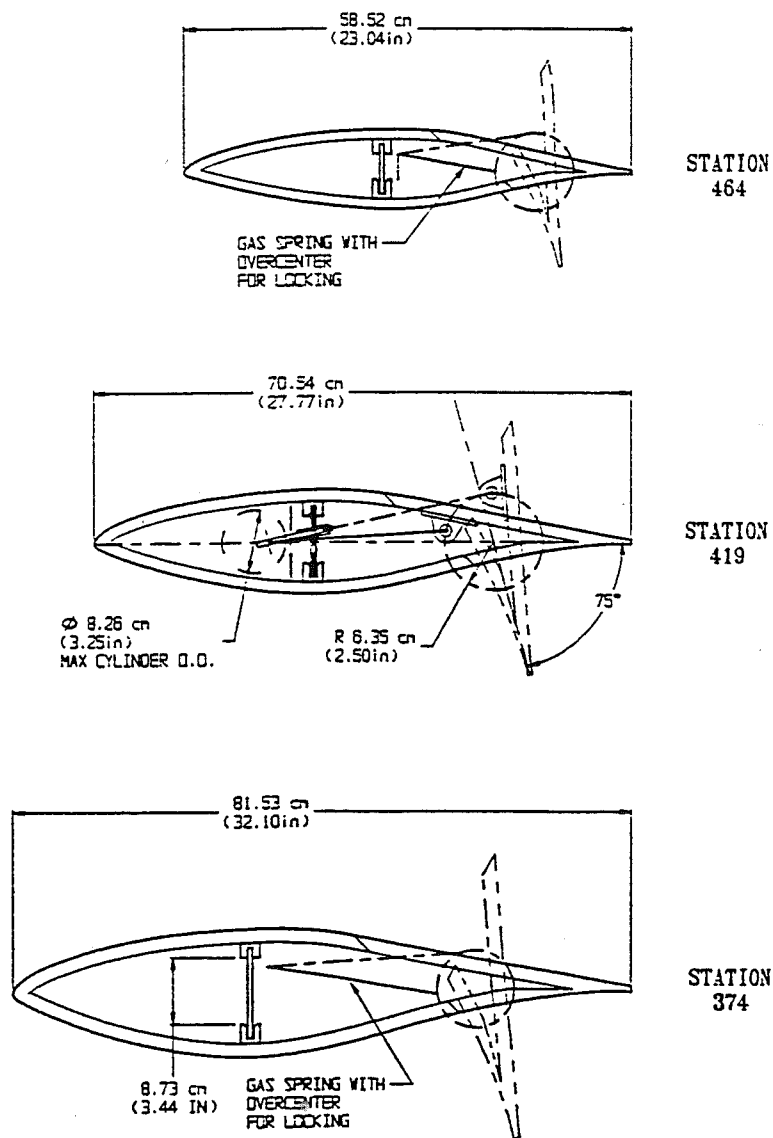


Figure 6-4. Sectional Layout of Mechanical Driver

6.2 Loads and Structural Analysis

For the current preliminary design, only the peak static loads and their effect on blade and device stresses have been examined. Due to the introduction of possible stress raisers at blade discontinuities in the spoiler-flap region, an investigation of blade fatigue would be necessary during the next stage of design effort. Loads and stresses are based upon the geometry described in Section 6.1.

6.2.1 Blade Loads and Structural Analysis

For comparative analysis, blade-flapwise and edgewise bending loads are assumed to remain the same as specified for the AWT-26/27 with tip brakes. The inboard edge of the spoiler-flap is the most critical section with respect to blade bending stresses, so the analysis has initially been limited to station 374. The bending loads shown in Table 6-2 have been taken from the AWT-26/27 *Loads Design Book* [16].

Table 6-2. Blade Bending Loads at Station 374

Edgewise		Flapwise	
kN-m	ft-kip	kN-m	ft-kip
35.8	26.4	25.8	19.0

Bending stresses were determined according to:

$$\sigma = Mc/I \quad (6-1)$$

where c is the distance from the neutral axis to the extreme fiber and I is the section moment of inertia. Figure 6-5 shows the cross-sectional properties of the blade at station 374 before and after installation of the device.

A summary of tensile and compressive stress increments for the AWT-26 blade are given in Table 6-3. The increments are a function of distance from the neutral axis to the extreme fiber and change in section moment of inertia. Using the constant bending moments, the stress increments were determined from the following ratio:

$$100 \cdot \left(1 - \frac{\sigma_1}{\sigma_2} \right) = 100 \cdot \left(1 - \frac{c_2 \cdot I_1}{c_1 \cdot I_2} \right), \quad (6-2)$$

where the subscripts 1 and 2 denoted the section properties before and after the modification, respectively. A significant increase in edgewise bending stress occurs. For the AWT-26 blade, a large edgewise margin of safety exists. Therefore, the structural reinforcement provided by the additional web at the blade trailing edge close-out, shown in Figure 6-5, provides a sufficient, but smaller, margin of safety. Bonding and shear tie details for transfer of tensile loads to the close-out ribs and blade would need to be addressed during a more detailed structural evaluation and design. To reduce stress concentrations that will affect the fatigue life of the blade at the corners of the spoiler-flap, analysis for the proper radius or taper should be conducted.

Table 6-3. Blade Percentage Stress Increments at Station 374

Flapwise Tension (high-pressure shell)	Flapwise Compression	Edgewise Tension (trailing edge)	Edgewise Compression
15%	23%	96%	270%

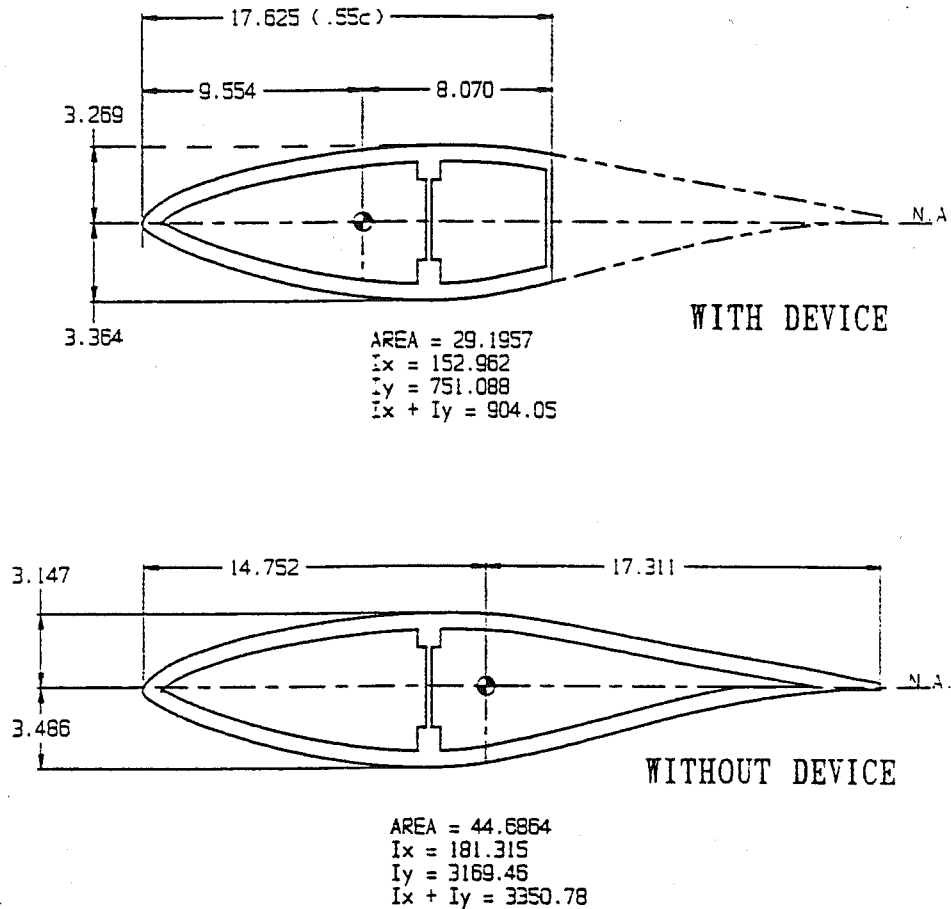


Figure 6-5. Station 374 Blade Section Properties (all dimensions in inches)

6.2.2 Device Loads and Structural Analysis

The rotor overspeed condition causes the highest device loads. Maximum bending loads occur when the device is open. The maximum bending stress results from overspeed deployment combined with pushrod force, and occurs at the point of device actuation at mid-span (station 416). Maximum bearing load is a result of centripetal load transfer from the device to the outboard hinge rib. It occurs during maximum overspeed when centripetal loads are also at a maximum.

The critical device loads are summarized in Table 6-4. Overspeed drag load results from the mid-device-span dynamic pressure at 90° to the free stream with a rotor speed of 75 rpm. Pushrod load is that which is required to keep the device open during overspeed, and is determined as the maximum overspeed hinge moment divided by the perpendicular distance from the hinge line to the point of actuation (arm length = 6.35 cm). Maximum hinge bearing load is the mass of the device times the centripetal acceleration during overspeed.

Table 6-4. Device Critical Loads

Maximum Drag Load		Maximum Hinge Moment		Maximum Pushrod Load		Maximum Hinge Bearing Load	
kPa	psf	N-m	in-lb	N	lb	N	lb
4.48	93.6	339	3000	5338	1200	10369	2331

For device bending stress analysis, the mechanical pushrod load was concentrated at the point of application and the aerodynamic drag loads were uniformly distributed along the device span. Stresses due to each were linearly superimposed, with the resulting critical stresses shown in Table 6-5. This analysis showed that additional structural modification may be needed to reduce the bending stresses to meet design factors of safety. Such modification might include addition of a mid-span rib, or stiffening of the device by either thickening or reinforcing the close-out web. The use of a 32 mm (1.25 in.) OD x 19 mm (0.75 in.) ID thrust washer to transfer the thrust bearing loads from the device to the blade would provide ample capability for carrying the hinge bearing loads. Accommodation for sealing the thrust bearing from moisture and airborne particles would reduce maintenance requirements on the bearings.

Table 6-5. Device Critical Stresses

Mid-Span Bending Stress (overspeed)		Hinge Bearing Stress (overspeed)	
kPa	psf	kPa	psf
356.6	7448	142.0	2966

6.3 Cost and Weight Estimates

Table 6-6 shows the comparative costs and weights of the present design and the existing AWT-26/27 tip vane. AWT-26/27 production tip vane costs are based on 1995 invoices, and weights are taken from measurement of production components. Appendix B contains a spreadsheet that details the estimates of production costs and weights for the spoiler-flap design. The spreadsheet contains notes which document the basis for each estimated cost. Major system components are priced from a single source, assuming part quantities for 100 AWT wind turbines. Other commercially available components are priced from catalogs, less an assumed 30% for quantity discounts. Where possible, hardware prices are based on AWT production invoices for comparable items. Estimates for custom wood and machined items are based upon existing cost-per-weight of blades and tip-vane components. Labor-hour estimates are based upon current AWT manufacturing experience. Due to the preliminary nature of the spoiler-flap design, additional labor and material costs are likely to occur as a result of detailed design for manufacture. These additional costs are estimated in the spreadsheet by a line item for "unspecified parts and processes."

Table 6-6 shows that production costs for the spoiler-flap design are estimated to be 5% lower than the baseline AWT-26/27 tip vane. Although this is encouraging, the preliminary level of the current design must be kept in mind. The greatest uncertainty in the cost estimates is the labor required to cut out, retrofit and reinstall the device on the blade.

Table 6-6. Cost and Weight Analysis Summary

	Installed Cost (total system)	Blade Component Weight (per blade)	Hub Component Weight (1 per turbine)
Spoiler-Flap	\$2,903	17.6 kg (38.8 lb)	16.8 kg (37 lb)
Current Tip Brake	\$3,057	12.7 kg (28.0 lb)	4.1 kg (9 lb)

Notes: Slip ring price and weight excluded from both systems.
Rectifier included in cost and weight for tip brake (not needed for spoiler-flap).
Both systems include installation labor.

Table 6-6 shows that the blade components of the spoiler-flap system are heavier than the baseline tip vane. However, the effect of the weight differential is somewhat offset by the device placement. The AWT-26/27 tip-vane weight is concentrated at the blade tip, whereas the spoiler-flap center of mass is further inboard. Therefore, the centripetal loading on the devices will be reduced by a factor of 400/516 (the ratio of device radial locations). The baseline weight of an AWT-26 blade is 454 kg (1000 lbs), so the 4.9 kg (10.8 lb) increase in blade component weight would result in an effective increase of 1.1% in total blade weight, once centripetal effects are included.

The estimated increase in blade component weight is not an anomaly of the current spoiler-flap design. During the design trade-off studies, weights were estimated for several candidate configurations, including aerodynamically deployed spoiler-flaps and flip-tips. In each case, the estimated blade-component weights were greater than the baseline AWT-26/27 tip vane. The greatest contributor to increased weight was the need for multiple hinge points and the associated structural reinforcements.

It was concluded that the spoiler-flap and flip-tip configurations did not hold significant promise for absolute reductions in blade component weight. However, small increases in system weight may be acceptable if other advantages are shown (e.g. noise and performance benefits due to improved tip shape).

At this level of analysis, the design appears to be competitive with the baseline configuration on a cost and weight basis. This is encouraging for a first-generation design, as improvements in both cost and weight may be obtained through design iterations.

7. Conclusions

Wind-tunnel tests have been conducted for a large number of plain-flap and spoiler-flap configurations. The wide range of parameters tested, and the quality of the data collected, have provided an excellent database for the present work and for other wind turbine designers who may be considering trailing-edge aerodynamic brakes.

The wind-tunnel results have been used to identify the aerodynamic performance and deployment characteristics of candidate configurations. Preliminary design effort on the flip-tip showed limited promise for improvements relative to a classic pitchable tip. Significant non-linearity of hinge-moment behavior was identified for both the flip-tip and spoiler-flap configurations. As a result, it was concluded that pure aerodynamic deployment of either configuration would be difficult to achieve.

The spoiler-flap, with active mechanical deployment, was selected for additional preliminary design effort. The result was a promising configuration for the AWT-26/27, with initial estimates of a small decrease in cost and an increase in weight when compared with the currently-used tip vane. This is encouraging for a first-generation design. However, there are several design issues that would require further work to increase confidence in these results, including:

- **Appropriate adjustment for finite aspect ratio and other three-dimensional effects.** As discussed in the text, the appropriate adjustments for aspect ratio effects on spoiler-flap data are unknown. The results of References 5 and 6 may provide more information on this issue, but it is unlikely that they will resolve it once and for all. Although this work used a best guess for the three-dimensional adjustments, prototype testing of the devices would be required to confidently establish the device sizing.
- **Aeroelastic / dynamic behavior of spoiler-flap and modified blade.** In the present design, the modified blade section (forward element) is much stiffer in flapwise bending than the spoiler-flap (rear element). By hinging the flap at both ends and supporting the device mid-span, it is expected that the spoiler deflections would generally follow those of the blade. This assumption would need to be validated through further analysis and field testing. A significant difference between blade and spoiler deflections could result in a mismatch between the aerodynamic surfaces, which would likely increase noise and decrease turbine performance.
- **Tolerances and gap-sealing requirements.** The design would require close tolerances on hinge location and orientation, both to ensure smooth deployment (no hinge binding) and proper device alignment. Maintaining flush aerodynamic surfaces and proper sealing of gaps would be necessary to minimize airfoil noise and drag. This could prove difficult on the three-dimensional complex curves of the AWT-26/27 rotor blade, with both taper and twist.
- **Greater detail of structural analysis.** The analysis of this report was based on loads at extreme operating conditions. Inspection of the operational envelope indicates that these load cases would dominate the design, but this has not been confirmed. Additionally, sizing and structural analysis must be performed for intermediate mechanisms, connections, and hardware, although none of these items are expected to be problematic.

- **Sensitivity of the device performance to icing conditions.** This may be particularly important if significant gaps are present at the device ends, as ice accumulation could seal the device closed.

The above issues may be addressed during further design of an aerodynamic braking system. Although none of these issues appear prohibitive, prototype testing of spoiler-flaps would be required to confidently establish the device performance.

8. References

1. Gipe, P., *Wind Energy Comes of Age*, John Wiley & Sons, New York, 1995.
2. Eggleston, D.M., and Stoddard, F.S., *Wind Turbine Engineering Design*, Van Nostrand Reinhold, New York, 1987.
3. Miller, L.S., *Experimental Investigation of Aerodynamic Devices for Wind Turbine Rotational Speed Control: Phase I*, NREL/TP-441-6913, Golden CO: National Renewable Energy Laboratory, February 1995.
4. Miller, L.S., *Experimental Investigation of Aerodynamic Devices for Wind Turbine Rotational Speed Control: Phase II*, NREL/TP-441-20507, Golden CO: National Renewable Energy Laboratory, February 1996.
5. Ramsay, R.R., Janiszewska, J.M., and Gregorek, G.M., *Wind Tunnel Testing of Three S809 Aileron Configurations for use on Horizontal Axis Wind Turbines*, Midwest Research Institute Contract Number XF-11009-3, publication pending.
6. Miller, L.S., Quandt, G.A., and Huang, S., *Atmospheric Tests of Trailing-Edge Aerodynamic Devices*, NREL publication pending.
7. Cheney, M.C., PS Enterprises, Inc., Advanced Wind Turbine Subcontract # AAA-4-12272-04, Subcontract Report pending.
8. Quandt, G.A., *Wind Turbine Trailing-Edge Aerodynamic Brake Design*, NREL/TP-441-7389, Golden CO: National Renewable Energy Laboratory, January 1996.
9. Johnson, B.L., *Facility Description of the Walter H. Beech 7x10 Foot Low-Speed Wind Tunnel*, Aerodynamic Laboratory, Wichita State University, Wichita KS, 1993.
10. Hoerner, S.F., *Fluid Dynamic Drag*, Hoerner Fluids Dynamics, Vancouver WA, 1965.
11. R. Lynette & Associates, *ESI-80 Rotor Performance and Reliability Enhancement Program, Final Report*, Smith Wind Energy Corp., National Renewable Energy Laboratory Subcontract HC-2-11101, March 1993.
12. McCarty, J., *PROP93 Users Guide Version 1.0*, Alternative Energy Institute, West Texas A&M University, Canyon TX, June 1993.
13. Advanced Wind Turbines, Inc., *Draft Aerodynamic Brake System Specification*, unreleased document, February 1996.
14. International Electrotechnical Commission, *Wind Turbine Generator System—Part 1: Safety Requirements*, International Standard 1400-1, December 1994.
15. Germanisher Lloyd, *Rules and Regulations, IV—Non-Marine Technology, Part 1—Wind Energy*, 1993.
16. Advanced Wind Turbines Inc., *Loads Design Book, SS003002*, Revision A, March 1996.

17. Spera, D.A., Esgar, J.B., Gougeon, M., and Zuteck, M.D., *Structural Properties of Laminated Douglas Fir/Epoxy Composite Material*, NASA Reference Publication 1236, DOE/NASA/20320-76, 1990.
18. Ramsay, R.R., Hoffmann, G.M., and Gregorek, G.M., *Effects of Grit Roughness and Pitch Oscillations on the S815 Airfoil*, Midwest Research Institute Contract Number XF-11009-3, August 1994.

APPENDIX A

WSU Wind Tunnel Test Data

WSU Wind Tunnel Test Data

The complete data set from the WSU/AWT/NREL aerodynamic brake wind tunnel test is available by request from NREL or WSU. The data are contained in an ASCII format text file, 'wsudata1.txt.' The data are arranged in columns, which contain run numbers, airfoil angle of attack, and aerodynamic coefficients, as shown in Table A-1. Aerodynamic coefficients are all corrected, and have been normalized as described in the report text. Table A-2 provides complete documentation of the configurations tested and the corresponding test run numbers. The test runs that indicate leading-edge grit roughness (LEGR) used #60 lapidary grit with the standard NREL roughness template as described in Reference 18.

The majority of configurations tested are presented in graphical form in this appendix, with a summary given in Table A-3.

Table A-1. Configuration of Data File 'wsudata1.txt'

Column Number	Data Stored
1	Run number
2	Corrected airfoil angle of attack (degrees)
3	Airfoil lift coefficient, C_L (wind axes)
4	Airfoil drag coefficient, C_D (wind axes)
5	Airfoil 1/4-chord moment coefficient, C_M (wind axes)
6	Wind tunnel dynamic pressure, q (psf)
7	Airfoil suction coefficient, C_S (airfoil axes)
8	Airfoil normal coefficient, C_N (airfoil axes)
9	Flap hinge moment coefficient

Table A-2. Run Log for WSU Aerodynamic Brake Wind Tunnel Test

Run #	Re	α	Configuration	Hinge	Device Chord	δ (°)	Comments
5	Low	1	S810	A-3	0.38	0	Baseline airfoil, gaps sealed
6	High	2	S810	A-3	0.38	0	"
7	Low	1	S810	A-3	0.38	0	Baseline airfoil, gap sealed with 51 mm (2 in.) strip of 3-M UV leading-edge tape
8	High	2	S810	A-3	0.38	0	"
9	High	2	S810	A-3	0.38	0	Repeat of run #8 to $\alpha = 24^\circ$
10	Low	1	S810	A-3	0.38	0	Repeat of run #9 to $\alpha = 24^\circ$
11	Low	1	S810	A-3	0.38	0	Baseline airfoil, gaps open
12	High	2	S810	A-3	0.38	0	"
13	Low	1	Spoiler-Flap	A-3	0.38	5	δ sweep for hinge A-3
14	Low	1	Spoiler-Flap	A-3	0.38	10	"
15	Low	1	Spoiler-Flap	A-3	0.38	30	"
16	Low	1	Spoiler-Flap	A-3	0.38	60	"
17	Low	1	Spoiler-Flap	A-3	0.38	90	"
18	High	2	Spoiler-Flap	A-3	0.38	5	Recheck for hinge A-3
19	High	2	Spoiler-Flap	A-3	0.38	10	"
20	Low	1	Spoiler-Flap	A-4	0.38	0	δ sweep for hinge A-4
21	Low	1	Spoiler-Flap	A-4	0.38	5	"
22	Low	1	Spoiler-Flap	A-4	0.38	10	"
23	Low	1	Spoiler-Flap	A-4	0.38	20	"
24	Low	1	Spoiler-Flap	A-4	0.38	30	"
25	Low	1	Spoiler-Flap	A-4	0.38	40	"
26	Low	1	Spoiler-Flap	A-4	0.38	60	"
27	Low	1	Spoiler-Flap	A-4	0.38	75	"
28	Low	1	Spoiler-Flap	A-4	0.38	90	"
29	Low	1	Spoiler-Flap	A-4	0.38	0	Repeat of run #20
30	Low	1	Spoiler-Flap	A-4	0.38	5	Repeat of run #21
31	High	2	Spoiler-Flap	A-4	0.38	0	Recheck for hinge A-4
32	High	2	Spoiler-Flap	A-4	0.38	5	"
33	High	2	Spoiler-Flap	A-4	0.38	10	"
34	Low	1	Spoiler-Flap	A-5	0.38	0	δ sweep for hinge A-5
35	Low	1	Spoiler-Flap	A-5	0.38	5	"
36	Low	1	Spoiler-Flap	A-5	0.38	10	"
37	Low	1	Spoiler-Flap	A-5	0.38	20	"
38	Low	1	Spoiler-Flap	A-5	0.38	30	"
39	Low	1	Spoiler-Flap	A-5	0.38	40	"
40	Low	1	Spoiler-Flap	A-5	0.38	60	"

Notes: α 1 $\equiv -6^\circ \leq \alpha \leq 90^\circ$, with 3° increments for $\alpha < 30^\circ$ and 5° increments for $\alpha > 30^\circ$.

α 2 $\equiv -6^\circ \leq \alpha \leq 45^\circ$, with 3° increments for $\alpha < 30^\circ$ and 5° increments for $\alpha > 30^\circ$.

α 3 $\equiv -6^\circ \leq \alpha \leq 15^\circ$, with 3° increments.

Re Low \equiv Reynolds number nominally 1 million for entire run.

Re High \equiv Reynolds number varies between 1.4 and 2.1 million throughout run, with wind tunnel operator maintaining maximum value without exceeding balance limits.

Table A-2. Run Log for WSU Aerodynamic Brake Wind Tunnel Test (continued)

Run #	Re	α	Configuration	Hinge	Device Chord	δ (°)	Comments
41	Low	1	Spoiler-Flap	A-5	0.38	75	δ sweep for hinge A-5
42	Low	1	Spoiler-Flap	A-5	0.38	90	"
43	Low	1	Spoiler-Flap	A-5	0.38	0	Repeat of run #34
44	Low	1	Spoiler-Flap	A-5	0.38	10	Repeat of run #36
45	High	2	Spoiler-Flap	A-5	0.38	0	Recheck of hinge A-5
46	High	2	Spoiler-Flap	A-5	0.38	10	"
47	High	2	Spoiler-Flap	A-5	0.38	20	"
48	High	2	Spoiler-Flap	A-5	0.38	60	"
49	Low	1	Plain Flap	A-2	0.38	0	δ sweep for hinge A-2
50	Low	1	Plain Flap	A-2	0.38	15	"
51	Low	1	Plain Flap	A-2	0.38	30	"
52	Low	1	Plain Flap	A-2	0.38	45	"
53	Low	1	Plain Flap	A-2	0.38	60	"
54	Low	1	Plain Flap	A-2	0.38	90	"
55	Low	1	Plain Flap	B-1	0.38	0	δ sweep for hinge B-1
56	Low	1	Plain Flap	B-1	0.38	15	"
57	Low	1	Plain Flap	B-1	0.38	30	"
58	Low	1	Plain Flap	B-1	0.38	45	"
59	Low	1	Plain Flap	B-1	0.38	60	"
60	Low	1	Plain Flap	B-1	0.38	75	"
61	Low	1	Plain Flap	B-1	0.38	90	"
62	Low	1	Vented Flap	C-2	0.38	0	δ sweep for hinge B-1
63	Low	1	Vented Flap	C-2	0.38	15	"
64	Low	1	Vented Flap	C-2	0.38	30	"
65	Low	1	Vented Flap	C-2	0.38	45	"
66	Low	1	S810	A-1	0.45	0	Baseline airfoil, gaps sealed
67	High	2	S810	A-1	0.45	0	"
68	Low	1	S810	A-1	0.45	0	Baseline airfoil, gaps open
69	High	2	S810	A-1	0.45	0	"
70	Low	1	Plain Flap	A-1	0.45	15	δ sweep for hinge A-1
71	Low	1	Plain Flap	A-1	0.45	30	"
72	Low	1	Plain Flap	A-1	0.45	45	"
73	Low	1	Plain Flap	A-1	0.45	60	"
74	Low	1	Plain Flap	A-1	0.45	75	"
75	Low	1	Plain Flap	A-1	0.45	90	"
76	Low	1	Spoiler-Flap	A-2	0.45	0	δ sweep for hinge A-2
77	Low	1	Spoiler-Flap	A-2	0.45	15	"
78	Low	1	Spoiler-Flap	A-2	0.45	30	"

Notes: α 1 $\equiv -6^\circ \leq \alpha \leq 90^\circ$, with 3° increments for $\alpha < 30^\circ$ and 5° increments for $\alpha > 30^\circ$.
 α 2 $\equiv -6^\circ \leq \alpha \leq 45^\circ$, with 3° increments for $\alpha < 30^\circ$ and 5° increments for $\alpha > 30^\circ$.
 α 3 $\equiv -6^\circ \leq \alpha \leq 15^\circ$, with 3° increments.
Re Low \equiv Reynolds number nominally 1 million for entire run.
Re High \equiv Reynolds number varies between 1.4 and 2.1 million throughout run, with wind tunnel operator maintaining maximum value without exceeding balance limits.

Table A-2. Run Log for WSU Aerodynamic Brake Wind Tunnel Test (continued)

Run #	Re	α	Configuration	Hinge	Device Chord	δ (°)	Comments
79	Low	1	Spoiler-Flap	A-2	0.45	45	δ sweep for hinge A-2
80	Low	1	Spoiler-Flap	A-2	0.45	60	"
81	Low	1	Spoiler-Flap	A-2	0.45	75	"
82	Low	1	Spoiler-Flap	A-2	0.45	90	"
83	Low	1	Spoiler-Flap	A-3	0.45	0	δ sweep for hinge A-3
84	Low	1	Spoiler-Flap	A-3	0.45	15	"
85	Low	1	Spoiler-Flap	A-3	0.45	30	"
86	Low	1	Spoiler-Flap	A-3	0.45	45	"
87	Low	1	Spoiler-Flap	A-3	0.45	60	"
88	Low	1	Spoiler-Flap	A-3	0.45	75	"
89	Low	1	Spoiler-Flap	A-3	0.45	90	"
90	Low	1	Spoiler-Flap	A-4	0.45	0	δ sweep for hinge A-4
91	Low	1	Spoiler-Flap	A-4	0.45	15	"
92	Low	1	Spoiler-Flap	A-4	0.45	30	"
93	Low	1	Spoiler-Flap	A-4	0.45	45	"
94	Low	1	Spoiler-Flap	A-4	0.45	60	"
95	Low	1	Spoiler-Flap	A-4	0.45	75	"
96	Low	1	Spoiler-Flap	A-4	0.45	90	"
97	Low	1	Spoiler-Flap	B-3	0.45	0	δ sweep for hinge B-3
98	Low	1	Spoiler-Flap	B-3	0.45	15	"
99	Low	1	Spoiler-Flap	B-3	0.45	30	"
100	Low	1	Spoiler-Flap	B-3	0.45	45	"
101	Low	1	Spoiler-Flap	B-3	0.45	60	"
102	Low	1	Spoiler-Flap	B-3	0.45	75	"
103	Low	1	Spoiler-Flap	B-3	0.45	90	"
104	Low	1	Spoiler-Flap	B-5	0.45	0	δ sweep for hinge B-5
105	Low	1	Spoiler-Flap	B-5	0.45	15	"
106	Low	1	Spoiler-Flap	B-5	0.45	30	"
107	Low	1	Spoiler-Flap	B-5	0.45	45	"
108	Low	1	Spoiler-Flap	B-5	0.45	60	"
109	Low	1	Spoiler-Flap	B-5	0.45	75	"
110	Low	1	Vented Flap	C-1	0.45	0	δ sweep for hinge C-1
111	Low	1	Vented Flap	C-1	0.45	15	"
112	Low	1	Vented Flap	C-1	0.45	30	"
113	Low	1	Vented Flap	C-1	0.45	45	"
114	Low	1	Vented Flap	C-1	0.45	60	"
115	Low	1	Vented Flap	C-1	0.45	75	"
116	Low	1	Vented Flap	C-1	0.45	90	"

Notes: α 1 $\equiv -6^\circ \leq \alpha \leq 90^\circ$, with 3° increments for $\alpha < 30^\circ$ and 5° increments for $\alpha > 30^\circ$.
 α 2 $\equiv -6^\circ \leq \alpha \leq 45^\circ$, with 3° increments for $\alpha < 30^\circ$ and 5° increments for $\alpha > 30^\circ$.
 α 3 $\equiv -6^\circ \leq \alpha \leq 15^\circ$, with 3° increments.
Re Low \equiv Reynolds number nominally 1 million for entire run.
Re High \equiv Reynolds number varies between 1.4 and 2.1 million throughout run, with wind tunnel operator maintaining maximum value without exceeding balance limits.

Table A-2. Run Log for WSU Aerodynamic Brake Wind Tunnel Test (continued)

Run #	Re	α	Configuration	Hinge	Device Chord	δ (°)	Comments
117	Low	1	Spoiler-Flap	C-3	0.45	0	δ sweep for hinge C-3
118	Low	1	Spoiler-Flap	C-3	0.45	15	"
119	Low	1	Spoiler-Flap	C-3	0.45	30	"
120	Low	1	Spoiler-Flap	C-3	0.45	45	"
121	Low	1	Spoiler-Flap	C-3	0.45	60	"
122	Low	1	Spoiler-Flap	C-3	0.45	85	"
123	Low	1	Spoiler-Flap	C-5	0.45	0	δ sweep for hinge C-5
124	Low	1	Spoiler-Flap	C-5	0.45	15	"
125	Low	1	Spoiler-Flap	C-5	0.45	30	"
126	Low	1	Spoiler-Flap	C-5	0.45	45	"
127	Low	1	Spoiler-Flap	C-5	0.45	60	"
128	Low	2	Partial Span	A-4	0.45	0	Full-span spoiler (90° upper) and split-flap (90° lower)
129	Low	2	Partial Span	A-4	0.45	0	Repeat run #128
130	Low	2	Partial Span	A-4	0.45	0	1/2-span spoiler (90° upper) and split-flap (90° lower)
131	Low	2	Partial Span	A-4	0.45	0	re-reduction of run #103 data
132	Low	2	Partial Span	A-4	0.45	0	1/3-span spoiler (90° upper) and split-flap (90° lower)
133	Low	2	Partial Span	A-4	0.45	0	Full-span spoiler (90° upper) and split-flap (45° lower)
134	Low	2	Partial Span	A-4	0.45	0	1/2-span spoiler (90° upper) and split-flap (45° lower)
135	Low	2	Partial Span	A-4	0.45	0	1/3-span spoiler (90° upper) and split-flap (45° lower)
136	Low	2	Partial Span	A-4	0.45	0	1/3-span split-flap only (45° down)
137	Low	2	Partial Span	A-4	0.45	0	1/2-span split-flap only (45° lower)
138	Low	2	Partial Span	A-4	0.45	0	Full-span split-flap only (45° lower)
139	Low	2	Partial Span	A-4	0.45	0	Full-span split-flap only (45° lower)
140	Low	2	Partial Span	A-4	0.45	0	1/2-span split-flap only (45° lower)
141	Low	2	Partial Span	A-4	0.45	0	1/3-span split-flap only (45° lower)
142	Low	2	Partial Span	A-4	0.45	0	1/3-span spoiler only (90° upper)
143	Low	2	Partial Span	A-4	0.45	0	1/2-span spoiler only (90° upper)

Notes: α 1 $\equiv -6^\circ \leq \alpha \leq 90^\circ$, with 3° increments for $\alpha < 30^\circ$ and 5° increments for $\alpha > 30^\circ$.
 α 2 $\equiv -6^\circ \leq \alpha \leq 45^\circ$, with 3° increments for $\alpha < 30^\circ$ and 5° increments for $\alpha > 30^\circ$.
 α 3 $\equiv -6^\circ \leq \alpha \leq 15^\circ$, with 3° increments.
Re Low \equiv Reynolds number nominally 1 million for entire run.
Re High \equiv Reynolds number varies between 1.4 and 2.1 million throughout run, with wind tunnel operator maintaining maximum value without exceeding balance limits.

Table A-2. Run Log for WSU Aerodynamic Brake Wind Tunnel Test (continued)

Run #	Re	α	Configuration	Hinge	Device Chord	δ (°)	Comments
144	Low	2	Partial Span	A-4	0.45	0	Full-span spoiler only (90° upper)
145	Low	1	Spoiler-Flap	A-4	0.45	0	Repeat of run #90
146	High	2	Spoiler-Flap	A-4	0.45	0	Hinge A-4 at high Re
147	Low	1	Spoiler-Flap	A-4	0.45	5	Hinge A-4 at small δ
148	Low	1	Spoiler-Flap	A-4	0.45	10	"
149	Low	1	Spoiler-Flap	A-4	0.45	15	Repeat of run #91
150	High	2	Spoiler-Flap	A-4	0.45	15	Hinge A-4 at high Re
151	High	2	Spoiler-Flap	A-4	0.45	30	"
152	High	2	Spoiler-Flap	A-4	0.45	45	"
153	High	2	Spoiler-Flap	A-4	0.45	60	"
154	High	2	Spoiler-Flap	A-4	0.45	75	"
155	Low	2	Spoiler-Flap	A-4	0.45	30	Hinge A-4 with rounded cove insert
156	Low	2	Spoiler-Flap	A-4	0.45	23	Hinge A-4 with rounded cove insert
157	Low	3	S810	A-4	0.45	0	Repeat measurement of low Re drag bucket with gap sealed (run # 66 at low α)
158	High	3	S810	A-4	0.45	0	Repeat measurement of high Re drag bucket with gap sealed (run # 67 at low α)
159	Low	3	S810	A-4	0.45	0	Gap-sealed, low Re drag bucket with 51 mm (2 in) strip of 0.15 mm (6 mil) thick leading-edge tape
160	Low	3	S810	A-4	0.45	0	Gap-sealed, high Re drag bucket with 51 mm (2 in) strip of 0.15 mm (6 mil) thick leading-edge tape
161	Low	2	Spoiler-Flap	A-4	0.45	0	Hinge A-4 with leading-edge grain roughness (LEGR)
162	High	2	Spoiler-Flap	A-4	0.45	0	"
163	Low	2	Spoiler-Flap	A-4	0.45	15	"
164	High	2	Spoiler-Flap	A-4	0.45	15	"
165	Low	2	Spoiler-Flap	A-4	0.45	30	"
166	High	2	Spoiler-Flap	A-4	0.45	30	"
167	Low	2	Spoiler-Flap	A-4	0.45	45	"
168	Low	2	Spoiler-Flap	A-4	0.45	60	"
169	Low	2	Spoiler-Flap	A-4	0.45	75	"
170	Low	2	Spoiler-Flap	A-4	0.45	90	"

Notes: α 1 $\equiv -6^\circ \leq \alpha \leq 90^\circ$, with 3° increments for $\alpha < 30^\circ$ and 5° increments for $\alpha > 30^\circ$.

α 2 $\equiv -6^\circ \leq \alpha \leq 45^\circ$, with 3° increments for $\alpha < 30^\circ$ and 5° increments for $\alpha > 30^\circ$.

α 3 $\equiv -6^\circ \leq \alpha \leq 15^\circ$, with 3° increments.

Re Low \equiv Reynolds number nominally 1 million for entire run.

Re High \equiv Reynolds number varies between 1.4 and 2.1 million throughout run, with wind tunnel operator maintaining maximum value without exceeding balance limits.

Table A-3. Summary of Appendix A Graphical Data

Figure Number	Title	Run Numbers Plotted
A-1	δ -Sweep for 38% Cord Plain Flap, Hinge A-2	49, 50, 51, 52, 53, 54
A-2	δ -Sweep for 38% Cord Spoiler-Flap, Hinge A-3	11, 13, 14, 15, 16, 17
A-3	δ -Sweep for 38% Cord Spoiler-Flap, Hinge A-4	20, 21, 22, 23, 24, 25, 26, 27, 28
A-4	δ -Sweep for 38% Cord Spoiler-Flap, Hinge A-5	34, 35, 36, 37, 38, 39, 40, 41, 42
A-5	δ -Sweep for 38% Cord Plain Flap, Hinge B-1	55, 56, 57, 58, 59, 60, 61
A-6	δ -Sweep for 38% Cord Vented Flap, Hinge C-2	62, 63, 64, 65
A-7	δ -Sweep for 45% Cord Plain Flap, Hinge A-1	70, 71, 72, 73, 74, 75
A-8	δ -Sweep for 45% Cord Spoiler-Flap, Hinge A-2	76, 77, 78, 79, 80, 81, 82
A-9	δ -Sweep for 45% Cord Spoiler-Flap, Hinge A-3	83, 84, 85, 86, 87, 88, 89
A-10	δ -Sweep for 45% Cord Spoiler-Flap, Hinge A-4	90, 147, 148, 91, 92, 93, 94, 95
A-11	δ -Sweep for 45% Cord Spoiler-Flap, Hinge B-3	97, 98, 99, 100, 101, 102, 103
A-12	δ -Sweep for 45% Cord Spoiler-Flap, Hinge B-5	104, 105, 106, 107, 108, 109
A-13	δ -Sweep for 45% Cord Vented Flap, Hinge C-1	110, 111, 112, 113, 114, 115, 116
A-14	δ -Sweep for 45% Cord Spoiler-Flap, Hinge C-3	117, 118, 119, 120, 121, 122
A-15	δ -Sweep for 45% Cord Spoiler-Flap, Hinge C-5	123, 124, 125, 126, 127
A-16	Repeatability Check on Spoiler-Flap	90, 91, 145, 149
A-17	Reynolds Number Effect on Spoiler-Flap	90, 146, 92, 151, 94, 153
A-18	Effect of Leading-Edge Roughness on Spoiler-Flap	90, 161, 92, 165, 94, 168
A-19	Effect of Gap Seal on 38% Chord Device	5, 6, 11, 12
A-20	Effect of Gap Seal on 45% Chord Device	66, 67, 68, 69
A-21	Effect of Leading-Edge Tape on Clean S810	66, 67, 7, 8, 159, 160
A-22	Effect of Hinge Location on Device at $\delta=45^\circ$	72, 79, 86, 93, 100, 113
A-23	Effect of Hinge Location on Device at $\delta=75^\circ$	74, 81, 88, 95, 102, 115

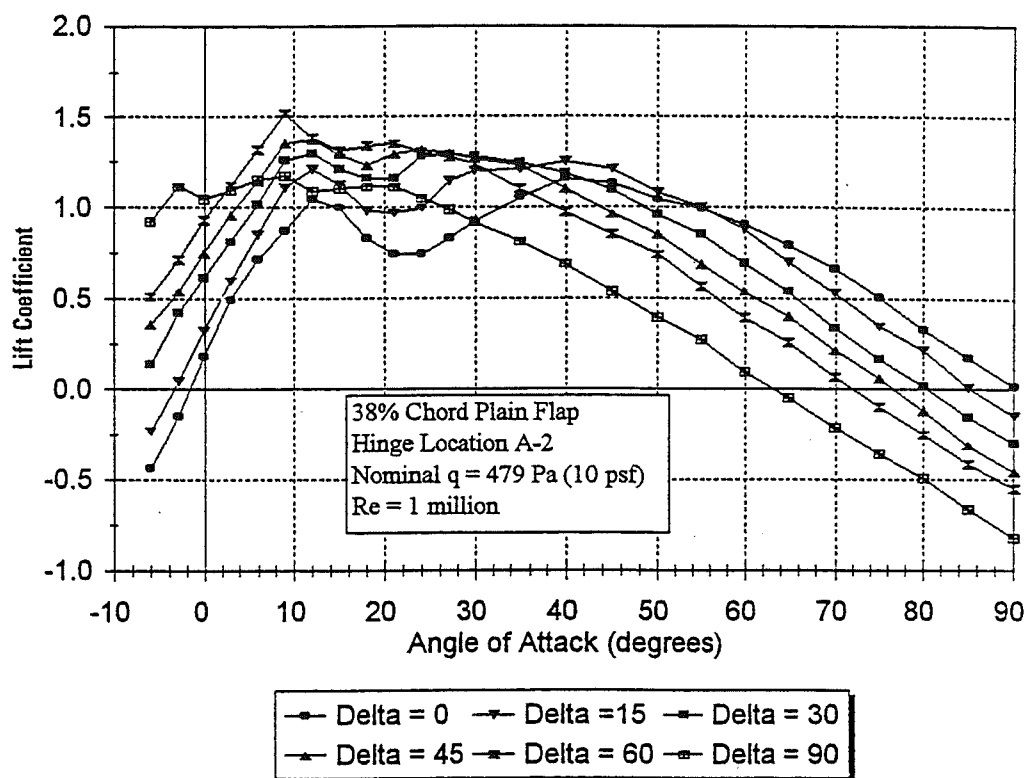


Figure A-1a. Lift Data, δ -Sweep for 38% Chord Plain Flap, Hinge A-2

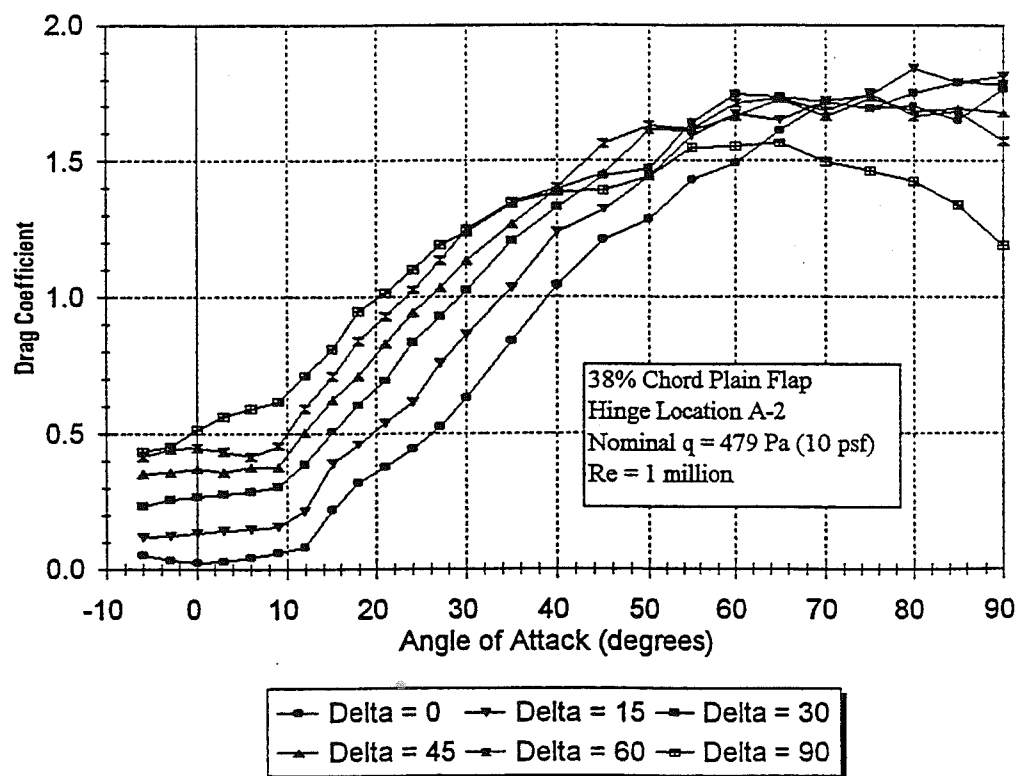


Figure A-1b. Drag Data, δ -Sweep for 38% Chord Plain Flap, Hinge A-2

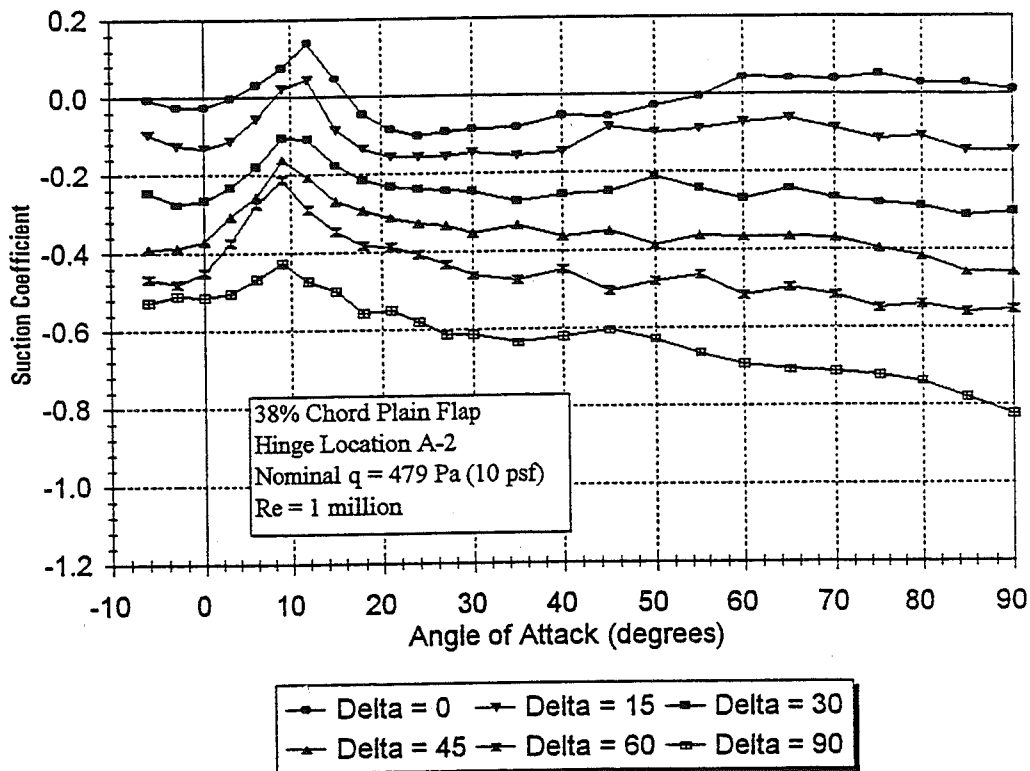


Figure A-1c. Suction Data, δ -Sweep for 38% Chord Plain Flap, Hinge A-2

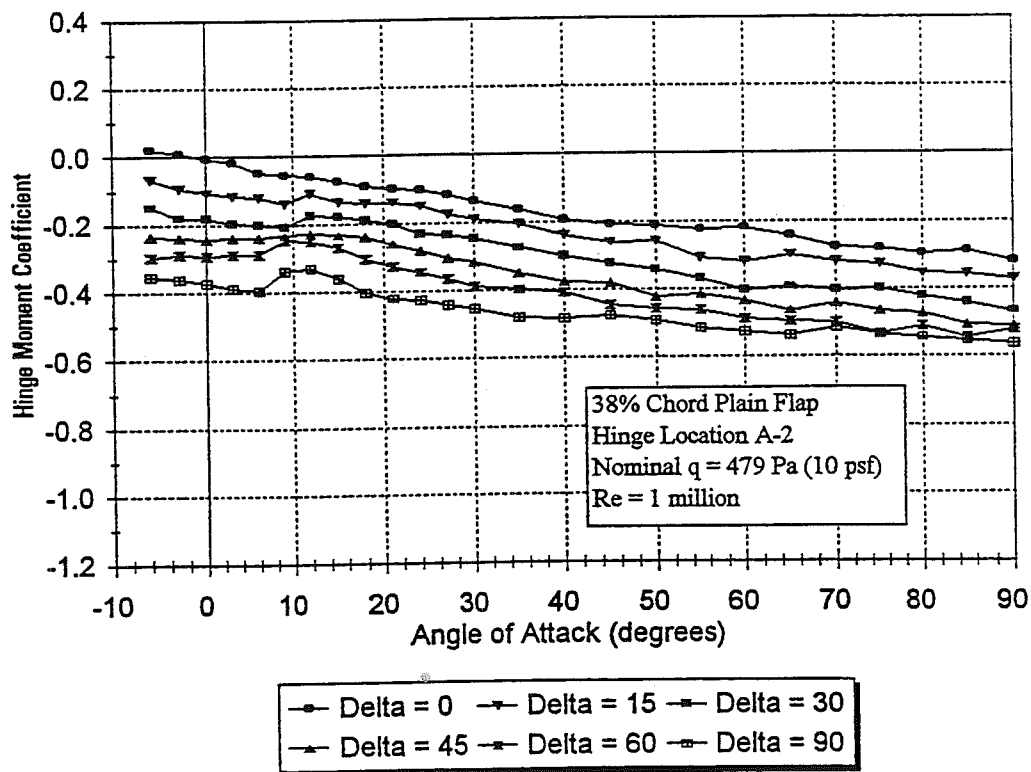


Figure A-1d. Hinge Moment Data, δ -Sweep for 38% Chord Plain Flap, Hinge A-2

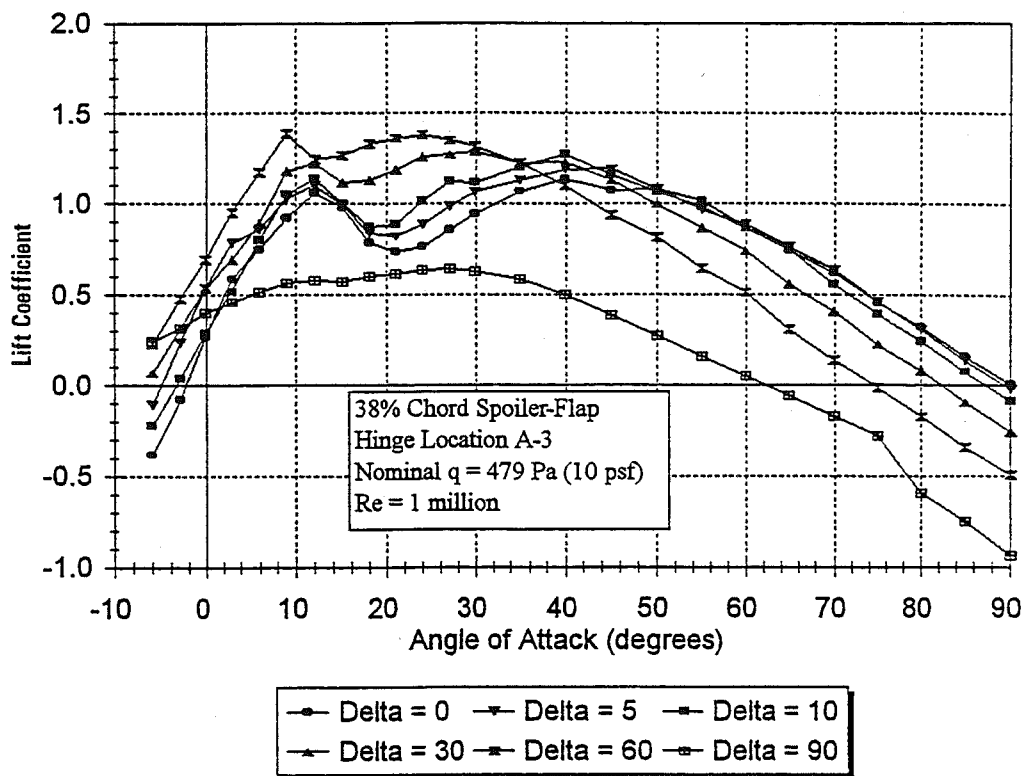


Figure A-2a. Lift Data, δ -Sweep for 38% Chord Spoiler-Flap, Hinge A-3

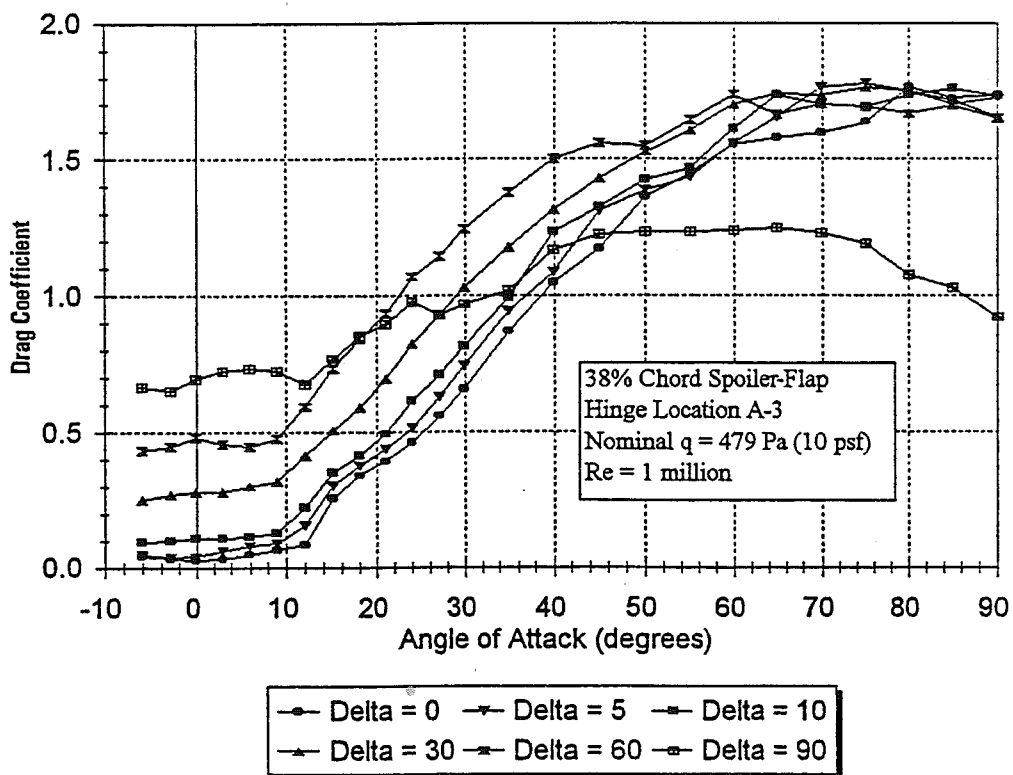


Figure A-2b. Drag Data, δ -Sweep for 38% Chord Spoiler-Flap, Hinge A-3

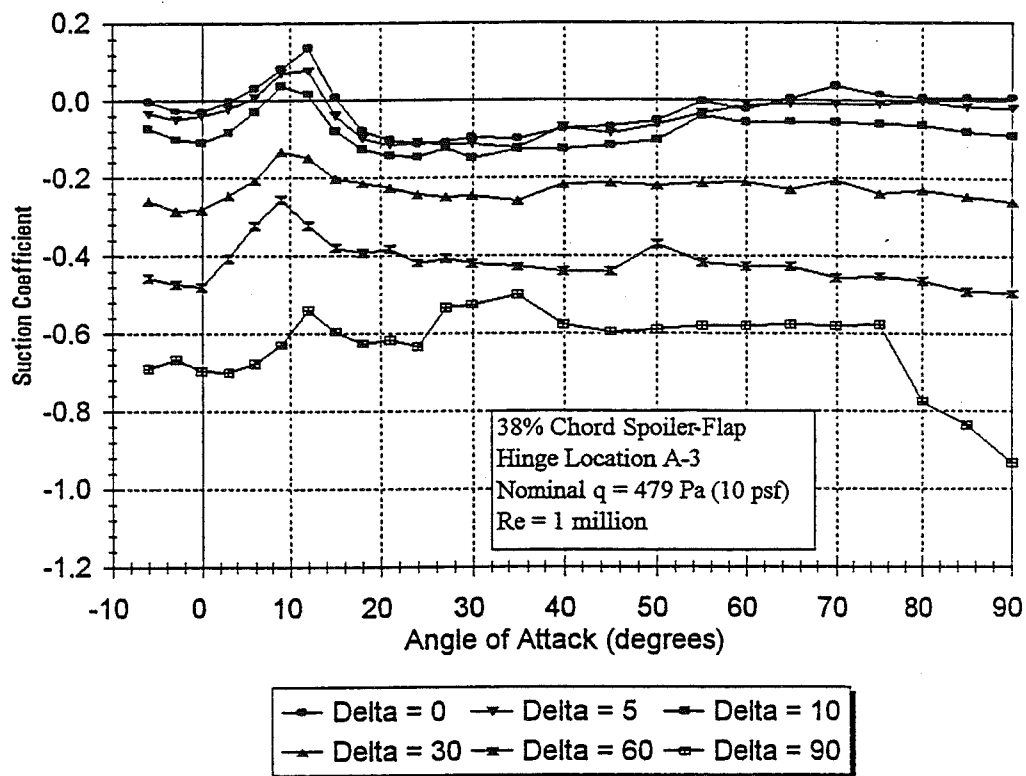


Figure A-2c. Suction Data, δ -Sweep for 38% Chord Spoiler-Flap, Hinge A-3

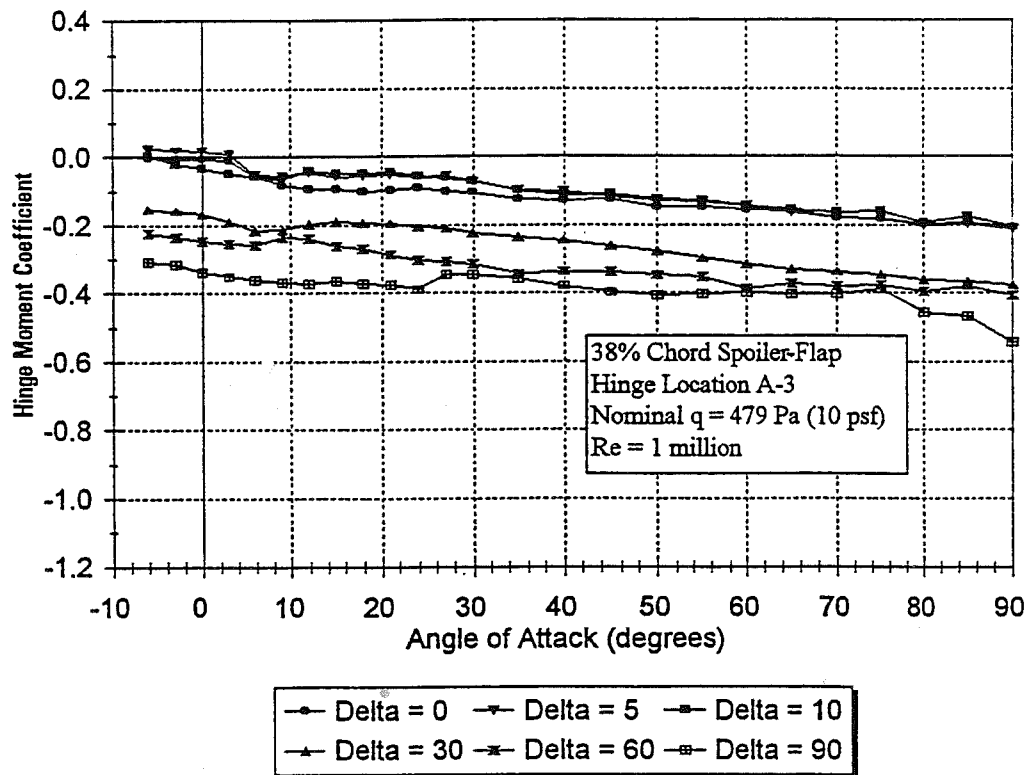


Figure A-2d. Hinge Moment Data, δ -Sweep for 38% Chord Spoiler-Flap, Hinge A-3

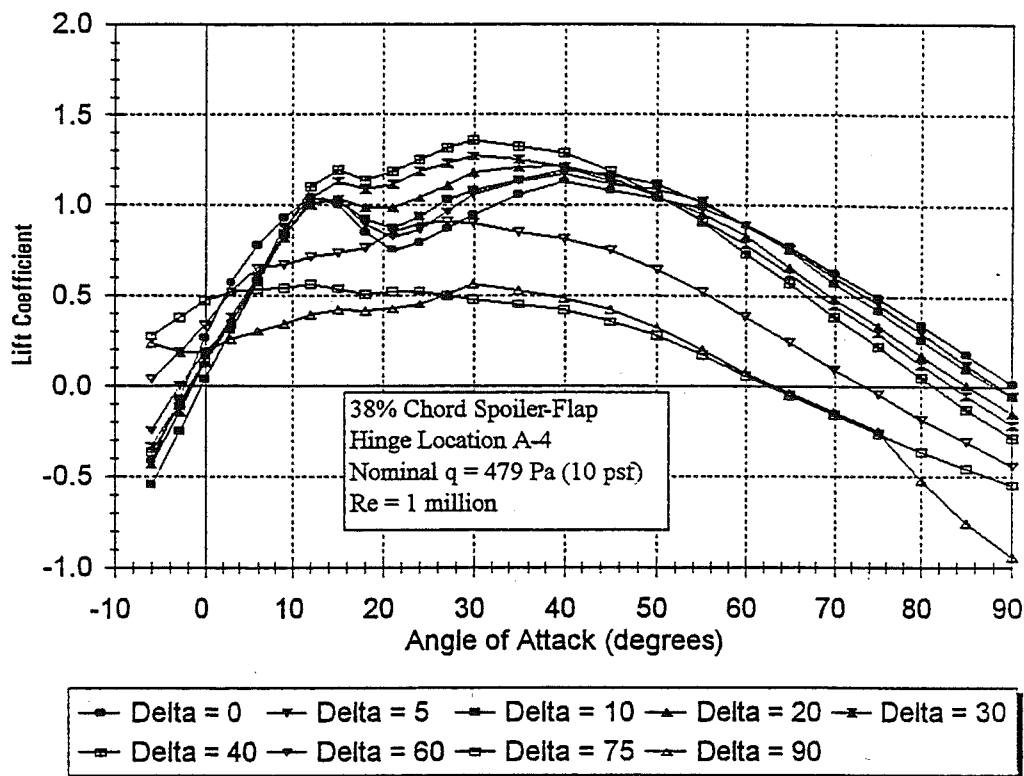


Figure A-3a. Lift Data, δ -Sweep for 38% Chord Spoiler-Flap, Hinge A-4

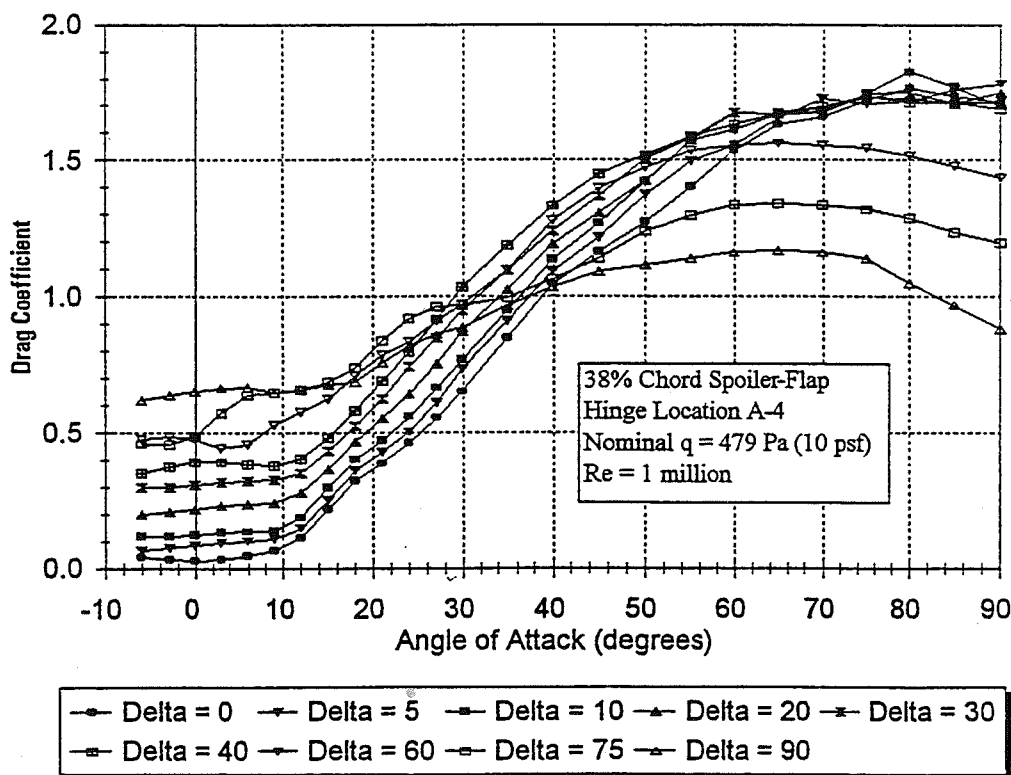


Figure A-3b. Drag Data, δ -Sweep for 38% Chord Spoiler-Flap, Hinge A-4

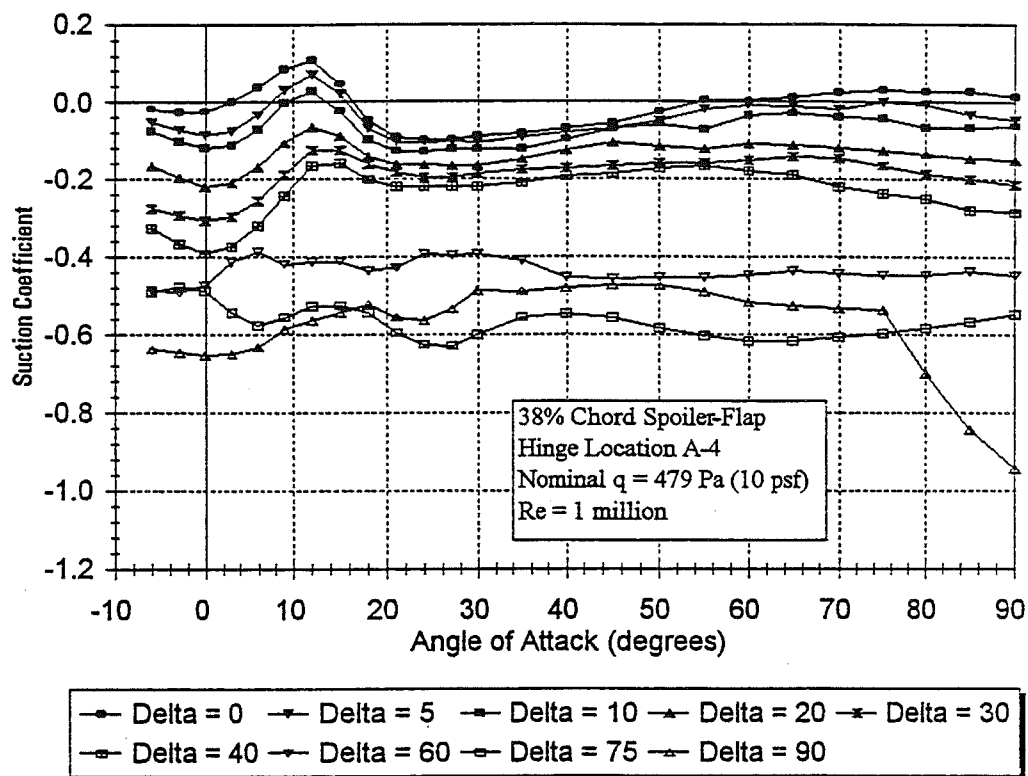


Figure A-3c. Suction Data, δ -Sweep for 38% Chord Spoiler-Flap, Hinge A-4

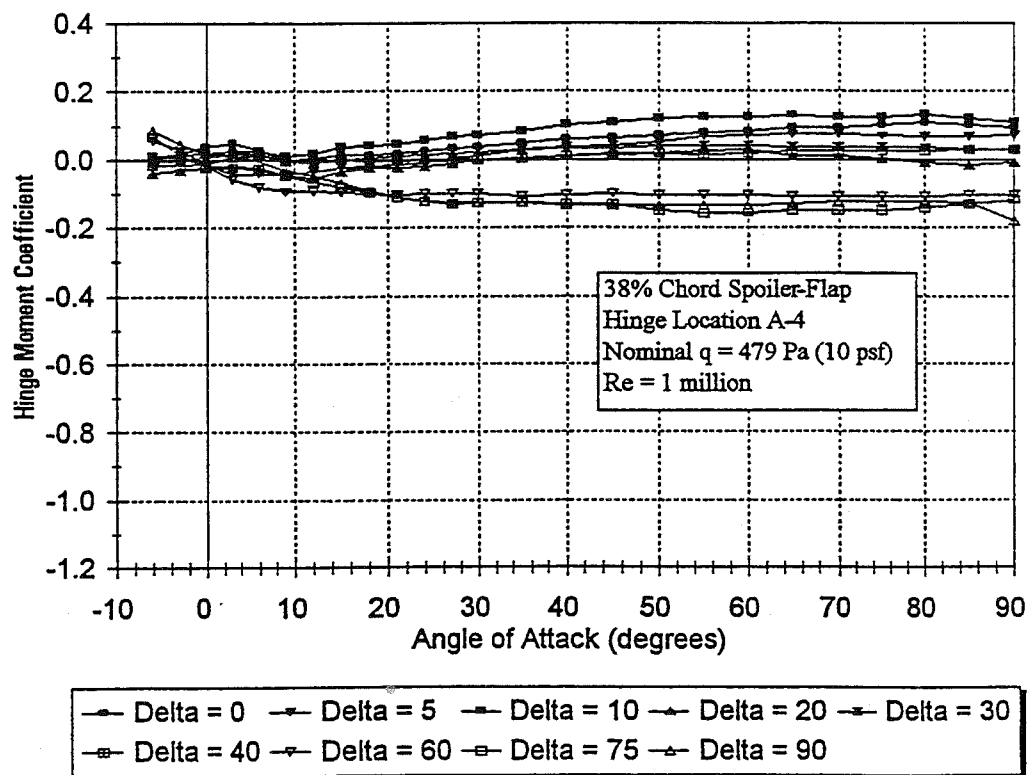


Figure A-3d. Hinge Moment Data, δ -Sweep for 38% Chord Spoiler-Flap, Hinge A-4

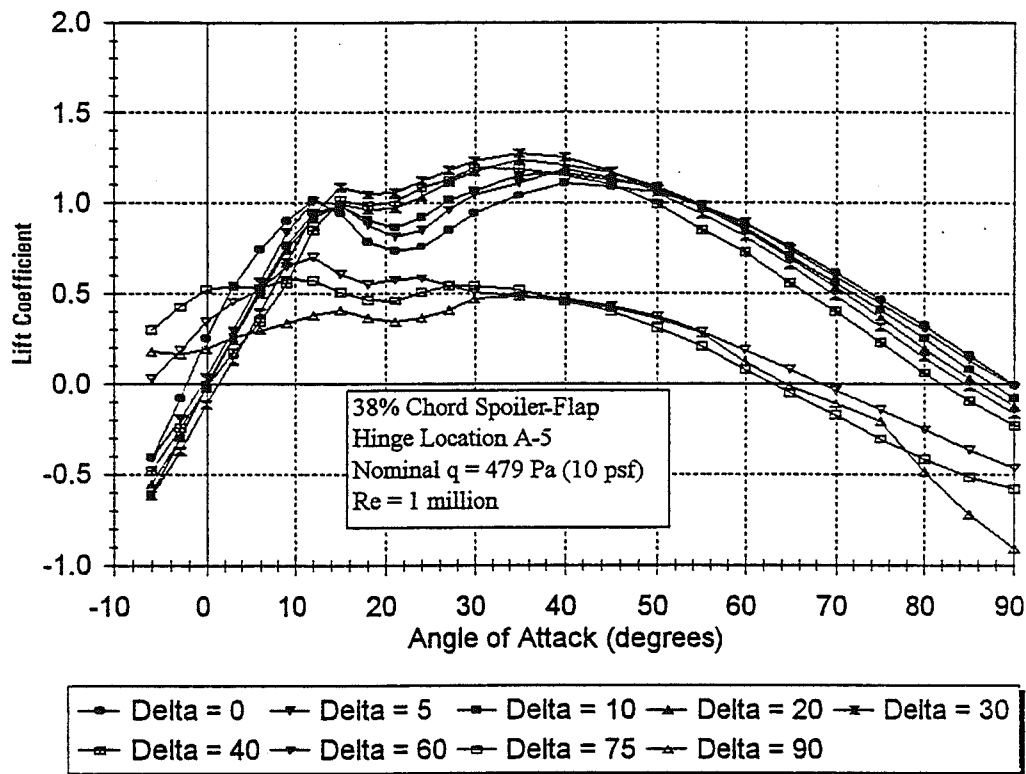


Figure A-4a. Lift Data, δ -Sweep for 38% Chord Spoiler-Flap, Hinge A-5

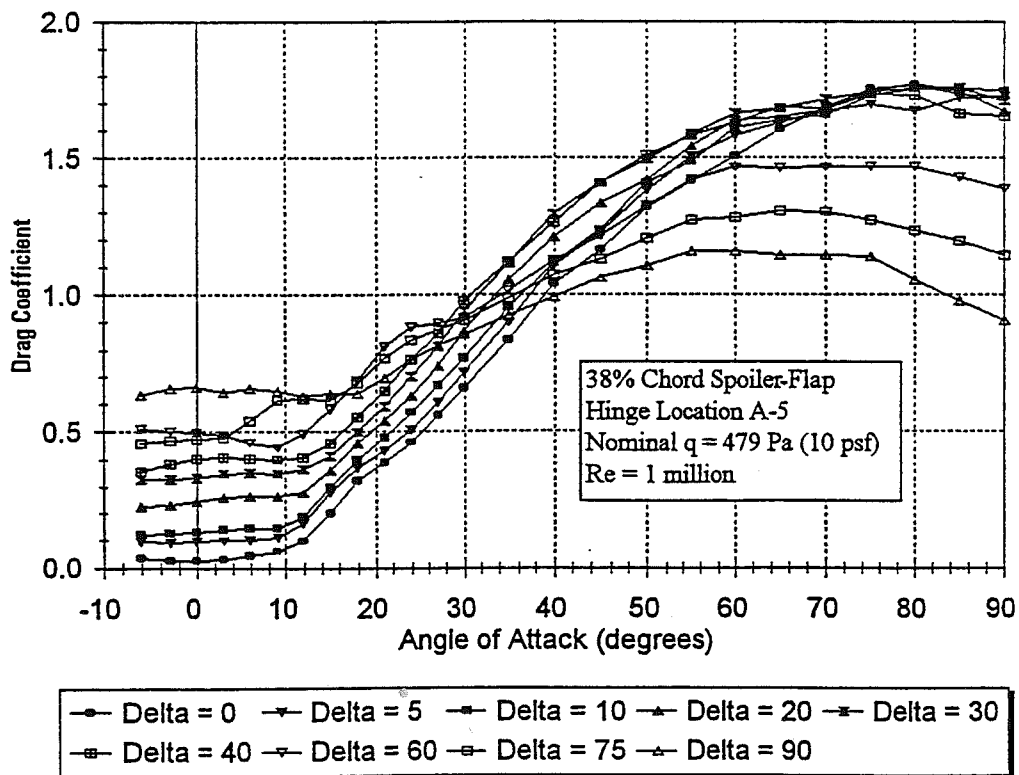


Figure A-4b. Drag Data, δ -Sweep for 38% Chord Spoiler-Flap, Hinge A-5

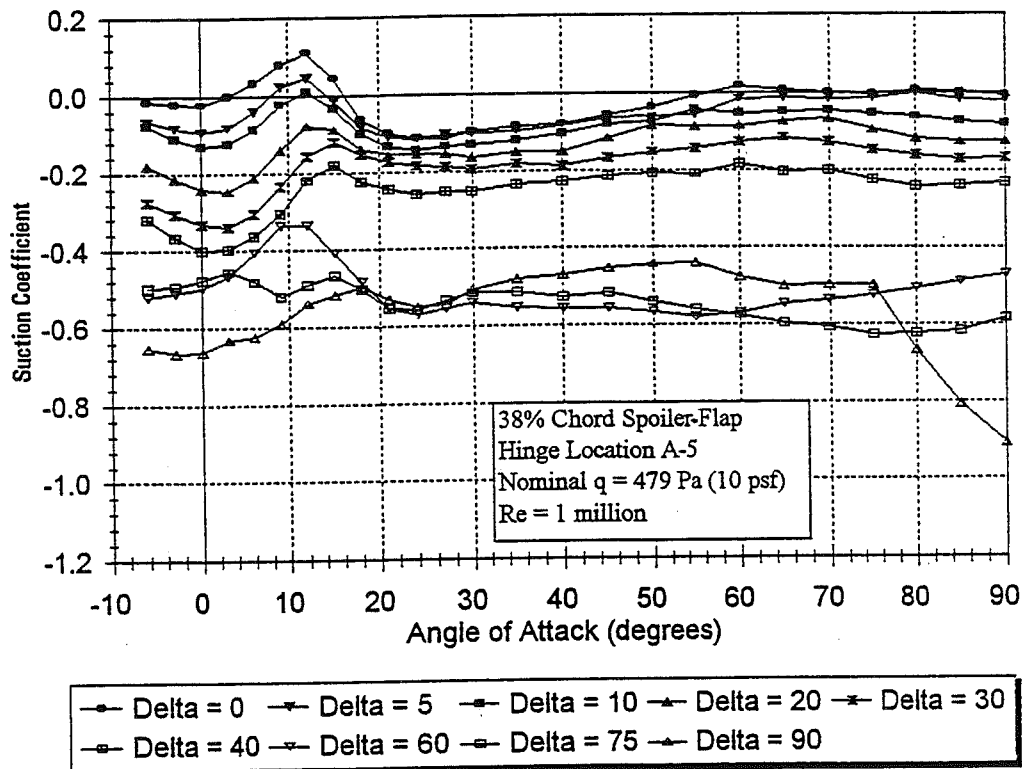


Figure A-4c. Suction Data, δ -Sweep for 38% Chord Spoiler-Flap, Hinge A-5

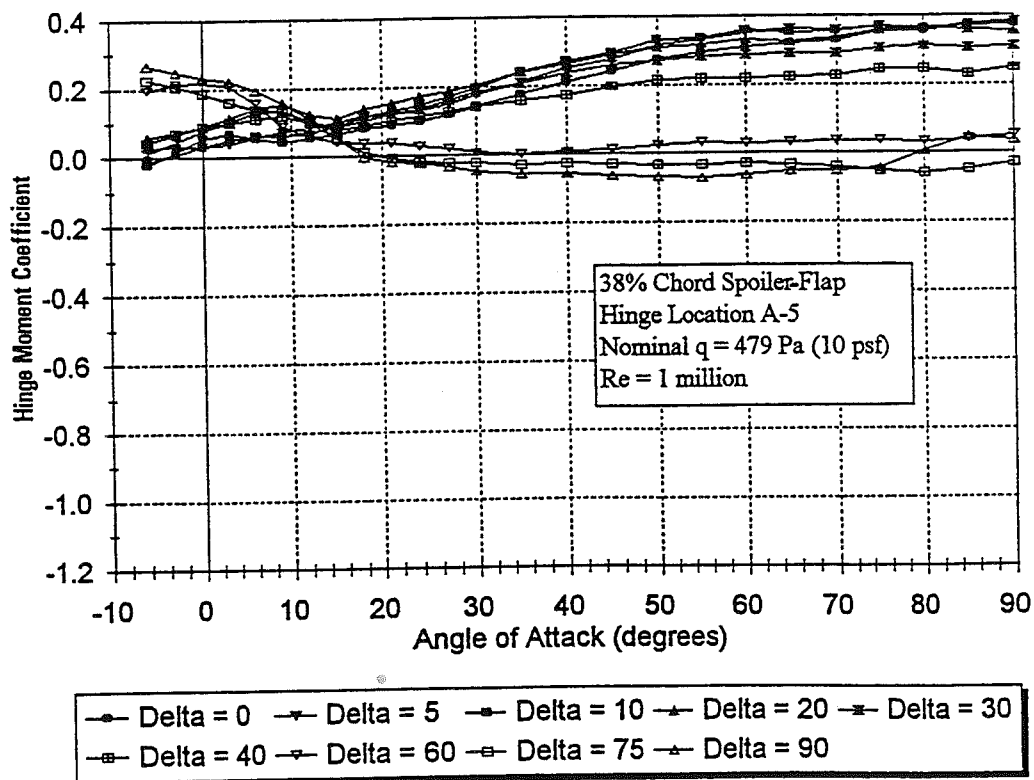


Figure A-4d. Hinge Moment Data, δ -Sweep for 38% Chord Spoiler-Flap, Hinge A-5

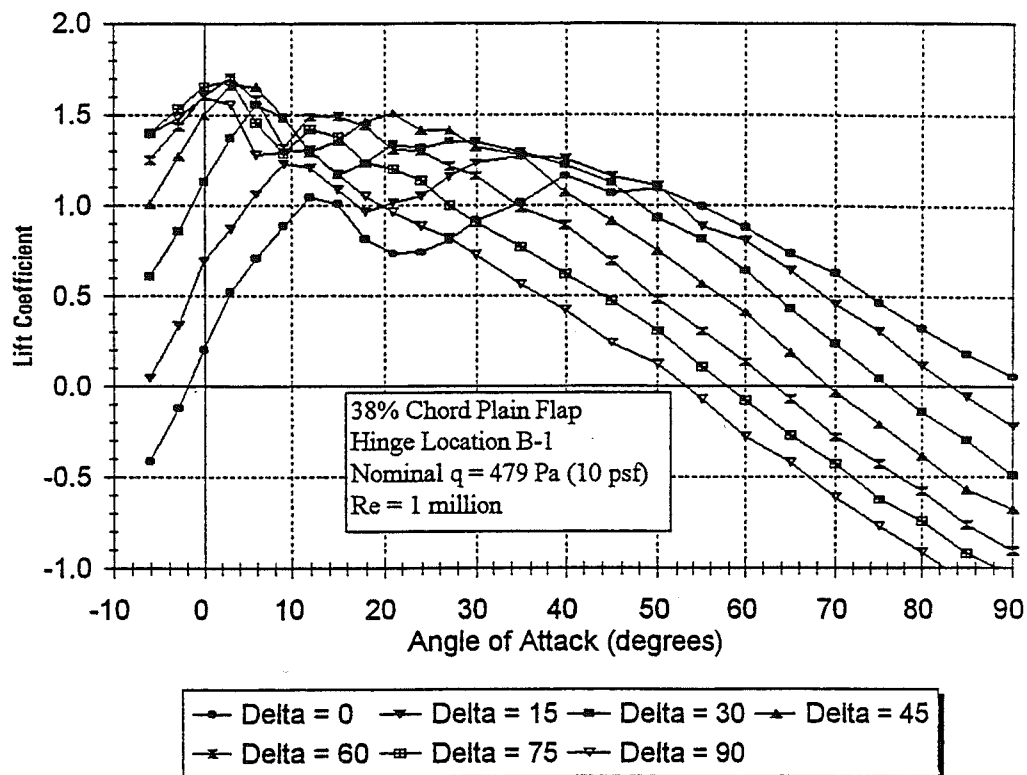


Figure A-5a. Lift Data, δ -Sweep for 38% Chord Plain Flap, Hinge B-1

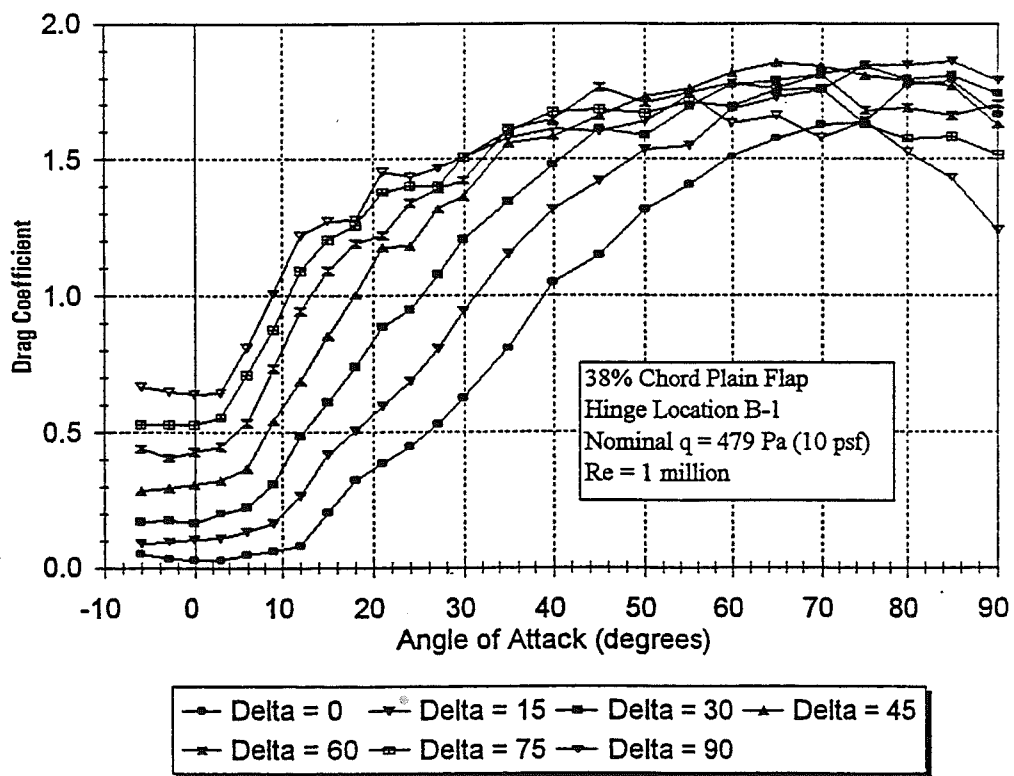


Figure A-5b. Drag Data, δ -Sweep for 38% Chord Plain Flap, Hinge B-1

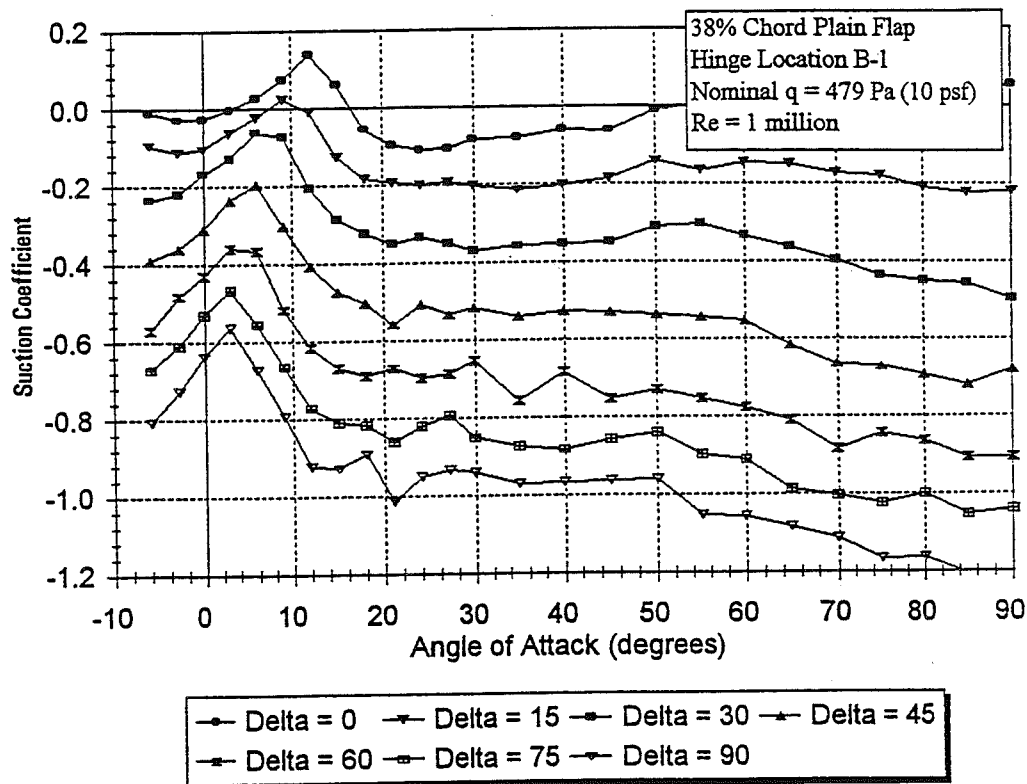


Figure A-5c. Suction Data, δ -Sweep for 38% Chord Plain Flap, Hinge B-1

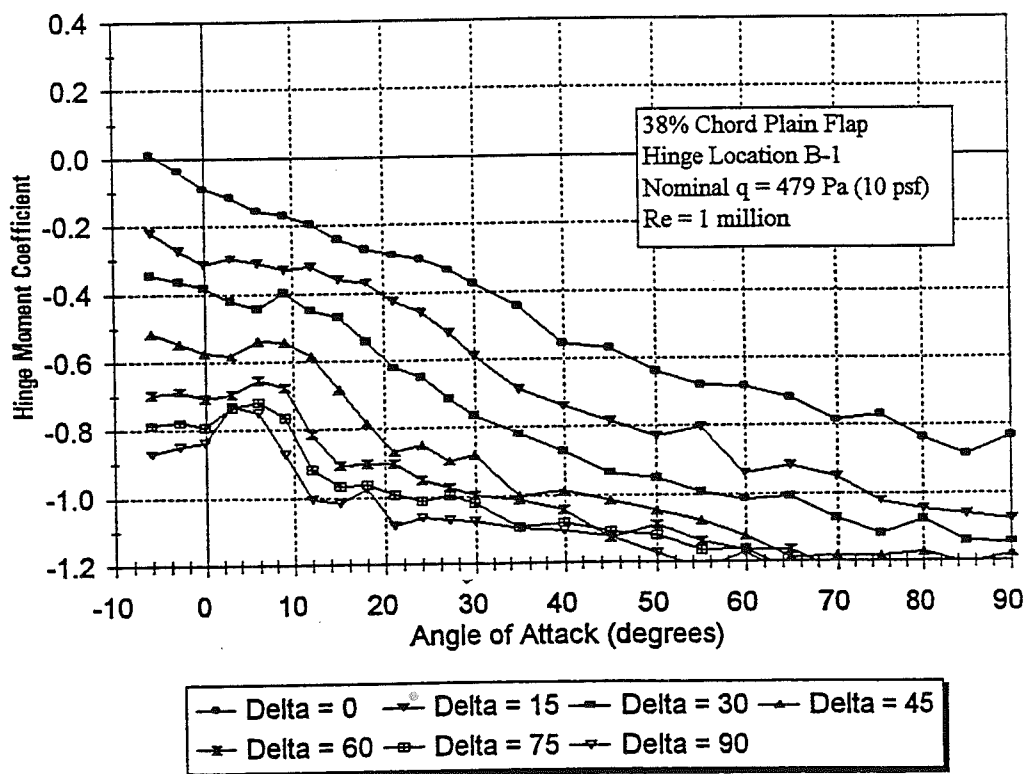


Figure A-5d. Hinge Moment Data, δ -Sweep for 38% Chord Plain Flap, Hinge B-1

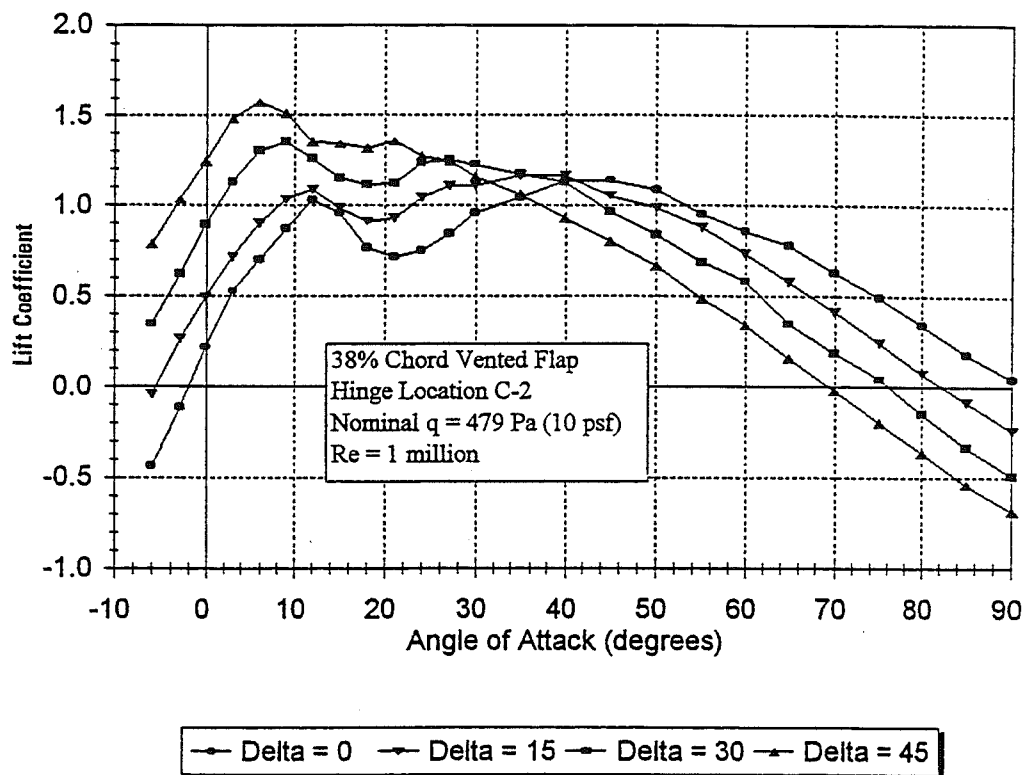


Figure A-6a. Lift Data, δ -Sweep for 38% Chord Vented Flap, Hinge C-2

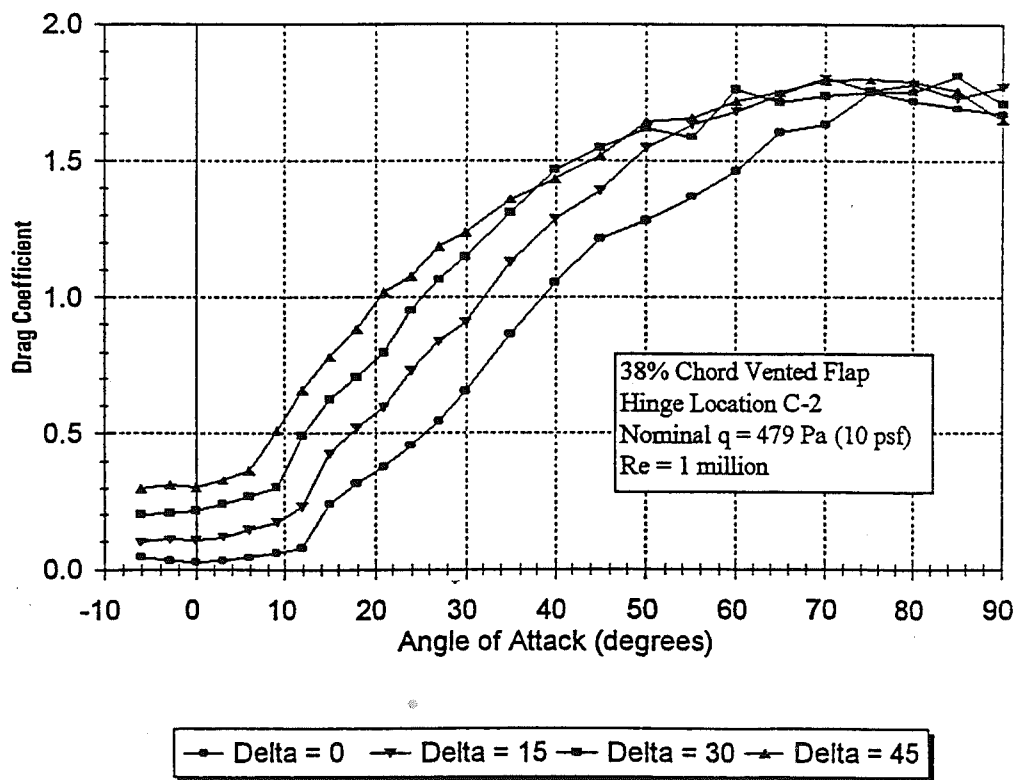


Figure A-6b. Drag Data, δ -Sweep for 38% Chord Vented Flap, Hinge C-2

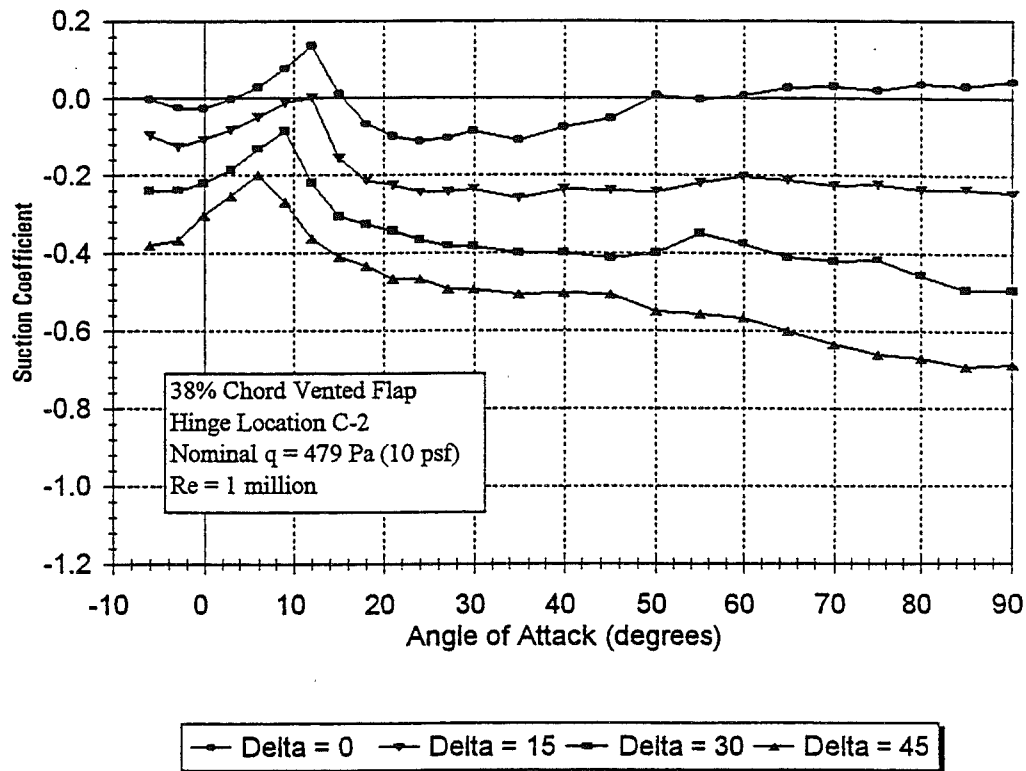


Figure A-6c. Suction Data, δ -Sweep for 38% Chord Vented Flap, Hinge C-2

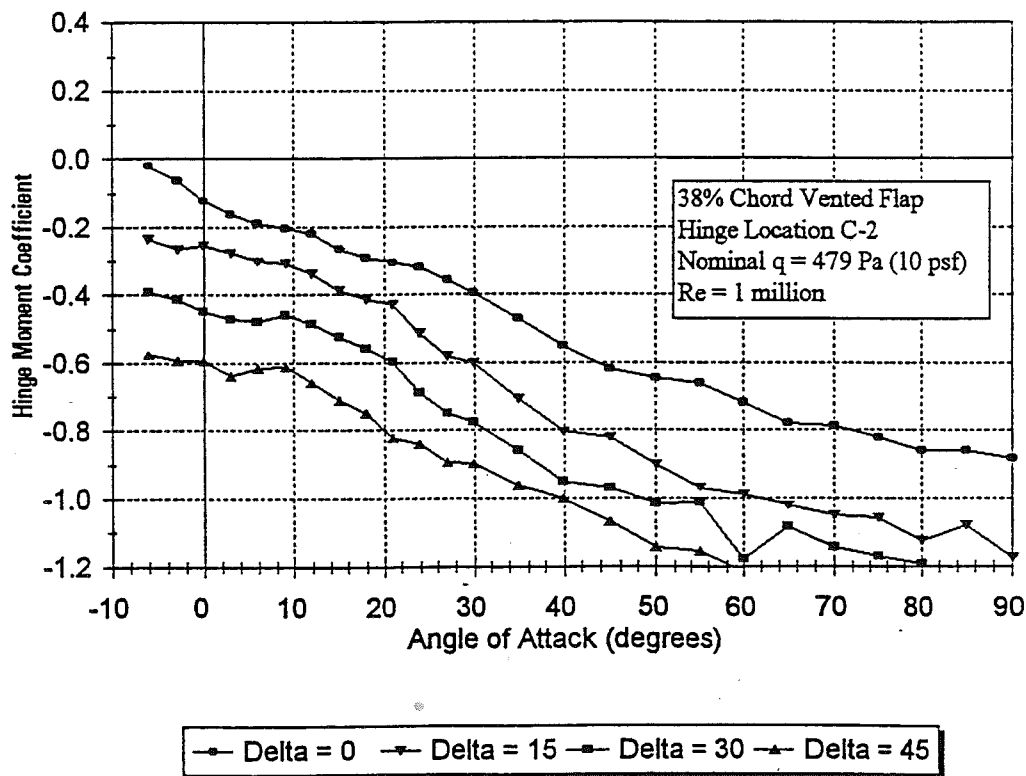


Figure A-6d. Hinge Moment Data, δ -Sweep for 38% Chord Vented Flap, Hinge C-2

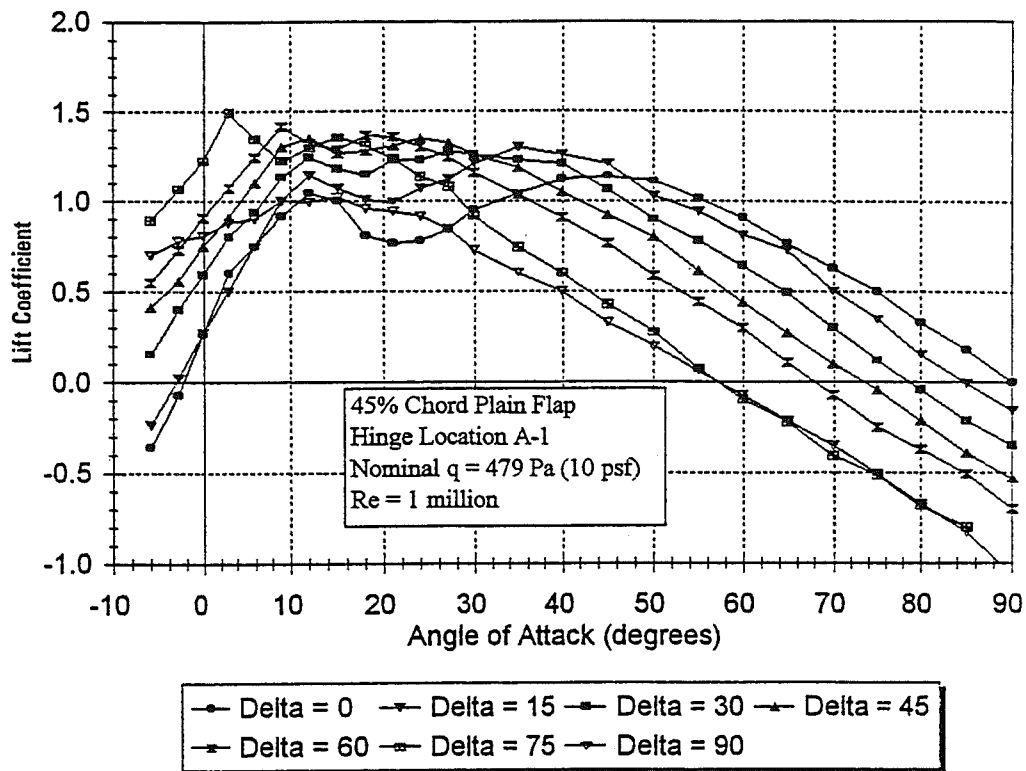


Figure A-7a. Lift Data, δ -Sweep for 45% Chord Plain Flap, Hinge A-1

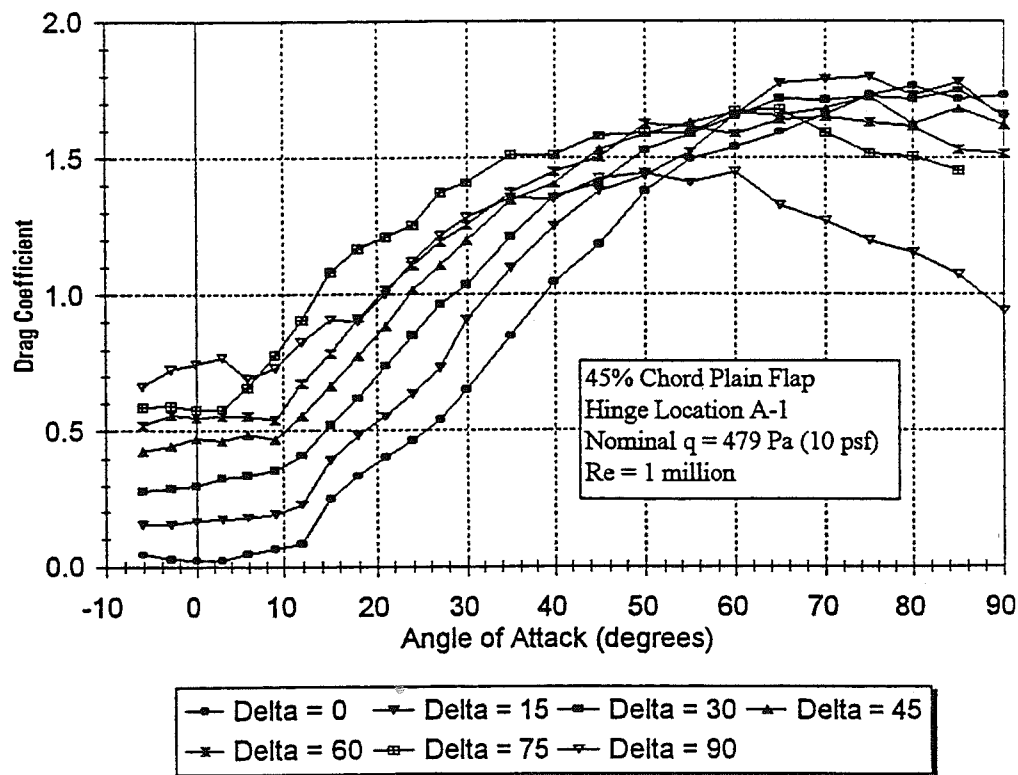


Figure A-7b. Drag Data, δ -Sweep for 45% Chord Plain Flap, Hinge A-1

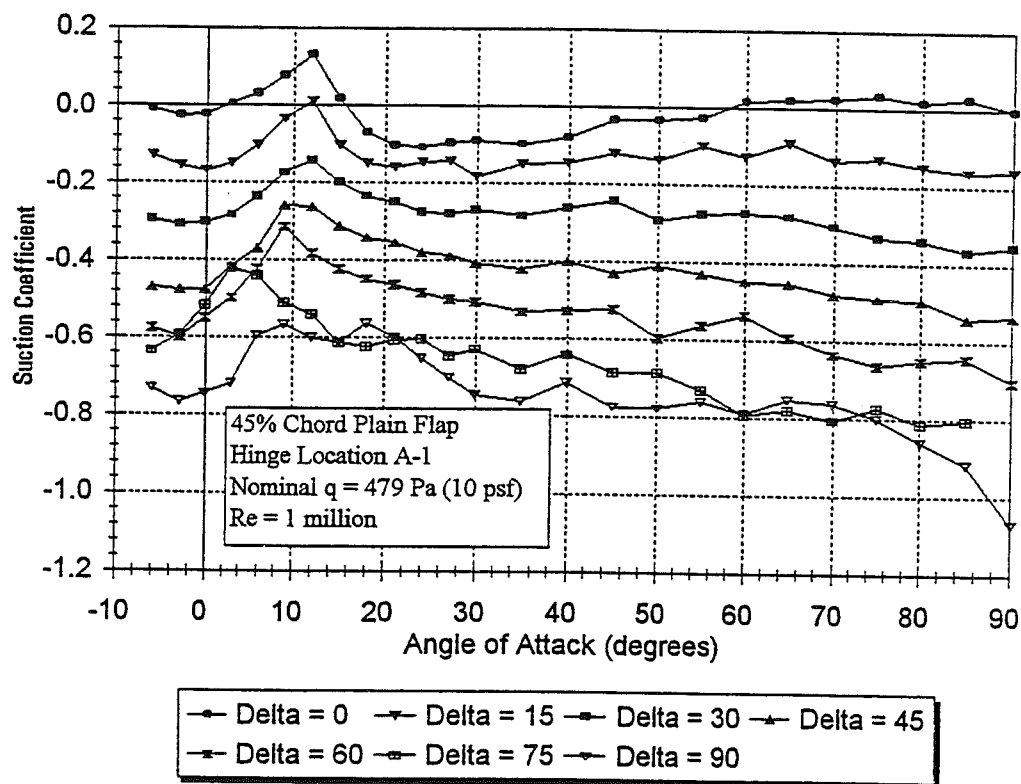


Figure A-7c. Suction Data, Δ -Sweep for 45% Chord Plain Flap, Hinge A-1

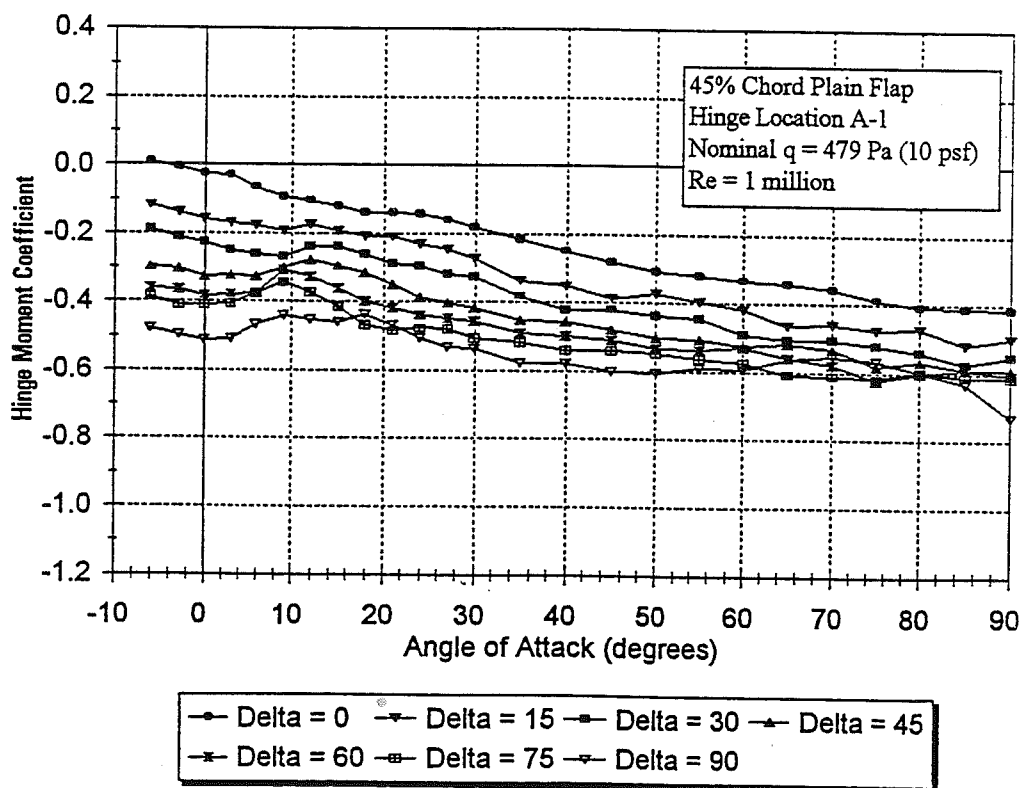


Figure A-7d. Hinge Moment Data, Δ -Sweep for 45% Chord Plain Flap, Hinge A-1

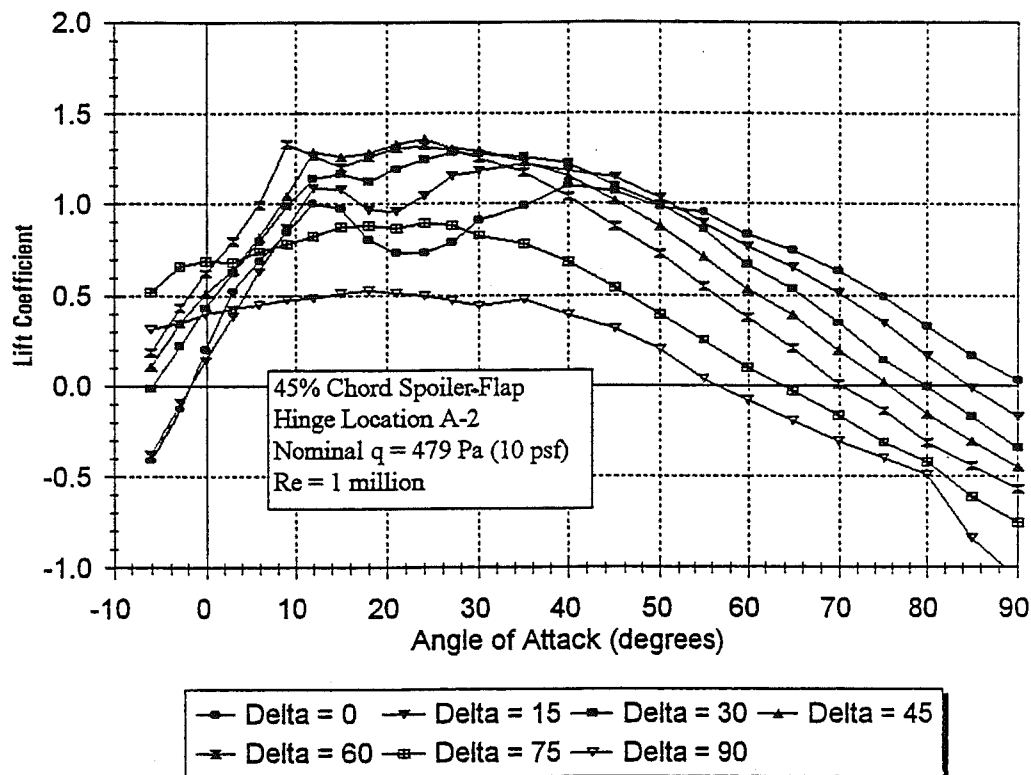


Figure A-8a. Lift Data, δ -Sweep for 45% Chord Spoiler-Flap, Hinge A-2

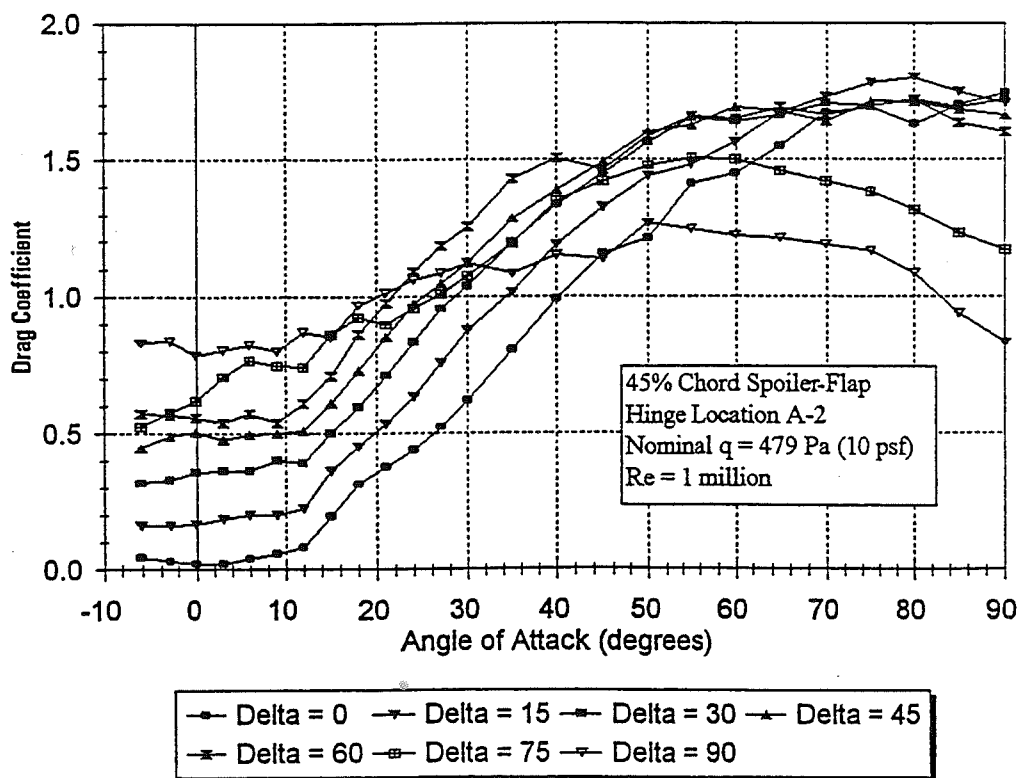


Figure A-8b. Drag Data, δ -Sweep for 45% Chord Spoiler-Flap, Hinge A-2

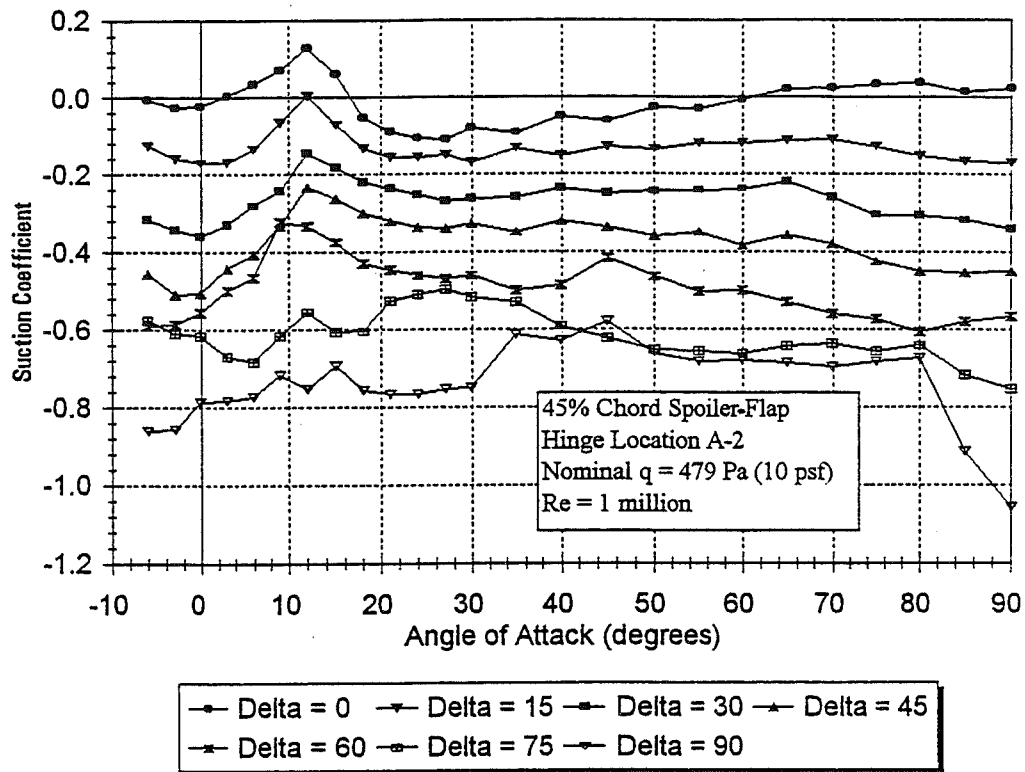


Figure A-8c. Suction Data, δ -Sweep for 45% Chord Spoiler-Flap, Hinge A-2

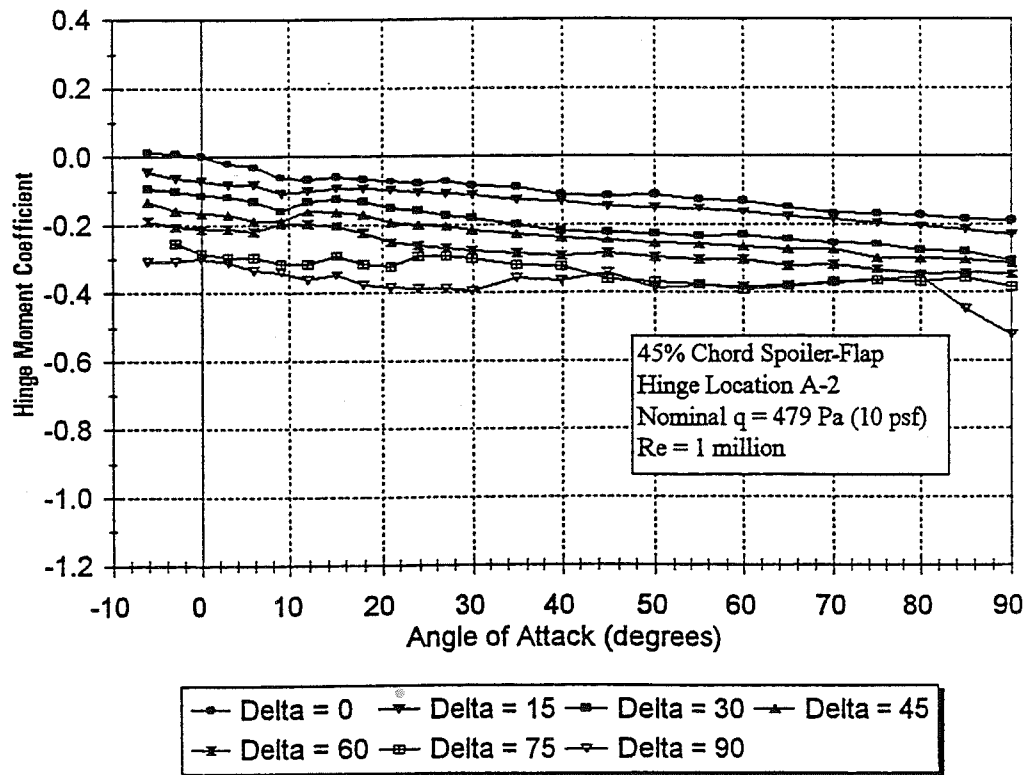


Figure A-8d. Hinge Moment Data, δ -Sweep for 45% Chord Spoiler-Flap, Hinge A-2

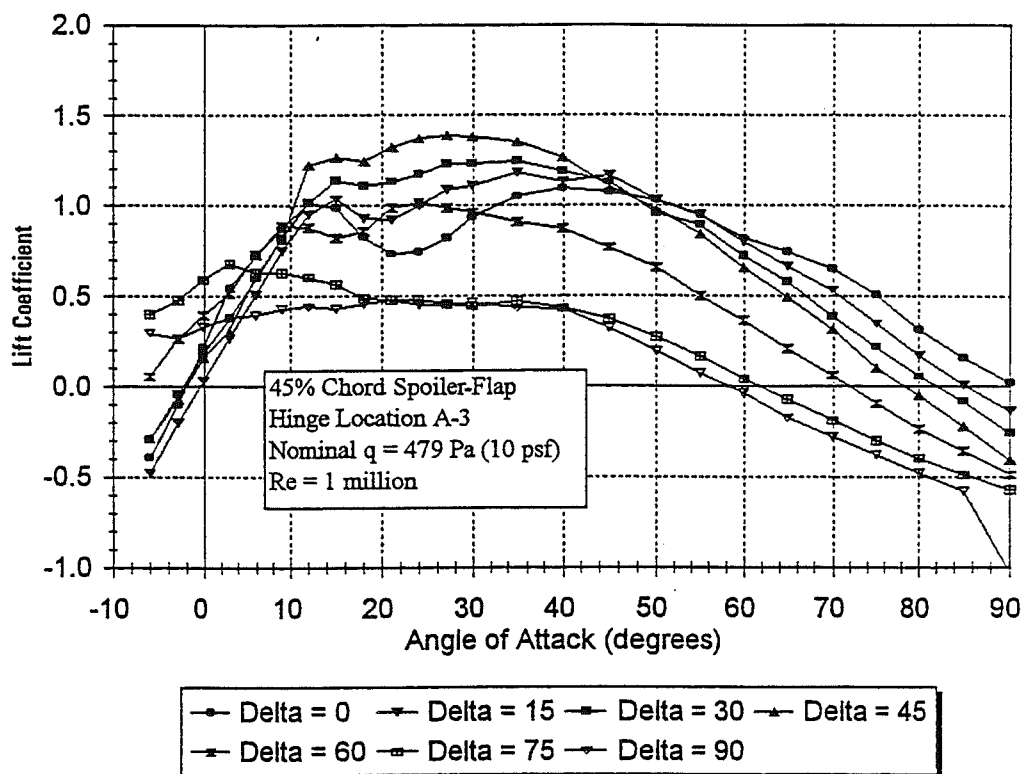


Figure A-9a. Lift Data, δ -Sweep for 45% Chord Spoiler-Flap, Hinge A-3

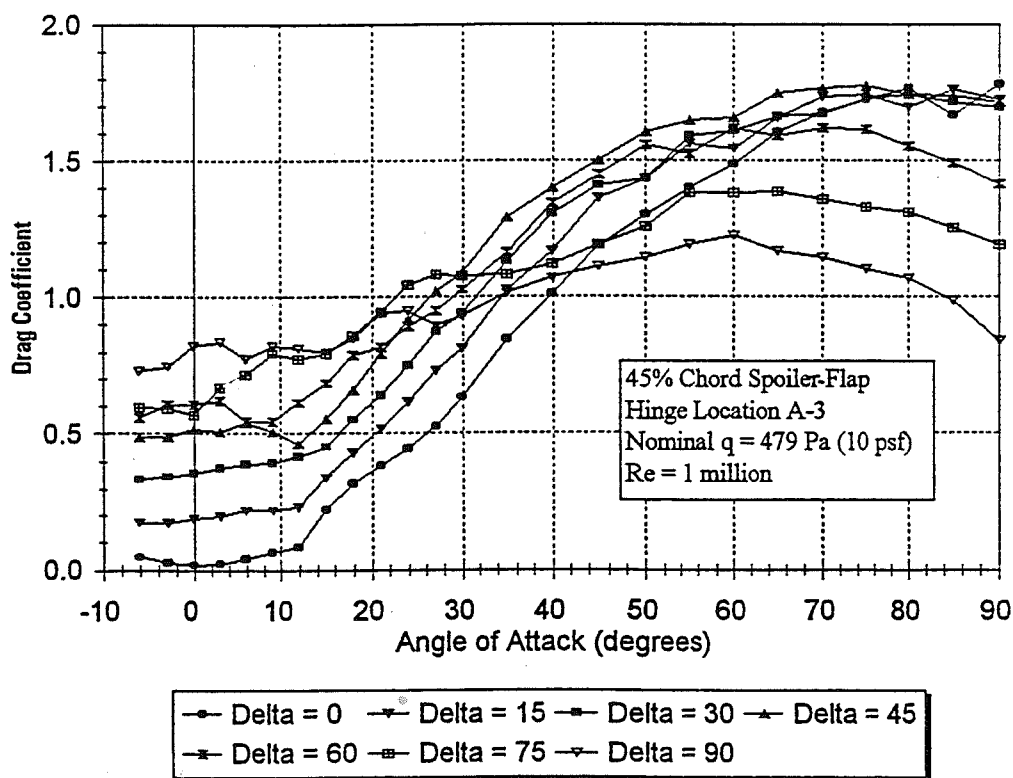


Figure A-9b. Drag Data, δ -Sweep for 45% Chord Spoiler-Flap, Hinge A-3

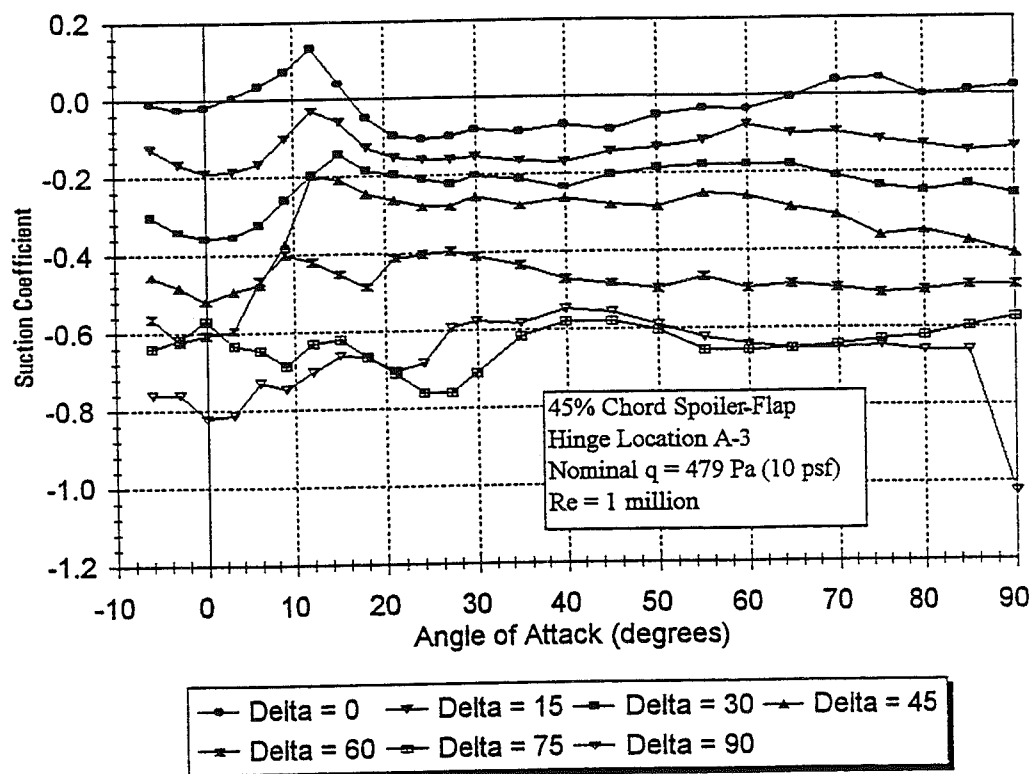


Figure A-9c. Suction Data, δ -Sweep for 45% Chord Spoiler-Flap, Hinge A-3

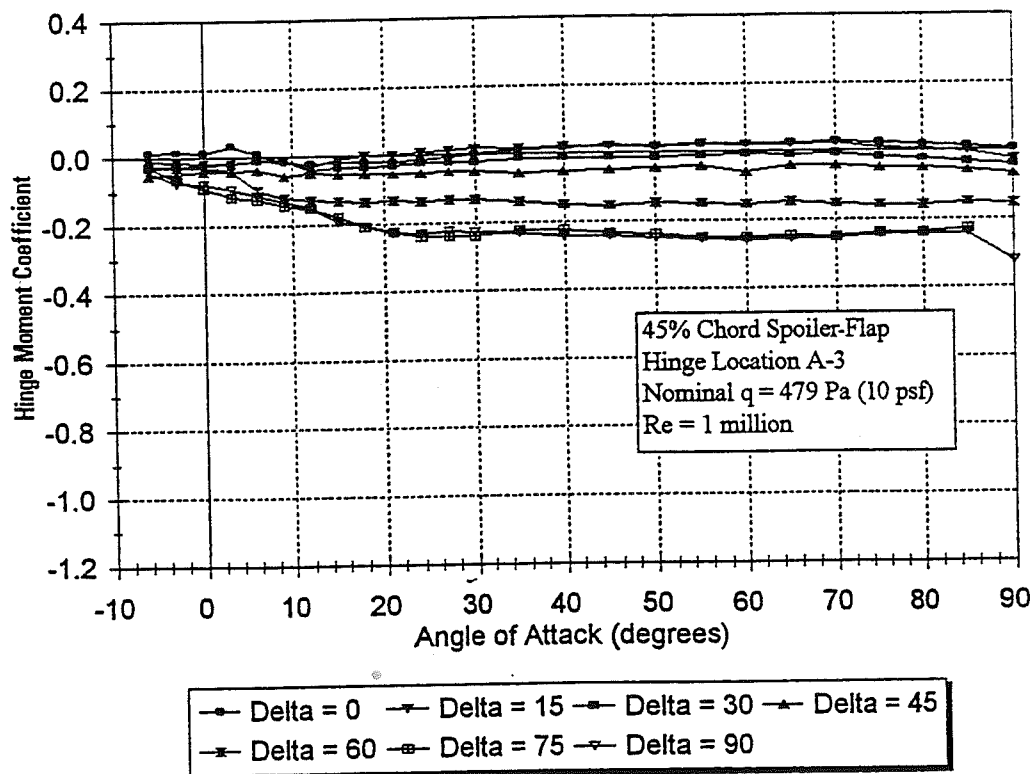


Figure A-9d. Hinge Moment Data, δ -Sweep for 45% Chord Spoiler-Flap, Hinge A-3

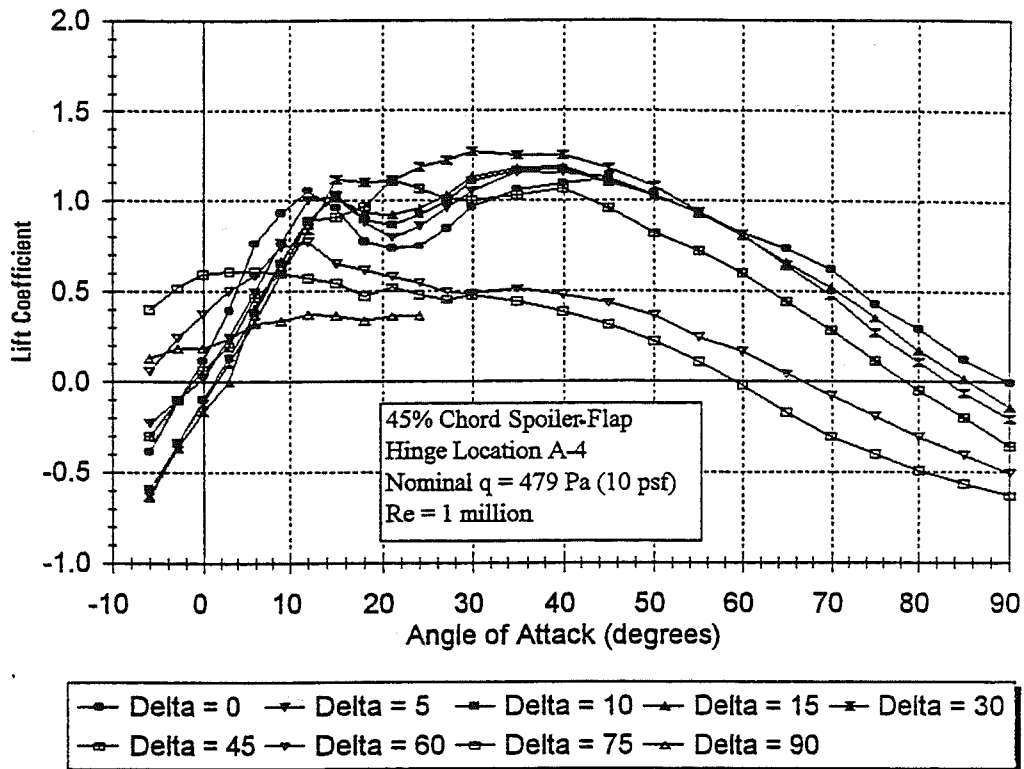


Figure A-10a. Lift Data, δ -Sweep for 45% Chord Spoiler-Flap, Hinge A-4

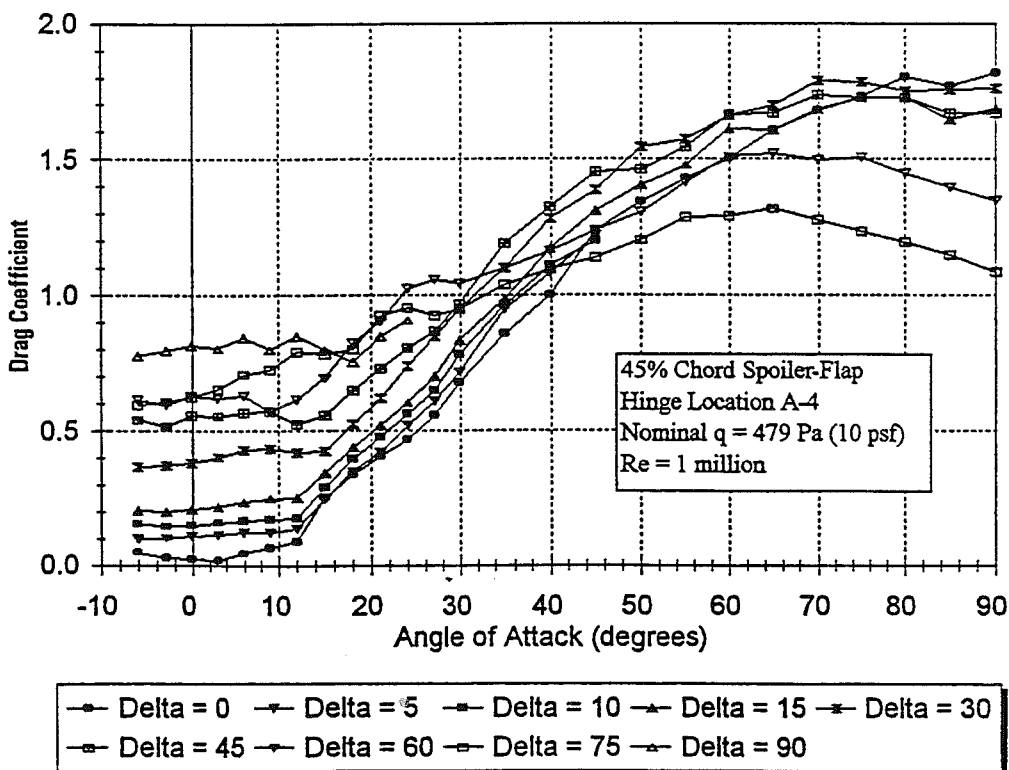


Figure A-10b. Drag Data, δ -Sweep for 45% Chord Spoiler-Flap, Hinge A-4

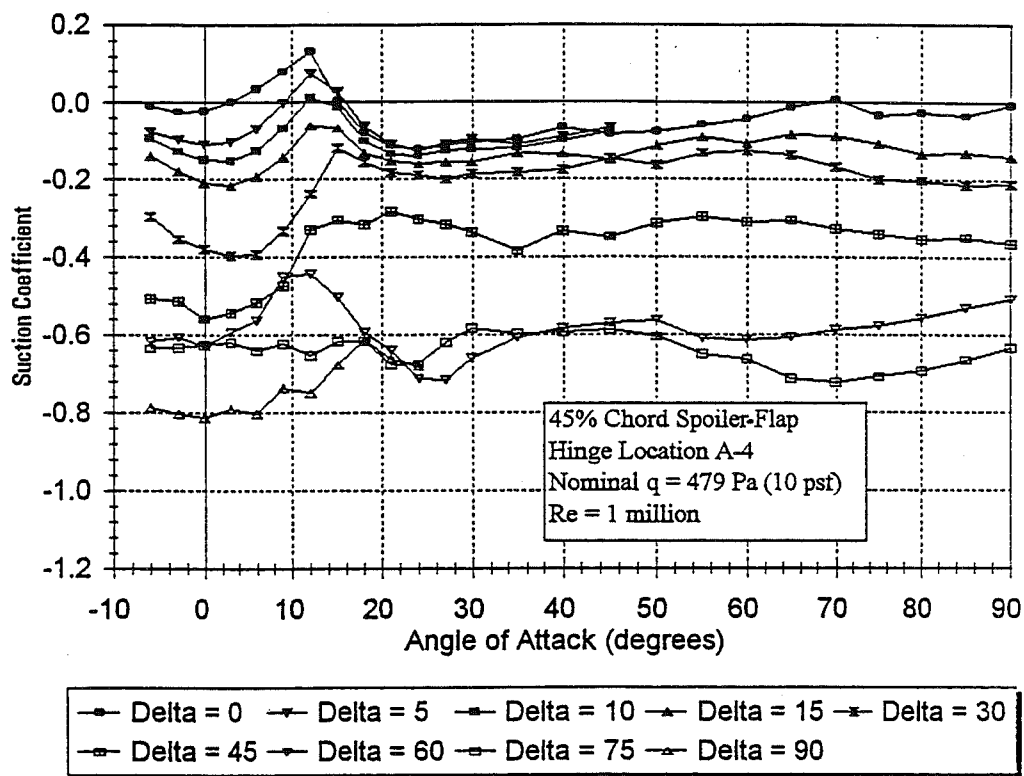


Figure A-10c. Suction Data, δ -Sweep for 45% Chord Spoiler-Flap, Hinge A-4

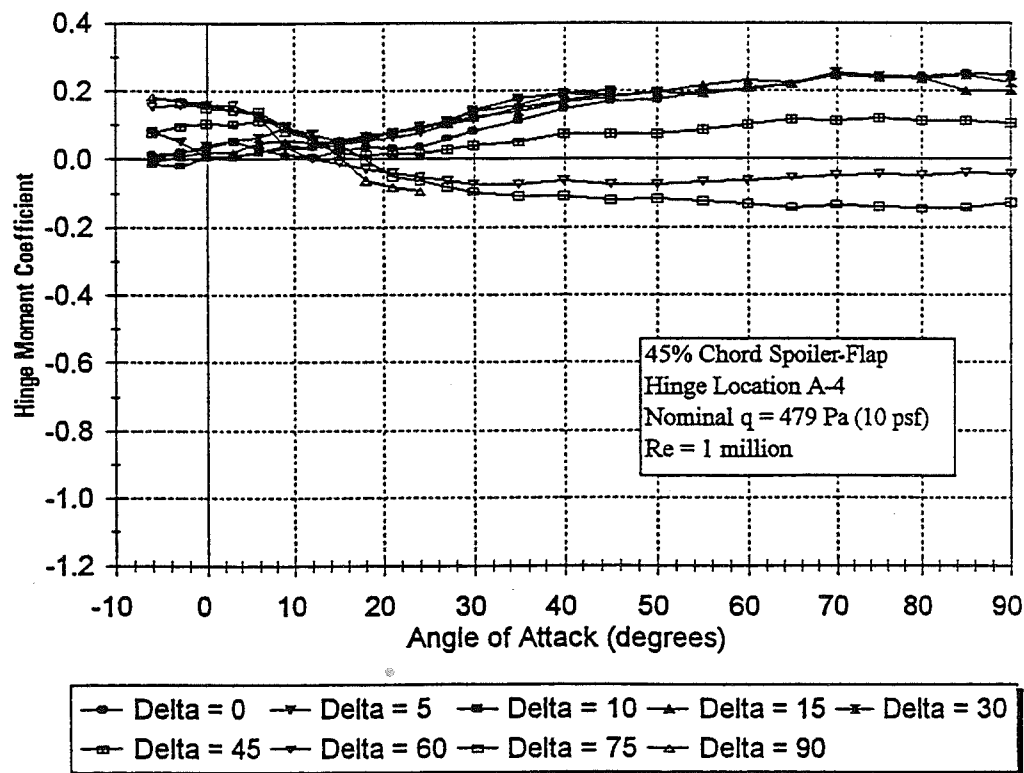


Figure A-10d. Hinge Moment Data, δ -Sweep for 45% Chord Spoiler-Flap, Hinge A-4

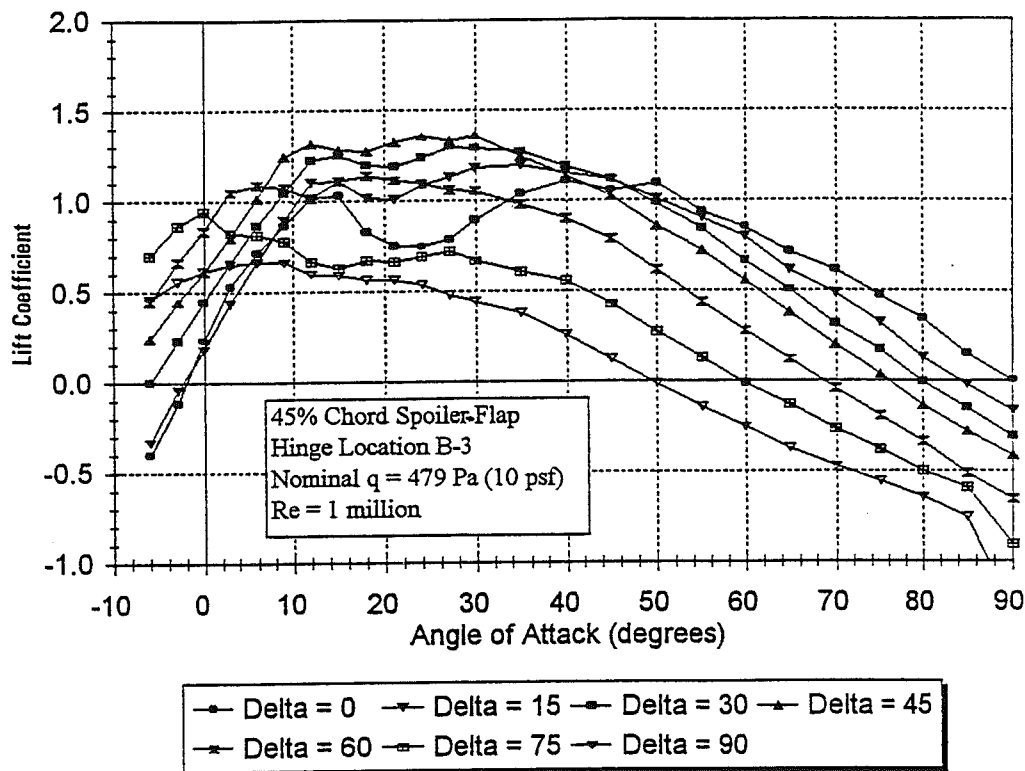


Figure A-11a. Lift Data, δ -Sweep for 45% Chord Spoiler-Flap, Hinge B-3

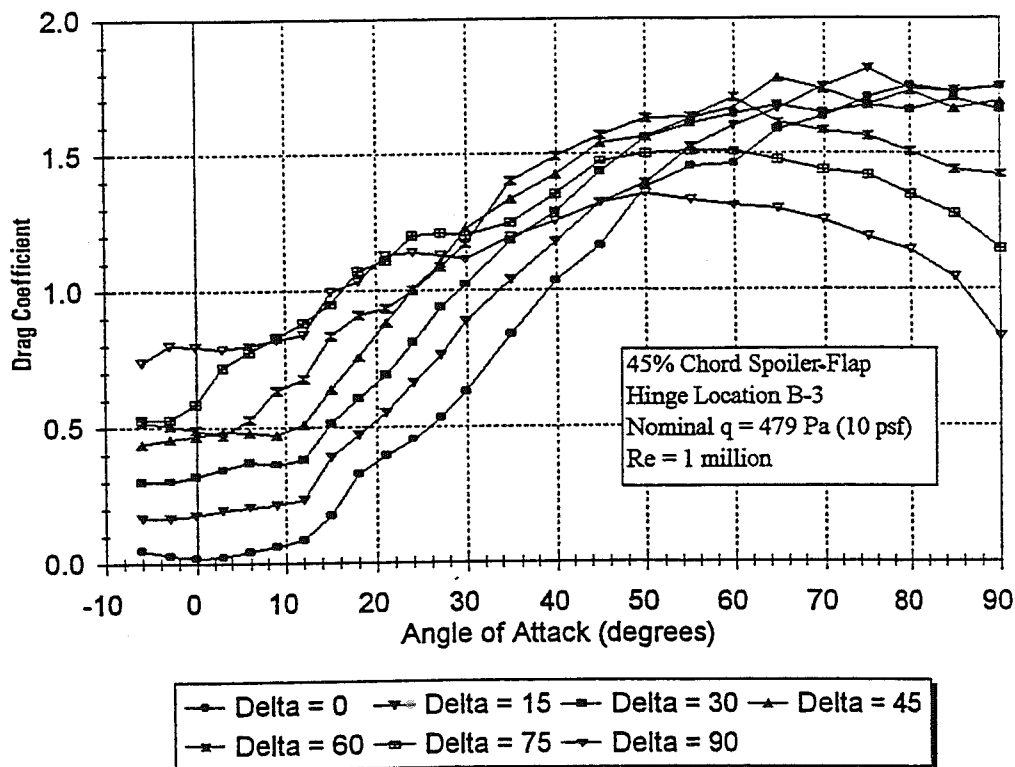


Figure A-11b. Drag Data, δ -Sweep for 45% Chord Spoiler-Flap, Hinge B-3

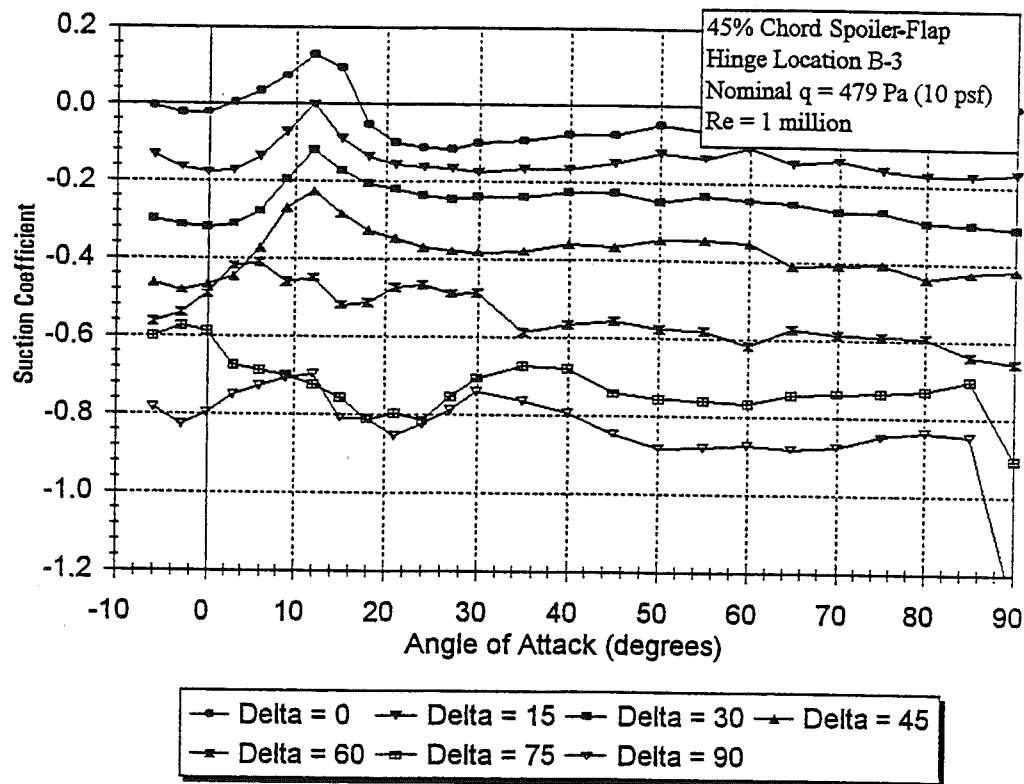


Figure A-11c. Suction Data, δ -Sweep for 45% Chord Spoiler-Flap, Hinge B-3

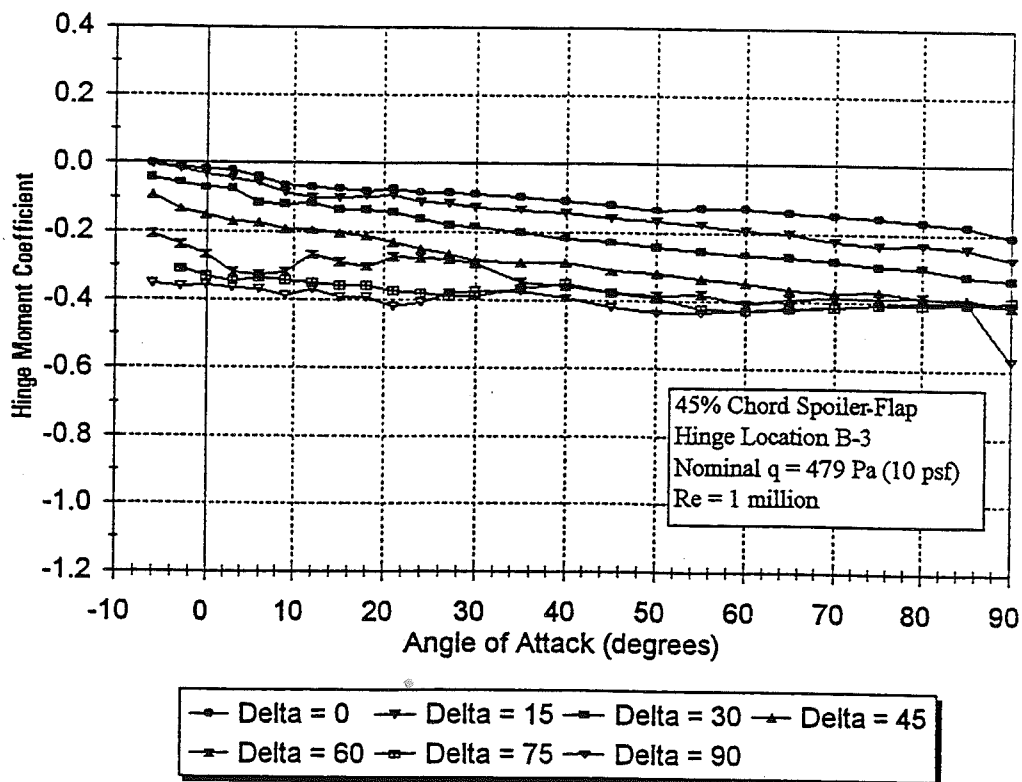


Figure A-11d. Hinge Moment Data, δ -Sweep for 45% Chord Spoiler-Flap, Hinge B-3

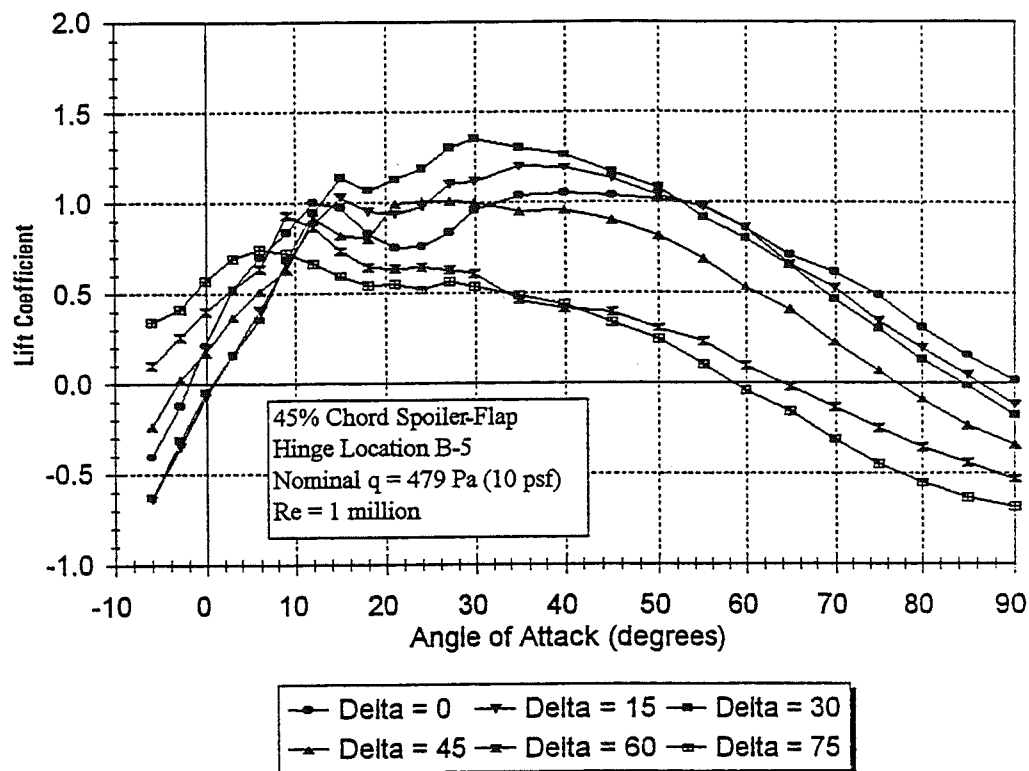


Figure A-12a. Lift Data, δ -Sweep for 45% Chord Spoiler-Flap, Hinge B-5

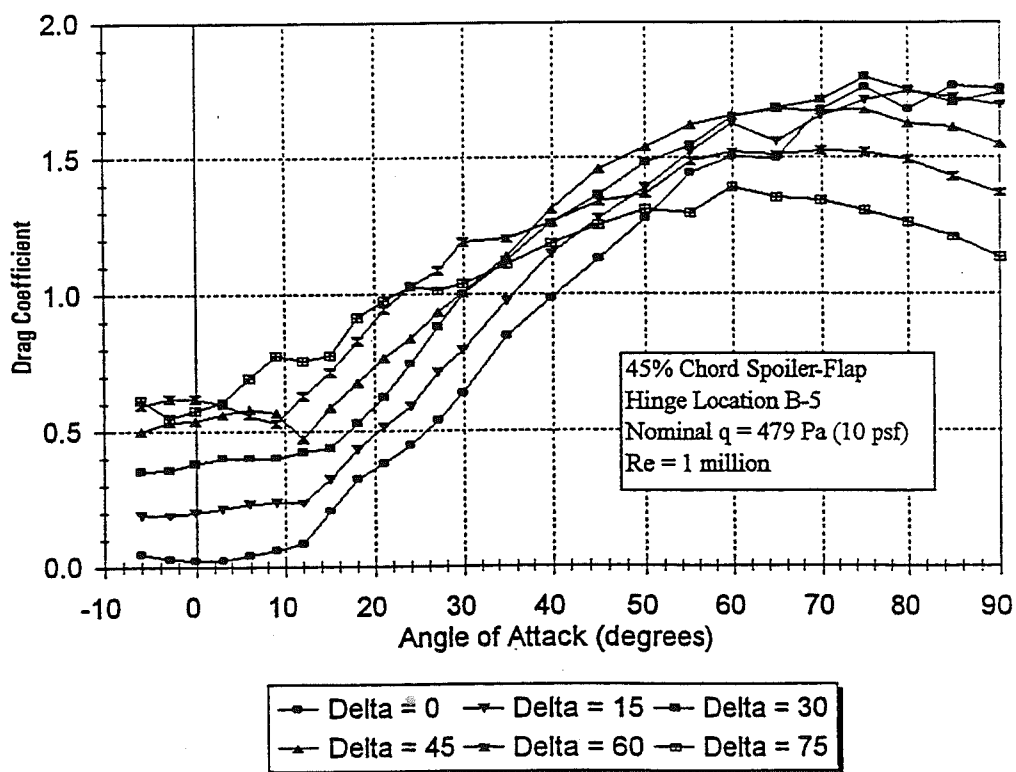


Figure A-12b. Drag Data, δ -Sweep for 45% Chord Spoiler-Flap, Hinge B-5

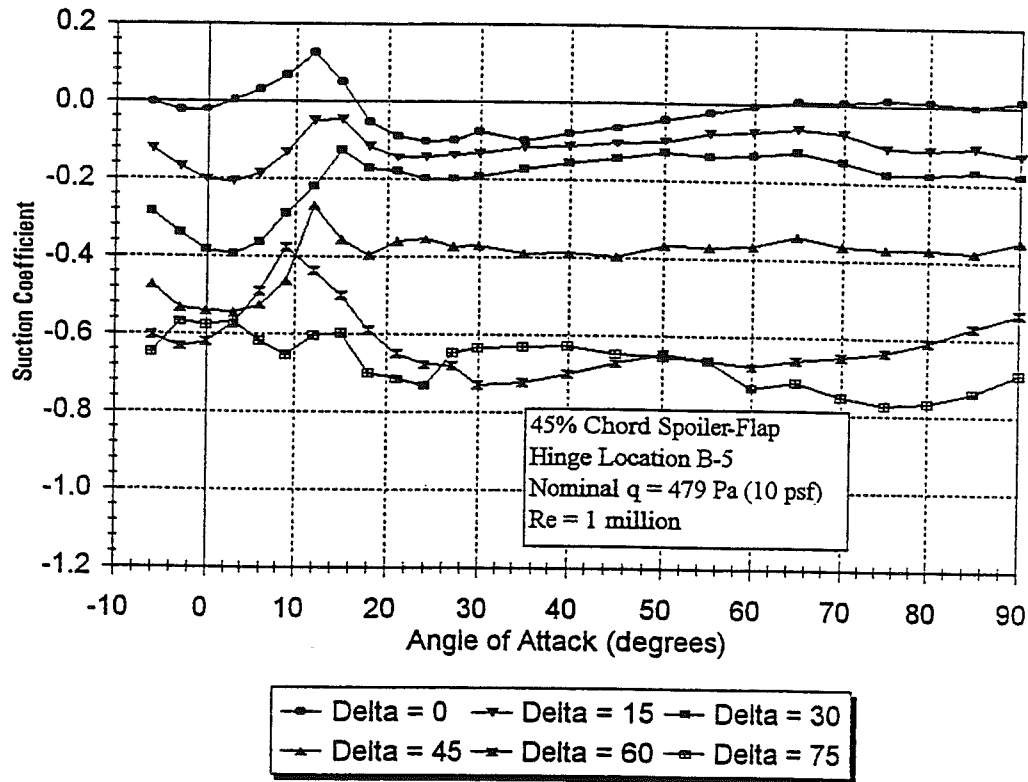


Figure A-12c. Suction Data, Δ -Sweep for 45% Chord Spoiler-Flap, Hinge B-5

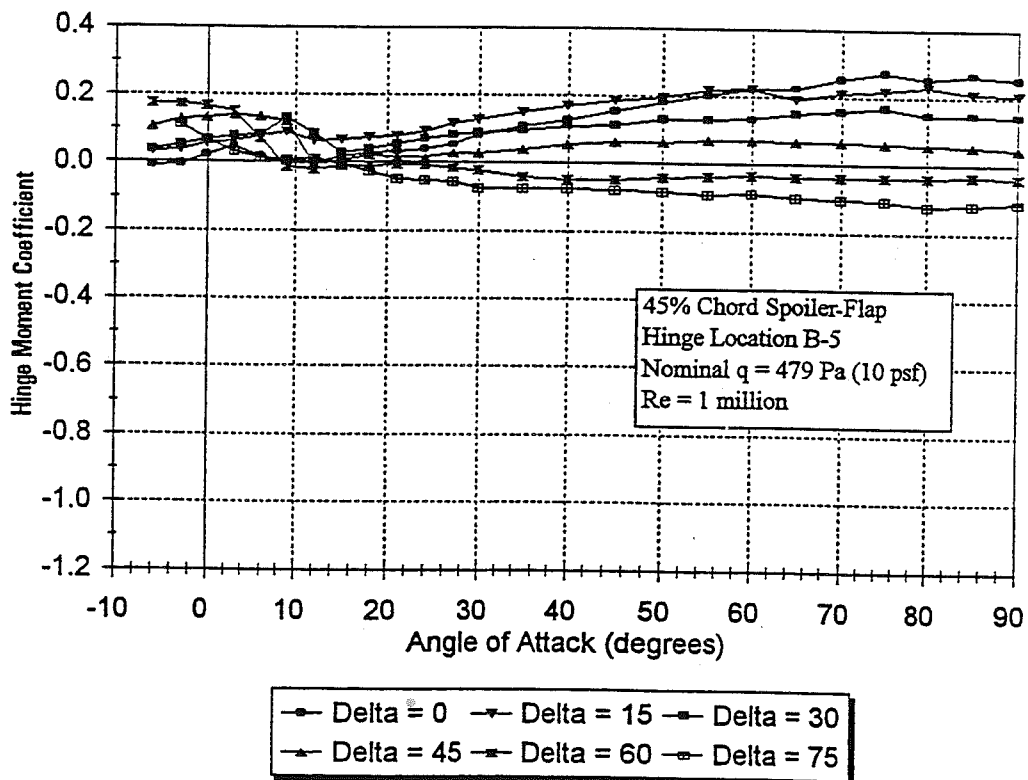


Figure A-12d. Hinge Moment Data, Δ -Sweep for 45% Chord Spoiler-Flap, Hinge B-5

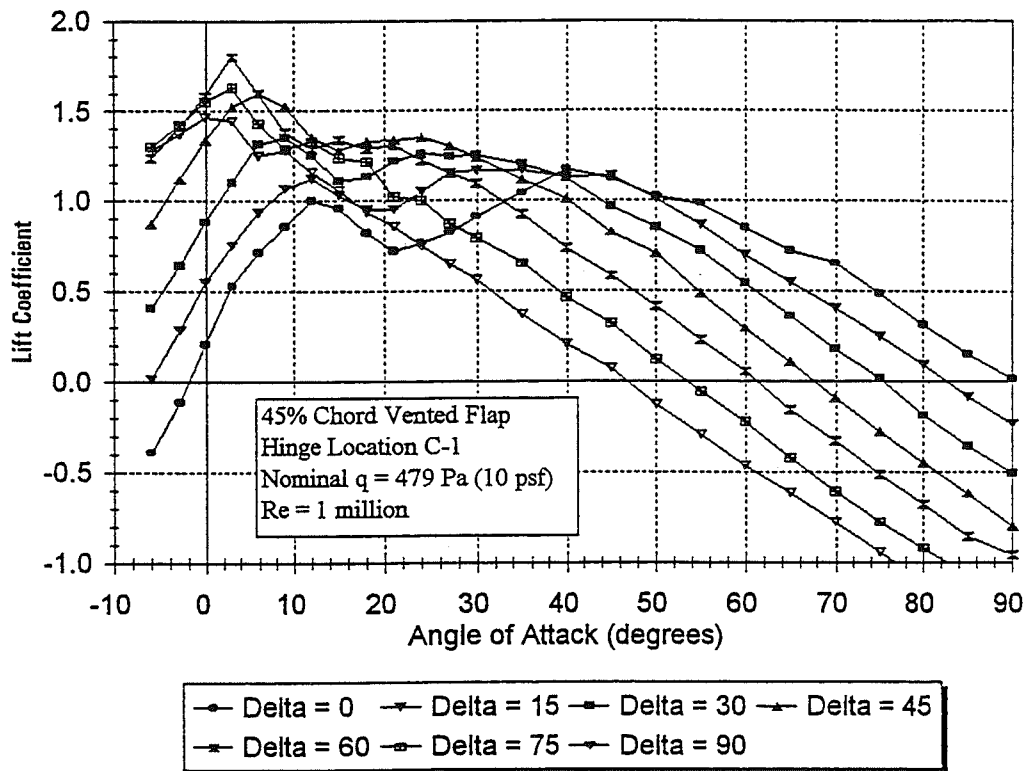


Figure A-13a. Lift Data, δ -Sweep for 45% Chord Vented Flap, Hinge C-1

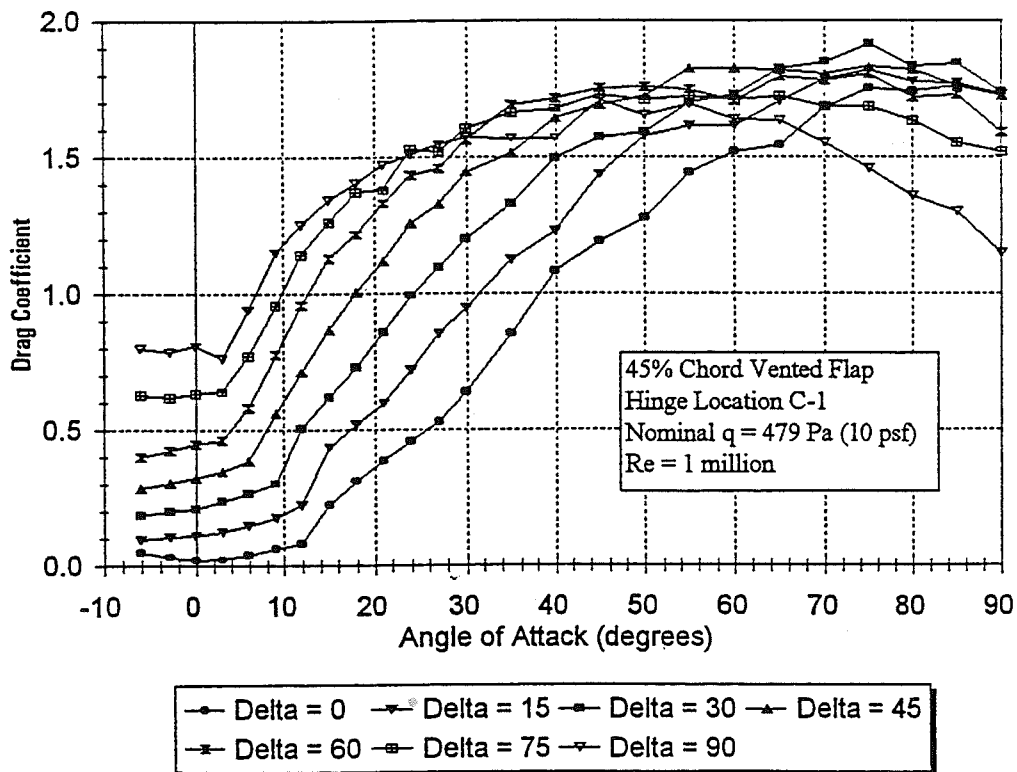


Figure A-13b. Drag Data, δ -Sweep for 45% Chord Vented Flap, Hinge C-1

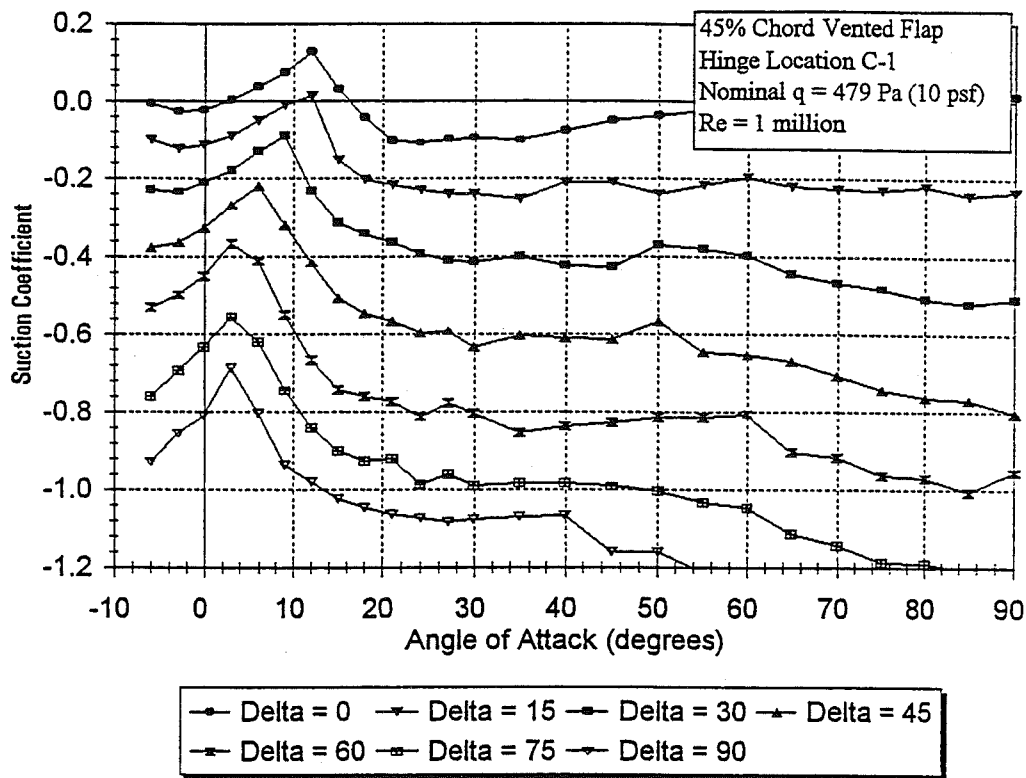


Figure A-13c. Suction Data, δ -Sweep for 45% Chord Vented Flap, Hinge C-1

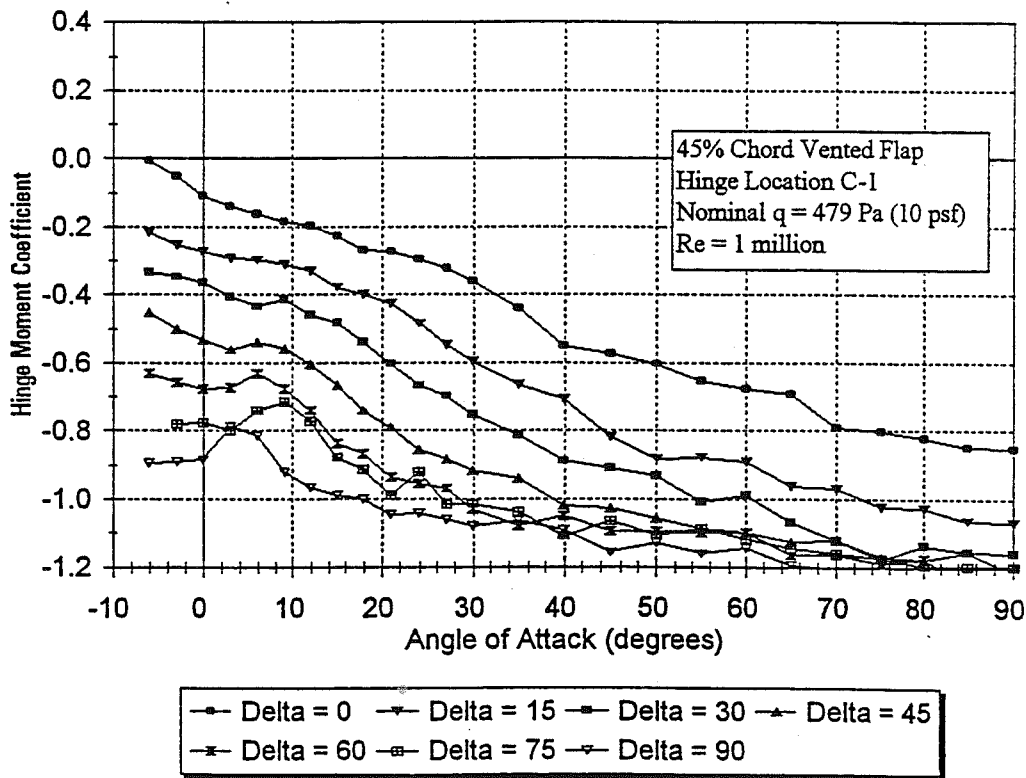


Figure A-13d. Hinge Moment Data, δ -Sweep for 45% Chord Vented Flap, Hinge C-1

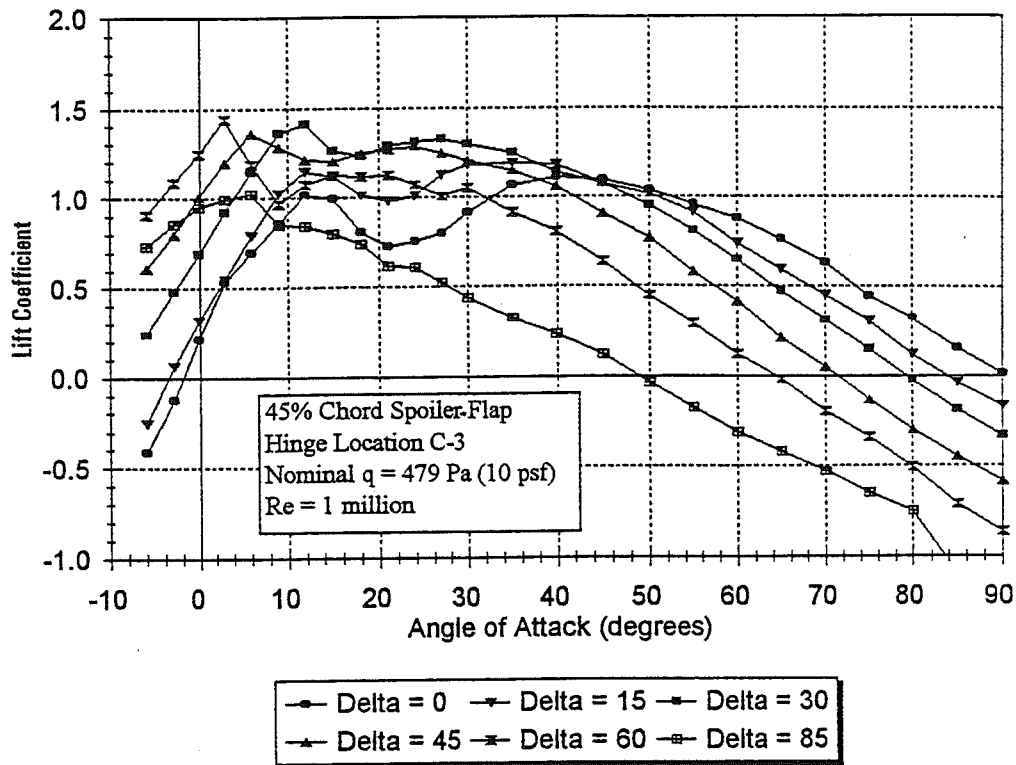


Figure A-14a. Lift Data, δ -Sweep for 45% Chord Spoiler-Flap, Hinge C-3

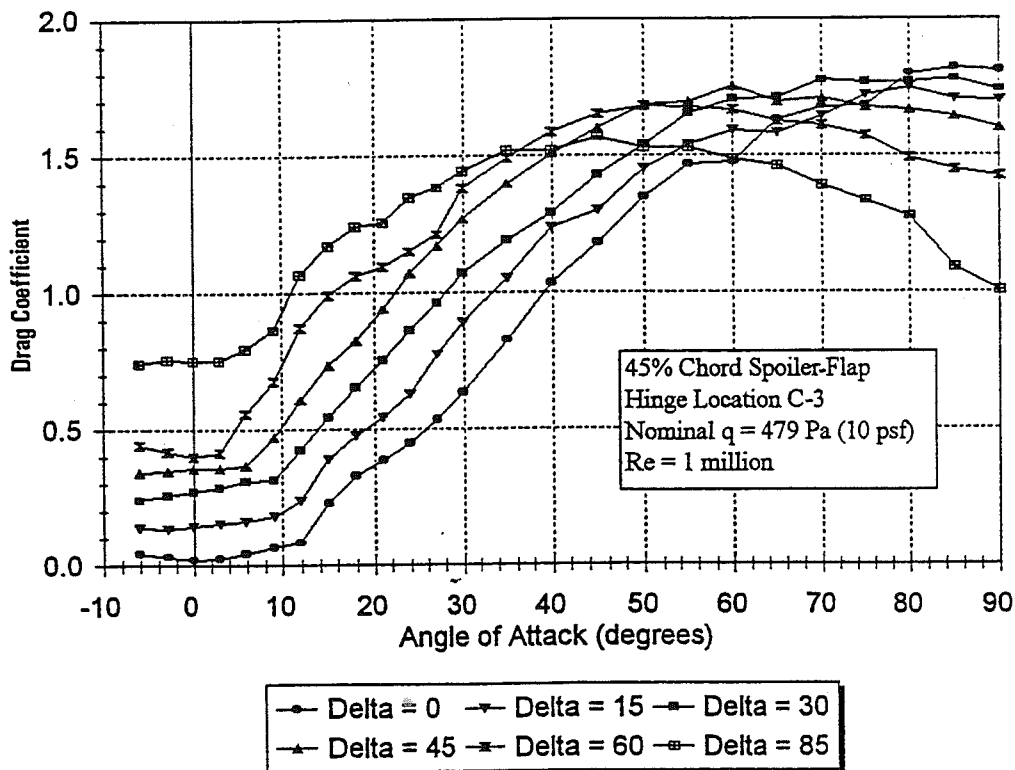


Figure A-14b. Drag Data, δ -Sweep for 45% Chord Spoiler-Flap, Hinge C-3

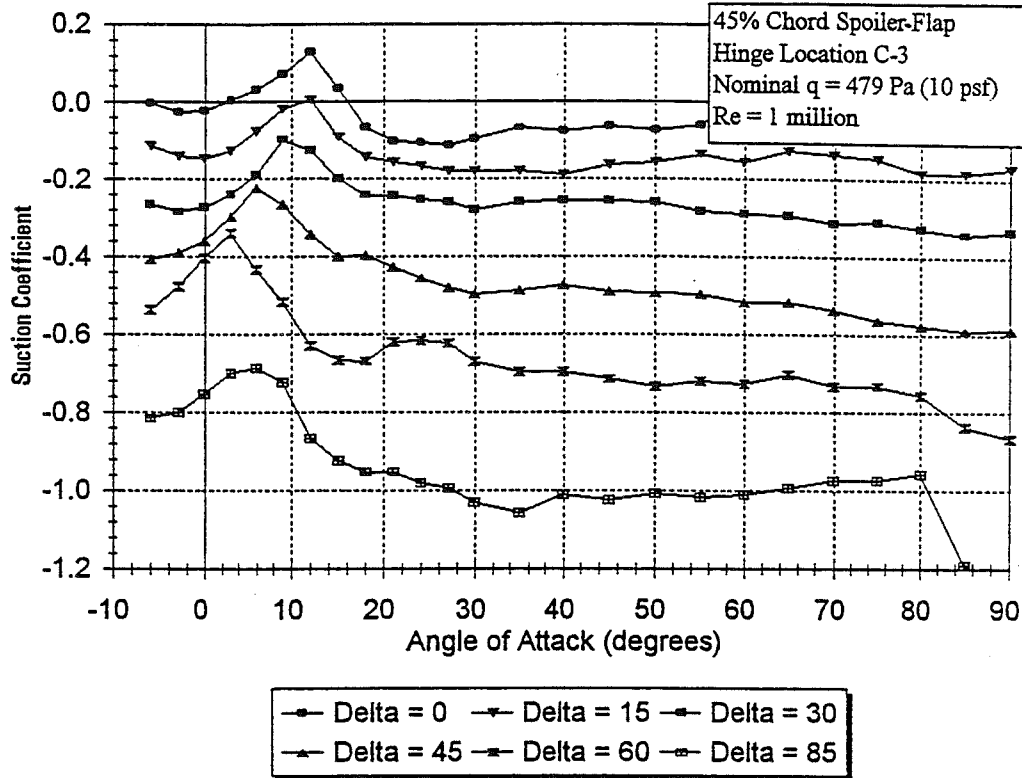


Figure A-14c. Suction Data, δ -Sweep for 45% Chord Spoiler-Flap, Hinge C-3

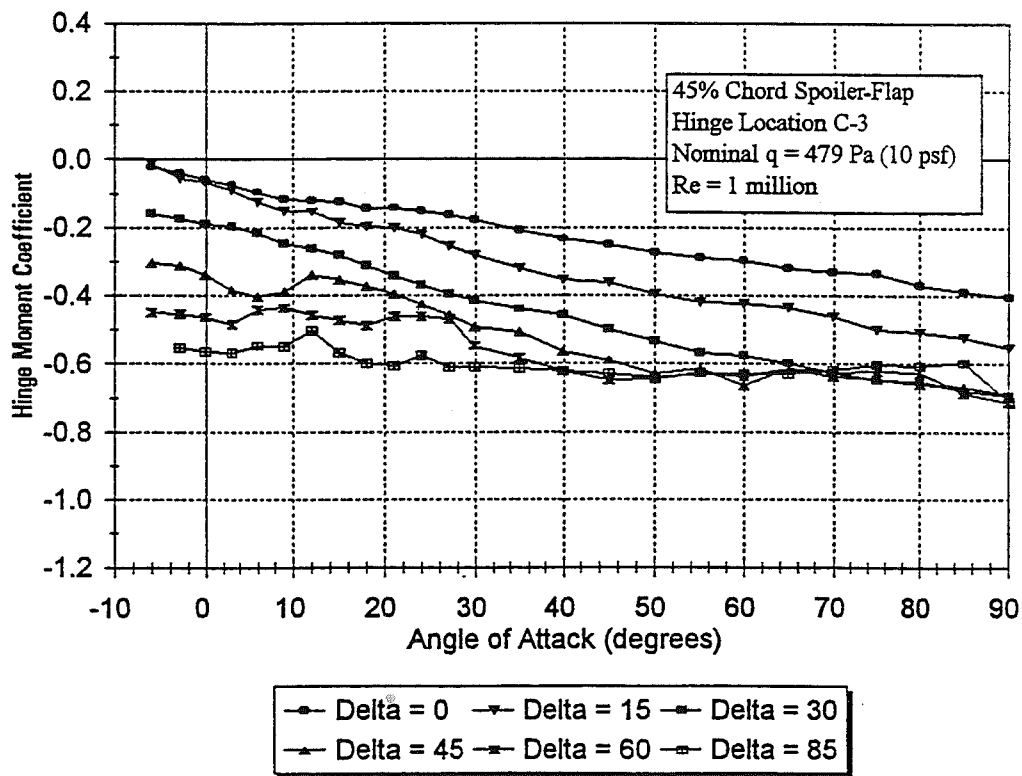
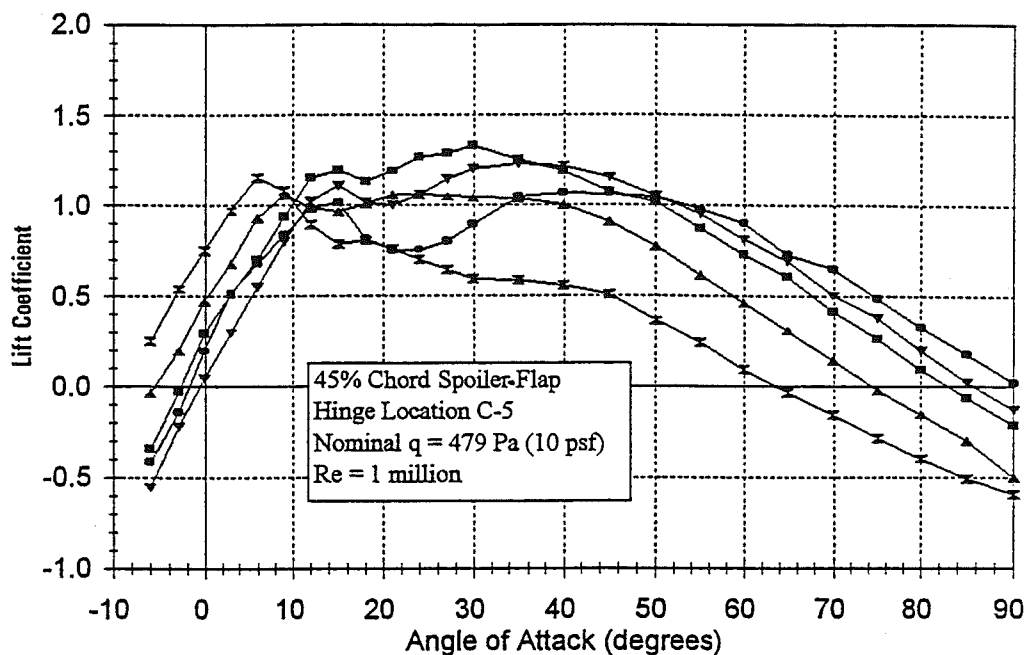
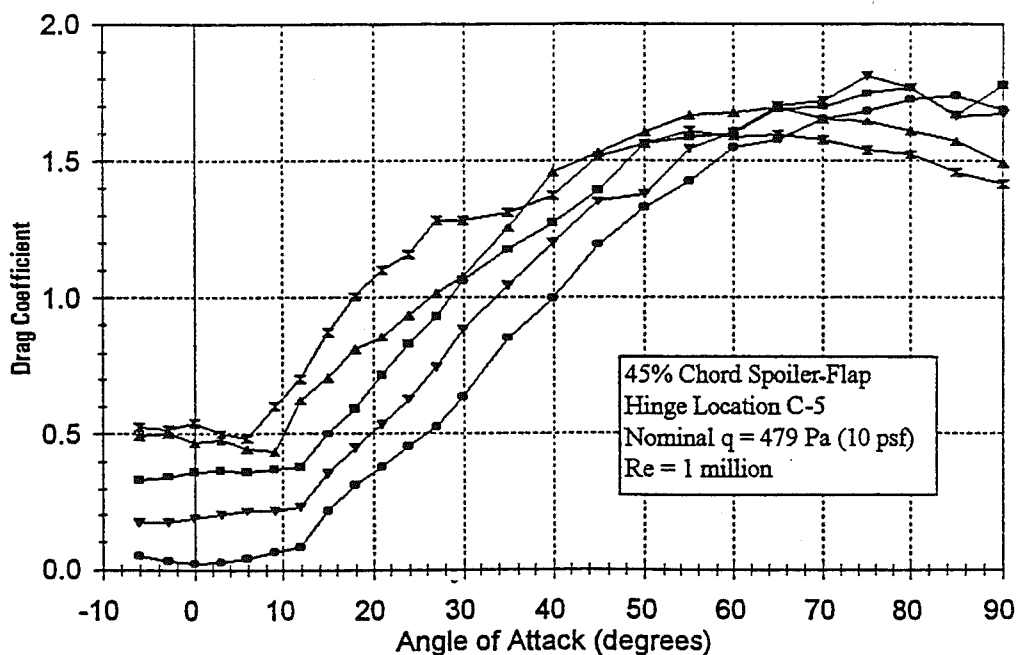


Figure A-14d. Hinge Moment Data, δ -Sweep for 45% Chord Spoiler-Flap, Hinge C-3



— Delta = 0 — Delta = 15 — Delta = 30 — Delta = 45 — Delta = 60

Figure A-15a. Lift Data, δ -Sweep for 45% Chord Spoiler-Flap, Hinge C-5



— Delta = 0 — Delta = 15 — Delta = 30 — Delta = 45 — Delta = 60

Figure A-15b. Drag Data, δ -Sweep for 45% Chord Spoiler-Flap, Hinge C-5

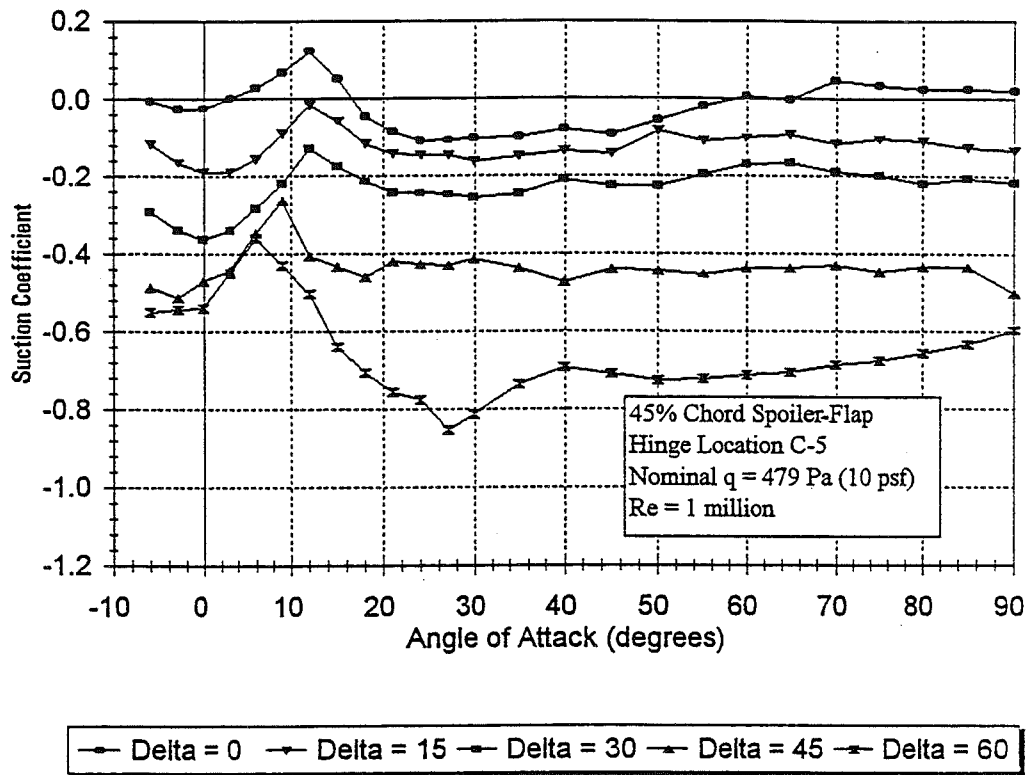


Figure A-15c. Suction Data, δ -Sweep for 45% Chord Spoiler-Flap, Hinge C-5

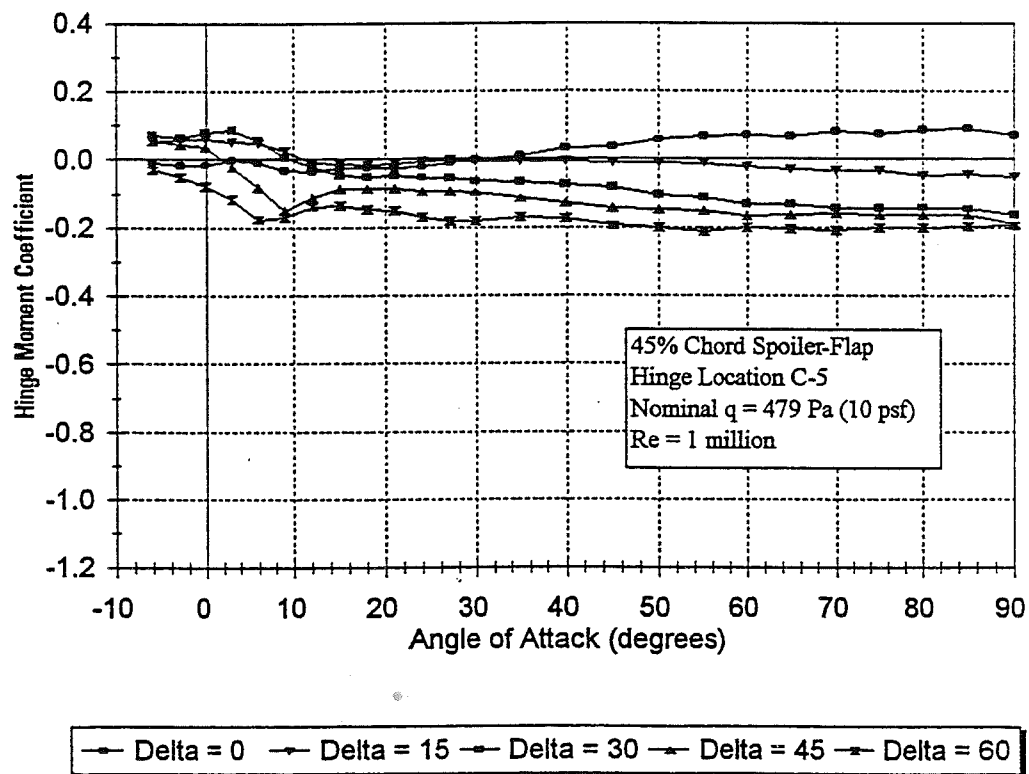


Figure A-15d. Hinge Moment Data, δ -Sweep for 45% Chord Spoiler-Flap, Hinge C-5

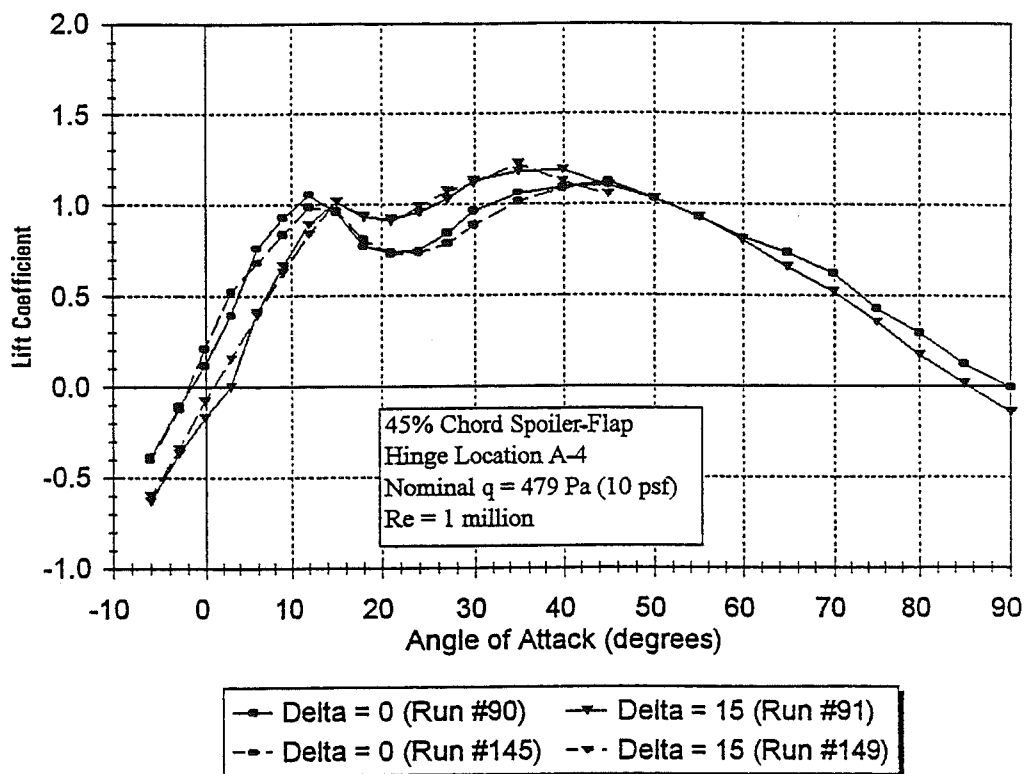


Figure A-16a. Lift Data, Repeatability Check on Spoiler-Flap

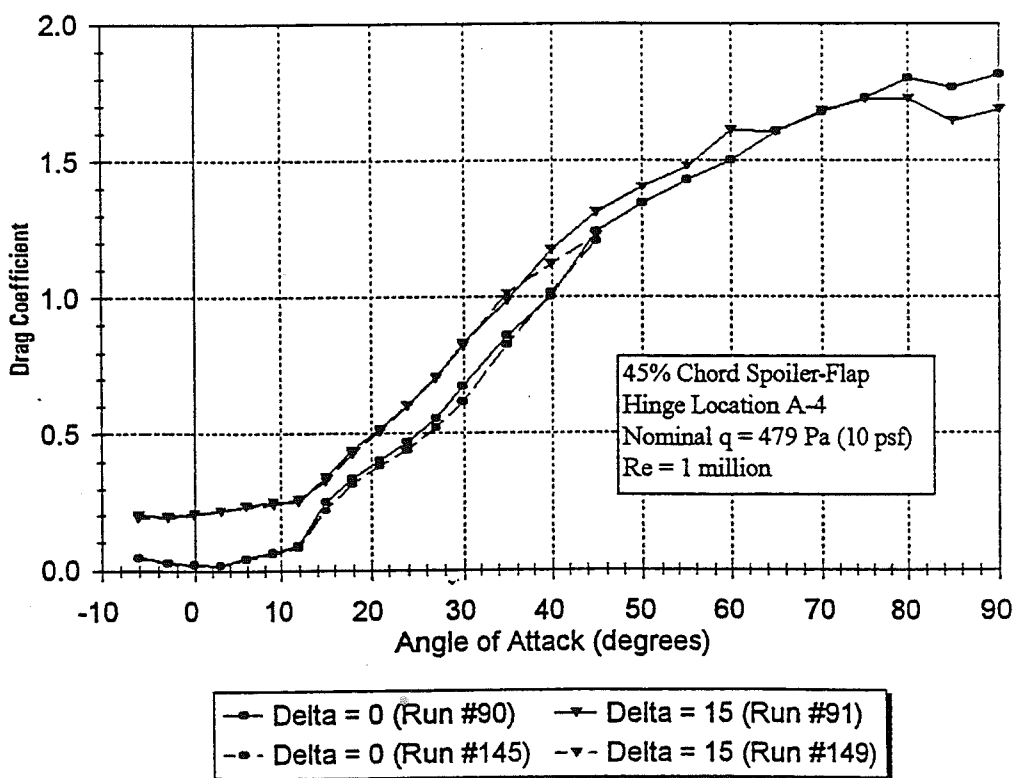


Figure A-16b. Drag Data, Repeatability Check on Spoiler-Flap

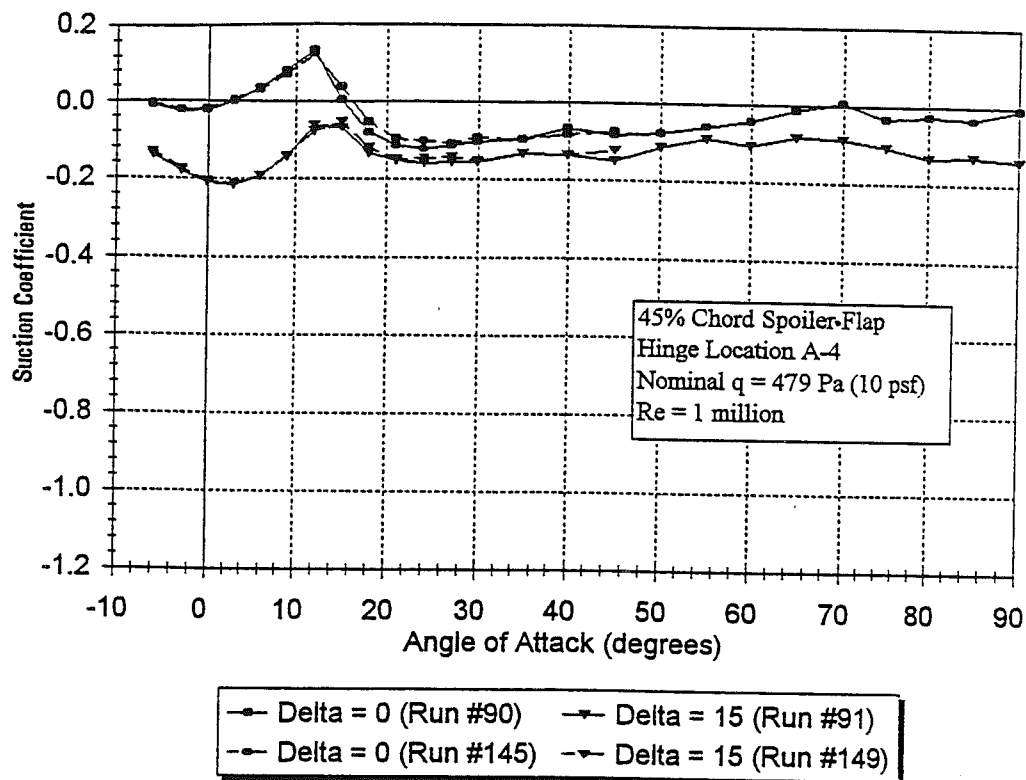


Figure A-16c. Suction Data, Repeatability Check on Spoiler-Flap

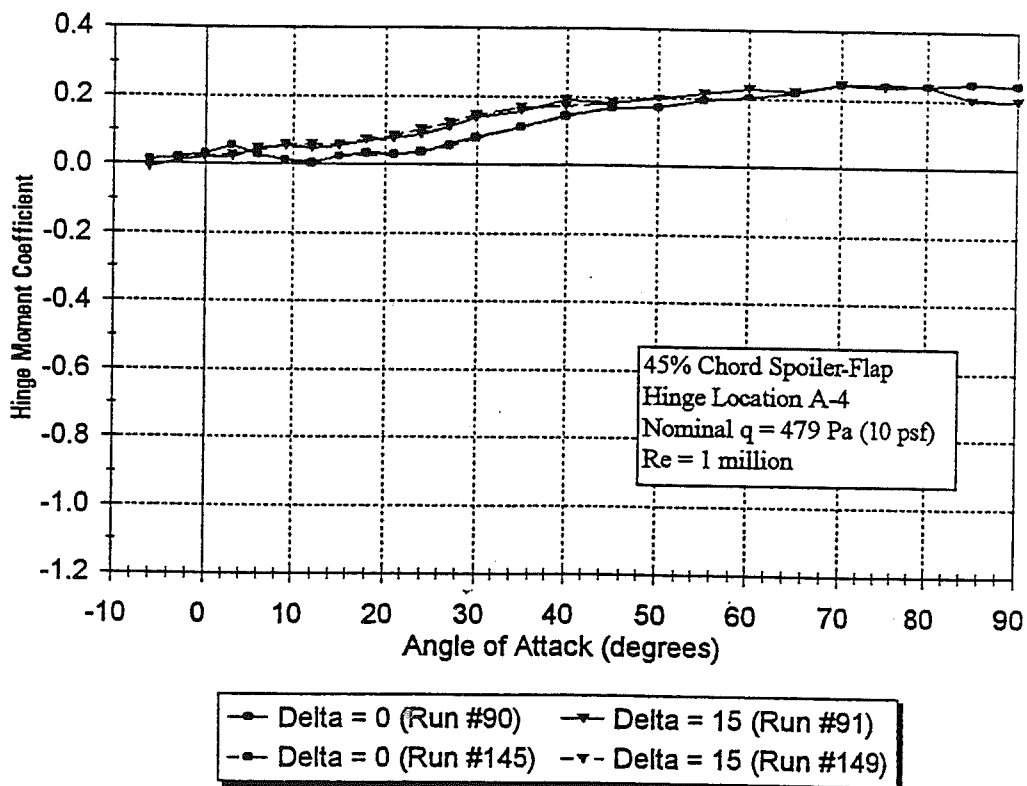


Figure A-16d. Hinge Moment Data, Repeatability Check on Spoiler-Flap

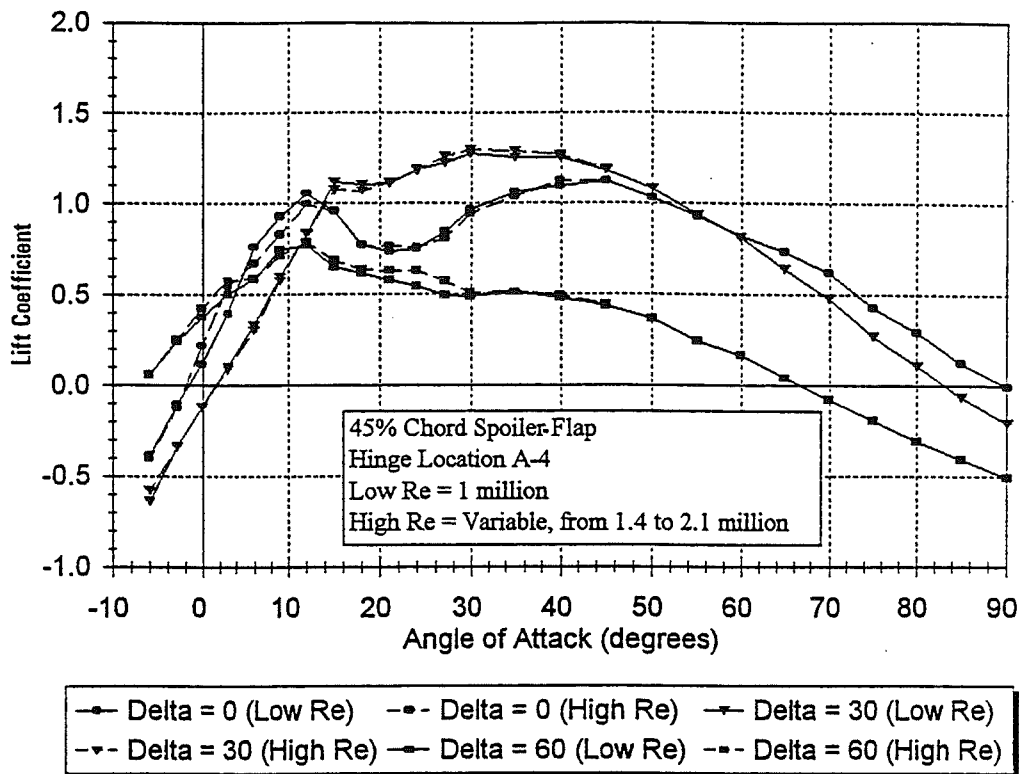


Figure A-17a. Lift Data, Reynolds Number Effect on Spoiler-Flap

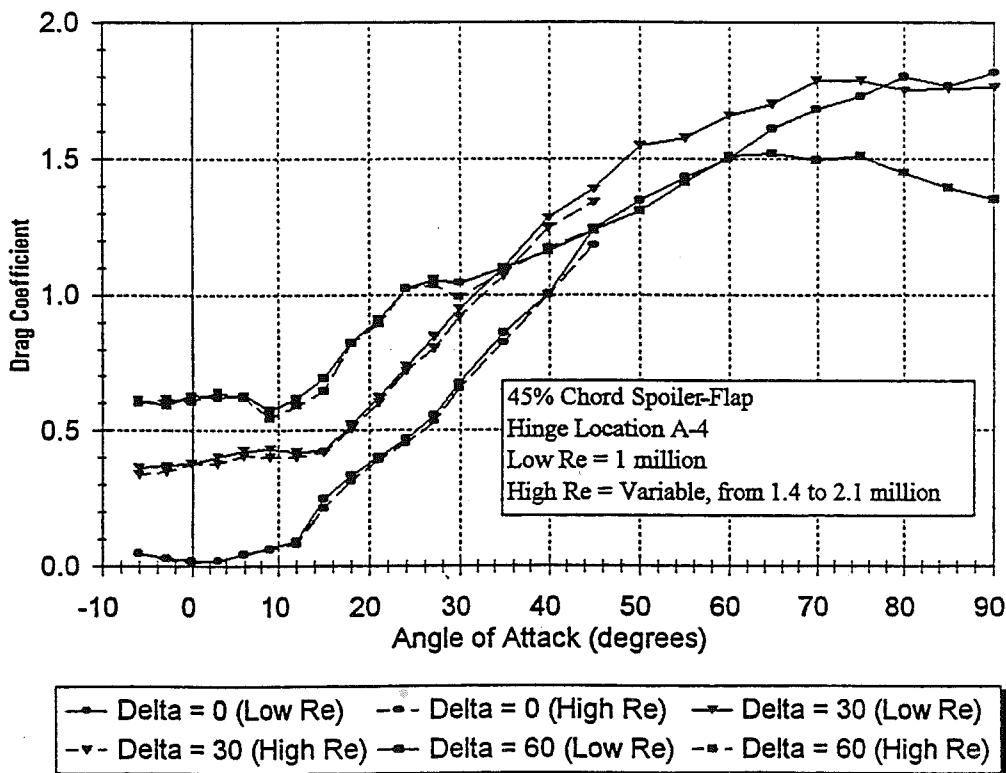


Figure A-17b. Drag Data, Reynolds Number Effect on Spoiler-Flap

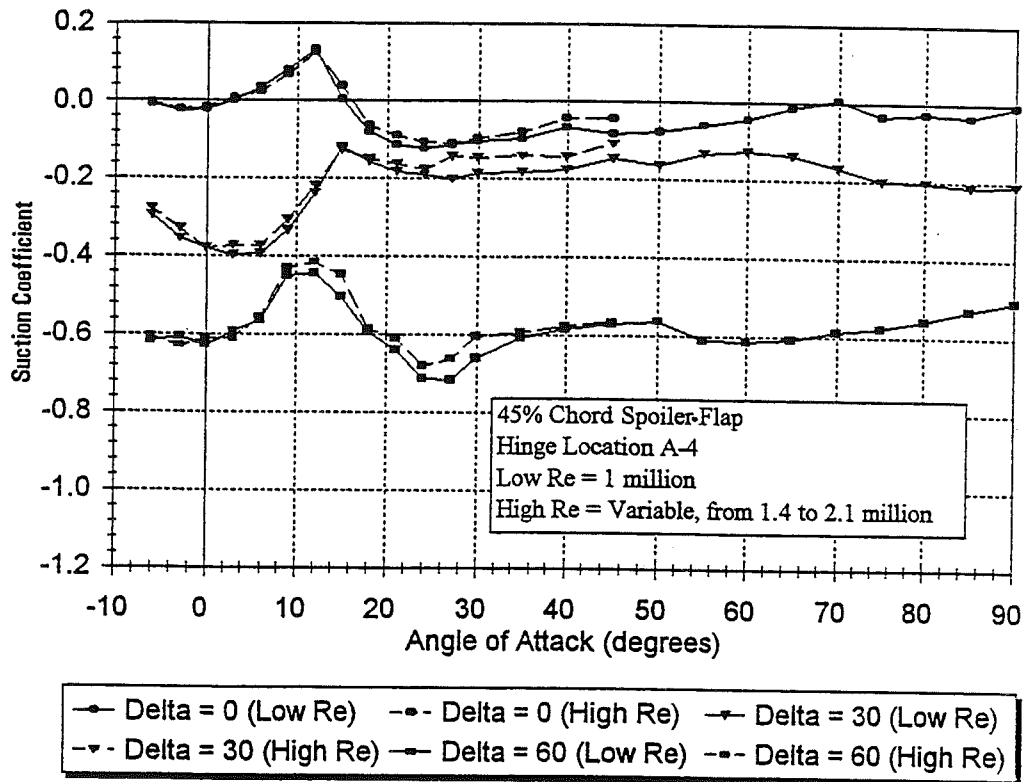


Figure A-17c. Suction Data, Reynolds Number Effect on Spoiler-Flap

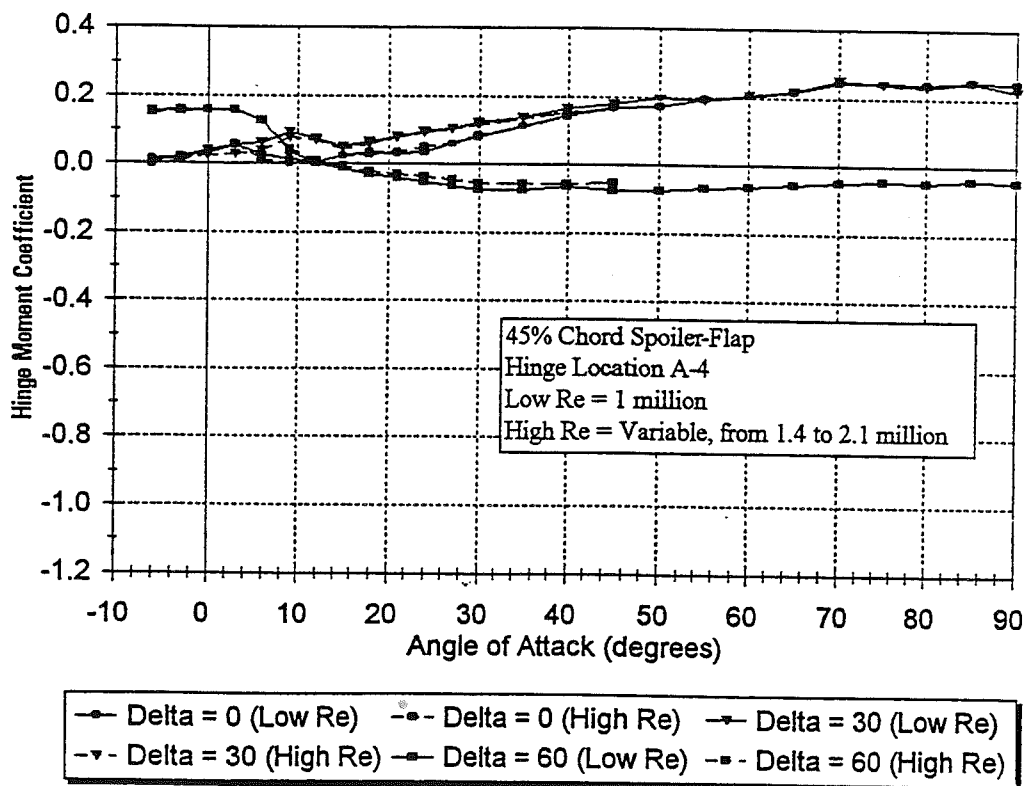


Figure A-17d. Hinge Moment Data, Reynolds Number Effect on Spoiler-Flap

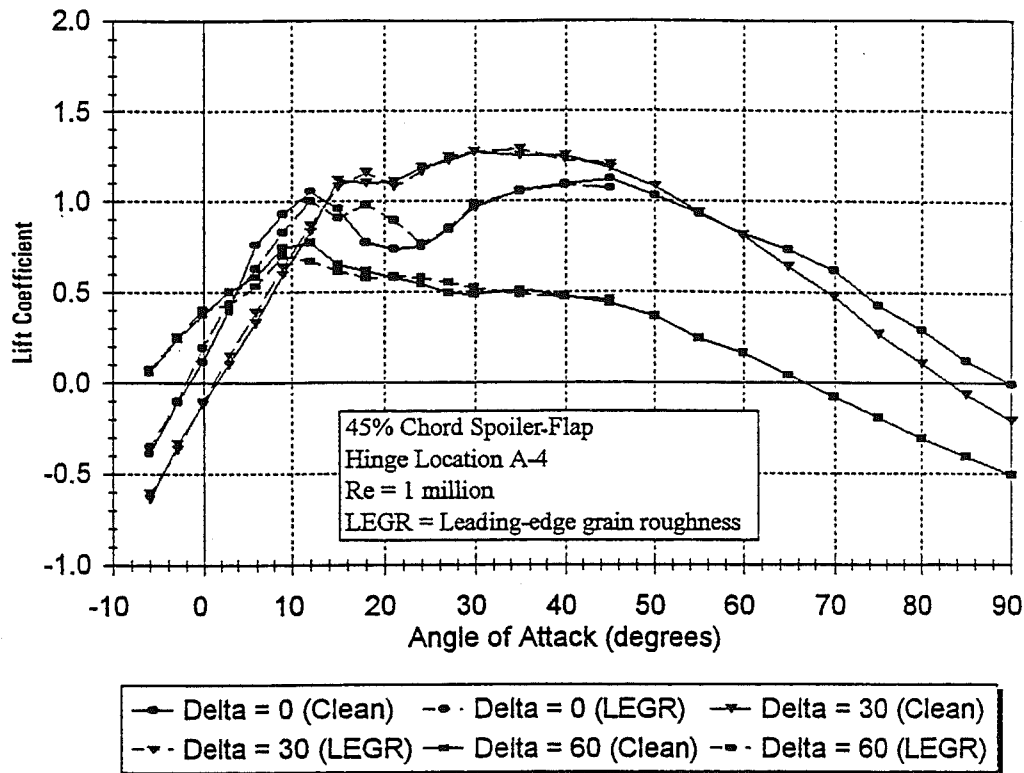


Figure A-18a. Lift Data, Effect of Leading-Edge Roughness on Spoiler-Flap

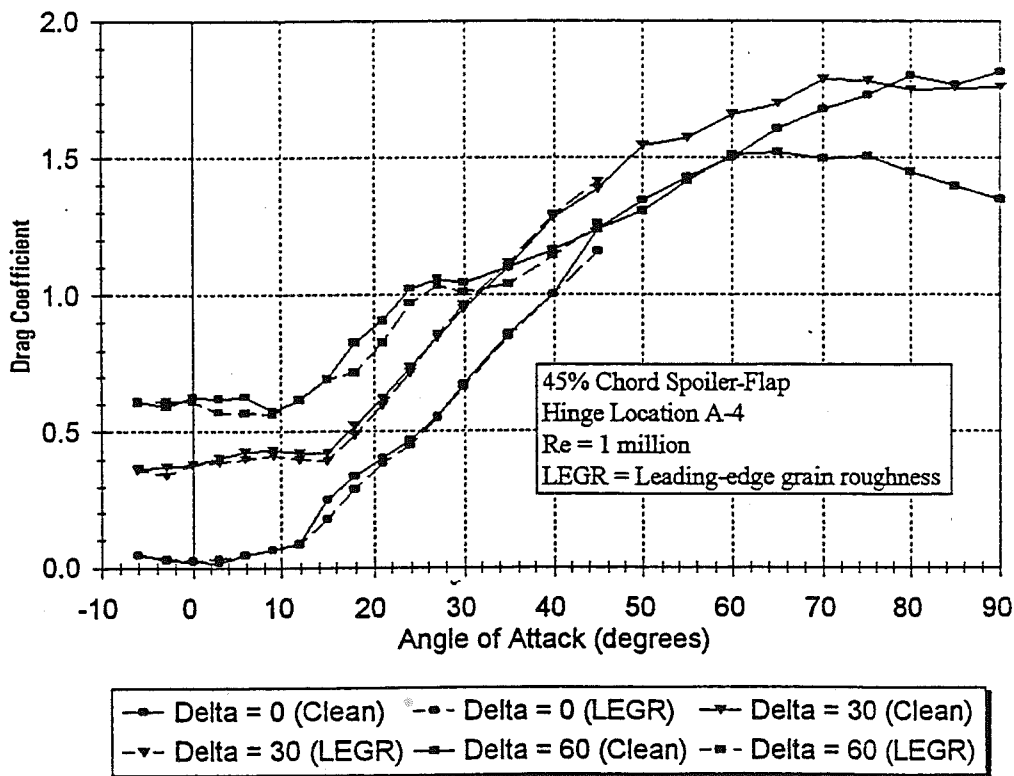


Figure A-18b. Drag Data, Effect of Leading-Edge Roughness on Spoiler-Flap

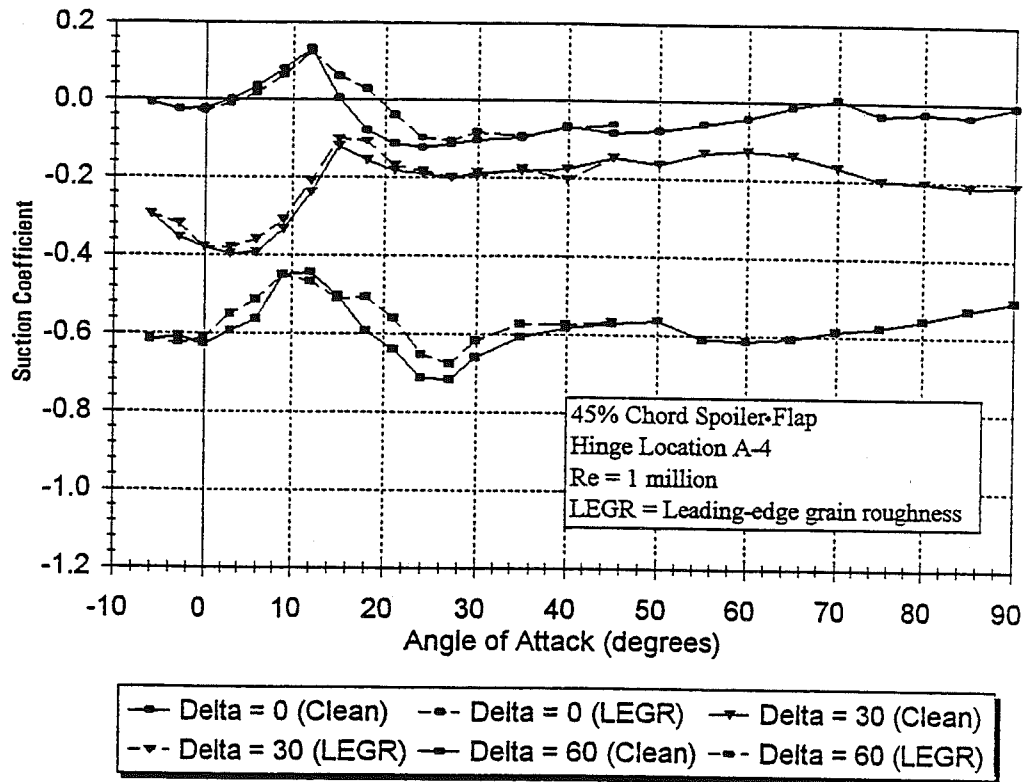


Figure A-18c. Suction Data, Effect of Leading-Edge Roughness on Spoiler-Flap

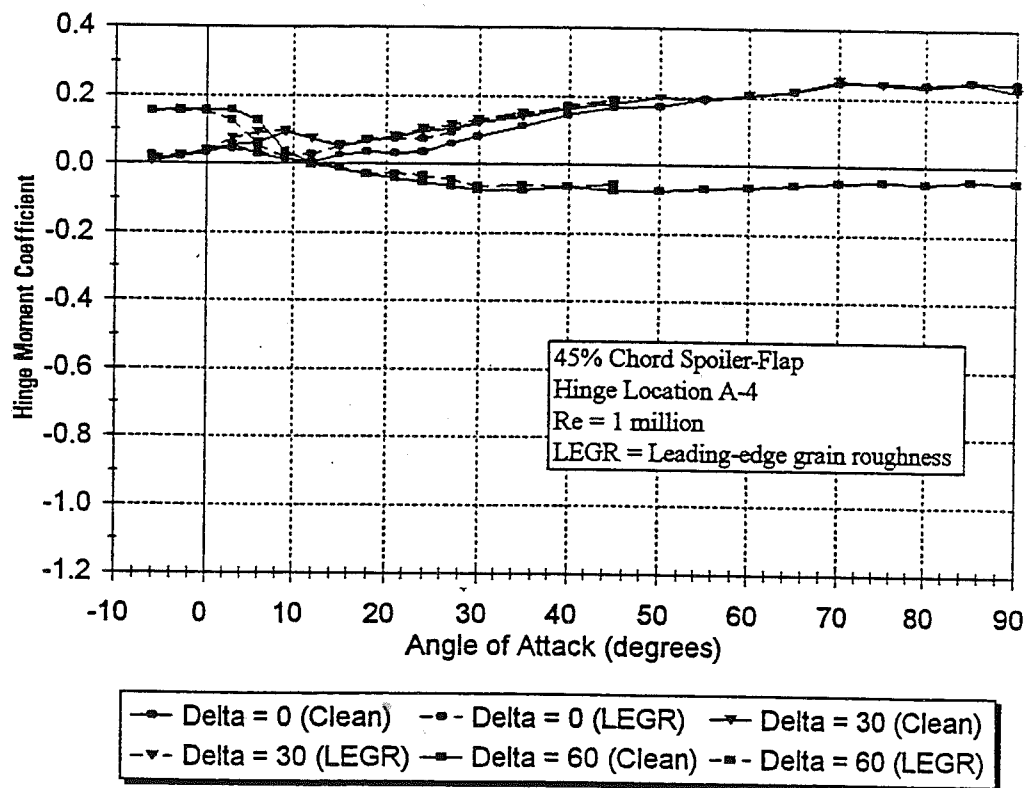


Figure A-18d. Hinge Moment Data, Effect of Leading-Edge Roughness on Spoiler-Flap

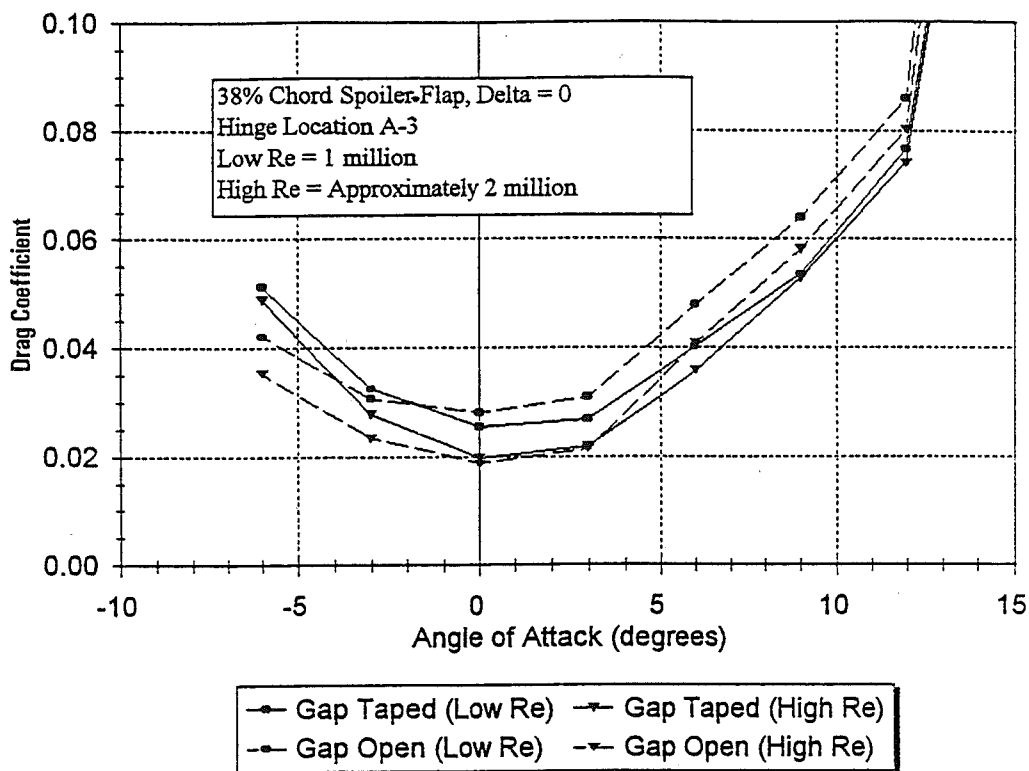


Figure A-19. Effect of Gap Seal on 38% Chord Device

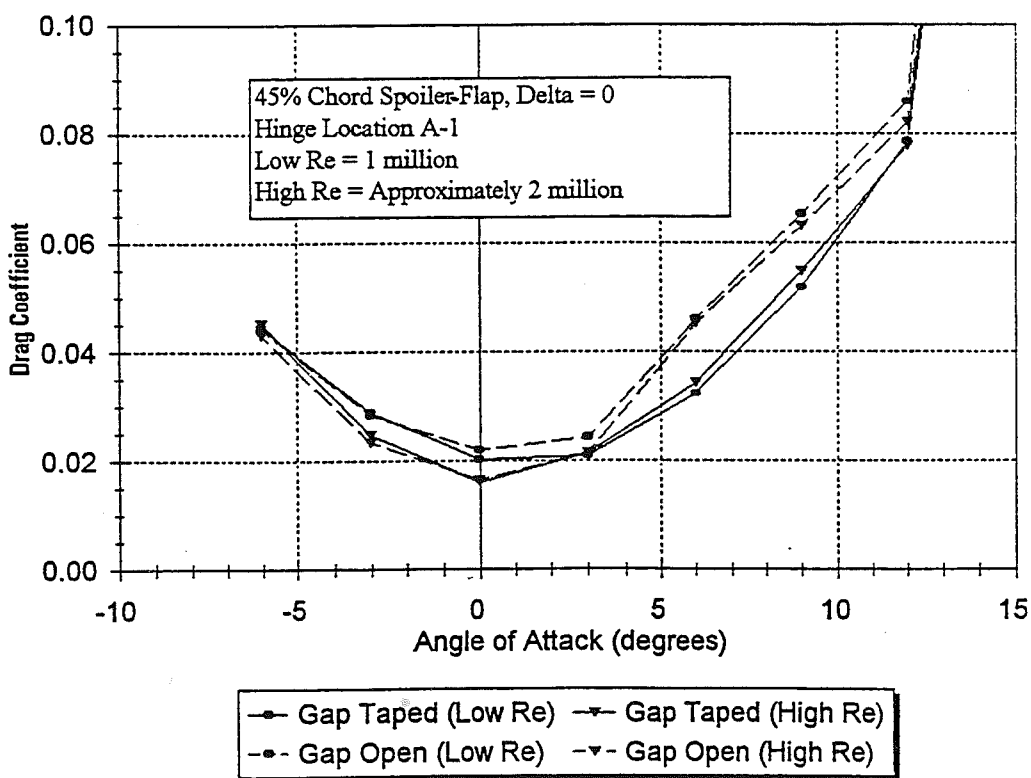


Figure A-20. Effect of Gap Seal on 45% Chord Device

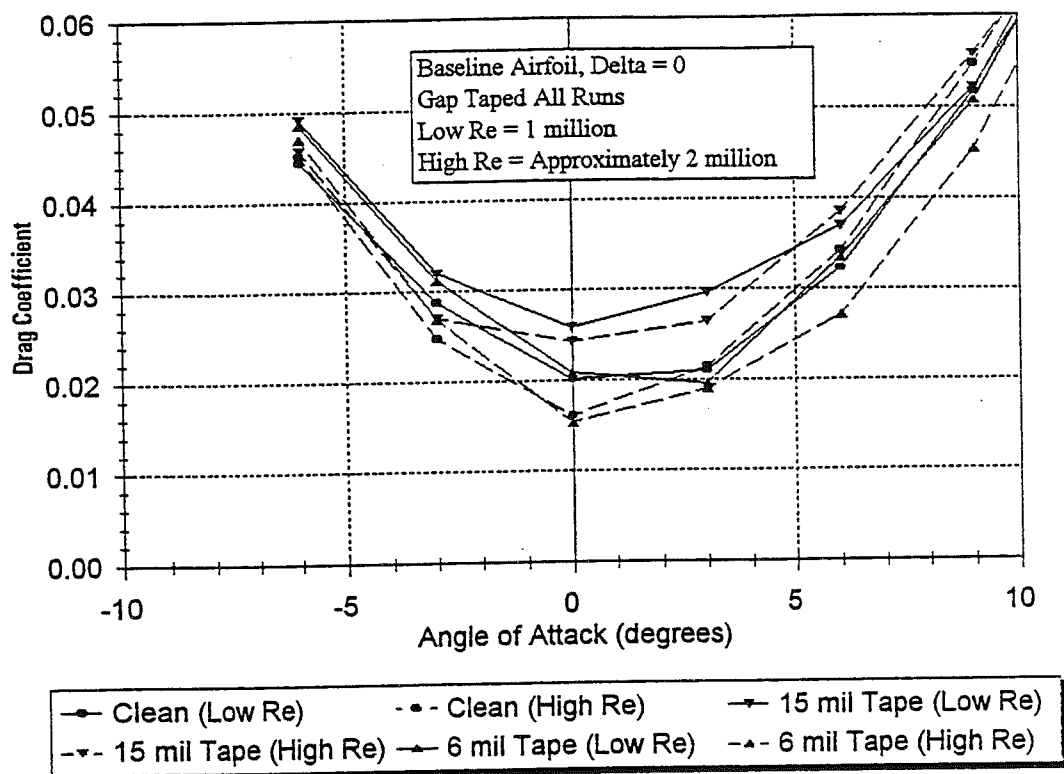


Figure A-21. Effect of Leading-Edge Tape on Clean S810

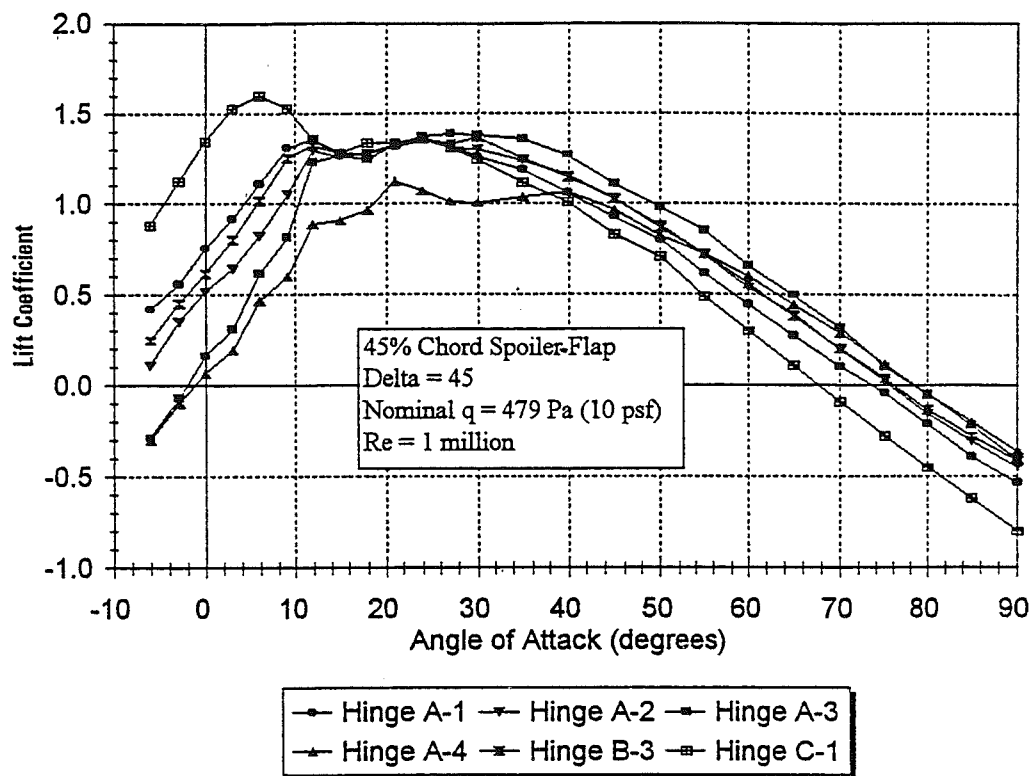


Figure A-22a. Lift Data, Effect of Hinge Location on Device at $\delta = 45^\circ$

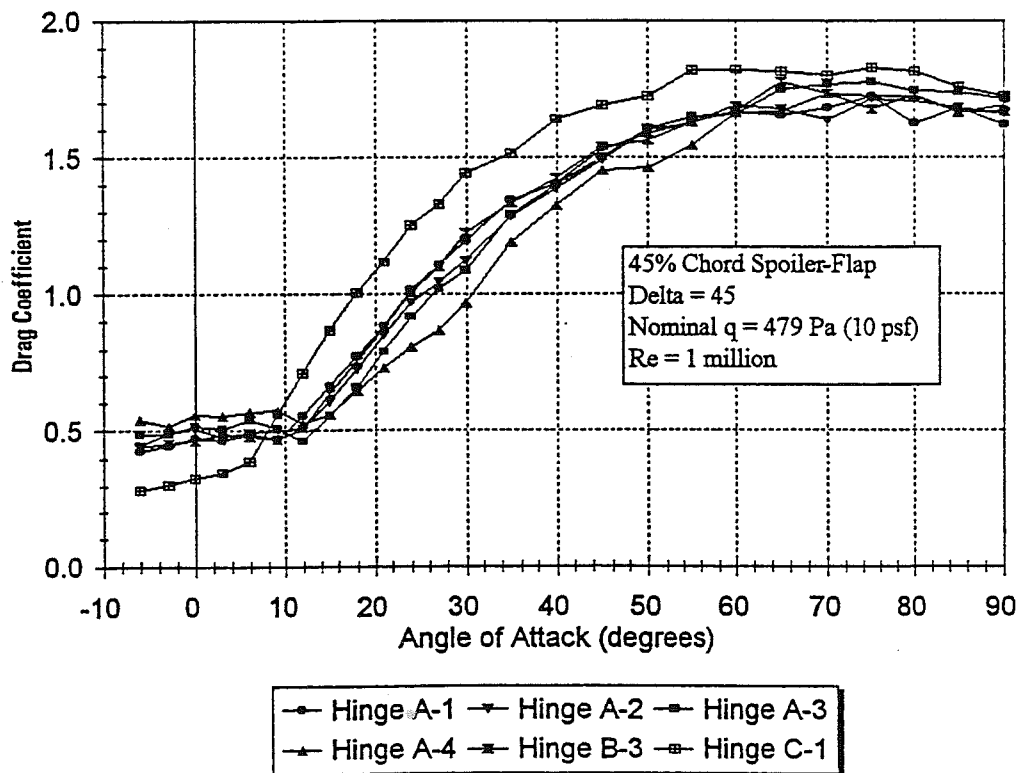


Figure A-22b. Drag Data, Effect of Hinge Location on Device at $\delta = 45^\circ$

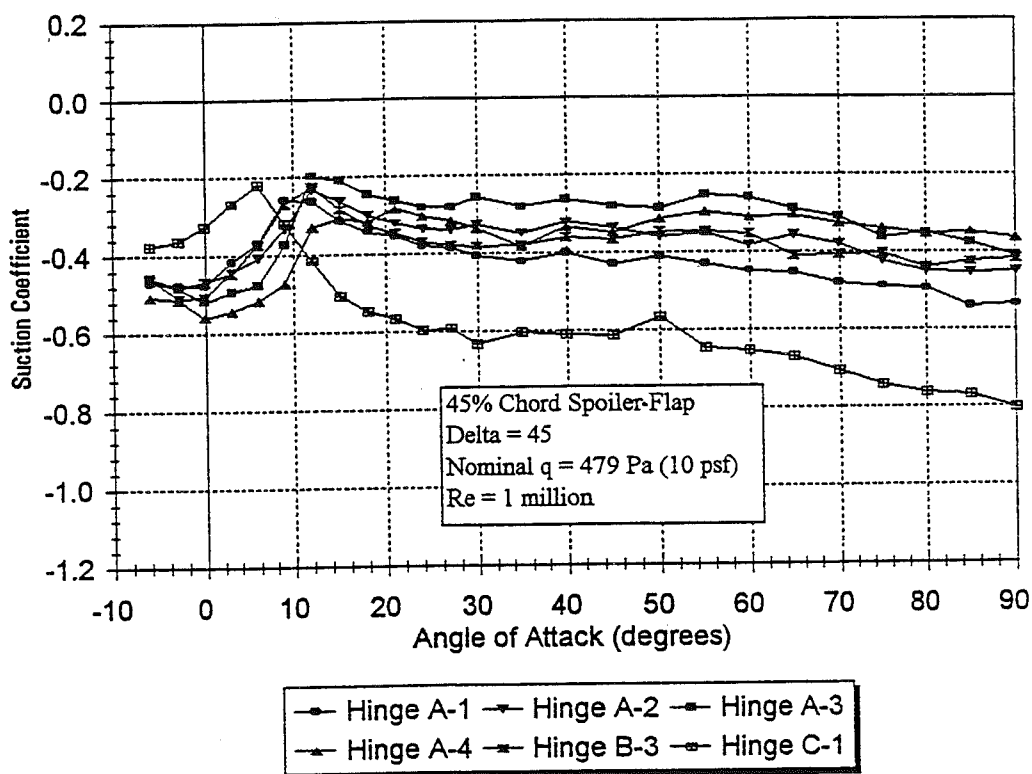


Figure A-22c. Suction Data, Effect of Hinge Location on Device at $\delta = 45^\circ$

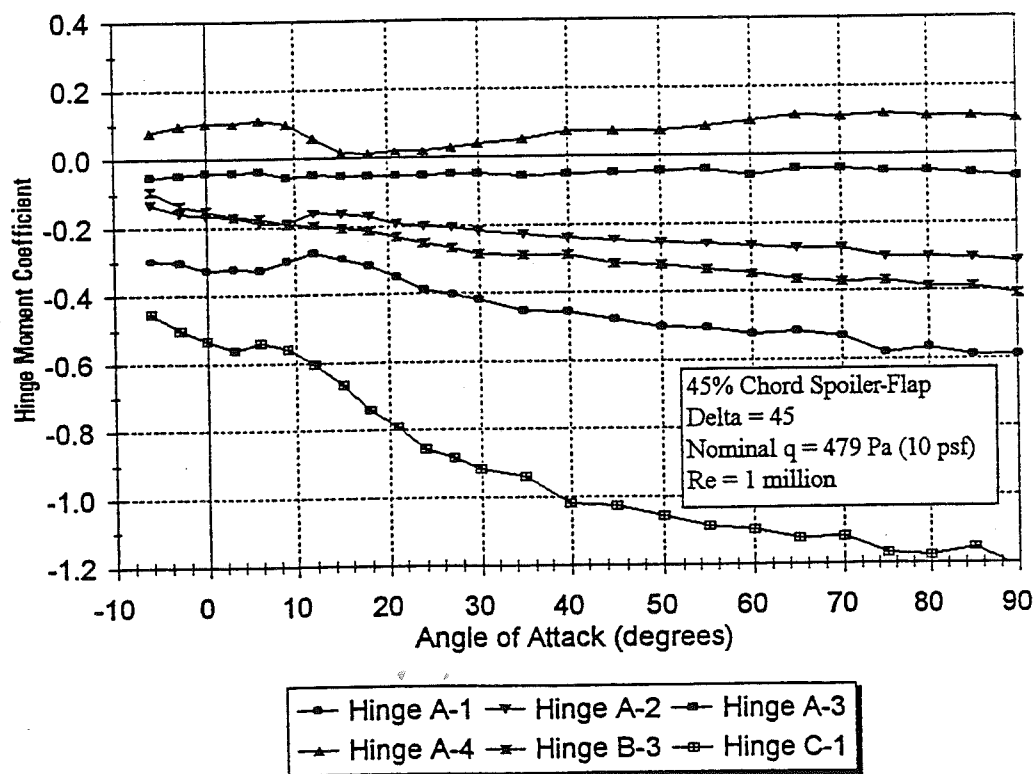


Figure A-22d. Hinge Moment Data, Effect of Hinge Location on Device at $\delta = 45^\circ$

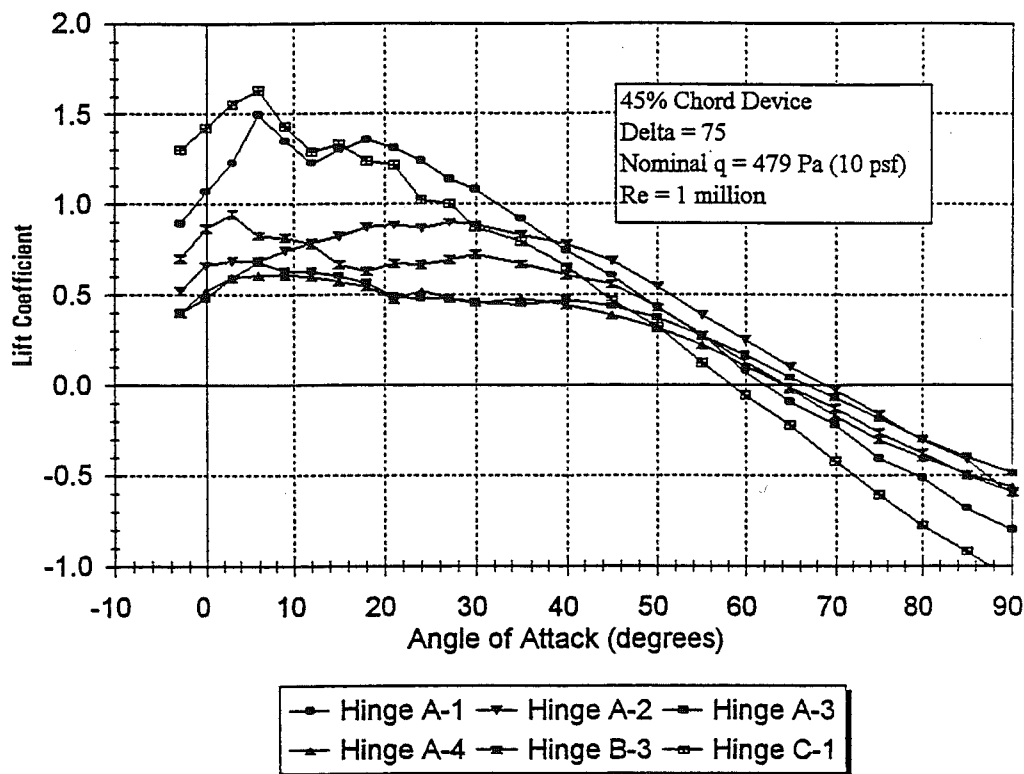


Figure A-23a. Lift Data, Effect of Hinge Location on Device at $\delta = 75^\circ$

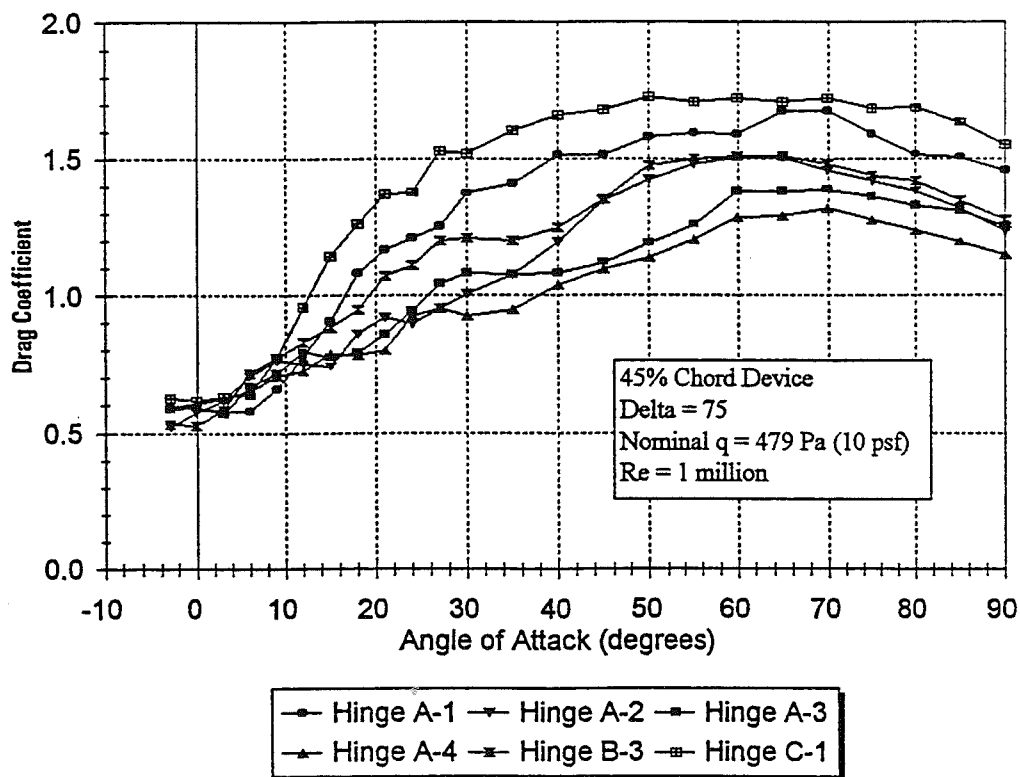


Figure A-23b. Drag Data, Effect of Hinge Location on Device at $\delta = 75^\circ$

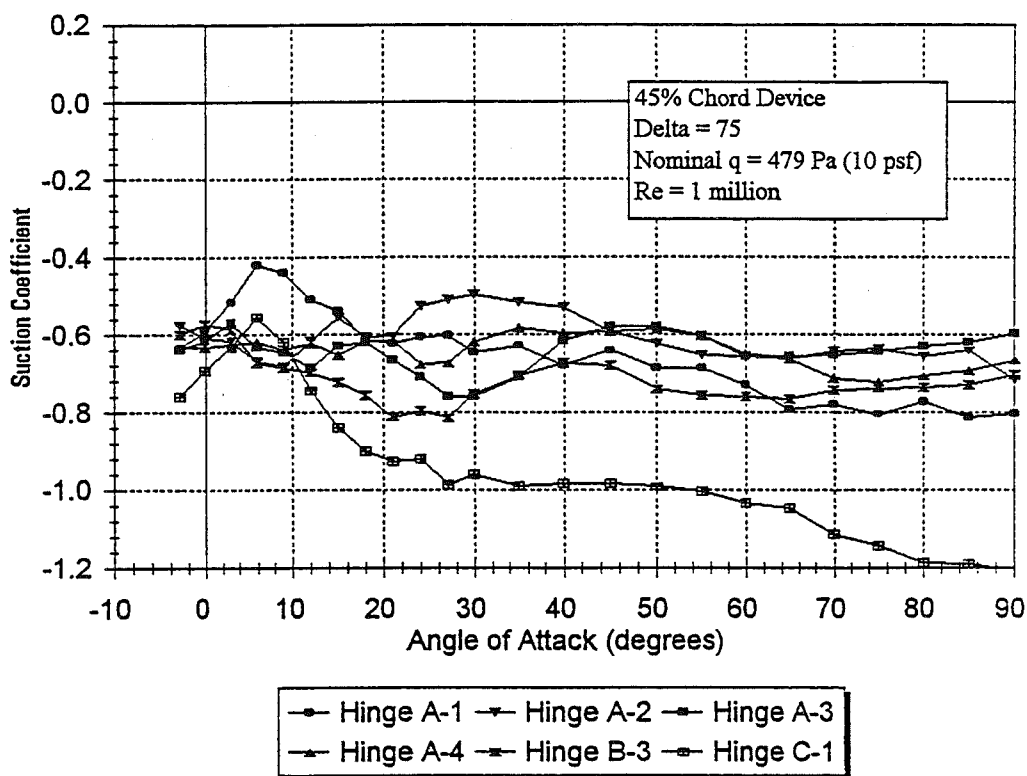


Figure A-23c. Suction Data, Effect of Hinge Location on Device at $\delta = 75^\circ$

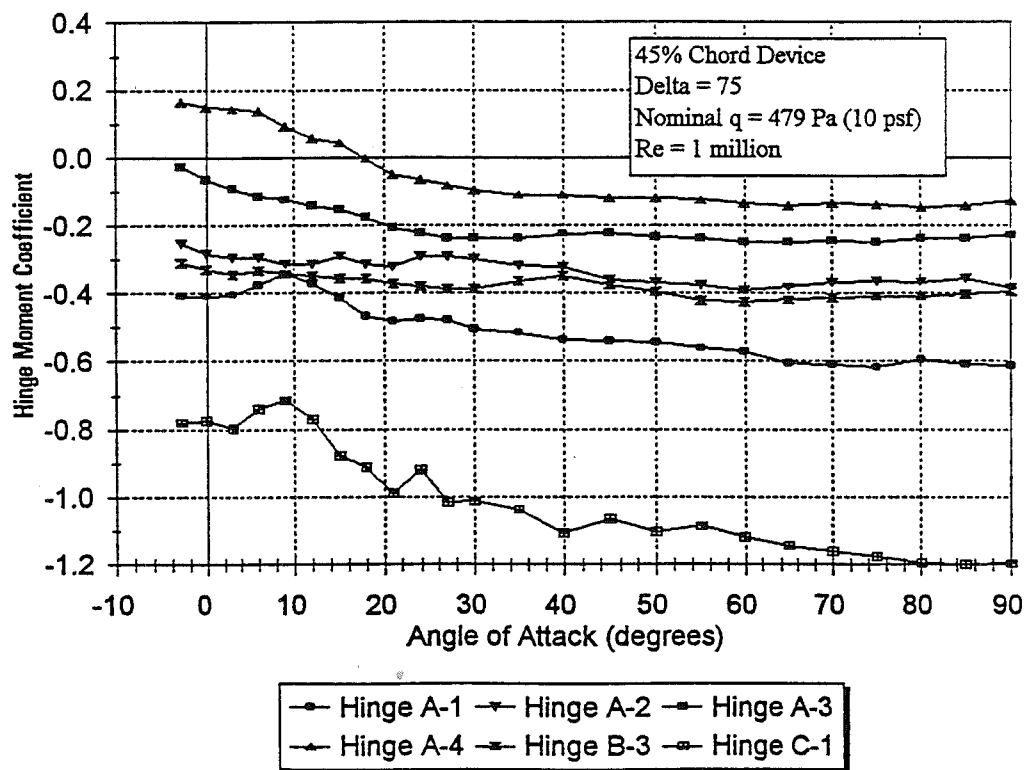


Figure A-23d. Hinge Moment Data, Effect of Hinge Location on Device at $\delta = 75^\circ$

APPENDIX B

Documentation of Cost and Weight Estimates

Spoiler-Flap Active Mechanical System, Pneumatic/Bellcrank, Hinge A-3, Cost Analysis

Qty.	Assembly/ Part No.	Cost Basis	Description	COST (\$)				Notes	
				Parts	ext.	Hours per assembly	Total Hours	Subtotal	(l) = labor
1	xx10000	(l)	System Assy.	-	-	1.0	1.0	35.00	(l) connect pneumatic fittings, rig spoiler-flap
2	xx63000	(l)	Blade Assy.	-	-	0.5	1.0	35.00	(l) install spoiler-flap, connect pushrod
2	xx63000-1	1	Gas Spring, outboard	16.00	32.00	0.1	0.2	39.00	clip to ball studs
2	xx63000-1	1	Gas Spring, inboard	16.00	32.00	0.1	0.2	39.00	clip to ball studs
4	xx63000-2	1	Gas Spring Connecting Bracket	0.99	3.96	0.2	0.8	31.96	(l) secure to rib
2	xx63100	(l)	43' Blade, notched	-	-	8.00	16.0	560.00	(l) Cut out rough spoiler-flap, dress edges, secure ribs and web blocking, install bellcrank assy, install cylinder attach bracket, secure gap seals, install air hose clips and air hose.
2	xx63100-1	2	Hose, Cylinder to Valve	7.00	14.00	0.5	1.0	35.00	40' x 10/ft. + 2 fittings @ \$3.00 ea., (l) assemble
2	xx63100-2	1	Pneumatic Cylinder	114.70	229.40	0.4	0.8	28.00	(l) secure with pins to brackets
2	xx63100-3	5	Cylinder Attach Bracket, with backup plate	15.00	30.00	0.5	1.0	35.00	(l) drill web blocking, secure bracket with 4 bolts
8	xx63100-4	3	Bracket Attach Bolts	0.50	4.00	-	-	4.00	
8	xx63100-5	3	Washers	0.10	0.80	-	-	0.80	
8	xx63100-6	3	Nuts	0.25	2.00	-	-	2.00	
2	xx63100-7	3	Clevis Pin	1.00	2.00	-	-	2.00	
30	xx63100-8	1	Gap seal	0.55	16.50	-	-	16.50	"p" seal, \$.55/ft.
2	xx63100-9	2	Thrust Bearing	2.11	4.22	-	-	4.22	Torrington FNTA-2035
8	xx63100-1	2	Thrust Washer	0.64	5.12	-	-	5.12	INA AS2035
4	xx63100-1	3	Hinge Bolt	2.50	10.00	-	-	10.00	
4	xx63100-1	3	Castellated Nut	0.95	3.80	-	-	3.80	
8	xx63100-1	3	Washer	0.35	2.80	-	-	2.80	
30	xx63100-1	2	hose guide eyelets	0.35	10.50	-	-	10.50	

Qty.	Assembly/ Part No.	Cost Basis	Description	COST (\$)					Notes
				Parts	ext.	Hours per assembly	Total Hours	Subtotal	
2	xx63110	4	Blade Rib, inboard hinge support, laminated wood	9.12	18.24	-	-	18.24	(I) = labor
2	xx63130	4	Blade Hinge Rib, outboard hinge support, laminated wood	3.50	7.00	-	-	7.00	
2	xx63140	5	Web blocking, cylinder attach bracket	2.00	4.00	-	-	4.00	
2	xx63150	5	Web blocking, bellcrank bracket	2.00	4.00	-	-	4.00	
2	xx63200	(I)	Spoller-Flap Assy.	-	-	1.5	3.0	105.00	(I) dress edges, bond ribs and webs, seal interior surfaces with epoxy
2	xx63210	(I)	Hinge Rib Assy, Inboard	-	-	1.0	2.0	70.00	(I) install gas strut mount stud, bore rib at hinge location, install thrust washer and thrust stud
2	xx63210-1	2	Gas Spring Connecting Bracket	0.70	1.40	0.2	0.4	14.00	(I) secure to rib
2	xx63211	4	Hinge Rib, Inboard, laminated wood	1.45	2.90	-	-	2.90	
2	xx63220-1	3	Clevis Bolt, pushrod attach	2.50	5.00	-	-	5.00	
2	xx63220-2	3	Nut, Castellated	0.50	1.00	-	-	1.00	
4	xx63220-3	3	Washer	0.10	0.40	-	-	0.40	
2	xx63230	(I)	Hinge Rib Assy, Outboard	-	-	1.0	2.0	70.00	(I) install gas strut mount stud, bore rib at hinge location, install thrust washer and thrust stud
8	xx63232	3	Hinge Stud	0.84	6.72	-	-	6.72	
2	xx63230-1	2	Gas Spring Connecting Bracket	0.99	1.98	0.2	0.4	14.00	(I) secure to rib
2	xx63231	4	Hinge Rib, outboard, laminated wood	0.84	1.68	-	-	1.68	
2	xx63240	4	Web, Inboard	5.00	10.00	-	-	10.00	1/4" birch ply

B-3

Qty.	Assembly/ Part No.	Cost Basis	Description	COST (\$)				Notes
				Parts	ext.	Hours per assembly	Total Hours	
								Subtotal
								(l) = labor
2	xx63250	4	Web, Outboard	5.00	10.00			10.00
2	xx63300	(l)	Pushrod Assy.		-	0.2	0.4	14.00
2	xx63300-1	2	Clevis	7.00	14.00			14.00
2	xx63300-2	2	Stop Nut	0.50	1.00			1.00
2	xx63300-3	2	Rod End, Solid Stem	10.50	21.00			21.00
2	xx63300-4	2	Rivet, rod end locking	0.70	1.40			1.40
2	xx63400	3	Bellcrank Assy.		-	0.3	0.6	21.00
2	xx63400-1	2	Bearing, cylinder connect	8.40	16.80			16.80
2	xx63400-2	2	Bearing, pushrod connect	17.50	35.00			35.00
2	xx63400-3	2	Bearing, bellcrank pivot	8.40	16.80			16.80
2	xx63400-4	3	Bolt, bellcrank pivot	2.50	5.00			5.00
2	xx63400-5	3	Nut, bellcrank pivot	0.50	1.00			1.00
4	xx63400-6	3	Washer, bellcrank pivot	0.10	0.40			0.40
8	xx63400-7	3	Bolt, bellcrank mount	0.50	4.00			4.00
8	xx63400-8	3	Nut, bellcrank mount	0.25	2.00			2.00
16	xx63400-9	3	Washer, bellcrank mount	0.10	1.60			1.60
2	xx63410	5	Bellcrank Machining	36.00	72.00			72.00
2	xx63420	5	Bellcrank Bracket, with backup plate	90.00	180.00			180.00
1	xx13000	(l)	Hub Assy.		-	2.0	2.0	70.00
1	xx13000-2	1	Compressor	329.70	329.70			329.70
1	xx13000-3	2	Custom air tank with mount brackets	105.00	105.00			105.00
1	xx13000-4	1	Solenoid Valve	18.80	18.80			18.80
1	xx13000-5	2	Hose, Compressor to Tank	7.00	7.00	0.5	0.5	17.50
1	xx13000-6	2	Hose, Tank to Valve	7.00	7.00	0.5	0.5	17.50
								24.50
								24.50
								70.00
								(l) install compressor, tank, and solenoid valve, install fuse box, wire components

Qty.	Assembly/ Part No.	Cost Basis	Description	COST (\$)				Notes
				Parts	ext.	Hours per assembly	Total Hours	
1	xx13100	(I)	Hub, Machined		-	0.8	0.8	(I) additional drilling for pneumatic system components
NA	6		Unspecified parts and processes	200.00	200.00		5.0	375.00
System Totals				\$ 1,517			39.6	\$ 1,386 \$ 2,903 Installed cost, 2 spoiler-flaps

hourly rate = 35.00, wrap

Legend for cost basis:

- 1 Based on price quote for part quantity required for 100 AWT wind turbines
- 2 Catalog price less assumed 30% discount for quantity purchase
- 3 Cost estimate based on AWT production invoices for comparable items
- 4 Cost estimated based on dollars per pound of production AWT wood-epoxy blades
- 5 Cost estimated based on dollars per pound of production AWT tip-vane hinge assembly
- 6 Cost estimate based on design and manufacturing experience of engineers at AWT and Advanced Blade Manufacturing, Inc. Due to the preliminary nature of the design, additional labor and material costs (unspecified parts and processes) are anticipated. Design details which may increase costs include:
 - Addition of access panels for inspection and maintenance of actuator system
 - High-durability weather proofing of all cut wood-epoxy surfaces (blade and flap)
 - Addition of damping or cushions to prevent hard mechanical stop of spoiler-flap during deployment
 - Additional cost of properly sealing spanwise gaps and end gaps to ensure smooth aerodynamic surfaces and minimal noise during turbine operation
 - Possible need for close-tolerance bolts
 - Possible need for structural reinforcement of blade or spoiler-flap
 - Addition of position sensor/switch for input to controller

Spoiler-Flap Active Mechanical System, Pneumatic/Bellcrank, Hinge A-3 Weight Analysis

Qty.	Assembly/ Part No.	Description	Wt. (lb)	ext.	subtot.	Total	Notes
1	xx10000	System Assy.					
2	xx63000	Blade Assy.					
2	xx63000-1	Gas Spring, outboard	2.00	4.00			
2	xx63000-1	Gas Spring, inboard	2.00	4.00			
4	xx63000-2	Gas Spring Connecting Bracket	0.10	0.40			
2	xx63100	43' Blade, notched					
2	xx63100-1	Hose, Cylinder to Valve	1.20	2.40			
2	xx63100-2	Pneumatic Cylinder	11.10	22.20			
2	xx63100-3	Cylinder Attach Bracket, with backup plate	0.50	1.00			
8	xx63100-4	Bracket Attach Bolts	0.02	0.16			
8	xx63100-5	Washers	0.01	0.08			
8	xx63100-6	Nuts	0.01	0.08			
2	xx63100-7	Clevis Pin	0.10	0.20			
30	xx63100-8	Gap seal	0.10	3.00			
2	xx63100-9	Thrust Bearing	0.10	0.20			
8	xx63100-10	Thrust Washer	0.05	0.40			
4	xx63100-11	Hinge Bolt	0.10	0.40			
4	xx63100-12	Castellated Nut	0.05	0.20			
8	xx63100-13	Washer	0.02	0.16			
30	xx63100-14	hose guide eyelets	0.01	0.30			
2	xx63110	Blade Rib, inboard hinge support, laminated wood 1/2 in thick	3.50	7.00			
2	xx63130	Blade Hinge Rib, outboard hinge support, laminated wood 1/2 in thick	2.00	4.00			

Qty.	Assembly/ Part No.	Description	Wt. (lb)	ext.	subtot.	Total	Notes
2	xx63140	Web blocking, cylinder attach bracket	0.50	1.00			
2	xx63150	Web blocking, bellcrank bracket	0.50	1.00			
2	xx63200	Spoiler-Flap Assy.					
2	xx63210-1	Gas Spring Connecting Bracket	0.10	0.20			
2	xx63211	Hinge Rib, inboard, laminated wood	2.00	4.00			
2	xx63220-1	Clevis Bolt, pushrod attach	0.10	0.20			
2	xx63220-2	Nut, Castellated	0.05	0.10			
4	xx63220-3	Washer	0.02	0.08			
8	xx63232	Hinge Stud	0.74	5.92			
2	xx63230-1	Gas Spring Connecting Bracket	0.10	0.20			
2	xx63231	Hinge Rib, outboard, laminated wood	1.00	2.00			
2	xx63240	Web, Inboard	1.00	2.00			
2	xx63250	Web, Outboard	1.00	2.00			
2	xx63300	Pushrod Assy.	1.50	3.00			
2	xx63300-1	Clevis	0.10	0.20			
2	xx63300-2	Stop Nut	0.02	0.04			
2	xx63300-3	Rod End, Solid Stem	0.10	0.20			
2	xx63300-4	Rivet, rod end locking	0.01	0.02			
2	xx63400	Bellcrank Assy.					
2	xx63400-1	Bearing, cylinder connect	0.01	0.02			
2	xx63400-2	Bearing, pushrod connect	0.01	0.02			
2	xx63400-3	Bearing, bellcrank pivot	0.06	0.12			
2	xx63400-4	Bolt, bellcrank pivot	0.05	0.10			
2	xx63400-5	Nut, bellcrank pivot	0.02	0.04			
4	xx63400-6	Washer, bellcrank pivot	0.01	0.04			

Qty.	Assembly/ Part No.	Description	Wt. (lb)	ext.	subtot.	Total	Notes
8	xx63400-7	Bolt, bellcrank mount	0.05	0.40			
8	xx63400-8	Nut, bellcrank mount	0.02	0.16			
16	xx63400-9	Washer, bellcrank mount	0.01	0.16			
2	xx63410	Bellcrank Machining	0.60	1.20			
2	xx63420	Bellcrank Bracket, with backup plate	1.50	3.00			
Total Blade Assembly (2 blades)							Total blade assembly weight is in addition to the baseline weight of AWT 26/27 wood-epoxy blade.
					77.60		
Total Blade Assembly (2 blades)							
1	xx13000	Hub Assy.					
1	xx13000-1	Hub Fuse Box	5.00	5.00			
1	xx13000-2	Compressor	15.00	15.00			
1	xx13000-3	Custom air tank with mount brackets	15.00	15.00			
1	xx13000-4	Solenoid Valve	1.00	1.00			
1	xx13000-5	Hose, Compressor to Tank	0.50	0.50			
1	xx13000-6	Hose, Tank to Valve	0.50	0.50			
Total Hub Assembly					37.00		Total hub assembly weight is in addition to the baseline weight of AWT 26/27 hub.
Total Spoiler-Flap System							
						114.60	

REPORT DOCUMENTATION PAGE

Form Approved
OMB NO. 0704-0188

Public reporting burden for this collection of information is estimated to average 1 hour per response, including the time for reviewing instructions, searching existing data sources, gathering and maintaining the data needed, and completing and reviewing the collection of information. Send comments regarding this burden estimate or any other aspect of this collection of information, including suggestions for reducing this burden, to Washington Headquarters Services, Directorate for Information Operations and Reports, 1215 Jefferson Davis Highway, Suite 1204, Arlington, VA 22202-4302, and to the Office of Management and Budget, Paperwork Reduction Project (0704-0188), Washington, DC 20503.

1.	2. REPORT DATE April 1997	3. REPORT TYPE AND DATES COVERED Subcontractor Report	
4. TITLE AND SUBTITLE Investigation of Aerodynamic Braking Devices for Wind Turbine Applications		5. FUNDING NUMBERS C: ZAA-5-12272-05 TA: WE713010	
6. AUTHOR(S) D. A. Griffin			
7. PERFORMING ORGANIZATION NAME(S) AND ADDRESS(ES) R. Lynette & Associates 425 Pontius Ave. North, Suite 150 Seattle, WA 98109		8. PERFORMING ORGANIZATION REPORT NUMBER	
9. SPONSORING/MONITORING AGENCY NAME(S) AND ADDRESS(ES) National Renewable Energy Laboratory 1617 Cole Blvd. Golden, CO 80401-3393		10. SPONSORING/MONITORING AGENCY REPORT NUMBER SR-440-22253 DE97000234	
11. SUPPLEMENTARY NOTES			
12a. DISTRIBUTION/AVAILABILITY STATEMENT National Technical Information Service U.S. Department of Commerce 5285 Port Royal Road Springfield, VA 22161		12b. DISTRIBUTION CODE UC-1213	
13. ABSTRACT (Maximum 200 words) This report documents the selection and preliminary design of a new aerodynamic braking system for use on the stall-regulated AWT-26/27 wind turbines. The goal was to identify and design a configuration that offered improvements over the existing tip brake used by Advanced Wind Turbines, Inc. Although the design objectives and approach of this report are specific to aerodynamic braking of AWT-26/27 turbines, many of the issues addressed in this work are applicable to a wider class of turbines. The performance trends and design choices presented in this report should be of general use to wind turbine designers who are considering alternative braking methods.			
14. SUBJECT TERMS renewable energy; wind energy; wind turbine design; wind turbines—electricity generation; wind turbine rotor design; trailing-edge devices; aerodynamic controls; spoiler-flap		15. NUMBER OF PAGES	
		16. PRICE CODE	
17. SECURITY CLASSIFICATION OF REPORT Unclassified	18. SECURITY CLASSIFICATION OF THIS PAGE Unclassified	19. SECURITY CLASSIFICATION OF ABSTRACT Unclassified	20. LIMITATION OF ABSTRACT UL